National Academy of Science of Ukraine
Bogolyubov Institute for Theoretical Physics

NEW TRENDS IN HIGH-ENERGY PHYSICS

Proceedings of the Conference held in Alushta (Crimea) on September 23-29, 2013

Edited by
László Jenkovszky, Denis Savchenko and Georgiy Stelmakh

Kiev 2013

FOREWORD

The XXIII-d International Conference on ***New Trends in High-Energy Physics*** (NTHEP), co-organized by the Bogolyubov Institute for Theoretical Physics, National Academy of Science of Ukrain, the Joint Institute for Nuclear Research (Dubna), the Institute for Nuclear Research, RAS (Moscow) and the Steklov Mathematical Institute RAS (Moscow), was held in Alushta, Crimea on September 23-29, 2013.

The present Proceedings contain written versions of the invited talks, grouped in two sections: 1. ***Experiment*** and 2. ***Phenomenology & Theory***. Within each section, the talks are ordered alphabetically, by the first author.

To speed up the publication, we minimized editorial intervention.

We thank the Authors for their invaluable contributions and apologize for the black-and-white reproduction of the color figures. This omission is compensated on our WEB page: http://crimea.bitp.kiev.ua/, where all papers of the present Proceedings appear in full color.

Editors

ISBN 978-966-02-7015-2

CONTENTS

2. PHENOMENOLOGY AND THEORY

CONFERENCE PROGRAM

8.00	Breakfast
14.00	Lunch
19.00	Dinner

September 23 (Monday)

16.00–22.00	*Arrival and registration*

September 24 (Tuesday)

9.00	*Opening*
	Quantum field theory:
	Chairman: R. Lednický
9.15	D. Shirkov
9.50	A. Slavnov
	Break & registration (continued)
	Chairman: R. Orava
12.00	L. Lipatov
12.35	A. Efremov
15.00–19.00	*Excursion 1*
19.00	*Welcome*

September 25 (Wednesday)

	LHC physics:
	Chairman: N. Rusakovich
9.00	S. Franchino
9.25	R. Brenner
9.50	M. Deile
10.15	R. Orava
10.40	M. Eads
	Break
	Chairman: M. Deile
11.20	G. Mitsuka
11.45	M. Pieri
12.10	M. Tomoto
12.35	E. Krishen
12.55	A. Chapelain
13.15	M. Taševský

14.00–19.30 *Excursion 2*

Phenomenological theory
Chairman: V. Magas

20.00 V. Braguta
20.25 A. Babich

September 26 (Thursday)

Astroparticle physics:
Chairman: I. Tserruya

9.00 D.Gorbunov
9.30 A. Kusenko
10.00 J. Řídký
10.25 L. Tkachev
10.45 A. Flanchik

Break

Experiment:
Chairman: A. Slavnov

11.45 N. Rusakovich
12.15 I. Tserruya
12.40 V. Kolesnikov

14.00–19.30 *Excursion 3*

Quantum field theory:
Chairman: M. Eads

20.00 S. Sibiryakov
20.25 V. Fadin
20.45 G. Stavraki
21.05 L. Martinovic

Break

Chairman: R. Brenner

21.20 D. Bykov
21.40 N. Gromov
22.00 A. Korchin

September 27 (Friday)

LHC physics:
Chairman: S. Franchino

9.00 Ch. Royon
9.25 V. Solovyev
9.50 R. Schicker

Break& group photo (in front of the dining room)

Chairman: R. Schicker

11.00 A. Lanyov
11.20 V. Pugatch
11.40 B. Popovici
12.00 A. Serghienko

Phenomenological theory:
Chairman Ch. Royon

15.00 S. Larin
15.20 V. Magas
15.40 A. Salii
16.00 O. Kuprash

19.30 *Conference dinner*

September 28 (Saturday)

Phenomenological theory:
Chairman D. Gorbunov

9.00 R. Lednický
9.25 T. Epelbaum
9.50 T. Mertens

Break

Experiment:
Chairman V. Pugatch

11.00 O. Kouznetsov
11.25 S. Uzunyan
11.50 P. Golubev

Experiment:
Chairman S. Fomin

15.00 L. Afanasyev
15.25 A. Polyarush
15.50 V. Libov
16.10 M. Stepaniuk

Break

Chairman O. Kuprash

17.00 S. Levonian
17.20 D. Lontkovskyi
17.35 I. Makarenko
17.50 P. Zarubin
18.10 I. Zarubina

September 29 (Sunday)

	Phomenological theory:
	Chairman L. Jenkovszky
9.00	S. Fomin
9.25	V. Myronenko
9.45	A. Zhovtan
10.00	*General discussion and Closing*
12.00	*Lunch and departure*

1. EXPERIMENT

LAST RESULTS OF DIRAC EXPERIMENT AT CERN

Leonid Afanasyev

Joint Institute for Nuclear Research

Abstract

The DIRAC experiment presented the latest results on study of $\pi^+\pi^-$ atom lifetime, observation of πK atoms and a long-lived states of $\pi^+\pi^-$ atoms.

1. Introduction

The DIRAC experiment aims to observe and study hydrogen-like atoms formed by pairs of $\pi^+\pi^-$ and $\pi^\pm K^\mp$ mesons using the 24 GeV extracted beam of PS CERN. The lifetime of these atoms is dictated by the strong interaction between the components. Thus combining of hadrons into a hydrogen-like atom opens a unique possibility to study a property of the strong interaction at the very low relative momenta which are of order of the atom Bohr momentum. For $\pi^+\pi^-$ atom it is 0.5 MeV, for πK — 0.8 MeV. Hence the region of QCD confinement becomes available for investigation.

The ground-state lifetime of $\pi^+\pi^-$ atom $\tau_{2\pi}$ is governed by the $\pi\pi$ S-wave scattering lengths a_I, with isospin $I = 0, 2$ [1]: $1/\tau_{2\pi} \propto |a_0 - a_2|^2$. For the πK atom the lifetime $\tau_{\pi K}$ depends on the πK S-wave scattering lengths with isospin $1/2$ and $3/2$ [2]: $1/\tau_{2\pi} \propto |a_{1/2} - a_{3/2}|^2$. The values of these scattering lengths can be rigorously calculated in Chiral Perturbation Theory (ChPT) [4, 5]. Thus the measurement of the hadronic hydrogen-like atom lifetimes provide an experimental test of the low-energy QCD perditions.

Moving after the production in the target, the Pionium atoms may either decay into $\pi^0\pi^0$ or evolve by excitation (de–excitation) to different quantum states and finally decay or survive (long-lived states)

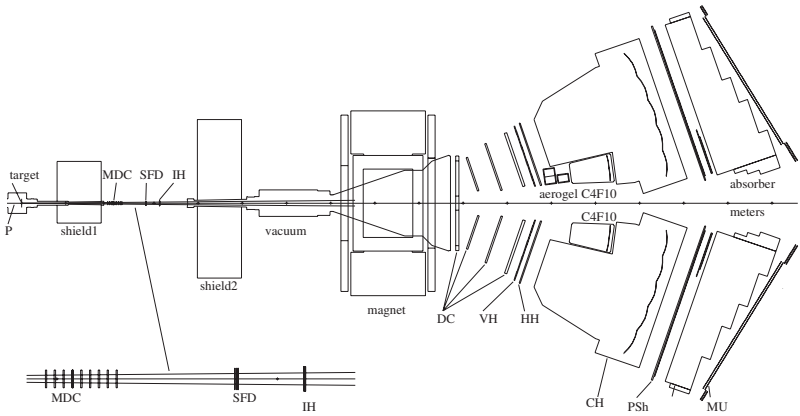

Fig. 1: DIRAC setup: MDC are microdrift gas chambers, SFD is a scintillating fiber detector and IH is a scintillation ionization hodoscope. Downstream the spectrometer magnet there are drift chambers (DC), vertical (VH) and horizontal (HH) scintillation hodoscopes, Cherenkov detectors containing nitrogen (CH), heavy gas C4F10 and aerogel radiators, shower detectors (PSh) and scintillation muon detectors (MU)

or break up (be ionized) by the electric field of the target atoms [7]. In the case of breakup, characteristic "atomic pairs" emerge with a low relative momentum Q in their center of mass ($Q < 3$ MeV/c), and small opening angle in the laboratory frame (< 3 mrad).

A high-resolution magnetic spectrometer ($\Delta p/p \sim 3 \times 10^{-3}$) is used [8] (Fig. 1) to identify the pairs and measure Q with sufficient precision to detect the pionium signal. This signal lies above a continuum background from free (unbound) "Coulomb pairs" produced from short lived sources ($\rho, \Delta \ldots$).Other background sources are "non-Coulomb pairs" where one or both pions originate from a long-lived source ($\eta, \eta', \Lambda, \ldots$) and accidental coincidences from different proton-nucleus interactions.

2. Results

Basing on 2008–2010 data the collaboration have double the number of observed "atomic pairs" n_A (see Fig. 2 compared to the already published results [9]. Processing of these data is in progress. The final expected accuracy in $|a_0 - a_2|$ is about 3%.

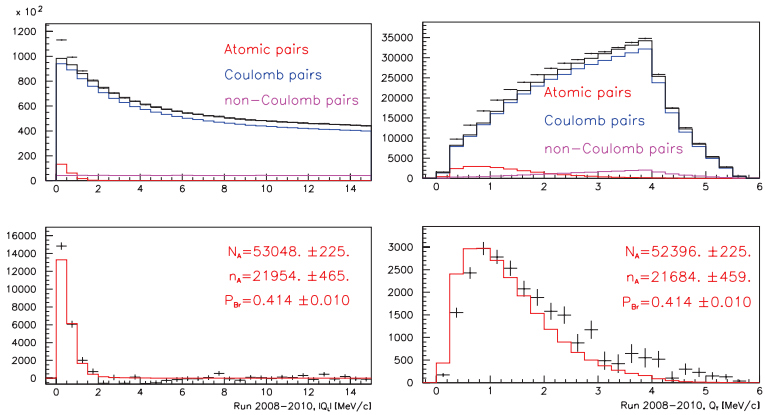

Fig. 2: Upper: experimental distributions of $\pi^+\pi^-$ pairs (points with error bars) over the longitudinal (Q_L) (left) and transverse (Q_T) (right) components of the pair CMS relative momentum Q, are fitted by a sum of simulated distributions of "atomic", "Coulomb" and "non-Coulomb" pairs. Free pairs ("Coulomb" and "non-Coulomb") shown by black line. Lower: difference of experimental and simulated distribution of "free" pairs comparing with simulated distributions of "atomic pairs"

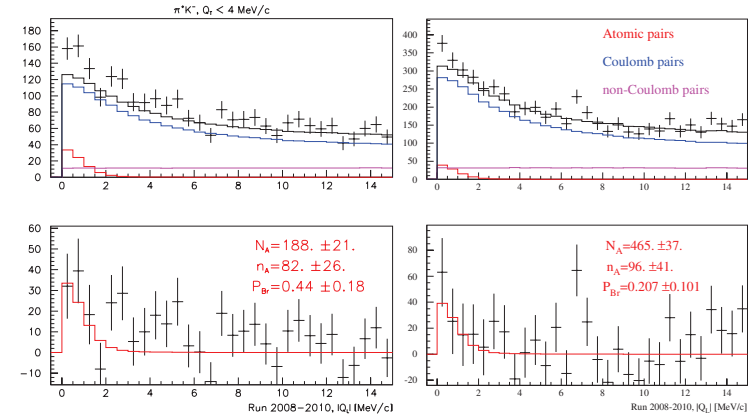

Fig. 3: Upper: experimental distribution over the longitudinal components of the pair CMS relative momentum (Q_L) of π^+K^- pairs (left) (points with error bars) and $K^+\pi^-$ (right) are fitted by a sum of simulated distributions of "atomic", "Coulomb" and "non-Coulomb" pairs. Free pairs ("Coulomb" and "non-Coulomb") shown by black line. Lower: difference of experimental and simulated distribution of "free" pairs comparing with simulated distributions of "atomic pairs"

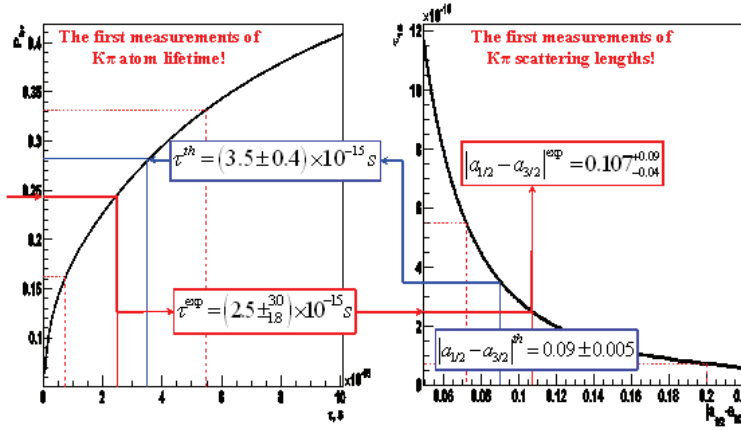

Fig. 4: Left: Probability of πK atom breakup as a function its lifetime allows extracting the lifetime from the experimental value the breakup probability (red line) and compare with the theoretical prediction (blue line). Right: Dependence of the lifetime on the scattering lengths allows extracting the preliminary results for the scattering lengths

Processing of the same data allows to extract 178 ± 49 πK "atomic pairs" (3.6σ significance) (see Fig. 3) and get the first estimation of its lifetime $\tau = \left(2.5^{+3.0}_{-1.8}\right) \times 10^{-15}$ s and evaluation of πK S-wave scattering length difference $|a_{1/2} - a_{3/2}| = 0.107^{+0.09}_{-0.04}$ (see Fig. 4).

During the 2011–2012 data taking DIRAC had as objective the observation of long lived states of $\pi^+\pi^-$ atoms [10]. To do so, behind the Beryllium foil of 100 μm installed in the primary proton beam, we have placed a Platinum foil of $2\mu m$ beyond the primary beam at the distance of 10 cm between them. The long lived states of $\pi^+\pi^-$ atoms produced in the Beryllium then break up in the Platinum resulting in observation of extra "atomic pairs". For significant suppression of the background of $\pi^+\pi^-$ pairs produced in the first foil a permanent magnet of 0.02 Tm bending power had been placed between the foils. The distribution of detected $\pi^+\pi^-$ pairs over longitudinal component of relative momentum Q_L with polynomial-fitted background is shown on Fig 5. The peak at zero with significance of 5σ is expected to be originate form breakup of the long-lived $\pi^+\pi^-$ atoms inside the Platinum foil.

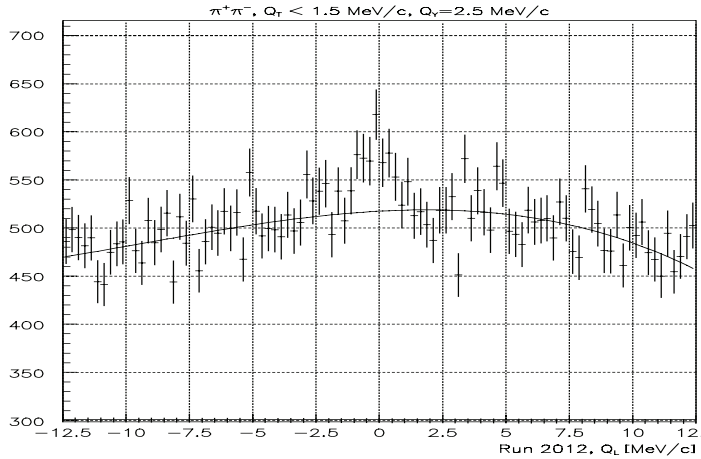

Fig. 5: Distribution of $\pi^+\pi^-$ pairs over longitudinal component of relative momentum Q_L with polynomial-fitted background. The peak at zero at the level of 5σ is expected to be originate form breakup of the long-lived $\pi^+\pi^-$ atoms inside the Platinum foil of 2 μm placed at 100 mm behind the primary Beryllium target

For the future, DIRAC plans to continue the experiment at the SPS CERN accelerator. We exact to gain about 20 in the detection rate of $\pi^+\pi^-$ and πK atoms.

1. J. Uretsky and J. Palfrey, Phys. Rev. **121**, 1798 (1961).
2. J. Schweizer, Phys. Lett. B **587**, 33 (2004).
3. J. Gasser *et al.*, Phys. Rep. **456**, 167 (2008).
4. S. Weinberg, Physica A **96**, 327 (1979); J. Gasser and H. Leutwyler, Phys. Lett. B **125**, 325 (1983); ibid Nucl. Phys. B **250**, 465, 517, 539 (1985).
5. G. Colangelo *et al.*, Nucl. Phys. B **603**, 125 (2001).
6. J. Bijnens, P. Dhonte and P. Talavera, JHEP **0405**, 036 (2004).
7. L.G. Afanasyev and A.V. Tarasov, Phys. At. Nucl. **59**, 2130 (1996); C. Santamarina *et al.*, J. Phys. B **36**, 4273 (2003); L. Afanasyev *et al.*, J. Phys. G **25**, B7 (1999); L. Afanasyev *et al.*, Phys. Rev. D **65**, 096001 (2002).
8. B. Adeva *et al.*, Nucl. Instrum. and Meth. A **515**, 467 (2003).
9. B. Adeva *et al.*, Physics Letters B **704** 24 (2011).
10. DIRAC-DOC-2012-01: PS212 Addendum 6, CERN-SPSC-2012-001 (SPSC-P-284-ADD-6).

TOTEM PHYSICS RESULTS

M. Deile
on behalf of the TOTEM Collaboration

CERN, 1211 Genève 23, Switzerland

Abstract

The TOTEM experiment [1, 2] at the LHC is dedicated to the measurement of elastic and diffractive scattering, total cross-section and forward particle production. This short contribution summarises the physics results and points to the respective publications.

1. Elastic Scattering

At the centre-of-mass energy $\sqrt{s} = 7\,\mathrm{TeV}$, the differential cross-section of elastic scattering, $\mathrm{d}\sigma/\mathrm{d}t$, has been measured in the squared four-momentum transfer range $0.005\,\mathrm{GeV}^2 < |t| < 2.5\,\mathrm{GeV}^2$ Fig. 1, extending from the almost exponential forward peak ($\propto \mathrm{e}^{-B|t|}$ with $B = (19.89 \pm 0.27)\,\mathrm{GeV}^{-2}$) [3] through the dip-bump region (with the minimum observed at $0.53\,\mathrm{GeV}^2$) to the large-$|t|$ domain exhibiting a power-law behaviour, $\propto |t|^{-7.8}$ [4]. The $|t|$-range analysed so far has been covered by two data sets and will be extended at its upper bound to about $3.5\,\mathrm{GeV}^2$ with a third data set already under analysis.

At $\sqrt{s} = 8\,\mathrm{TeV}$, analyses of two data sets with different machine optics are in progress. With the new $\beta^* = 1000\,\mathrm{m}$ optics, $|t|$ values as low as $6 \times 10^{-4}\,\mathrm{GeV}^2$ were reached, and the Coulomb-nuclear interference was observed for the first time at the LHC. This interference makes it possible to determine the phase $\phi(t = 0)$ of the nuclear amplitude $A(t = 0)$ via the parameter $\rho = \cot\phi(0) = \mathcal{R}A(0)/\mathcal{I}A(0)$. This very-low-$|t|$ data set reaches an upper limit of about $0.2\,\mathrm{GeV}^2$ and overlaps with the second set recorded at $\beta^* = 90\,\mathrm{m}$ and covering

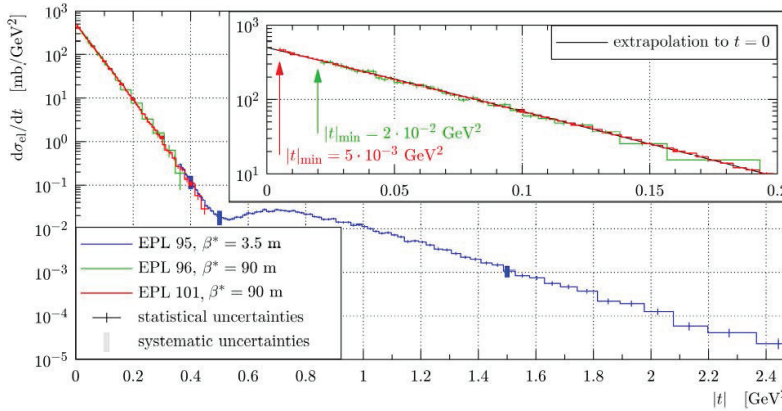

Fig. 1: Differential cross-section of elastic scattering measured at $\sqrt{s} = 7\,\text{TeV}$

the range $0.01\text{GeV}^2 < |t| < 1.4\,\text{GeV}^2$. Thanks to the high statistics of these data, both the dip and bump are clearly visible. The lower-$|t|$ region of this $\beta^* = 90\,\text{m}$ data set has been extrapolated to $t = 0$ and thus used for the total cross-section determination with the luminosity-independent method (see Section 2).

TOTEM also recorded data at $\sqrt{s} = 2.76\,\text{TeV}$. The analysis is ongoing, and the expected $|t|$ range extends from about 0.06 to about $0.4\,\text{GeV}^2$. Therefore the dip will not be covered.

2. Total and Inelastic pp Cross-Sections

At $\sqrt{s} = 7\,\text{TeV}$, four papers on total and inelastic cross-section measurements were published.

- Refs. [5] and [3]: The pp elastic scattering differential cross-section $\mathrm{d}\sigma/\mathrm{d}t$ was normalised with the luminosity from CMS. After extrapolation to $t = 0$, the total pp cross-section was calculated using the optical theorem

$$\sigma_{\text{tot}}^2 = \frac{16\pi\,(\hbar c)^2}{1+\rho^2} \left.\frac{\mathrm{d}\sigma_{\text{el}}}{\mathrm{d}t}\right|_{t=0}, \tag{1}$$

with $\rho = 0.141 \pm 0.007$ from the COMPETE [6] preferred-model extrapolation. Finally, the inelastic cross-section was obtained

by subtraction:

$$\sigma_{\text{inel}} = \sigma_{\text{tot}} - \sigma_{\text{el}}. \tag{2}$$

The results reported in the two papers are based on independent data sets from different LHC fills with different beam intensities.

- Ref. [7]: The inelastic pp cross-section was directly measured with the forward trackers T1 and T2, using the luminosity from CMS for normalisation. Addition of the elastic cross-section from [3] yields a ρ-independent result for the total cross-section.

- Ref. [8]: The total cross-section was obtained from the elastic and inelastic event counts, applying the luminosity-independent method:

$$\sigma_{\text{tot}} = \frac{16\pi\,(\hbar c)^2}{1+\rho^2}\,\frac{\mathrm{d}N_{\text{el}}/\mathrm{d}t|_{t=0}}{N_{\text{el}}+N_{\text{inel}}}. \tag{3}$$

At the same time this method yields the integrated luminosity:

$$\mathcal{L}_{\text{int}} = \frac{1+\rho^2}{16\pi\,(\hbar c)^2}\,\frac{(N_{\text{el}}+N_{\text{inel}})^2}{\mathrm{d}N_{\text{el}}/\mathrm{d}t|_{t=0}}. \tag{4}$$

The result was found to be in excellent agreement with the CMS measurement.

Furthermore, the elastic and inelastic rate measurements can be combined with the CMS luminosity measurement to obtain

$$\rho^2 = 16\pi\,(\hbar c)^2\,\mathcal{L}_{\text{int}}\,\frac{\mathrm{d}N_{\text{el}}/\mathrm{d}t|_{t=0}}{(N_{\text{el}}+N_{\text{inel}})^2} - 1 \;= 0.009 \pm 0.056 \tag{5}$$

or $|\rho| = 0.145 \pm 0.091$.

The four results, having very different systematic dependences, are in excellent agreement.

At the energy of 8 TeV, the luminosity-independent results on elastic, inelastic and total cross-section were published [9]. Moreover, the ongoing analysis of the $\beta^* = 1000$ m data, allowing the separation of Coulomb and nuclear effects, will yield a methodically more accurate result for the total cross-section. A numerical overview of the cross-section results is given in Table 1.

At $\sqrt{s} = 2.76$ TeV TOTEM aims at applying all three total cross-section determination methods. The inelastic part of the analysis is almost completed, the elastic part is ongoing.

T a b l e 1: Cross-section summary. The errors represent the full systematic uncertainties; the statistical uncertainties are negligible and therefore omitted

$\sqrt{s}$ [TeV]	Method	Data Set	$\sigma_{\rm tot}$ [mb]	$\sigma_{\rm inel}$ [mb]	$\sigma_{\rm el}$ [mb]
7	elastic only: Eq. (1)	June 2011 [5]	98.3 ± 2.8	73.5 ± 1.6	24.8 ± 1.2
7	elastic only: Eq. (1)	October 2011 [3]	98.6 ± 2.2	73.2 ± 1.3	25.4 ± 1.1
7	ρ-indep. (el. + inel.)	October 2011 [7]	99.1 ± 4.3	73.7 ± 3.4	25.4 ± 1.1
7	$\mathcal{L}_{\rm int}$-indep.: Eq. (3)	October 2011 [8]	98.0 ± 2.5	72.9 ± 1.5	25.1 ± 1.1
8	$\mathcal{L}_{\rm int}$-indep.: Eq. (3)	July 2012 [9]	101.7 ± 2.9	74.7 ± 1.7	27.1 ± 1.4

3. Forward Charged Particle Multiplicity

The Telescope T2 is an efficient tagger for an almost unbiassed sample of inelastic events due to its low p_T acceptance threshold ($\sim$40 MeV) and large acceptance to inelastic events (> 90 %). Based on a special low-pileup run at $\sqrt{s} = 7\,\text{TeV}$, the charged particle pseudorapidity density $\mathrm{d}N_{ch}/\mathrm{d}\eta$ for $5.3 < |\eta| < 6.4$ was determined in events with at least one charged particle with transverse momentum above 40 MeV in this same pseudorapidity range [11]. This was the first measurement of $\mathrm{d}N_{ch}/\mathrm{d}\eta$ at such forward rapidities.

For $\sqrt{s} = 8\,\text{TeV}$, TOTEM and CMS are presently pursuing a joint analysis of $\mathrm{d}N_{ch}/\mathrm{d}\eta$ on the same events both for the central tracker ($|\eta| < 2.3$) and for the very forward T2 ($5.3 < |\eta| < 6.4$), all triggered by T2 in a common low-pileup run. Since $\mathrm{d}N_{ch}/\mathrm{d}\eta$ depends strongly on the event class – it is different for diffractive and non-diffractive events – the analysis is performed separately on an inclusive sample and vsubsamples enhanced and depleted in single diffraction. The final results are expected to be published soon.

4. Diffractive Scattering

Various studies of soft and hard diffractive scattering are in progress.

- Double diffractive (DD) cross-section:
  The DD cross-section in the forward region [10] was measured using a $\beta^* = 90\,\text{m}$ run at 7 TeV with a low pileup probability ($\sim$0.05 inelastic events per bunch crossing). A forward DD sample was obtained by triggering with T2, requiring at least one charged particle in both T2 arms and no charged particles

Table 2: The forward double diffractive (DD) cross-section measurements and their MC predictions. $|\eta^+|_{\min}$ ($|\eta^-|_{\min}$) refers to the primary particle with smallest $|\eta|$ in the positive (negative) hemisphere. The Pythia and Phojet estimates for the total σ_{DD} are 8.1 mb and 3.9 mb, respectively

$\|\eta^+\|_{\min}$	$\|\eta^-\|_{\min}$	TOTEM [μb]	Pythia 8.108 [μb]	Phojet 1.12 [μb]
$[4.7, 5.9]$	$[4.7, 5.9]$	65 ± 20	70	44
$[4.7, 5.9]$	$[5.9, 6.5]$	26 ± 5	36	23
$[5.9, 6.5]$	$[4.7, 5.9]$	27 ± 5	36	23
$[5.9, 6.5]$	$[5.9, 6.5]$	12 ± 5	17	12
$[4.7, 6.5]$	$[4.7, 6.5]$	116 ± 25	159	101

in T1. This strategy allows a very pure ($\sim$70%) DD sample to be selected, but only a few % of the total DD cross-section are kinematically covered. The measurement was corrected to be representative for DD events with a central rapidity gap from $\eta = -4.7$ to $\eta = +4.7$, corresponding approximately to events where both diffractive systems have masses between 3.4 and 8 GeV.

The results – both for the total accessible $\eta_{\min}$ range on each side, and for a 2×2 matrix of subranges – are reported in Table 2 and compared with predictions of Monte Carlo models. Using data taken in common with CMS at $\sqrt{s} = 8$ TeV in 2012, a much larger fraction of σ_{DD} can be measured with good purity.

- Single diffractive (SD) cross-section:
  A study of SD events at 7 TeV is performed on a data set triggered with T2. SD-like (proton + gap + diffractive system) events are selected requiring only one proton in the RPs, charged particles in the T2 arm opposite to the proton and none in the other arm. The events are classified according to their diffractive mass, M_{diff}, based on the charged particle configuration in T1 and T2 (Table 3). Here the relation $M^2_{\text{diff}} = s\text{e}^{-\Delta\eta}$ is used, where $\Delta\eta$ is the rapidity gap between the very forward proton and the charged particle in T1 and T2 closest in η to the proton.

  The aim of the study is to determine $\text{d}\sigma_{SD}/\text{d}t$ and its integral over t for each class separately.

T a b l e 3: Classification of the single diffractive events into different ranges of the diffractive mass $M_{\rm diff}$ and proton momentum loss ξ. The "opposite" and "same" side of the IP are defined relative to the proton detected in the RP)

$M_{\rm diff}$ [GeV]	ξ	Event signature
$3.4 \div 8$	$2 \times 10^{-7} \div 10^{-6}$	p + opposite T2, no T1
$8 \div 350$	$10^{-6} \div 0.0025$	p + opposite T2 + opposite T1
$350 \div 1100$	$0.0025 \div 0.025$	p + opposite T2 + same side T1

- Central Diffraction (CD):
  A CD data set has been collected in a 12 hour run together with CMS at 7 TeV with the $\beta^* = 90\,\mathrm{m}$ optics. In addition to the TOTEM-standalone analysis of the differential cross-section in $t_{1,2}$ and $\xi_{1,2}$, a joint CMS+TOTEM analysis of exclusive central production of mass states, with quantum numbers 0^{++} favoured by selection rules, is in progress. With more statistics to be collected after the Long Shutdown of LHC, the search for new centrally produced states, like e.g. glue balls, will come into reach.

1. The TOTEM Collaboration, JINST **3,** S08007 (2008).
2. The TOTEM Collaboration, CERN-PH-EP-2013-173; arXiv:1310.2908.
3. The TOTEM Collaboration, EPL **101,** 21002 (2013).
4. The TOTEM Collaboration, EPL **95,** 41001 (2011).
5. The TOTEM Collaboration, EPL **96,** 21002 (2011).
6. J.R. Cudell *et al.* (COMPETE Collaboration), Phys. Rev. Lett. **89**, 201801 (2002).
7. The TOTEM Collaboration, EPL **101,** 21003 (2013).
8. The TOTEM Collaboration, EPL **101,** 21004 (2013).
9. The TOTEM Collaboration, Phys. Rev. Lett. **111,** 012001 (2013).
10. The TOTEM Collaboration, CERN-PH-EP-2013-170 (2013), arXiv:1308.6722.
11. The TOTEM Collaboration, EPL **98**, 31002 (2012).

RECENT RESULTS FROM THE D0 EXPERIMENT

M. Eads
for the D0 Collaboration

Northern Illinois University,
DeKalb, Illinois, USA

Abstract

The D0 experiment, located at the Fermilab Tevatron proton-antiproton collider continues to analyze its full dataset. Recent results in Higgs boson physics, electroweak physics, and top physics are presented.

1. Introduction

The D0 experiment is located at the Tevatron collider at Fermi National Accelerator laboratory in Batavia, Illinois, USA. The Tevatron collided protons and antiprotons at a center of mass energy of 1.96 TeV from 2002 until 2011, known as Run II. The D0 experiment is a general-purpose collider detector and collected a data sample of approximately 10 fb^{-1} [1]. Since the shutdown of the collider, efforts have continued to fully exploit this unique data set. In particular, recent results exploring the properties of the Higgs boson, the mass of the W-boson, the mass of the top quark, and the cross section for single top quark production have been recently released.

2. Higgs Boson Results

The Higgs mechanism is a crucial cornerstone of the standard model (SM) of particle physics (worthy of the 2013 Nobel prize in physics)

and the discovery of the Higgs boson by the Atlas and CMS collaborations represents the final missing piece of the SM [2]. However, the task remains to fully characterize the recently-discovered boson and to verify that it is indeed the Higgs boson of the SM. Detailed measurements of the Higgs boson properties, such as mass, spin/parity, and decay branching ratios are essential to determining if the new boson is in fact the simplest Higgs boson found in SM, or if it is instead a more complicated Higgs boson, as can be found in supersymmetric theories.

The SM Higgs boson is a scalar particle, having a spin/parity (J^P) assignment of 0^+. LHC experiments have performed measurements testing this SM expectation against other more exotic J^P assignments such as 0^- and 2^+ [3]. These results are consistent with a SM Higgs boson, but the analyses utilize characteristics of events where the Higgs boson decayed to bosons. However, the dominant decay mode of a Higgs boson with a mass of $\sim$125 GeV is a bottom-antibottom quark pair.

The current sensitivity of the Tevatron to $H \to b\overline{b}$ decays is still important in the global effort to study the Higgs boson [4]. The D0 collaboration has performed an analysis to test whether the Higgs boson signal in the $b\overline{b}$ final states is more consistent with with a J^P assignment of 0^+ or 2^+ [5] [1]. The analysis is based on the technique described in Ref. [6], which shows that the visible mass of all final state products in a Higgs boson event is sensitive to the J^P value of the Higgs boson. The D0 analysis utilizes existing results for Higgs boson production in association with a vector boson, with the individual analyses targeting the final states of $WH \to l\nu b\overline{b}$ [7], $ZH \to \nu\nu b\overline{b}$ [8], or $ZH \to llb\overline{b}$ [9]. Multivariate techniques are used to increase the signal-to-background ratio. The invariant mass or transverse mass (for channels containing neutrinos) for the most sensitive sub-channel in the three analyses is shown in Fig. 1.

A CL_S method with a negative log likelihood ratio test statistic is used to test the 0^+ versus the 2^+ hypothesis. The 0^+ hypothesis is prefered, with the observed exclusion depending on whether the Higgs boson signal strength (μ) is assumed to have the SM value

[1] Since the conference, the D0 collaboration has also released an analysis testing the 0^+ versus 0^- hypothesis. See D0note 6406 (unpublished).

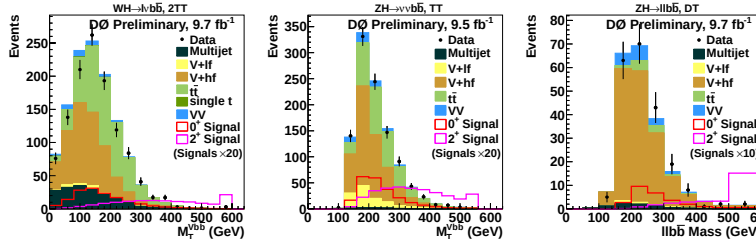

Fig. 1: This figure shows the transverse mass for the $l\nu b\bar{b}$ channel (left), transverse mass for the $\nu\nu b\bar{b}$ channel (middle), and invariant mass for the $llb\bar{b}$ channel (right). Only the most sensitive sub-channel is shown

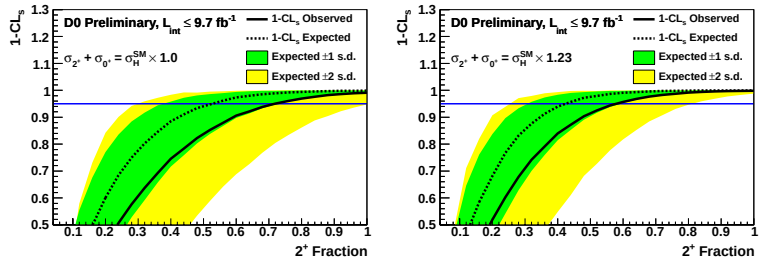

Fig. 2: Exclusion values for the fraction of 2^+ admixture, assuming the SM higgs boson signal strength (left) and the best fit signal strength (right)

(1.0) or is constrained to the best-fit value (1.23). Using $\mu = 1.0$, the 2^+ hypothesis is excluded at 99.9% confidence level (CL). Using $\mu = 1.23$, the 2^+ hypothesis is excluded at 99.2% CL. In addition, an admixture of 0^+ and 2^+ is also tested, as shown in Fig. 2. At 95% CL, a fraction of 2^+ greater than 0.71 for $\mu = 1.0$ (0.57 for $\mu = 1.23$) has been excluded.

3. Precision Physics Results

One of the lasting legacies of the Tevatron has been, and will continue to be, its precision measurement of the W-boson mass. A recent combination has been performed that combines all of the Run I and Run II results from from the CDF and D0 collaborations [10]. The individual measurements (which utilize up to 5.3 fb^{-1} of data) and

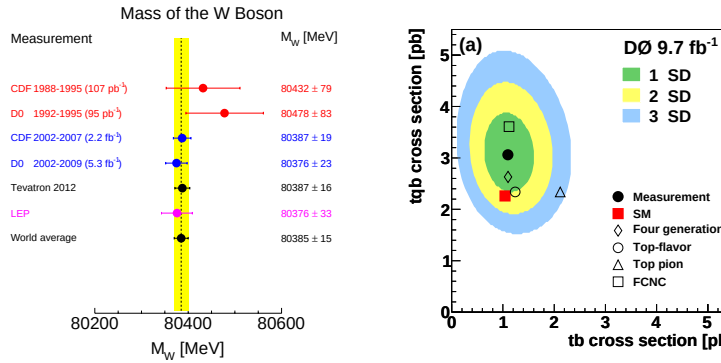

Fig. 3: The Tevatron measurements of the W-boson mass and the combined value (left). The measured values of the s-channel and t-channel single top cross sections (right)

the combined result are shown in Fig. 3. The combined value of the W-boson mass for all Tevatron results is 80 387 $\pm$ 16 MeV. Combining this with the results from LEP, the result is 80 385 $\pm$ 15 MeV. Efforts are ongoing to complete the measurement of the W-boson mass utilizing the full dataset, and the uncertainty will be reduced even further.

Another lasting legacy of the Tevatron is the precision measurement of the top quark mass [11]. As shown in Fig. 4, the CDF and D0 collaborations currently have measurements of the top mass in many different channels that utilize up to 8.7 fb^{-1} of data. A combination of all these results has been performed, resulting in a combined value of the top mass of 173.20 $\pm$ 0.87 GeV [11]. As with the W-boson mass, efforts are ongoing to complete measurements of the top mass using the complete Run II data sample.

The Tevatron experiments also have unique sensitivity to single top quark production in the s-channel. The latest measurement of single top quark production at D0 utilizes separate multivariate discriminants to separate the s- and t-channel contributions to the cross section, as shown in Fig. 3 [12]. The significance of the measurement of the s-channel single top production cross section is 3.7 standard deviations, providing the first evidence for this extremely rare process. This measurement also provides insight into models of physics

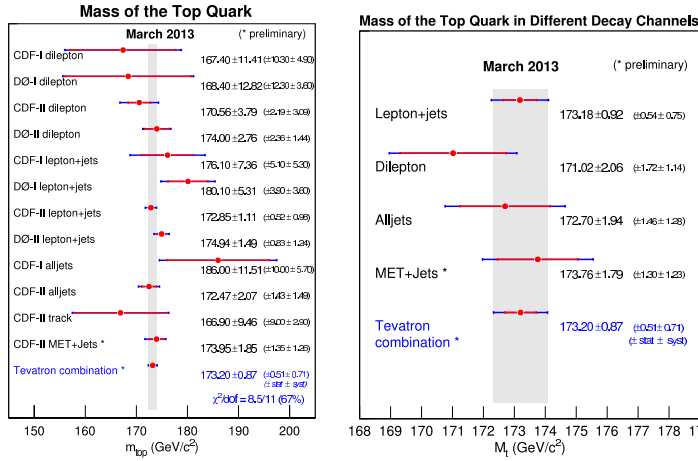

Fig. 4: The individual top mass measurements from CDF and D0 and the combined value (left). The combined top mass values in individual top decay channels (right)

beyond the standard model, as various models will result in different ratios of the s- to t-channel cross section.

4. Summary

Although the D0 experiment ceased data taking in September of 2011, the collaboration is working actively to fully exploit the 10 fb^{-1} of $p\overline{p}$ collision data. Recent efforts have focused on measuring the properties of the Higgs boson. The D0 experiment has also made significant contributions to the precision measurements of SM particles, including the mass of the W-boson and the top quark. When combined with the results of the CDF experiment, these results are the most precise in the world. Furthermore, for the first time the D0 experiment has found evidence of s-channel single top production. The experimental program at D0 has not yet reached its conclusion. Nine years of data taking has resulted in an extremely well-understood detector, and this will be exploited for future precision measurements.

1. V.M. Abazov, *et al.* (D0 Collaboration), Nucl. Inst. Meth. Phys. Res. A **565**, 463 (2006); V.M. Abazov, *et al.* (D0 Collaboration), Nucl. Inst. Meth. Phys. Res. A **552**, 372 (2005); M. Weber, *et al.* (D0 Collaboration), Nucl. Inst. Meth. Phys. Res. A **566**, 182 (2006); M. Abolins, *et al.* (D0 Collaboration), Nucl. Inst. Meth. Phys. Res. A **584**, 75 (2007).
2. ATLAS Collaboraton, Phys. Lett. B **716**, 1 (2012); CMS Collaboration, Phys. Lett. B **716**, 30 (2012).
3. ATLAS Collaboration, ATLAS-CONF-2013-040, unpublished; CMS Collaboration, CMS-HIG-13-016, unpublished.
4. V.M. Abazov, *et al.* (D0 Collaboration), Phys. Rev. D **88**, 052011 (2013); T. Aaltonen, *et al.*, (CDF and D0 Collaborations), Phys. Rev. D **88**, 052014 (2013).
5. D0 Collaboration, D0note 6387, unpublished.
6. J. Ellis, D.S. Hwang, V. Sanz, and T. You, J. High Energy Phys. **1211**, 134 (2012).
7. V.M. Abazov, *et al.* (D0 Collaboration), Phys. Rev. D **88**, 052008 (2013).
8. V.M. Abazov, *et al.* (D0 Collaboration), Phys. Lett. B **716**, 285 (2012).
9. V.M. Abazov, *et al.* (D0 Collaboration), Phys. Rev. D **88**, 052010 (2013).
10. T. Aaltonen, *et al.* (CDF and D0 Collaborations), Phys. Rev. D **88**, 052018 (2013).
11. CDF and D0 Collaborations, arXiv: 1305.3929, unpublished.
12. V.M. Abazov, *et al.* (D0 Collaboration), Phys. Lett. B. **726**, 656 (2013).

STANDARD MODEL MEASUREMENTS WITH THE ATLAS DETECTOR

S. Franchino
on behalf of the ATLAS collaboration

CERN

Abstract

An overview of the latest Standard Model results obtained with the ATLAS experiment at LHC is presented. Isolated photons, high transverse momentum jets and electroweak phenomena have been studied. Accurate tests of perturbative QCD has been performed to improve the understanding of the parton distribution functions and to better define properties of events that are background to new physics searches. The production cross-section and the mass of the top quark have also been precisely measured.

1. The ATLAS Detector

ATLAS [1], an all-purpose detector running at the proton-proton collider LHC at CERN, has been designed to cover a wide range of physics topics. It consists of inner detectors for track and vertex reconstruction, calorimeters to identify and measure the energy of electromagnetic and hadronic showers, and chambers for muon tracking, triggering and momentum measurement. The inner detector is located inside a 2T solenoid, while the muon spectrometer is inside an air-core toroid system.

The LHC machine delivered an integrated luminosity of 40 pb^{-1} in 2010 and 5 fb^{-1} in 2011 at $\sqrt{s}$ =7 TeV, 25 fb^{-1} at $\sqrt{s}$ = 8 TeV in 2012 and, in 2011, an additional 0.2 pb^{-1} at $\sqrt{s}$ = 2.76 TeV.

Many Standard Model (SM) measurements have been performed by ATLAS. They allow to validate the SM in a new energy regime, to constrain models of new physics (such as anomalous couplings), to

improve the precision of known SM parameters and to better understand processes that are backgrounds for other studies or searches. In the following a brief review of most recent Quantum Chromodynamics (QCD), electroweak (EW) and top physics results will be given.

2. Photon and Jet Measurements

The ATLAS collaboration is studying a wide range of QCD phenomena. Accurate tests of perturbative QCD (pQCD), including differential studies of the event kinematics, are performed thanks to the high statistics of collected data for the production of isolated photons or high-p_T jets. Such measurements are not only a fundamental test of pQCD predictions but they are also sensitive to the parton density functions (PDF).

Cross-section measurements of photons in association with jets [2] and of diphotons [3] provide a direct probe of short-distance physics. The agreement with the next-to-leading (NLO) or higher-order (NNLO) QCD calculations is excellent. Results coming from the photon plus jet analysis can be used to study the relative contributions of direct and fragmentation processes in the description of the isolated-photon production.

The ratio of inclusive jet cross section taken at two different LHC energies is sensitive to the gluon density of the proton [4], while the jet-multiplicity ratio is sensitive to the strong coupling constant, α_S, with reduced sensitivity to the uncertainties of the PDFs [5]. α_S has then been measured as: $\alpha_S(M_Z) = 0.111 \pm 0.006\,(\mathrm{exp})^{+0.016}_{-0.003}\,(\mathrm{theory})$. The running of α_S as predicted by QCD has been confirmed up to a scale of 800 GeV.

3. Electroweak

Precise measurements of the cross-section and properties of the heavy electroweak gauge bosons W and Z are possible because of their high production rates. Fundamental tests of the QCD at NNLO have been performed thanks to the 1-2% precision achieved for the total cross-sections measurements for inclusive production and leptonic decays of W and Z in the electron and muon channels. These results [6] are in good agreement with the theory predictions. This is evidence of the

universality of PDFs and validity of pQCD calculations up to the kinematic ranges probed in W and Z production at the LHC. Differential cross-section results have been compared with QCD predictions calculated to NNLO in the fiducial regions of the measurements. They allow for maximum sensitivity to details of the PDFs used in these calculations. Interesting differences between sets of PDFs have been observed, both in integrated and differential fiducial cross-sections.

Total and differential ($\mathrm{d}\sigma/\mathrm{d}m_{ee}$) cross-sections of neutral current Drell-Yan (DY) production in the region $116 < m_{ee} < 1500\,\mathrm{GeV}$, above the Z-pole, have been measured and compared with the predictions of pQCD at NNLO [7]. The measured dm_{ee} distribution is consistent with predictions. Because of the simple signature and low background, the experimental uncertainty is very small and allows a precision test of pQCD and in the future can help to constrain the poorly known PDFs of antiquarks at large x.

Another performed measurement is the forward-backward asymmetry for the neutral current DY process [8]. It is measured using dielectron (including electrons detected in the forward calorimeter which extend the covered phase space to the region less sensitive to the PDF uncertainties) and dimuon final states. The result has been used to extract a measurement of the effective weak mixing angle: $\sin^2\theta_W^{\mathrm{eff}} = 0.2297 \pm 0.0004(\mathrm{stat}) \pm 0.0009(\mathrm{syst})$ which is consistent with the previous measurements and as precise as the D0 result. The dominant uncertainty comes from the limited knowledge of the PDFs.

The production of jets in association with a W or Z boson in pp collisions at 7 TeV can be used to study multi-leg QCD diagrams and probe EW production via the vector boson fusion mechanism. The cross-sections, differential in several kinematic variables, have been measured up to high jet multiplicities and can be compared directly to fixed-order predictions at NLO in pQCD and to Monte Carlo generators based on NLO or leading-order matrix elements supplemented by parton showers [9].

Measurements of vector bosons in association with heavy flavor, such as W+c production, have a unique sensitivity to the flavour decomposition of the proton, especially the strange density. In the analysis presented here [10], differential cross-sections are compared to QCD predictions at NLO. In this case the charm tagging has been done by reconstruction of exclusive hadronic decay modes of $D^{(*)}$

mesons. The ratio $\sigma(WD^{(*)})/\sigma(W)$ is measured inclusively and differentially as a function of the D meson transverse momentum and the pseudorapidity of the lepton from the W decay. These results are compared to the predictions using different NLO and NNLO PDF sets that differ in their parameterizations of the s-quark PDF. The agreement is best with the predictions obtained with the epWZ [11] and NNPDF2.3coll [12] PDF sets, in which the s-quark and d-quark sea contributions are comparable at x of 0.01.

The self couplings of the bosons are predicted by the SM and non-zero anomalous triple gauge couplings would provide evidence of a new physics process. Differential and total cross-sections for ZZ and WZ production (both at $\sqrt{s}$ =7 and 8 TeV) are seen to be in good agreement with the predictions of the SM at NLO and are used to place limits on anomalous triple gauge boson couplings [13].

4. Top Quark

Since its discovery at the Tevatron in 1995, the top quark has remained one of the most exciting topics for particle physicists. One of the interesting questions is whether the top quark plays a special role in the SM, in particular in EW symmetry breaking. The top quark is the heaviest known fundamental particle and it has unique properties that are well defined by the SM. It has a large couplings to the Higgs boson, and it is the only quark that decays before hadronisation so it is possible to study the properties of the bare quark. Besides its potential role in EW symmetry breaking, the top quark plays very often an important role in many scenarios for new physics beyond the SM (BSM). LHC can be seen as a top factory, indeed, about 6.6 million top pairs and 3 million single tops have been produced in ATLAS since 2011. Their production is dominated by the gluon fusion process. Precise measurements [14] of total $t\bar{t}$ cross-section have been performed both at $\sqrt{s}$ = 7 and 8 TeV. A good knowledge of those cross-sections is important BSM searches and Higgs physics as $t\bar{t}$ is often the main source of background. All performed cross-section measurements result to be in agreement with SM expectations.

The top-quark mass is an essential parameter of the SM. It has been measured from 1-lepton analysis to be in perfect agreement with what was obtained by Tevatron. The dominating uncertainties are

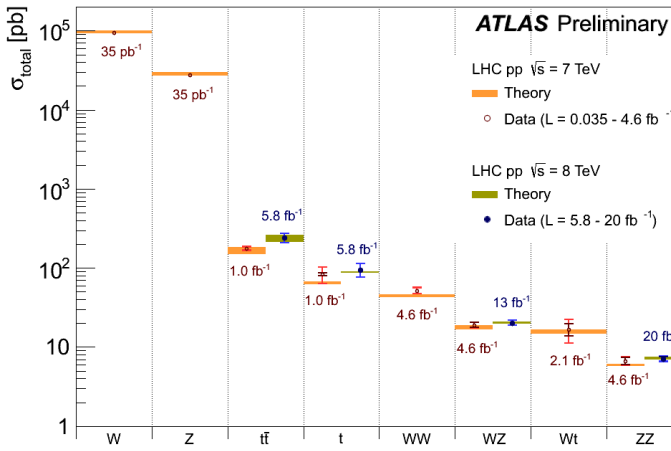

Fig. 1: Summary of several SM total production cross-section measurements, compared with theoretical expectations. Error bars represent statistical uncertainties in dark-color and in lighter color the systematics and luminosity ones [15]

the large b-tagging efficiency systematics and the jet energy scale for light flavour and b-jets.

5. Conclusion

Since the starting of LHC in 2010, the ATLAS detector has shown very good performance both in efficiency of data taking, and in physics analysis. The high integrated luminosity allows detailed measurements of SM processes. Furthermore, new measurements are already probing observables at unprecedented level of accuracy and in phase space regions never exploited before. Total cross-sections measurements of inclusive production in many cases reached a precision of 1-2% allowing fundamental tests of QCD at NNLO. These results are summarized in Fig. 1 and are in good agreement with the theoretical predictions (at NLO or higher).

1. ATLAS collaboration, JINST **3** S080001 (2008).
2. ATLAS collaboration, Nucl. Phys, B **875**, 483 (2013).
3. ATLAS collaboration, Phys. Rev. D **85**, 012003 (2012).

4. ATLAS collaboration, Eur. Phys. Jour. C **73**, 2509 (2013).

5. ATLAS collaboration,
ATLAS-CONF-2013-041: https://cds.cern.ch/record/1543225.

6. ATLAS collaboration, Phys. Rev. D **85**, 072004 (2012).

7. ATLAS collaboration, Phys. Lett. B **725**, 223-242 (2013).

8. ATLAS collaboration,
ATLAS-CONF-2013-043: https://cds.cern.ch/record/1544035.

9. ATLAS collaboration, JHEP **07**, 032 (2013).

10. ATLAS collaboration, ATLAS-CONF-2013-045:
https://cds.cern.ch/record/1546800.

11. ATLAS collaboration, Phys. Rev. Lett. **109**, 012001 (2012).

12. R.D. Ball *et al.*, Nucl. Phys. B **867**, 244-289 (2013).

13. ATLAS collaboration,
ATLAS-CONF-2013-020: https://cds.cern.ch/record/1525555,
ATLAS-CONF-2013-021: https://cds.cern.ch/record/1525557.

14. ATLAS collaboration,
ATLAS-CONF-2012-024: https://cds.cern.ch/record/1430733,
ATLAS-CONF-2012-149: https://cds.cern.ch/record/1493488,
ATLAS-CONF-2013-046: https://cds.cern.ch/record/1547327.

15. ATLAS collaboration:
https://twiki.cern.ch/twiki/bin/view/AtlasPublic/CombinedSummaryPlots

STATUS OF THE NICA/MPD PROJECT

V.I. Kolesnikov and A.I. Zinchenko
for the MPD Collaboration

Joint Institute for Nuclear Research (JINR)

Abstract

A general-purpose detector for studying heavy-ion collisions at the NICA facility is under construction at JINR. The NICA/MPD physics program, basic design requirements, and the MPD experimental setup will be described. Results of detector simulation and the expected performance for selected observables will be presented.

1. Introduction

Experimental studies of QCD matter at high baryon densities provides new perspectives to resolve the most fundamental problems of the underlying theory – confinement and chiral symmetry breaking. Our knowledge about the QCD phase structure at intermediate μ_B is poor: theory suggests a first-order transition at large μ_B and its turn into a crossover at small baryon densities (and high T), hence, for consistency, the critical endpoint (CEP) is expected to exist. However a rigorous proof on such a QCD structure is not yet available and new reliable experimental data on the nature and properties of the phase transition are needed.

The goal of the NICA research program at JINR is to investigate a wide range of physics phenomena in heavy-ion collisions including phases of nuclear matter and EoS at high baryon density, properties of the hadron spectral function and features of hyperon-nucleon interaction in the medium, critical behavior of the QCD matter and the spin structure of the nucleon [1]. The new NICA facility [2] will be capable to provide ion beams with the design luminosity of 10^{27} cm^{-2}c^{-1}

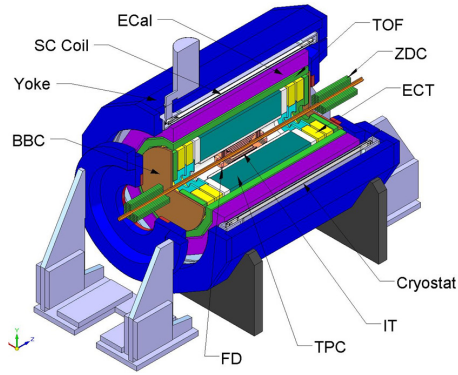

Fig. 1: Schematic view of the MPD detector

(for gold ions) in the energy range from $\sqrt{s} = 4$ to 11A GeV. In 2018, we will start a detailed energy and system size scan focusing on hadroproduction and dilepton studies, event-by-event fluctuations and correlations. Production of composite objects with strangeness (hypernuclei) are of particular interest, since they are a unique tool to probe new nuclear structures or unknown properties of the baryonic interaction, which cannot be seen from the study of ordinary nuclei.

2. MPD Detector

The **M**ulti**P**urpose **D**etector (MPD) is designed to fully exploit the NICA physics potential. It is a spectrometer with a large uniform acceptance (full azimuth) capable of detecting and identifying hadrons, electrons and gammas at the very high event rate achieved at NICA [3]. All the elements of the detector (see Fig. 1) are ordered inside a superconducting solenoid generating a magnetic field of up to 0.6 T. Tracking will be performed with a cylindrical Time Projection Chamber (TPC) with a MWPC-based readout. The TPC is required to have a high efficiency and momentum resolution over the pseudorapidity range $|\eta| < 2$. Having of about 65 measured space points per a track, TPC will enable particle identification via the specific energy loss (dE/dx) measurement with a precision better than 8%. At large pseudorapidities TPC tracking will be supplemented by a multi-layer straw tube tracker (ECT) located just after the TPC end

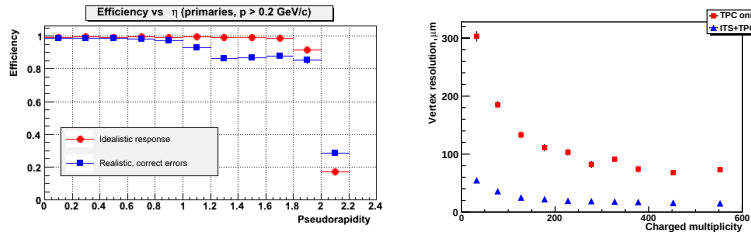

Fig. 2: (Left panel) Tracking efficiency in TPC versus η for an ideal and realistic TPC response. (Right) Primary vertex reconstruction resolution (σ_z) as a function of charged track multiplicity

plates. The Inner Tracker (IT) will consist of four layers of double-sided silicon microstrip detectors serving mainly for determination of the position of the primary interaction vertex and secondary decay vertices. The Time-Of-Flight (TOF) system made by RPC (Resistive Plate Chambers) is intended for charged hadron identification. The TOF detector covers $|\eta| < 3$ and its performance should allow the separation of kaons from protons up to a total momentum of 3 GeV/c. Behind the TOF detector, a high segmented electromagnetic calorimeter (ECAL) for electron and gamma identification will be located. Arrays of quartz counters (FD) are meant for fast timing and triggering, and two sets of hadron calorimeters (ZDC), covering the pseudorapidity region $2.5 < |\eta| < 4$, will measure the forward going energy for centrality selection and event plane analysis. A more detailed description of the detector components can be found elsewhere [4].

3. MPD performance studies and R&D

MPD tracking and PID performance. The MPD performance studies were performed within the MPDRoot framework [4], which provides an interface to external event generators (like UrQMD), transport codes (Geant3,4), and implements MPD detector response simulations and event reconstruction algorithms. Tracking and vertexing performance of MPD are shown in Fig. 2 for single track efficiency and spatial resolution along the beam axis σ_z. As one can see, the detector is able to provide highly efficient tracking up to $\eta = 2$,

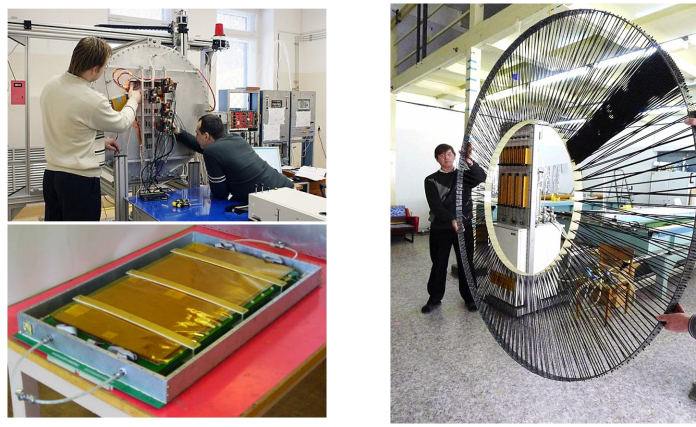

Fig. 3: (Upper left) A first assembled TPC prototype in laboratory measurements. (Bottom left) A full-scale TOF module. (Right) One of the ECT endcap wings

and a resolution better than 40 microns can be achieved in central collisions.

Progress in MPD prototyping. During the years 2012-13, the main MPD R&D activities were aimed at developing of novel techniques in construction of TPC, TOF, IT and ECT detectors, as well as at production and tests of the first detector prototypes (see Fig. 3). For example, to ensure lightweight and mechanical stability of the TPC, its supporting elements will be made from composite materials in collaboration with industry. Also, to ensure accurate tracking at large-η, a new construction technology for ECT modules was developed allowing the alignment of straw tubes with a 100 micron precision within an object of 2 meters in diameter.

MPD potential for hypernuclei measurements. The feasibility of precise hypernuclei measurements at NICA has been investigated with the event generator DCM. The model implements a coalescence-based algorithm for (hyper)nuclei formation and calculated yields of fragments are in a good agreement with experimental data [5]. Roughly $5 \cdot 10^5$ central Au+Au collisions at $\sqrt{s} = 5$A GeV were analyzed including full event reconstruction, particle identification by means of combined dE/dx (Fig. 4) and TOF measure-

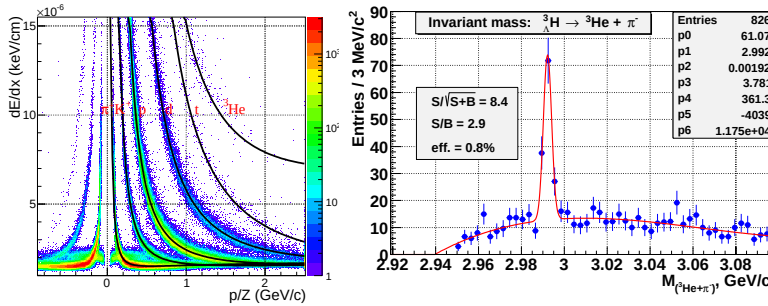

Fig. 4: (Left) Specific energy loss of π, K, p, d, t and ^3He in the MPD TPC gas mixture. PID selection is based on a 3σ band relative to the dE/dx-paramemeterization shown by the solid line. (Right) Invariant mass distribution of ^{3}He and π^- candidates from central Au+Au collisions at $\sqrt{s} = 5$A GeV. A Gaussian plus polynomial fit (solid line) is superimposed on the signal distribution (symbols)

ments, and search for secondary vertices. To improve the signal-to-background ratio, a set of quality and topological cuts were applied on the number of TPC space points and the distance between the daugthers at the decay vertex. The results for ${}^3_\Lambda\mathrm{He} \rightarrow {}^3\mathrm{He} + \pi^-$ are shown in Fig. 4 (right panel). With the overall reconstruction efficiency of about 1% and design NICA luminosity we expect roughly 500 reconstructed ${}^3_\Lambda$He candidates per day of data taking. Such high event rates provide a good opportunity to gain further insights into production mechanism and properties of hypernuclei.

1. A.N. Sissakian and A.S. Sorin, J. Phys. G: Nucl. Part. Phys. **36**, 064069 (2009); A. Sissakian, O. Shevchenko, A. Nagaytsev and O. Ivanov, arXiv:hep-ph/0807.2480v4
2. NICA Conceptual Design Report. Dubna, 2008. *http://nica.jinr.ru/files/NICA_CDR.pdf*
3. Kh.A. Abraamyan *et al*, Nucl. Intrum. Methods A **628**, 99 (2011).
4. MPD Conceptual Design Report. Dubna, 2011. *http://nica.jinr.ru/files/MPD_CDR_en.pdf*
5. J. Steinheimer, K. Gudima, A. Botvina, I. Mishustin, M. Bleicher, H. Stocker, Phys. Lett. B **714**, 85-91 (2012).

THE COMPASS EXPERIMENT AT CERN

O. Kouznetsov
on behalf of the COMPASS collaboration

Joint Institute for Nuclear Research,
Joliot Curie 6, 141980 Dubna, Russia

Abstract

COmmon Muon and Proton Apparatus for Structure and Spectroscopy (COMPASS) is a fixed target experiment at CERN dedicated to studies of the spin structure of the nucleon and of the spectroscopy of hadrons. During the years 2002–2004, 2006–2007 and 2010–2011, the COMPASS collaboration has studied the spin structure of the nucleon by scattering polarized 160(200) GeV/c muons on polarized deuterium and proton targets. During 2008 and 2009, the world leading data sets diffractive and centrally produced events were collected with 190 GeV/c hadron beams which are currently being analyzed using Partial Wave Analysis (PWA) technique.

1. The COMPASS Set-Up

The COMPASS experiment at CERN scrutinize how nucleons and other hadrons are built up from quarks and gluons. The main physics observables studied by the Collaboration are the polarization of the constituents of a polarized nucleon, the mass and decay patterns of the light hadronic system with either exotic quantum numbers or strong gluonic excitation.

The COMPASS set-up was designed for beams of 100 to 200 GeV/c and was built around two large dipole magnets, defining two consecutive spectrometers, covering large and small scattering angles separately. Particle identification is performed using a RICH counter and both electromagnetic and hadron calorimeters. Until 2006, the polarized target was filled with a ^{6}LiD target material (mainly deuterium),

for which polarizations better than 50% are routinely achieved. In 2007 we began using ammonia (NH_3, mainly proton), reaching polarizations of 90% and higher. A full description of the spectrometer can be found in [1].

For the run with a hadron beam, several major modifications of the COMPASS setup were made (see [2] for details). The major part of the hadron data were collected using a 40 cm long liquid hydrogen target.

2. Muon Program

Worldwide experimental efforts in the last few decades have lead to numerous results extending our knowledge of the nucleon spin structure. But major challenges like the "spin crisis" still remain since 1988, when the EMC experiment found that only a small fraction of the nucleon spin is carried by the quarks: $\Delta\Sigma = 12 \pm 9 \pm 14\%$ [3]. The EMC result has been confirmed by a series of deep inelastic scattering experiments giving, on average, a contribution from the quarks $\Delta\Sigma$ to the nucleon spin off $\sim 30\%$.

The spin $1/2$ of the nucleon can be decomposed as $1/2 = 1/2\Delta\Sigma + \Delta G + L_{q+g}$ and one can conclude that the missing contribution to the nucleon spin must come from the gluons ΔG, and/or from the orbital angular momenta L_{q+g}. The gluon polarization can be directly measured via the spin asymmetry of the Photon-Gluon Fusion (PGF) process [4]. The fragmenting $q\bar{q}$ pairs are then detected with two different, but complementary methods. In the first method ("open charm"), the events where the charmed quark hadronized into a D^0 or a D^* meson are selected. In the second method ("high-p_T pairs"), the PGF events are identified by requiring that two oppositely charged high-transverse momentum hadrons are detected in coincidence.

All gluon polarization measurements of the COMPASS are summarized in Fig. 1 together with the SMC [5] and HERMES [6] results. The world results for direct measurements of the $\langle \frac{\Delta g}{g} \rangle$ are dominated by COMPASS and indicate a small value of ΔG the first moment Δg. These results as also confirmed by the COMPASS "open charm" measurement at NLO [7], which also predicts a small value for the gluon spin contribution to the nucleon.

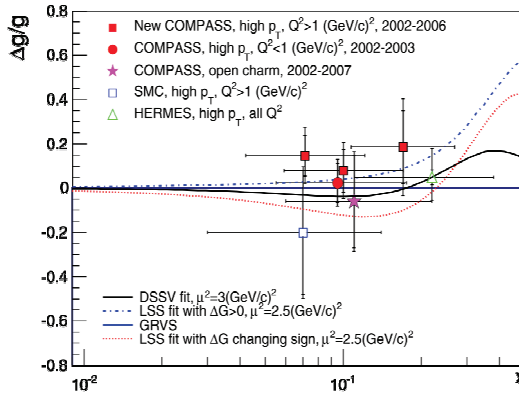

Fig. 1: Summary of the world efforts for the direct $\langle \frac{\Delta g}{g} \rangle$ measurement at LO in QCD

Review of another recent COMPASS results on longitudinal and transverse spin structure of the nucleon can be found in the following talks [8].

3. Hadron Program

At the COMPASS beam energy, 190 GeV/c, three production mechanisms are accessible. The diffractive dissociation is a likely production mechanism for spin exotic hybrids, provided they exist. The central production should be suitable for glueball production. The Coulomb production tests ground for χPT. QCD and derived models predict in particular the existence of $q\bar{q}g$ hybrids, which are difficult to identify experimentally due to mixing with ordinary $q\bar{q}$ mesons. However, some of them might have quantum numbers forbidden for $q\bar{q}$ systems, e.g. $J^{PC} = 0^{--}$, 0^{+-}, 1^{-+}. Their observation would therefore provide a fundamental confirmation of QCD.

3.1. Observation of $\pi_1(1600)$ spin-exotic state

First physics result from the COMPASS hadron program [9] were obtained from the pilot run in 2004 using a 190 GeV/c π^- beam impinging on a lead target: π^- Pb $\rightarrow \pi^-\pi^-\pi^+$.

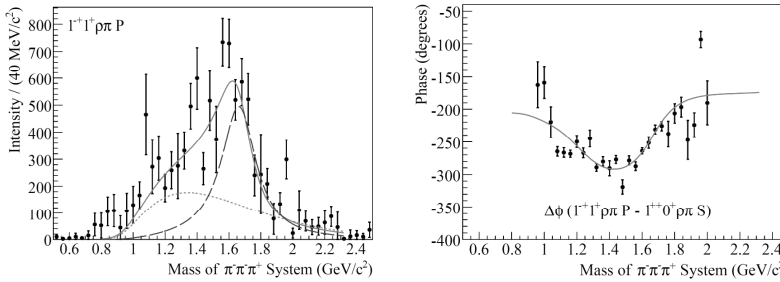

Fig. 2: Pb target, charged final state, 2004 data. Left: Intensity of spin-exotic $1^{-+}1^{+}[\rho\pi]P$ wave as a function of 3π invariant mass for 4-momentum transfer $0.1 < t' < 1.0$ $(\mathrm{GeV/c})^2$. A background and a BW function have been used in the mass dependent fit to describe this partial wave. Right: Phase difference between the $1^{-+}1^{+}[\rho\pi]P$ and the $1^{++}0^{+}[\rho\pi]S$ waves

The Figure 2 shows the spin-exotic $1^{-+}1^{+}[\rho\pi]P$ signal. The mass-dependent fit gives the values of the mass and width of $1660 \pm 10^{+0}_{-64}$ and $269 \pm 21^{+42}_{-64}$ MeV/c^2 respectively which is consistent with the hybrid candidate $\pi_1(1600)$ [10]

3.2. Search for the $\pi_1(1600)$ state in 2008-2009 data

A much bigger data set was taken by COMPASS with a liquid hydrogen target, surpassing the existing world statistics by a factor of more than 20. In addition to the $\pi^-\pi^+\pi^-$ final state with approximately 100M events, the dataset containing neutral pions, $\pi^0\pi^0\pi^-$, with more than 2.4M events has been analyzed. A preliminary mass independent PWA of the available data confirms the enhancement in the intensity around $M_X = 1.6$–1.7 GeV/c^2 [11]. The phase motion with respect to the $1^{++}0^{+}[\rho\pi]S$ wave (Fig. 3) is also consistent with the 2004 data. Figure 3, which showing the $1^{-+}1^{+}[\rho\pi]P$ wave, a large bump is observed at around 1.1 GeV/c^2 for which the interpretation is under investigation. A mass-dependent fit, leakage studies and background studies of e.g. the Deck [12] effect are ongoing for more definite conclusions. It was found also that for hydrogen, the M = 1 states, including the spin-exotic $1^{-+}1^{+}[\rho\pi]P$, are suppressed with respect to lead data, whereas M = 0 are more populated in hydrogen, giving a sum of the M substates which remains unchanged [13]. PWA, where the $\pi^-\pi^+\pi^-$ and the $\pi^0\pi^0\pi^-$ final states are compared,

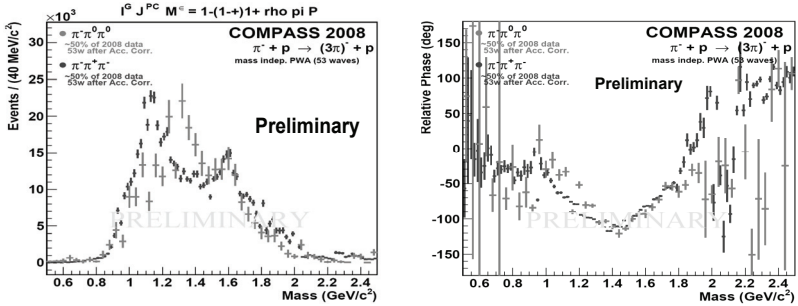

Fig. 3: H target, charged and neutral final states, 2008 data. Left: Intensity of spin-exotic $1^{-+}1^{+}[\rho\pi]P$ wave as a function of 3π invariant mass for 4-momentum transfer $0.1 < t' < 1.0$ (GeV/c)^2. Right: Phase difference between the $1^{-+}1^{+}[\rho\pi]P$ and the $1^{++}0^{+}[\rho\pi]S$ waves

show good agreement between the observed wave intensities and the predictions using isospin and Bose symmetry [11].

3.3. Physics with Kaon and Proton beams

The possibility to tag beam kaons with the CEDARs in combination with the RICH identification of final state kaons makes COMPASS an excellent tool for studying kaon diffraction. In a recent study, the reaction $K^- p \to K^- \pi^+ \pi^- p_{recoil}$ is investigated [14]. Recent results from the ongoing PWA show a spectrum of states which is mostly in agreement with previous results from the ACCMOR collaboration [15]. Channels with kaons in the final state are also of interest, in particular $\pi^- p \to (K\bar{K}\pi)\pi^- p_{recoil}$, where COMPASS can provide about an order of magnitude more events than a previous measurement by BNL [16].

Review of another recent COMPASS results on hadron program can be found in the following talks [17].

4. Conclusion

COMPASS is one of the major players in the study of the nucleon spin structure. Direct measurements of the gluon polarization $\langle \frac{\Delta g}{g} \rangle$ indicate a small value of the first moment ΔG. These results are

the probable signature for a predominant role of the angular orbital momentum of quarks and gluons in the nucleon spin decomposition.

COMPASS has excellent potential to contribute for searching QCD allowed states like multiquarks, glueballs and hybrids because it has access to diffractive dissociation and central production reactions. A large amount of data, 10-100 times the world statistics, were collected with a hadron beam in 2008-2009. Interesting results have started to emerge. A candidate for $\pi_1(1600)$ spin-exotic state ($\rho\pi$ channel) in the 2004 short pilot run was already observed. Preliminary analysis of the $\pi^-\pi^+\pi^-$ and the $\pi^0\pi^0\pi^-$ final states reconstructed in 2008-2009 data do not contradict this observation but needs further work for better understanding of background.

1. P. Abbon *et al.*, Nucl.Instr. Meth. A **577**, 455 (2007).
2. O. Kouznetsov, Nucl. Phys. Proc. Suppl. **187**, 159 (2009).
3. J. Ashman *et al.*, Phys. Lett. B **206**, 364 (1988).
4. L. Silva DIS2013, Marseilles, France, 22-26 April 2013.
5. B. Adeva *et al.*, Phys. Rev. B **70**, 012002 (2004).
6. A. Airapetian *et al.*, Phys. Rev. Lett. **84**, 2584 (2000).
7. C. Adolph, Phys. Rev. D **87**, 052018 (2013).
8. C. Marchand INPC2013, Florence, Italy 2-7 June 2013; N. Makke, EPS-HEP 2013 Stockholm, Sweden, 18-24 July 2013; A. Bressan Structure of Nucleons and Nuclei, Como, Italy, 10-14 June 2013.
9. M. Alekseev *et al.*, Phys. Rev. Lett. **104**, 241803 (2010).
10. S.U. Chung *et al.*, Phys. Rev. D **65**, 072001 (2002); A.R. Dzierba *et al.*, Phys. Rev. D **73**, 072001 (2006); Y. Khokhlov, Nucl. Phys. A **663**, 596 (2000).
11. F. Nerling, Meson2012, Cracow, Poland, 31 May–5 June 2012.
12. R.T. Deck, Phys. Rev. Lett. **13**, 169 (1964).
13. B. Ketzer, QNP2012, Palaiseau, France, 16-20 April 2012.
14. P. Jasinski, DPG2012, Mainz, Germany, 19-23 March 2012.
15. C. Daum *et al.*, Nucl. Phys. B **187**, 1 (1981).
16. J.H. Lee *et al.*, Phys. Lett. B **323**, 327 (1994).
17. B.Grube International Conference on the Structure of Baryons, Glasgow, UK, 24-28 June 2013; K. Schönning International Conference on the Structure of Baryons, Glasgow, UK, 24-28 June 2013; A. Austregesilo 15th conference on Elastic and Diffractive scattering, EDS Blois 2013, Saariselkä, Finland, 9-13 September 2013.

OVERVIEW OF ALICE RESULTS

E.L. Kryshen for the ALICE Collaboration

CERN, CH-1211 Geneva 23, Switzerland

Abstract

Selected ALICE results on the global event properties, particle spectra, azimuthal anisotropy, heavy flavour and quarkonium production in Pb–Pb collisions at $\sqrt{s_{NN}} = 2.76$ TeV are presented. First results on p–Pb collisions at $\sqrt{s_{NN}} = 5.02$ TeV are briefly reviewed.

ALICE (A Large Ion Collider Experiment) is aimed to study hot and dense QCD matter produced in heavy ion collisions at LHC [1]. ALICE collected about 10 μb^{-1} and 100 μb^{-1} of Pb–Pb collisions at $\sqrt{s_{NN}} = 2.76$ TeV during the first heavy ion runs in 2010 and 2011, respectively. In the beginning of 2013, LHC delivered 30 nb^{-1} of p–Pb collisions at $\sqrt{s_{NN}} = 5.02$ TeV, important reference data for the Pb–Pb studies. Selected results based on these data samples are briefly summarised in the following.

ALICE measurements of the global event observables indicate that the matter, produced in Pb–Pb collisions at LHC, reveal even more extreme properties than at lower energies. The charged-particle density at mid rapidity amounts to $dN/d\eta \approx 1600$ in central Pb–Pb collisions at LHC, factor 2.2 higher than in central Au-Au collisions at RHIC [2]. It corresponds to an initial energy density of about 15 GeV/fm^3 (at a conventional value of 1 fm/c for the thermalization time), factor 3 higher than in Au–Au collisions at the top energy of RHIC. The measured slope of the direct photon spectrum, $T = 304 \pm 51$ MeV [3], suggests that the initial temperature of the produced medium goes well above the critical temperature of 150–160 MeV predicted for the deconfinement state transition by lattice QCD calculations. The volume of the produced fireball, measured

with two-pion Bose-Einstein correlations, increases by factor of two from RHIC to LHC, while the matter lifetime, roughly proportional to the longitudinal dimension of the fireball, turns out to be more than 10 fm/c, 20% higher than at RHIC, in line with hydrodynamic predictions [4].

Further constraints on the evolution of the produced medium come from the measurement of the momentum-space anisotropy (flow) which is quantified by the Fourier decomposition of azimuthal particle distributions. Large elliptic flow (or second Fourier coefficient, v_2), observed both at RHIC and LHC energies [5], appears to be consistent with the dynamics of an almost perfect liquid characterized by the shear viscosity to entropy density ratio η/s close to the lower bound of $1/4\pi$ from AdS/CFT. Furthermore, the elliptic flow of identified particles reveals a clear mass ordering at low p_{T} [6], being explained by the strong collective dynamics of the medium. However, the Number of Constituent Quark (NCQ) scaling of the elliptic flow, observed at RHIC and considered as a direct consequence of the coalescence hadronization mechanism, is not that good at LHC energies [6]. Significant triangular flow (third Fourier coefficient, v_3), measured by ALICE [7], appears to be highly sensitive to the η/s ratio and initial state fluctuations providing promising tools to constrain hydrodynamic models.

ALICE measurements of the low-momentum proton, pion and kaon p_{T} spectra in central Pb–Pb collisions agree with hydrodynamic predictions within 20% supporting hydrodynamic interpretation of the data at LHC [8]. Hydro-inspired blast wave fits to these spectra allowed to extract mean collective velocity of the transverse expansion which was found to be about 65% of speed of light, 10% higher than at RHIC and in good agreement with the observed tendency from the RHIC energy scan.

ALICE also measured integrated particle yields for various particle species. At lower energies, the yields were surprisingly well described in terms of a simple thermal model with a common chemical freeze-out temperature T_{ch} [9]. However, thermal fits for 0–20% central collisions at LHC provide unexpectedly low $T_{\mathrm{ch}} = 152 \pm 3$ MeV and fail to describe the yields of multistrange hyperons [10]. On the other hand, a model with $T_{\mathrm{ch}} = 164$ MeV, extrapolated from the RHIC data, instead seems to agree with the ratios involving multi-

strange hyperons, but missing p/π and Λ/π ratios. Arguably, the significant deviation from the thermal model can be explained by the final-state interactions in the hadronic phase.

High-p_{T} hadrons are produced in hard interactions at early stages of heavy ion collisions and can be used as effective tomography probes of the produced medium. Energy loss of hard partons in the medium may result in a strong suppression of high-p_{T} hadrons (jet quenching) which was indeed observed at RHIC and quantified in terms of the nuclear modification factor R_{AA} (p_{T} spectra in AA collisions normalized to appropriately scaled pp spectra). The suppression of high-p_{T} hadrons appeared to be even stronger in central Pb–Pb collisions at LHC with R_{AA} reaching minimum of about 0.14 for $p_{\mathrm{T}} \approx 6$ GeV/c and slowly increasing at high p_{T} [11].

The suppression for open heavy flavour D^0, D^+ and D^{*+} mesons reaches factor 5 at $p_{\mathrm{T}} \sim 10$ GeV/c [12], almost as large as that observed for light hadrons (dominated by pions from gluon fragmentation) providing an indication of no strong colour charge or mass dependence of the in-medium energy loss. The observed elliptic flow of prompt D^0 mesons is also comparable with v_2 of light hadrons [13] suggesting that the azimuthal anisotropy of the system is effectively transferred to charm quarks via multiple interactions in the medium.

Suppression of hidden charm mesons due to colour-screening effects was one of the first signals predicted for the formation of deconfined phase and indeed observed at SPS and RHIC. However, high abundance of charm quarks at LHC may also result in an enhancement of bound $c\bar{c}$ states via regeneration in thermalized QGP medium. The J/ψ suppression, measured by ALICE versus number of participants N_{part}, appeared to flatten at $\langle N_{\mathrm{part}} \rangle \sim 100$ being much weaker than at RHIC for central collisions [14]. Such a centrality dependence and additional rapidity and p_{T} differential studies suggest that $c\bar{c}$ regeneration processes indeed play an important role at LHC energies. The observed hint for a non-zero elliptic flow for J/ψ in semi-central Pb-Pb collisions is also in favour of this picture [15].

J/ψ production has been also measured at forward and mid rapidity in ultraperipheral collisions (UPC) which are dominated by photon-induced reactions [16, 17]. In the LO pQCD, coherent J/ψ photoproduction cross section is proportional to the squared nuclear gluon density providing a direct tool to study poorly known gluon

shadowing in nuclei at small $x \sim 10^{-3} - 10^{-2}$, one of the most important initial state effects in heavy ion collisions. ALICE measurements appear to be in good agreement with a model which incorporates nuclear gluon shadowing according to EPS09LO global fits [18].

Proton-nucleus collisions provide futher tools to study initial and final state effects in cold nuclear matter and establish a baseline for the interpretation of heavy-ion results. The pseudorapidity dependence of the charged particle density in non-single-diffractive p–Pb events, measured by ALICE [19], is well described by DPMJET and the HIJING 2.1 generator with gluon shadowing tuned to describe RHIC d–Au data and consistent with EPS09 fits. Gluon saturation models predicted a steeper pseudorapidity dependence. The nuclear modification factor R_{pPb} of charged particles is consistent with unity at transverse momentum above 2 GeV/c indicating that the strong suppression of hadron production measured in Pb–Pb collisions at LHC is not an initial state effect but is a consequence of jet quenching in hot QCD matter [20]. ALICE also measured the J/ψ suppression pattern in p–Pb collisions, an important baseline for the interpretation of the J/ψ suppression in Pb–Pb [21]. The results are in agreement with models incorporating EPS09 shadowing or coherent parton energy losses, while Color-Glass condensate predictions are disfavoured by this measurement.

p–Pb collisions also appeared to be good for surprises. The analysis of two-particle angular correlations in high-multiplicity p–Pb collisions showed the presence of a ridge structure elongated in the pseudorapidity direction, so-called near-side ridge. Subtraction of correlation pattern for low-multiplicity events revealed a symmetric structure on the away side, similar to modulations caused by elliptic flow in Pb–Pb [22]. The dependence of v_2 coefficient, corresponding to these modulations, on p_{T} for identified particles exhibit a mass ordering pattern similar to Pb–Pb in agreement with hydrodynamic models [23]. Other models attribute the effect to gluon saturation in Pb or to parton-induced final-state effects.

In conclusion, the ALICE collaboration obtained a wealth of interesting physics results from the first heavy ion runs at LHC revealing many new phenomena not observed at lower energies. ALICE is entering a charm era of precision measurements and is looking forward to new discoveries in Pb–Pb collisions at higher energy.

1. K. Aamodt *et al.* [ALICE Collaboration], J. Instrum. **3**, S08002 (2008).
2. K. Aamodt *et al.* [ALICE Collaboration], Phys. Rev. Lett. 105, 252301 (2010).
3. M. Wilde for the ALICE collaboration. arXiv:1210.5958 [nucl-ex].
4. K. Aamodt *et al.* [ALICE Collaboration], Phys. Lett. B **696**, 328 (2011).
5. K. Aamodt *et al.* [ALICE Collaboration], Phys. Rev. Lett. **105**, 252302 (2010).
6. F. Noferini for the ALICE Collaboration, Nucl. Phys. A **904-905**, 483c (2013).
7. B. Abelev *et al.* [ALICE Collaboration], Phys. Lett. B **719**, 18 (2013).
8. B. Abelev *et al.* [ALICE Collaboration], Phys. Rev. Lett. **109**, 252301 (2012).
9. A. Andronic, P. Braun-Munzinger, and J. Stachel, Phys. Lett. B **673**, 142 (2009).
10. F. Bellini for the ALICE Collaboration, PoS ICHEP2012, 413 (2013).
11. K. Aamond *et al.* [ALICE Collaboration], Phys. Lett. B **696**, 30 (2011).
12. B. Abelev *et al.* [ALICE Collaboration], JHEP **1209**, 112 (2012).
13. B. Abelev *et al.* [ALICE Collaboration], Phys. Rev. Lett. **111**, 102301 (2013).
14. B. Abelev *et al.* [ALICE Collaboration], Phys. Rev. Lett. **109**, 072301 (2012).
15. E. Abbas *et al.* [ALICE Collaboration], arXiv:1303.5880 [nucl-ex].
16. B. Abelev *et al.* [ALICE Collaboration], Phys. Lett. B **718**, 1273 (2013).
17. E. Abbas *et al.* [ALICE Collaboration], arXiv:1305.1467 [nucl-ex].
18. K.J. Eskola, H. Paukkunen and C.A. Salgado, JHEP **0904**, 065 (2009).
19. B. Abelev *et al.* [ALICE Collaboration], Phys. Rev. Lett. **110**, 032301 (2013).
20. B. Abelev *et al.* [ALICE Collaboration], Phys. Rev. Lett. **110**, 082302 (2013).
21. B. Abelev *et al.* [ALICE Collaboration], arXiv:1308.6726 [nucl-ex].
22. B. Abelev *et al.* [ALICE Collaboration], Phys. Lett. B **719**, 29 (2013).
23. B. Abelev *et al.* [ALICE Collaboration], arXiv:1307.3237 [nucl-ex].

RECENT CMS RESULTS OF SEARCHES FOR PHYSICS BEYOND STANDARD MODEL

Alexander V. Lanyov
on behalf of the CMS Collaboration

Joint Institute for Nuclear Research, 141980 Dubna, Russia
e-mail: Alexander.Lanyov@cern.ch

Abstract

Recent results from CMS on searches for physics beyond the Standard Model are reviewed. We present the searches performed using up to 20 fb^{-1} of data from the $\sqrt{s} = 8$ TeV LHC run in 2012.

1. Introduction

The predictions of the Standard Model (SM) describe the observed particle physics data well, the recent discoveries of Higgs boson [1–4] and the rare decay $B_s \to \mu^+\mu^-$ [5, 6] do not show deviations from the SM predictions within the present experimental uncertainties. Still, many theoretical models are considered for physics beyond SM (BSM), inspired by the ideas from the electroweak symmetry breaking, the hierarchy problem, grand unification, supersymmetry, search for dark matter particles, and others [7].

The Compact Muon Solenoid (CMS) detector is one of the two general purpose detectors located at the Large Hadron Collider (LHC). It has a 3.8 T superconducting solenoid, the all-silicon inner tracker, the crystal electromagnetic calorimeter and the brass-scintillator hadronic calorimeter, the muon system covering the pseudorapidity region $|\eta| < 2.4$, details can be found in [8,9]. The first physics run was

completed in 2012, around 5 fb^{-1} integrated luminosity was obtained at the center-of-mass energy $\sqrt{s} = 7$ TeV and 20 fb^{-1} at $\sqrt{s} = 8$ TeV, resulting in variety of searches for BSM physics in many analyses.

2. Search for Physics beyond the Standard Model

The search for new physics at CMS has been performed in various channels for different theoretical models predicting deviations from SM. One of the important directions is the search for narrow resonances in the dilepton channels (the dimuon and dielectron ones). Many models of new physics predict the existence of narrow resonances at the TeV mass scale decaying to a pair of charged leptons [10, 11] and exotic hadron states [12], in particular, Sequential Standard Model Z'_{SSM} with SM-like couplings, the Z'_{ψ} predicted by grand unified theories [10], and Kaluza–Klein graviton excitations arising in the Randall–Sundrum (RS) model of a possible warped extra dimension scenario with one extra spatial dimension [13]. The recent measurement by CMS has used the data at $\sqrt{s} = 8$ TeV and integrated luminosities up to 20 fb^{-1} in both the dimuon and dielectron channels [14]. The search for resonances is based on a shape analysis of dilepton mass spectra in order to be robust against uncertainties in the absolute background level. The spectra are consistent with expectations from SM and the upper limits have been determined on the product of the cross section and branching fraction for Z' to lepton pairs relative to the SM Z boson production. The obtained upper limits on the cross section ratio

$$R_{\sigma} = \frac{\sigma(pp \to Z' + X \to \ell\ell + X)}{\sigma(pp \to Z + X \to \ell\ell + X)}$$

at 95% confidence level (C.L.) are shown in Fig. 1 for the two separate dilepton channels and their combination. No significant peaks in the mass spectra have been found, therefore the following 95% C.L. lower limits on the mass of Z' resonances has been determined: 2960 GeV for Z'_{SSM} and 2600 GeV for Z'_{ψ}. The results can be also generalized for other models [15].

CMS has also established the limits for other Z' channels: τ-lepton pair $\tau\tau$ [16], dibosons ZZ [17], $t\bar{t}$ pair [18], anomalous production of

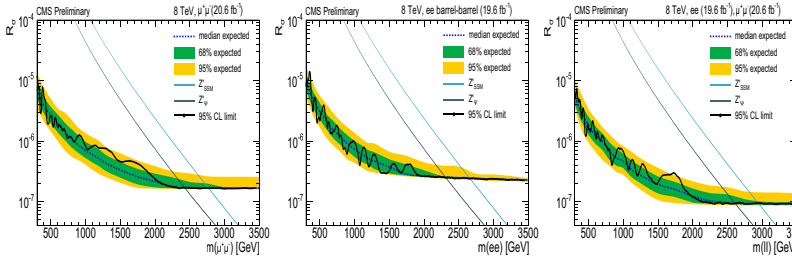

Fig. 1: 95% C.L. limits for the product of Z' cross section and branching ratios in different channels: $\mu^+\mu^-$, e^+e^-, and combined l^+l^-, from left to right

highly boosted Z bosons decaying to dimuons [19]; and W' channels: semileptonic $l\nu$ [20], diboson WZ [21] and heavy quarks bt [22].

Narrow resonances in the dijet channel have been studied and the upper limits at the 95% C.L. on the resonance cross section have been determined (Fig. 2 left plot). By comparing these generic limits with theoretical predictions for the cross section of several models of new particles, CMS sets specific lower limits on the mass of string resonances, excited quarks, axigluons, colorons, s8 resonances, E_6 diquarks, W' and Z' bosons, and RS gravitons up to 1–5.1 TeV [23].

CMS has performed a search for signals from the production of right-handed W_R bosons and heavy neutrinos N_ℓ ($\ell = e, \mu$), that arise naturally in the left-right symmetric extension to SM [24], no excess over expectations from SM processes was observed [25]. For models with an exact left-right symmetry, and assuming that either N_e or N_μ is the only right-handed neutrino accessible at LHC energies, CMS has excluded the region in the two-dimensional parameter (M_{W_R}, M_{N_ℓ}) space that extends beyond $M_{W_R} = 2.5$ TeV. Assuming degenerate neutrino masses for all neutrino flavors, and combining the 8 TeV electron and muon channel results, exclusion in the (M_{W_R}, M_{N_ℓ}) mass plane extending to $M_{W_R} = 2.8$ TeV was obtained (Fig. 2 middle plot). Combining the 7 and 8 TeV data for the muon channel only, and assuming that N_μ is light enough to be produced at the LHC, CMS has excluded right-handed W_R boson up to mass $M_{W_R} = 2.9$ TeV.

One of the most spectacular predictions of theories with the low-scale quantum gravity is an opportunity of microscopic black hole production in proton-proton collisions at the LHC energies. Such mod-

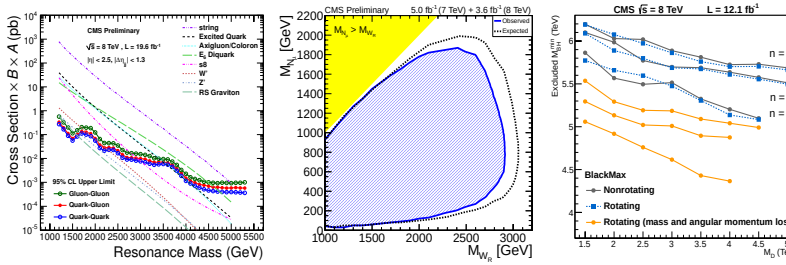

Fig. 2: Obtained limits in the search for new physics: limits for masses of narrow dijet resonances, heavy neutrino and right-handed W_R boson, and minimum masses of black holes as a function of the reduced Planck scale

els are motivated mainly by the puzzling large difference between the electroweak scale (~ 0.1 TeV) and the Planck scale ($M_{\mathrm{Pl}} \sim 10^{16}$ TeV), known as the hierarchy problem. CMS has released a new analysis at $\sqrt{s} = 8$ TeV with 12 fb^{-1} [26] to search for the black hole production in a model with n large, flat, extra spatial dimensions (ADD model) [27]. The events with the large total transverse energy have been analyzed for the presence of multiple energetic jets, leptons, and photons, which are typical signals of evaporating semiclassical and quantum black holes. New indicative limits have been found excluding semiclassical black holes with masses below 4.3 to 6.2 TeV, see Fig. 2 (right) for the minimum black hole mass excluded at 95% C.L. as function of the reduced Planck scale for various BlackMax black hole models [28] without the stable remnant and a number of extra dimensions of $n = 2, 4, 6$. The results of the analysis could be also suitable for other models in which heavy objects appear and decay to final states with a large scalar sum of objects' transverse energies of the order of several TeV. Signatures of extra dimensions were also searched for in the mass spectrum for diphotons [29], dimuons [30] and dielectrons [31], setting the 95% C.L. limits for the string scale M_s up to 4.94 TeV.

Leptoquarks carrying both baryon and lepton numbers are predicted by many SM extensions, such as grand unification theories, technicolor and composite models. CMS has published recent results for the search of the pair-produced second-generation scalar leptoquarks in the events with at least two jets and two possible leptonic channels: either two charged leptons ($\mu\mu jj$) or a charged lepton and

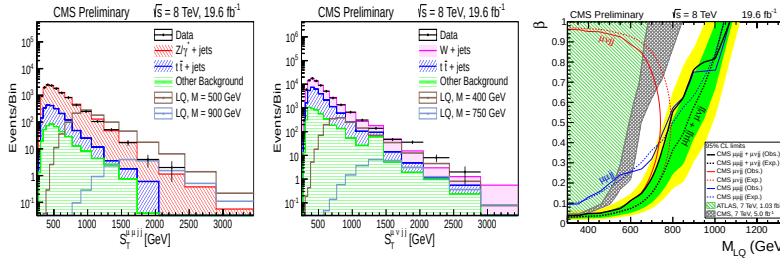

Fig. 3: Distributions on the scalar sum of transverse momenta of four objects S_T for $\mu\mu jj$ and $\mu\nu jj$ channels, and the obtained 95% C.L. limits for second-generation scalar leptoquarks

significant missing transverse energy ($\mu\nu jj$). The second generation scalar leptoquarks with masses less than 1070 (785) GeV have been excluded for $\beta = 1(0.5)$, where β is the branching fraction of a leptoquark to a charged lepton and a quark [32]. There was observed a small excess in the data in the second channel, but still it is within the calculated systematic and statistical uncertainties, therefore a higher-than-expected cross-section upper limit is visible for small values of β in the right plot of Fig. 3.

CMS also put limits for new resonances decaying to ZZ and WW states [33, 34], leptonic decays of W' bosons [35], dark matter particles [36, 37], long-lived neutral or charged particles [38–40]. Studies beyond two generations of quarks included searches for anomalous $t\bar{t}$ production [41], and vector-like quarks [42–44].

Many other searches for deviations from SM were carried out in CMS, see Fig. 4 for the graphical summary of the obtained limits on the masses and scales for various BSM models [45].

3. Conclusions

Excellent performance of LHC and CMS has provided a large dataset of pp collisions, 5 fb^{-1} at $\sqrt{s} = 7$ TeV and 20 fb^{-1} at $\sqrt{s} = 8$ TeV. In the search for new physics the experiment has managed, in particular, to exclude new particles in the 2–3 TeV range in the dilepton channels and 5 TeV for dijets, allowing to improve the limits imposed by the previous studies [45].

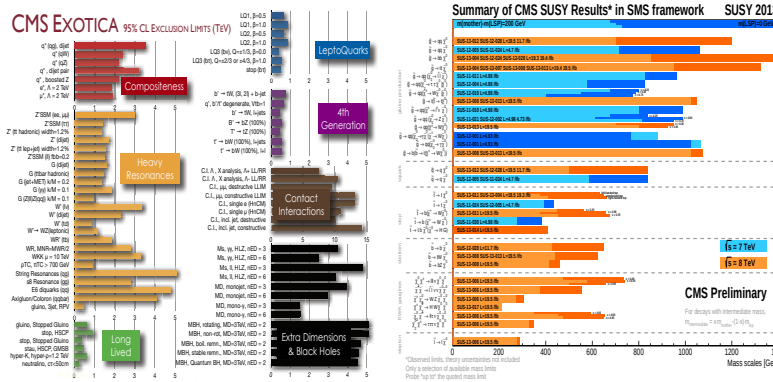

Fig. 4: Present summaries of searches for Exotica and supersymmetry in CMS

Further efforts should increase the precision of measurements and give the answers for some burning questions from the theoretical point of view. The analysis of the whole dataset taken in 2012, and the planned transition to the full design LHC center-of-mass energy of 13–14 TeV can provide answers for, at least, some of these questions, and there is also a chance to discover new unexplained features of high-energy physics, not yet predicted by the theory, as we have already seen in the past. With the new LHC data the CMS collaboration will be able to extend the mass range for these analyses well beyond the present highest points [46].

Acknowledgments

The author would like to express the gratitude to the members of the CMS Collaboration for fruitful cooperation, and to the participants of the Conference for useful discussions.

1. ATLAS Collaboration, Phys. Lett. B **716**, 1 (2012) [arXiv:1207.7214].
2. CMS Collaboration, Phys. Lett. B **716**, 30 (2012) [arXiv:1207.7235].
3. CMS Collaboration, JHEP **1306**, 081 (2013) [arXiv:1303.4571].
4. Contributions by M. Pieri and M. Tomoto in this Proc. and references therein.
5. LHCb Collaboration, Phys. Rev. Lett. **111**, 101805 (2013), [arXiv:1307.5024].

6. CMS Collaboration, Phys. Rev. Lett. **111**, 101804 (2013) [arXiv:1307.5025].
7. CMS Collaboration, J. Phys. G **34**, 995 (2007).
8. CMS Collaboration, CERN-LHCC-2006-001.
9. CMS Collaboration, JINST **3**, S08004 (2008).
10. A. Leike, Phys. Rept. **317**, 143 (1999) [arXiv:hep-ph/9805494].
11. T.G. Rizzo, hep-ph/0610104.
12. A. Ali and W. Wang, Phys. Rev. Lett. **106**, 192001 (2011) [arXiv:1103.4587].
13. L. Randall and R. Sundrum, Phys. Rev. Lett. **83**, 4690 (1999).
14. CMS Collaboration, CMS-PAS-EXO-12-061.
15. CMS Collaboration, Phys. Lett. B **720**, 63 (2013) [arXiv:1212.6175].
16. CMS Collaboration, Phys. Lett. B **716**, 82 (2012) [arXiv:1206.1725].
17. CMS Collaboration, Phys. Lett. B **718**, 1208 (2013) [arXiv:1209.3807].
18. CMS Collaboration, Phys. Rev. D **87**, 072002 (2013) [arXiv:1211.3338].
19. CMS Collaboration, Phys. Lett. B **722**, 28 (2013) [arXiv:1210.0867].
20. CMS Collaboration, CMS-PAS-EXO-12-010.
21. CMS Collaboration, CMS-PAS-EXO-12-025.
22. CMS Collaboration, Phys. Lett. B **718**, 1229 (2013) [arXiv:1208.0956].
23. CMS Collaboration, CMS-PAS-EXO-12-059.
24. W.-Y. Keung and G. Senjanovic, Phys. Rev. Lett. **50**, 1427 (1983).
25. CMS Collaboration, CMS-PAS-EXO-12-017.
26. CMS Collaboration, JHEP **1307**, 178 (2013) [arXiv:1303.5338].
27. N. Arkani-Hamed *et al.*, Phys. Lett. B **429**, 263 (1998) [hep-ph/9803315].
28. D.-C. Dai *et al.*, Phys. Rev. D **77**, 076007 (2008) [arXiv:0711.3012].
29. CMS Collaboration, Phys. Rev. Lett. **108**, 111801 (2012) [arXiv:1112.0688].
30. CMS Collaboration, CMS-PAS-EXO-12-027.
31. CMS Collaboration, CMS-PAS-EXO-12-031.
32. CMS Collaboration, CMS-PAS-EXO-12-042.
33. CMS Collaboration, CMS-PAS-EXO-12-021.
34. CMS Collaboration, CMS-PAS-EXO-12-022.
35. CMS Collaboration, CMS-PAS-EXO-12-060.
36. CMS Collaboration, CMS-PAS-EXO-12-048.
37. CMS Collaboration, CMS-PAS-EXO-13-004.
38. CMS Collaboration, JHEP **1307**, 122 (2013) [arXiv:1305.0491].
39. CMS Collaboration, arXiv:1305.0491.

40. CMS Collaboration, CMS-PAS-EXO-12-038.
41. CMS Collaboration, arXiv:1309.2030.
42. CMS Collaboration, CMS-PAS-B2G-12-015.
43. CMS Collaboration, CMS-PAS-B2G-12-019.
44. CMS Collaboration, CMS-PAS-B2G-12-021.
45. CMS Collaboration, CMS Physics Results web page
https://twiki.cern.ch/twiki/bin/view/CMSPublic/PhysicsResults
46. CMS Collaboration, arXiv:1307.7135.

INCLUSIVE DIS AT HIGH Q^2 AT HERA

S. Levonian

DESY, Notkestraße 85, 22607 Hamburg, Germany

Abstract

With recently published HERA II data both H1 and ZEUS collaborations completed their inclusive deep inelastic scattering (DIS) analyses. This report summarises main results of the cross sections measurements for inclusive neutral- (NC) and charged-current (CC) DIS reactions obtained using full HERA $e^{\pm}p$ samples of ~ 0.5 fb^{-1} per experiment, with the emphasis on high Q^2 regime.

1. Introduction

Deep inelastic scattering data from ep collider HERA provide unique information on the proton structure down to 10^{-18}m. At the same time these data represent a powerful laboratory to test the Standard Model both in electroweak and QCD sectors in a wide kinematic range of negative four-momentum transfer squared, Q^2, up to 50000 GeV^2 and Bjorken x down to 10^{-6}. Data of HERA I run (1992–2000) were used to measure unpolarised ep cross sections with the emphasis on low x and low and medium Q^2 regime where high precision of $1-2\%$ was achieved, and corresponding HERAPDF 1.0 [1] has been extracted. High luminosity HERA II run (2003–2007) with 3-fold increase of e^+p and 10-fold increase of e^-p statistics allowed to improve precision of high Q^2 and high x domain, which is a topic for this report. Together with access to $\sqrt{Q^2}$ comparable to the masses of the Z and W bosons, a longitudinal polarisation of lepton beam ($\pm 35\%$ in average) also gives an opportunity to probe the chiral structure of the electroweak interactions. In particular, the structure function $xF_3^{\gamma Z}$ is determined with improved statistical precision, and NC parity violating structure function $F_2^{\gamma Z}$ is extracted for the first time.

Detailed description of the analyses and results presented below can be found in [2, 3].

2. Results

At HERA II left handed (L) and right handed (R) polarised lepton beams yield polarised $e^{\pm}p$ cross sections. Still, unpolarised cross sections are also measured by merging L and R data sets and correcting remaining small polarisation using pQCD fits to obtain HERA II cross sections with $P_e = 0$. H1 combines then these new unpolarised NC and CC HERA II cross sections with previously published HERA I cross sections, taking into account correlated systematic uncertainties. A total of 854 data points are averaged to 413 cross section measurements. The data show good consistency with a total $\chi^2/\mathrm{ndf} = 412.1/441$. Finally, all H1 unpolarised cross sections undergo combined QCD analysis using HERAFitter framework [1, 4] based on QCD evolution code QCDNUM, thus yielding new H1PDF 2012 parton density functions, as shown in Fig. 1. One can see, that the new high Q^2 data have a visible impact on all distributions, especially in the xD distribution (where $D = d + s$).

The polarised single differential cross sections $\mathrm{d}\sigma_{\mathrm{NC}}/\mathrm{d}Q^2$ are used to construct the asymmetry

$$A^{\pm} = \frac{2}{P_L^{\pm} - P_R^{\pm}} \cdot \frac{\sigma^{\pm}(P_L^{\pm}) - \sigma^{\pm}(P_R^{\pm})}{\sigma^{\pm}(P_L^{\pm}) + \sigma^{\pm}(P_R^{\pm})}$$

and compare it to pQCD expectation using the H1PDF 2012 fit. The magnitude of the asymmetry is observed to increase with increasing Q^2 and is positive in e^+p and negative in e^-p scattering, thus confirming the parity violation effects of electroweak interactions at large Q^2 as predicted by the SM. Since for a given lepton charge the difference in the left and right polarised NC cross sections is sensitive to $F_2^{\gamma Z}$ as well as $xF_3^{\gamma Z}$ and xF_3^Z, it is possible to extract directly parity violating structure function $F_2^{\gamma Z}$ by taking proper differences for e^+p and e^-p data, for which $xF_3^{\gamma Z}$ and xF_3^Z terms cancel. Such measurement is performed double differentially in x and $Q^2 \geq 200$ GeV^2. To improve statistical significance the measurements are transformed to a common Q^2 value of 1500 GeV^2 and are averaged in each x bin

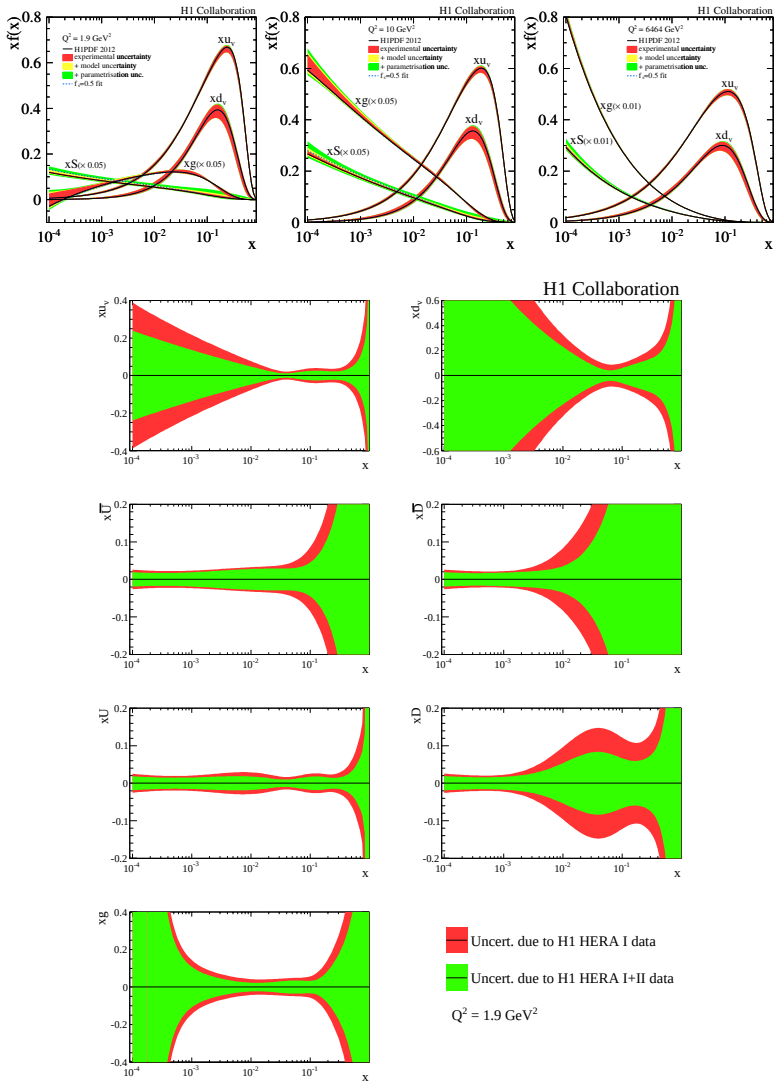

Fig. 1: H1PDF 2012. Top row: parton distribution functions at the starting scale $Q^2 = 1.9\,\mathrm{GeV}^2$ (left), at the evolved scale of $10\,\mathrm{GeV}^2$ (middle) and M_W^2 (right). Bottom part: comparison of relative experimental uncertainties of the PDFs extracted from HERA I (outer) vs HERA I+II (inner) data sets under the same fit conditions to assess the effect of the new high Q^2 measurements

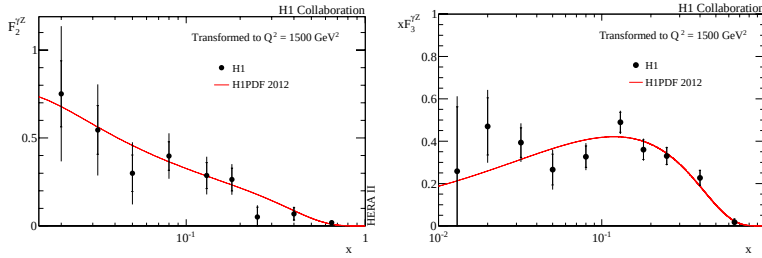

Fig. 2: Structure functions $F_2^{\gamma Z}$ (left) and $xF_3^{\gamma Z}$ (right) transformed to $Q^2 = 1\,500\,\mathrm{GeV}^2$ for data (solid points) and the expectation from H1PDF 2012 (solid curve). The inner error bars represent the statistical uncertainties and the full error bar corresponds to the total measurement uncertainty

(see Fig. 2). In turn, γZ interference term $xF_3^{\gamma Z}$ is the dominant contribution to xF_3 and is determined from new combined HERA I+II NC *unpolarised* cross sections by neglecting pure Z boson exchange term. The measurement is transformed to $Q^2 = 1500$ GeV^2 and then averaged for fixed x values. The averaged $xF_3^{\gamma Z}$ is shown in Fig. 2. Both $F_2^{\gamma Z}$ and $xF_3^{\gamma Z}$ structure functions are well described by the H1PDF 2012 fit. While the $F_2^{\gamma Z} \propto (q + \bar{q})$ reflects total parton composition in the proton, the $xF_3^{\gamma Z}$ constrains valence distribution $(2u_v + d_v)$.

The Q^2 dependence of NC and CC cross sections for $P_e = 0$ is shown in Fig. 3(left). A typical precision of these measurements are $\sim 1.5\%$ (NC) and $\sim 4\%$ (CC). The NC cross sections exceed the CC cross sections at $Q^2 \simeq 200$ GeV^2 by more than two orders of magnitude. The steep decrease of the NC cross section with increasing Q^2 is due to the dominating photon exchange cross section which is proportional to $1/Q^4$. In contrast the CC cross section is proportional to $\left[M_W^2/(Q^2 + M_W^2)\right]^2$ and approaches a constant value at $Q^2 \simeq 300$ GeV^2. The NC and CC cross sections are of comparable size at $Q^2 \sim 10^4$ GeV^2, thus illustrating the unified behaviour of the electromagnetic and the weak interactions in DIS.

The total CC cross sections for $Q^2 > 400\,\mathrm{GeV}^2$ and $y < 0.9$ for the different longitudinal lepton beam polarisations are shown in Fig. 3(right) and compared to the SM expectations using the HERAPDF 1.5 parametrisation [5]. They agree within one standard devi-

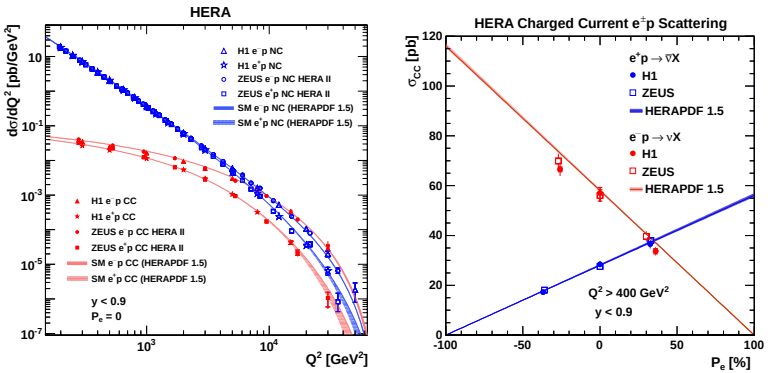

Fig. 3: Left: Q^2 dependence of the NC and CC cross sections $d\sigma/dQ^2$ for the combined HERA I+II (H1) and HERA II (ZEUS) unpolarised e^-p and e^+p data. Right: Dependence of the $e^\pm p$ CC cross sections on the longitudinal lepton beam polarisation P_e. The inner and outer error bars represent the statistical and total errors, respectively. The data are compared to the Standard Model expectation based on the HERAPDF 1.5 set [5]

ation. For H1 data a linear fit to the polarisation dependence of the measured cross sections is performed
taking into account the correlated systematic uncertainties between the measurements. The fit extrapolated to the point $P_e = +1$ for e^-p and $P_e = -1$ for e^+p results in vanishing cross sections. This result excludes the existence of charged currents involving right handed fermions mediated by a boson of mass M_W^R below 214 and 194 GeV at 95% CL for e^-p and e^+p scattering respectively, assuming SM couplings and a light ν_e^R.

3. Conclusions

With addition of HERA II data, the inclusive DIS cross sections for $e^\pm p$ interactions at $\sqrt{s} = 319$ GeV are now measured in the range of $0.045 \leq Q^2 \leq 50000$ GeV^2 and $6 \cdot 10^{-7} \leq x \leq 0.65$, spanning six orders of magnitude in (x, Q^2) plane. These data allowed to extract proton PDFs with improved accuracy, especially at high x.

The NC lepton polarisation asymmetry $A^\pm$, sensitive to parity violation, is determined, and the structure function $F_2^{\gamma Z}$ is measured for the first time. At high Q^2 the structure function $xF_3^{\gamma Z}$ is deter-

mined using unpolarised NC cross sections. All these measurements are in excellent agreement with the SM predictions. A linear scaling of the polarisation dependence of the CC total cross section is observed in accordance with the SM. The data are consistent with the absence of right handed weak currents.

1. H1 and ZEUS Collab., F.D. Aaron *et al.*, JHEP **01**, 109 (2010).
2. H1 Collab., F.D. Aaron *et al.*, JHEP **09**, 061 (2012).
3. ZEUS Collab., S. Chekanov *et al.*, Eur. Phys. J. C **61**, 223 (2009);
   ZEUS Collab., S. Chekanov *et al.*, Eur. Phys. J. C **62**, 625 (2009);
   ZEUS Collab., S. Chekanov *et al.*, Eur. Phys. J. C **70**, 945 (2010);
   ZEUS Collab., H. Abramowicz *et al.*, Phys. Rev. D **87**, 052014 (2013).
4. H1 Collab., F.D. Aaron *et al.*, Eur. Phys. J. C **64**, 561 (2009).
5. H1 and ZEUS Collab., H1-prelim-10-142, ZEUS-prel-10-018.

BEAUTY AND CHARM PRODUCTION AT HERA

Vladyslav Libov
on behalf of the H1 and ZEUS Collaborations

DESY, Notkestraße 85, 22607 Hamburg, Germany

Abstract

Recent measurements of charm and beauty production at HERA are presented. Data are compared to NLO QCD predictions in various schemes which treat differently heavy quark mass. Overall, a good description of the data is found. Determination of the charm quark mass from reduced charm production cross sections is discussed.

1. Heavy Flavour Production at HERA

The production of charm and beauty quarks at HERA, an electron-proton collider with a center-of-mass energy of 318 GeV, is interesting in several aspects. In the lowest order, heavy quarks are produced via boson-gluon fusion, hence this process is sensitive to the *gluon content of the proton* and provides means to study the validity of the gluon density determined from scaling violations of the inclusive structure function F_2. Beauty and charm production allows studies of *the multiple-hard-scale problem* in perturbative QCD which arises because the heavy quark mass is not the only hard scale in this process: at very high photon virtuality Q^2 or quark momentum the perturbative expansion can diverge due to presence of large logarithmic terms. This led to formulation of several calculation schemes which differ by the treatment of heavy quark masses. The *fixed-flavour-number scheme (FFNS)* is a rigorous calculation taking mass effects fully into account; it is expected to break down at high values of Q^2 or quark

momentum due to large logarithms mentioned above, while it should work well at lower scales. On the other hand, the *zero-mass variable-flavour-number scheme (ZMVFNS)* neglects the mass entirely, therefore it is appropriate only at very high scales where mass effects are indeed negligble. The *general-mass variable-flavour-number scheme (GMVFNS)* combines the two approaches: it converges to FFNS at low scales and to ZMVFNS at high scales. HERA data gives possibility to test these schemes. Furthermore, charm and beauty data allow the determination of the charm and beauty *quark masses*, respectively. Finally, charm production contributes up to 30% to the inclusive cross section, hence understanding of this process is important for global parton density function (PDF) analyses.

In this report, several recent heavy flavour measurements by H1 and ZEUS Collaborations at HERA are reviewed. Section 2.1 describes the results on beauty, while charm production is covered in Section 2.2. Both photoproduction ($Q^2 \ll 1$ GeV^2) and deep inelastic scattering (DIS, $Q^2 > 1$ GeV^2) regimes are considered.

2. Recent Results from HERA

2.1. Beauty Production

The H1 Collaboration performed a measurement of beauty photoproduction [1], where two electrons from semileptonic beauty hadron decays were used to identify b-quark production. This method allows detection of events with very low beauty quark momentum and thus extends the kinematic range of the previous studies. Figure 1(a) shows the measured beauty production cross section as a function of the average quark transverse momentum (with respect to the incoming proton direction). The measurement is compared to the NLO QCD predictions in the fixed-flavour-number scheme (FFNS). A good agreement is observed. Figure 1(b) shows a summary of beauty photoproduction measurements at HERA. A good description of the data by FFNS in the whole momentum range ($3 < p_T < 30$ GeV) can be observed.

2.2. Charm Production

The H1 Collaboration measured photoproduction of charm quarks by means of $D^{*\pm}(2010)$-meson identification [2]. This method gives

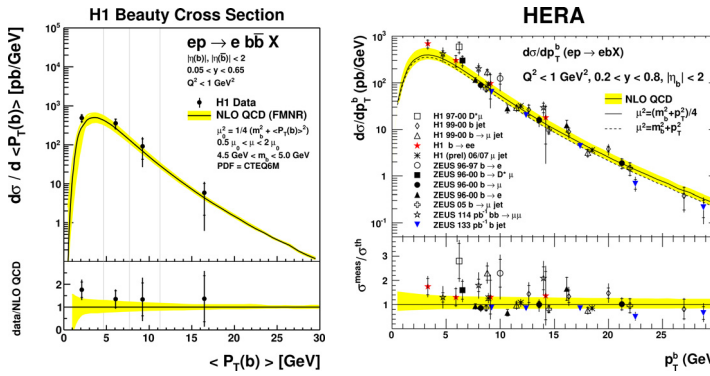

(a) (b)

Fig. 1: (a) Beauty photoproduction cross section as a function of the average quark transverse momentum [1]. (b) Summary of beauty photoproduction measurements at HERA. On both plots, points represent the data, while lines show the NLO QCD predictions (shaded area for the uncertainty)

the best signal-over-background ratio among the existing techniques of charm tagging. Figure 2 shows the $D^{*\pm}(2010)$-meson production cross section as a function of its pseudorapidity[1]. The measurement is compared to the NLO QCD predictions in the FFNS and GMVFNS schemes. Both schemes describe the data well, however theoretical uncertainties are much larger than the experimental uncertainties, especially for the GMVFNS predictions.

In a recent measurement, ZEUS employed the same technique to study charm production in deep inelastic scattering [3]. Figure 3(a) shows the $D^{*\pm}(2010)$-meson production cross section as a function of the photon virtuality Q^2, compared to FFNS predictions. The FFNS predictions describe the data up to highest achievable values of Q^2. Figure 3(b) shows a measurement of $D^{*\pm}(2010)$ production in DIS by H1 [4] confronted to ZMVFNS predictions. The ZMVFNS calculations fail to describe the data.

2.3. Measurement of the Charm Quark Mass

Heavy flavour measurements at HERA allow determination of the heavy quark masses. In order to increase the data precision, ZEUS

[1]The pseudorapidity of a particle, η, is defined as $\eta = -\ln\tan(\theta/2)$ where θ is the angle between the particle and the incoming proton.

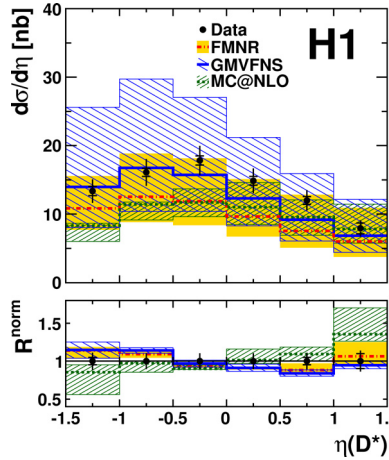

Fig. 2: $D^{*\pm}(2010)$-meson photoproduction cross section as a function of the pseudorapidity. Also shown are NLO QCD predictions in the FFNS and GMVFNS schemes as well as from the NLO Monte Carlo code MC@NLO

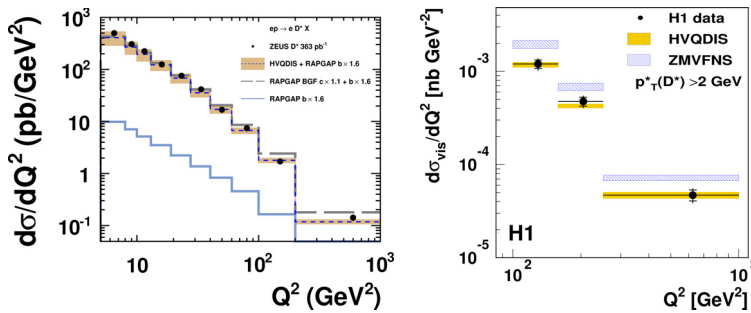

(a) (b)

Fig. 3: $D^*(2010)$-meson production cross section in DIS as a function of the photon virtuality Q^2 from ZEUS (a) and H1 (b). Points represent the data, lines (boxes) show the NLO QCD predictions

and H1 Collaborations combined their results on *reduced* cross sections of charm production in DIS [5]. The reduced cross sections are defined in the following way:

$$\sigma_{\mathrm{red}}^{c\bar{c}} = \frac{d^2\sigma^{c\bar{c}}}{dxdQ^2}\frac{xQ^4}{2\pi\alpha^2(1+(1-y)^2)}, \tag{1}$$

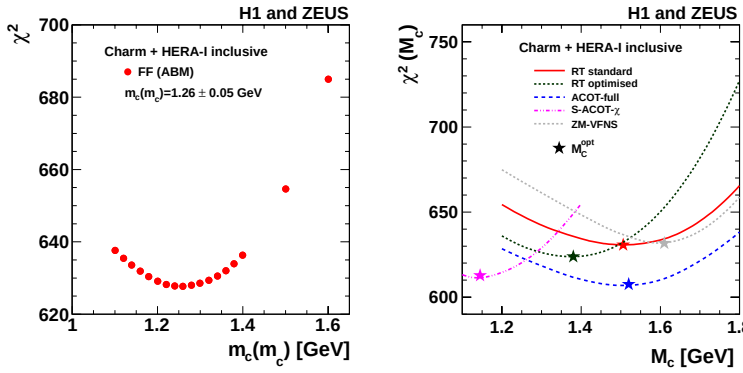

(a) (b)

Fig. 4: (a) The χ^2-value of the NLO QCD fit using charm reduced cross sections and ep inclusive DIS cross sections as a function of the running charm quark mass used in the calculation. The FFNS scheme was used for predictions. (b) Same as (a) for various GMVFNS schemes

where $d^2\sigma^{c\bar{c}}/dxdQ^2$ is the double differential cross section of charm quark-antiquark pair production[2]. These combined results, together with inclusive ep neutral and charged current DIS cross sections were used to measure the charm quark mass. An NLO QCD analysis (PDF fit) in FFNS was performed using these data as input, with various values of the charm quark mass used in the calculation. The so called ABM running mass definition [6] was used. The resulting dependence of the χ^2 of each fit as a function of the mass is shown in Fig. 4(a). The resulting mass value, taken at the minimal χ^2 is:

$$m_c = 1.26 \pm 0.05_{\rm exp} \pm 0.03_{\rm mod} \pm 0.02_{\rm param} \pm 0.02_{\alpha_s}\,{\rm GeV}, \qquad (2)$$

where uncertainties from various sources are indicated.

A similar mass scan was also performed using various GMVFNS schemes. In these schemes the quark mass definition is not unique. As can be seen from the Figure 4(b), each scheme indeed prefers a different value of the mass parameter. By using the respective optimal

[2]Reduced cross sections are obtained from the *visible* double differential cross sections (i.e. measured in a restricted kinematic phase space due to limited detector acceptance) by extrapolating them to the full phase space with help of NLO QCD predictions.

value for each scheme, the spread between predictions (had the same value been used) reduces significantly. One of the applications is stabilising predictions of the processes sensitive to the charm quark mass. As an example, the uncertainty on the predictions of W or Z boson production at LHC drops from $\sim 6\%$ to $\sim 2\%$.

3. Summary

Several recent beauty and charm measurements at HERA were presented. In general, the description of the data by NLO QCD predictions in the fixed-flavour-number scheme is good, while the zero-mass variable-flavour-number scheme fails to describe the measurements.

Charm quark running mass was measured with competitive precision from the combined reduced charm production cross sections. The obtained value is consistent with the world average [7]. Charm mass parameter was determined for various general-mass variable-flavour-number schemes; using the respective value for each scheme reduces the uncertainty of the corresponding prediction for W and Z predictions at LHC.

1. H1 Collaboration, F.D. Aaron *et al.*, Eur. Phys. J. C **72**, 2148 (2012).
2. H1 Collaboration, F.D. Aaron *et al.*, Eur. Phys. J. C **72**, 1995 (2012).
3. ZEUS Collaboration, I. Abt *et al.*, JHEP **1305**, 023 (2013).
4. H1 Collaboration, F.D. Aaron *et al.*, Phys. Lett. B **686**, 91-100 (2010).
5. H1 and ZEUS Collaborations, H. Abramowicz *et al.*, Eur. Phys. J. C **73**, 2311 (2013).
6. S. Alekhin and S. Moch, Phys. Lett. B **699**, 345 (2011).
7. Particle Data Group, K. Nakamura *et al.*, J. Phys. G **37**, 075021 (2010).

SPECTROSCOPY OF THE EXCITED CHARM MESONS AND MEASUREMENT OF FRAGMENTATION FRACTIONS

Denys Lontkovskyi
On behalf of the ZEUS collaboration

Deutsches Elektronen-Synchrotron, DESY,
Notkestrasse 85, D-220603 Hamburg, Germany

Abstract

Precise measurements from the ZEUS experiment of fractions of charm quarks fragmenting into a particular charm hadron were presented. The measurements refer to the charm quarks produced in photoproduction processes in ep collisions at HERA. The new data are compatible with previous measurements from HERA and from e^+e^- experiments, supporting the hypothesis of universality of charm fragmentation. The study of the production and the measurements of masses of neutral and charged excited charm mesons $D_1(2420)$, $D_2^*(2460)$ and widths of the neutral states $D_1(2420)^0$, $D_2^*(2460)^0$, and the helicity parameter of $D_1(2420)^0$ were presented. The results are compared with previous measurements and with theoretical predictions.

1. Introduction

The production of charm quarks at HERA may reach in certain regions of phase space up to 30% of the total inelastic cross section. The installation of a silicon microvertex detector during an upgrade of the ZEUS detector and the increase of the integrated luminosity in the HERA II running period boosted the success of the heavy-quark physics program of the ZEUS experiment.

The presented analyses [1,2] are based on the HERA II data samples accumulated during the 2003–2007 years and amount to about

370 pb^{-1} of an integrated luminosity that is more than 3 times larger with respect to the previous measurements [3,4]. Usage of the silicon microvertex detector allowed precise tagging of secondary vertices from weakly decaying charm hadrons leading to a significant reduction of the background from light flavour decays.

2. Charm Fragmentation Fractions

Fragmentation fractions of charm quark into particular hadron is a non-perturbative quantity that cannot be predicted by Quantum Chromodynamics (QCD) and have to be measured. It is usually assumed that fragmentation is independent of the charm quark production mechanism and universal for e^+e^-, ep, pp or other hadronic collisions. Precise knowledge of fragmentation fractions is important for comparison of perturbative QCD (pQCD) predictions for charm production at HERA and elsewhere.

The phase space of these measurements is defined by the virtuality of the exchanged photon $Q^2 < 1\,\mathrm{GeV}^2$ and the photon-proton centre-of-mass energy $130 < W < 300\,\mathrm{GeV}$. The relative production rates of D^0, D^+, D^{*+}, D_s^+ and the Λ_c baryon were measured[1]. The charm fragmentation fractions were determined for hadrons produced with transverse momentum $p_T\,(D, D^*, \Lambda_c) > 3.8\,\mathrm{GeV}$ and pseudorapidity $|\eta\,(D, D^*, \Lambda_c)| < 1.6$.

The D^0 mesons were reconstructed using the decay mode $D^0 \to K^-\pi^+$. In each event, two oppositely charged tracks were combined to form D^0 candidates. To calculate the invariant mass of the pair, the kaon and pion mass assignment were assumed in turn for each track. In order to increase the significance of the D^0 signal, additional cuts on the quality of D^0 daughter tracks, on the quality of the reconstructed secondary vertex and on the distance between the production and decay points were applied.

The D^0 candidates with invariant mass in a small mass window around the nominal D^0 mass were combined with an additional track that could be a "soft" pion, π_s, from a $D^{*+} \to D^0\pi_s^+$ decay. Additional cuts on p_T of the "soft" pion were applied in order to ensure a reasonable quality of the reconstruction of D^{*+} candidates.

[1]For all studied charm hadrons, the charge conjugated states are implied.

The corresponding D^0 candidate was assigned to the class "with ΔM tag if the mass difference, $\Delta M = M(K\pi\pi_s) - M(K\pi)$, was in the range $0.143 < \Delta M < 0.148\,\mathrm{GeV}$. All remaining D^0 candidates were assigned to the class of candidates "without ΔM tag". The "ΔM tagging" allows an unambiguously fixing of the K/π mass assignment and determining the contribution of candidates with incorrect mass assignment in the "without ΔM tag" sample. Reflections from $D^0 \to K^+K^-$ and $D^0 \to \pi^+\pi^-$ were subtracted using the simulated reflection shapes normalised to the $D^0 \to K^-\pi^+$ signal according to normalisation ratios observed in simulations. The numbers of D^0 mesons, extracted from the fit to invariant mass $M(K\pi)$ distributions were $N^{\mathrm{tag}}\left(D^0\right) = 7281 \pm 104$ and $N^{\mathrm{untag}}\left(D^0\right) = 27787 \pm 680$ for selections with and without ΔM tag, respectively.

Additional $D^{*+} \to D^0\pi_s^+$ decays were reconstructed with the D^0 having $p_T\left(D^0\right)$ and $\eta\left|\left(D^0\right)\right|$ outside $p_T\left(D^0\right) > 3.8\,\mathrm{GeV}$ and $\eta\left|\left(D^0\right)\right| < 1.6$ kinematic region. Further cuts were imposed on the decay products to improve the D^{*+} signal-to-background ratio. The combinatorial background was estimated from the wrong charge track combinations. The number of additional reconstructed D^{*+} mesons determined from the fit was $N^{add}\left(D^{*+}\right) = 2139 \pm 59$.

The D^+ mesons were reconstructed using the decay mode $D^+ \to K^-\pi^+\pi^+$. To ensure good quality of reconstruction, cuts on the decay products as well as on the quality of the secondary vertex were applied. The background from D^{*+} decays and from reflections of $D_s^+ \to \phi\pi^+ \to K^+K^-\pi^+$ was suppressed by applying additional cuts on the invariant mass of decay products. The number of reconstructed D^+ mesons yielded from the fit was $N\left(D^+\right) = 18917 \pm 324$.

The D_s^+ mesons were reconstructed using the decay mode $D_s^+ \to \phi\pi^+$ with $\phi \to K^+K^-$. Reflections from decays of D^+ and Λ_c^+ were added to the fit function using the reflection shapes from simulations after normalisation to the measured D^+ and Λ_c^+ signals. The number of reconstructed D_s^+ mesons determined from the fit was $N\left(D_s^+\right) = 2802 \pm 141$.

The Λ_c^+ baryons were reconstructed using the decay mode $\Lambda_c^+ \to K^-p\pi^+$. To calculate the invariant mass, $M\left(K^-p\pi^+\right)$, the proton (pion) mass was assigned to the track of the same-charge pair with larger (smaller) momentum and the kaon mass was assigned to the third track. Reflections from D^+ and D_s^+ decay were subtracted

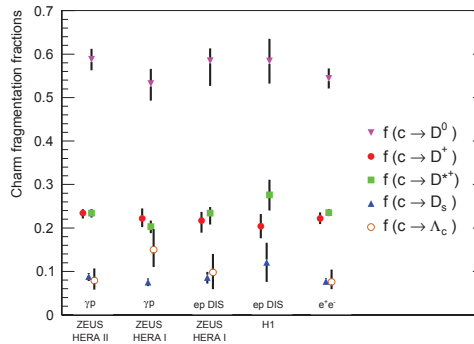

Fig. 1: Fractions of charm quarks hadronising as a particular charm hadron. The photoproduction measurements from the presented analysis are shown (first column) and compared to previous HERA results and to e^+e^- data

using the simulated reflection shapes normalised to the measured D^+ and D_s^+ production rates. The number of reconstructed Λ_c^+ baryons yielded from the fit was $N(\Lambda_c^+) = 7682 \pm 964$.

It was shown in the previous study [3] that the equivalent phase-space treatment for the non-strange charm mesons minimises differences between fragmentation fractions measured in the accepted and the full phase-space. To compare the inclusive D^+ and D^0 cross sections with the inclusive D^{*+} cross the "equivalent", $\sigma^{\mathrm{eq}}(D^+)$ and $\sigma^{\mathrm{eq}}(D^0)$ were used. The total yield of lowest mass charm-strange baryons, Ξ_c^+, Ξ_c^0, Ω_c^0, was estimated to be 14% of that of the Λ_c^+. To take this into account the Λ_c^+ cross section was scaled by the factor 1.14.

The fragmentation fraction for the measured states, determined in the kinematic region $Q^2 < 1\,\mathrm{GeV}^2$, $130 < W < 300\,\mathrm{GeV}$, $p_T(D, D^*, \Lambda_c) > 3.8\,\mathrm{GeV}$ and $|\eta(D, D^*, \Lambda_c)| < 1.6$ are illustrated in Fig. 1. The results are in good agreement with all previous measurements and have a precision which is competitive with measurements in e^+e^- collisions. The new measurements support the hypothesis of universality of charm fragmentation.

3. Excited Charm Mesons

In the previous study [4] of properties of the radially excited charm states it was found that the width of the D_1^0 was significantly above

the 2008 world-average value [5] and the helicity parameter different from predictions of Heavy Quark Effective Theory (HQET) [6, 7] and from previous determinations [8]. The presented analysis, based on an independent data sample of a higher integrated luminosity, performs a study of the production of the neutral, D_1^0, D_2^{*0}, and charged, D_1^+, D_2^{*+}, excited charm states.

The D_1^0 and D_2^{*0} mesons were reconstructed in the decay mode $D^{*+}\pi^-$ by combining each D^{*+} candidate with an additional track, assumed to be a pion (π_a), with a charge opposite to that of the D^*. The D_2^{*0} mesons were also reconstructed in the decay mode $D_2^{*0} \to D^+\pi^-$ by combining each D^+ candidate with an additional track with pion mass assignment. The D^{*+} mesons were identified via the decay modes $D^{*+} \to D^0\pi_s^+ \to (K^-\pi^+)\,\pi_s$ and $D^{*+} \to D^0\pi_s^+ \to (K^-\pi^+\pi^-\pi^+)\,\pi_s^+$. The D^+ mesons were reconstructed from the decay mode $D^+ \to K^-\pi^+\pi^+$ and D^0 mesons were reconstructed from the decay $D^0 \to K^-\pi^+$. Selection cuts were applied to the reconstructed states and their decay products to ensure reasonable acceptance and good reconstruction quality. Figs. 2(a,b) show distributions of the invariant mass of reconstructed combinations, $M\,(D^{*+}\pi_a)$(a) and $M\,(D^+\pi_a)$(b), where $\Delta M^{\rm ext}$ is the "extended" mass difference, $\Delta M^{\rm ext} = M\,(K\pi\pi_s\pi_a) - M\,(K\pi\pi_s)$ or $\Delta M^{\rm ext} = M\,(K\pi\pi\pi\pi_s\pi_a) - M\,(K\pi\pi\pi\pi_s)$ on Fig. 2(a) and $\Delta M^{\rm ext} = M\,(K\pi\pi\pi_a) - M\,(K\pi\pi)$ on Fig. 2(b).

It is expected that due to the difference in helicity parameters $h\left(D_1^0\right) = 3$ and $h\left(D_2^{*0}\right) = -1$ these states will contribute differently in different intervals of the helicity angle, $|\cos\alpha|$. To increase sensitivity to the parameters of different states a simultaneous χ^2 fit to the invariant mass spectra shown in Figs. 2(b(upper)) and Figs. 2 (a,b,c,d(lower)) was performed. Each signal was fitted to a relativistic D-wave Breit-Wigner function convoluted with a Gaussian resolution function. The feed-down component is described in [2]. Some of the parameters, such as masses and widths of wide states $D^{*0}\,(2400)$ and $D^0\,(2430)$, were fixed in the fit because of low sensitivity to their values.

The measured masses and widths are consistent with the previous ZEUS measurement [4], latest PDG values [9] and the BABAR measurements [10]. The determined D_1^0 helicity parameter, $h\left(D_1^0\right) = 7.8^{+6.7}_{-2.7}\,(\text{stat.})^{+4.6}_{-1.8}\,(\text{syst.})$, allowing some S/D-wave mixture, is consis-

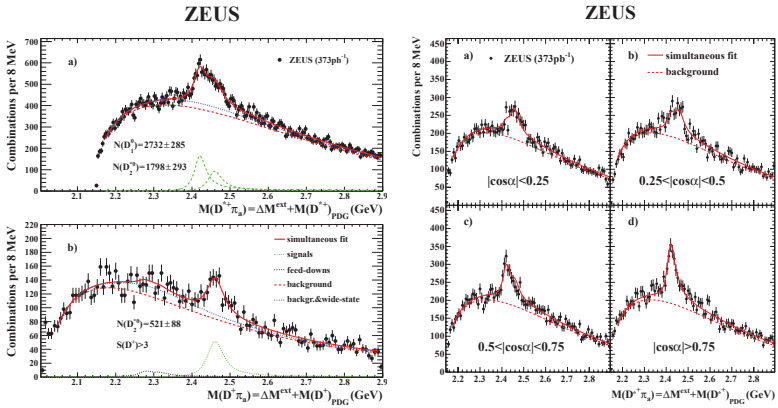

Fig. 2: (Left) The mass distributions (dots) a) $M\left(D^{*+}\pi_a\right)$ and b) $M\left(D^{+}\pi_a\right)$. The solid curves are the result of a simultaneous fit to a) D_1^0 and D_2^{*0} and to b) D_2^{*0} and feed-downs plus background function (dashed curves). The contributions of the wide states $D_1\,(2430)^0$ and $D_0^*\,(2400)^0$ are given between the dashed and dotted curves. The lowest curves are the contributions of the D_1^0 and D_2^{*0} to the fit. (Right) The mass distributions (dots) $M\left(D^{*+}\pi_a\right)$ in four helicity intervals

tent with the BABAR value and somewhat above HQET prediction of $h = 3$ and measurements by CLEO [11].

To reconstruct charged excited charm states $D_1\,(2420)$ and $D_2^*\,(2460)^+$, for the D^0 candidate a combination with an additional track, assumed to be a pion, was formed, and "extended" mass difference $\Delta M^{ext} = M\left(K\pi\pi_a\right) - M\left(K\pi\right)$ was calculated. Fig. 3 presents the invariant mass, $M\left(D^0\pi_a\right)$, of $D^0\pi_a$ combinations. A D_2^{*+} signal is clearly seen at the nominal mass of this state. The further structure is associated to incomplete reconstruction of decay chains $D_1^+, D_2^{*+} \to D^{*0}\pi^+$ with $D^{*0} \to D^0\pi^0$ or $D^{*0} \to D^0\gamma$, the feed-downs. A χ^2 fit to the invariant mass spectrum was performed in order to determine the properties of the states. Due to insufficient sensitivity of the data to some of the fit parameters, they were fixed to the recent PDG values. The measured masses of D_1^+ and D_2^{*+} agree well with the PDG values and with other measurements.

In addition to the spectroscopic and decay properties of the excited charm states, fragmentation fractions for the neutral and charged exited charm mesons were measured. The analysis presents the first

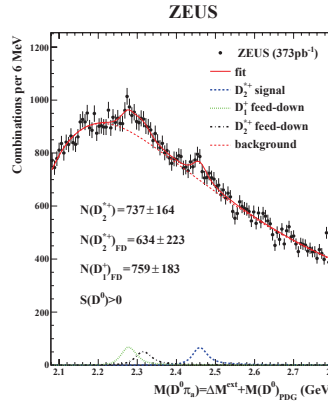

Fig. 3: The invariant mass distribution (dots) $M\left(D^0\pi_a\right)$. The solid curve is the result of a fit. The lowest curves are the contributions of the individual states to the fit

measurement of $f\left(c \to D_1^+\right)$ and $f\left(c \to D_2^{*+}\right)$. This measurement agrees with the prediction of the tunnelling model [12].

4. Conclusions

All presented results contribute to the precise measurements of production of charm states at HERA. New data on fragmentation fractions are consistent with the previous measurements at HERA and in e^+e^- collisions and support the hypothesis of universality of charm quark fragmentation. The new data on excited neutral charm states is consistent with the previous measurements in ZEUS and other experiments. The excited charged charm states were observed for the first time at HERA and the fractions of charm quarks fragmenting into these states were measured for the first time.

1. ZEUS Coll., S. Chekanov *et al.*, DESY-13-106, to be published in JHEP.
2. ZEUS Coll., S. Chekanov *et al.*, Nuclear Phys. B **866**, 229 (2013).
3. ZEUS Coll., S. Chekanov *et al.*, Eur. Phys. J. C **44**, 351 (2005).
4. ZEUS Coll., S. Chekanov *et al.*, Eur. Phys. J. C **60**, 25 (2009).
5. Particle Data Group, C. Amsler *et al.*, Phys. Lett. B **667**, 1 (2008).
6. N. Isgur and M.B. Wise, Phys. Lett. B **232**, 113 (1989).

7. M. Neubert, Phys. Rev. A **245**, 259 (1994).
8. BELLE Coll., K. Abe *et al.*, Phys. Rev. D **69**, 112002 (2004).
9. Particle Data Group, K. Nakamura *et al.*, J. Phys. G **37**, 075021 (2010).
10. BABAR Coll., P. del Amo Sachez *et al.*, Phys. Rev. D **82**, 111101 (2010).
11. CLEO Coll., P. Avery *et al.*, Phys. Lett. B **331**, 236 (1994).
12. Yi-Jin Pei, Phys. Rev. Lett. **103**, 051803 (2009).

JET PHYSICS AT HERA AND EXTRACTION OF α_s

I. Makarenko
on behalf of the H1 and ZEUS collaborations

Deutsches Elektronen-Synchrotron,
Notkestrasse 85, 22607 Hamburg, Germany

Abstract

Jet physics at HERA continues providing precision measurements towards understanding QCD and improving the determination of the proton parton distribution functions(PDFs). The most recent results obtained by the ZEUS collaboration on inclusive-jets in photoproduction(PHP) and by the H1 collaboration on normalised multi-jet cross sections at high-Q^2 neutral current deep inelastic scattering(NC DIS) are presented. The differential jet cross sections are compared to QCD calculations at next-to-leading-order(NLO) QCD and values for the strong coupling $\alpha_s(M_Z)$ are extracted.

1. Introduction

Analyses of jet production processes at HERA provide a solid ground for testing perturbative QCD as well as valuable input for determining the parton density functions of the proton. Values of α_s can be extracted from these measurements and a test of the running can be performed.

2. Inclusive-Jet Photoproduction and Determination of α_s

Inclusive-jet cross sections in photoproduction [1] have been measured in the reaction $ep \to e + \text{jet} + X$ for photon virtuality $Q^2 < 1$ GeV^2 and γp centre-of-mass energies in the region $142 < W_{\gamma p} < 293$ GeV

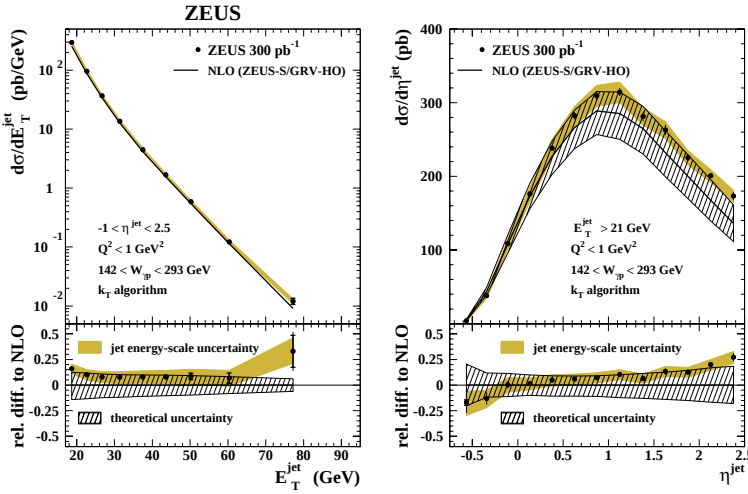

Fig. 1: The measured differential cross-sections $d\sigma/dE_T^{\rm jet}$ and $d\sigma/d\eta^{\rm jet}$ based on the k_T jet algorithm for inclusive-jet photoproduction (dots) in the kinematic region given by $Q^2 < 1$ GeV^2 and $142 < W_{\gamma p} < 293$ GeV. The NLO QCD calculations (solid lines), corrected to include hadronisation effects and using the ZEUS-S (GRV-HO) parameterisations of the proton (photon) PDFs, are also shown

with the ZEUS detector at HERA using an integrated luminosity of 300pb^{-1}. Jets were identified using the inclusive k_T jet algorithm in the laboratory frame. Single-differential cross sections are presented in Fig. 1 as functions of the jet transverse energy, $E_T^{\rm jet}$, and jet pseudorapidity, $\eta^{\rm jet}$.

The NLO QCD calculations were computed using the program by Klasen, Kleinwort and Kramer [2]. The predictions give a good description of the measurements.

The measured single-differential cross section $d\sigma/dE_T^{\rm jet}$ was used to determine value of $\alpha_s(M_Z)$. The extracted value of $\alpha_s(M_Z)$ is:

$$\alpha_s(M_Z) = 0.1206^{+0.0023}_{-0.0022}({\rm exp.})^{+0.0042}_{-0.0035}({\rm th.}).$$

The energy-scale dependence of α_s was determined from a NLO QCD fit to the measured $d\sigma/dE_T^{\rm jet}$ cross section. Values of α_s were extracted at each mean value of measured $E_T^{\rm jet}$. The extracted values of α_s as a function of $E_T^{\rm jet}$ are shown in Fig. 2.

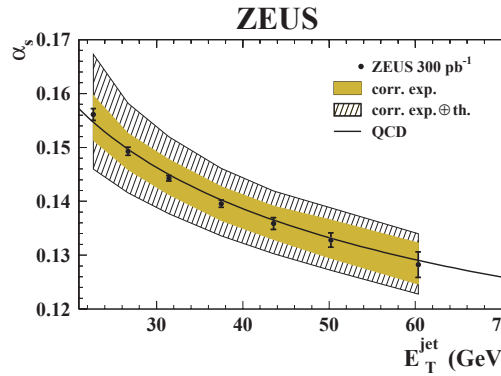

Fig. 2: The α_s values determined at various $E_T^{\rm jet}$ values from the analysis of the measured $d\sigma/dE_T^{\rm jet}$ cross section (dots)

The data demonstrate the running of α_s over a large range in $E_T^{\rm jet}$ from a single experiment. The predicted running of the strong coupling [3] calculated at two loops is in good agreement with the data.

3. Normalised Multi-Jet Cross Sections at High-Q^2 NC DIS and Extraction of α_s

Normalised inclusive jet, dijet and trijet with respect to inclusive differential cross sections in NC DIS [4] were made, for boson virtualities $150 < Q^2 < 15000$ GeV^2 and inelasticity of the interaction $0.2 < y < 0.7$, with the H1 detector at HERA, shown in Fig. 3. Jets were reconstructed in the Breit frame of reference using the inclusive k_T jet algorithm. The obtained jet cross sections are corrected for detector effects using a regularised unfolding procedure [5] and statistical correlations between the multijets and the inclusive DIS events are taken into account. The unfolded normalised jet cross sections are compared to QCD calculations at NLO. The data are well described by the predictions.

The strong coupling is determined by performing a χ^2-minimisation procedure with $\alpha_s(M_Z)$ as a free parameter. $\alpha_s(M_Z)$ is determined for each of the three normalised jet cross section measurements individually as well as for all three simultaneously.

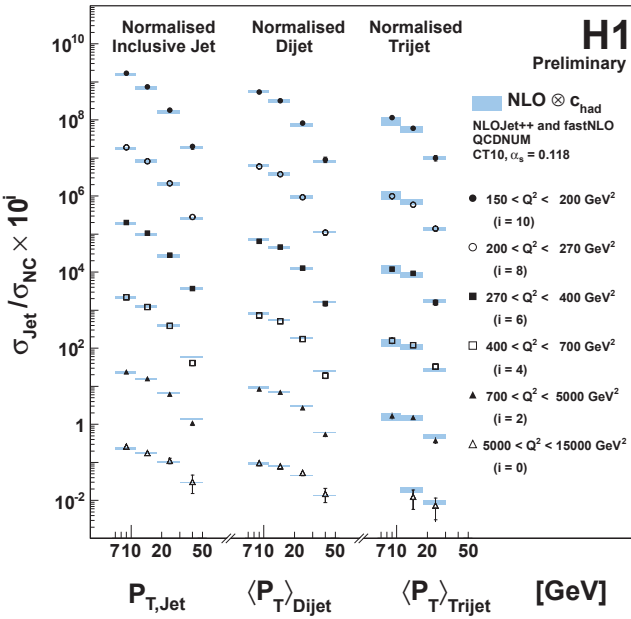

Fig. 3: Normalised inclusive-jet cross sections as functions of Q^2 and p_T and normalised dijet and normalised trijet cross section as function of Q^2 and $\langle p_T \rangle$ with comparison to NLO QCD predictions by NLOJET++ [6, 7] and QCDNUM [8] using the CT10 PDF set and $\alpha_s(M_Z) = 0.118$

$$\alpha_s(M_Z)|_{\text{normalised inclusive jets}} = 0.1197 \pm 0.0008(\text{exp.}) \pm$$
$$\pm 0.0012(\text{had.}) \pm 0.0014(\text{pdf.}) \pm 0.0054(\text{theo.})$$
$$\alpha_s(M_Z)|_{\text{normalised dijets}} = 0.1142 \pm 0.0010(\text{exp.}) \pm$$
$$\pm 0.0009(\text{had.}) \pm 0.0017(\text{pdf.}) \pm 0.0048(\text{theo.})$$
$$\alpha_s(M_Z)|_{\text{normalised trijets}} = 0.1185 \pm 0.0018(\text{exp.}) \pm$$
$$\pm 0.0016(\text{had.}) \pm 0.0013(\text{pdf.}) \pm 0.0043(\text{theo.})$$

The extracted $\alpha_s(M_Z)$ values from the normalised inclusive jets and from the normalised dijets indicate some tension, however all three values are compatible within the theoretical uncertainty and are also compatible with previous H1 publications [9] and with the

world average [10]. In order to ensure that observables have a small dependence on (missing) higher orders, the simultaneous fit to the three normalised jet cross section measurements was repeated using only bins with k-factors smaller 1.3. The k-factor which is defined as the ratio of the cross section calculated in NLO and LO $k = \sigma_{NLO+LO}/\sigma_{LO}$, is an indicator for missing higher orders in the QCD calculation. The resulting $\alpha_s(M_Z)$ is determined to be:

$$\alpha_s(M_Z) = 0.1163 \pm 0.0011(\text{exp.}) \pm 0.0008(\text{had.}) \pm$$

$$\pm 0.0014(\text{pdf.}) \pm 0.0040(\text{theo.})$$

The result is consistent with previous results in H1 publications [9].

4. Conclusions

Recent high precission jet cross section measurement in photoproduction and NC DIS at HERA have been presented. The data are well described by NLO QCD predictions. Precise values of $\alpha_s(M_Z)$ were obtained and a test of the running was performed. The obtained values of $\alpha_s(M_Z)$ have high ecxperimental precision. The total error is dominated by the theoretical uncertainty.

1. ZEUS Coll., H. Abramowicz *et al.*, Nucl. Phys. B **864**, 1 (2012).
2. M. Klasen, T. Kleinwort and G. Kramer, Eur. Phys. J. Direct C **1**, 1 (1998).
3. D.J. Gross and F. Wilczek, Phys. Rev. Lett. **30**, 1343 (1973); H.D. Politzer, Phys. Rev. Lett. **30**, 1346 (1973); D.J. Gross and F. Wilczek, Phys. Rev. D **8**, 3633 (1973); H.D. Politzer, Phys. Rep. **14**, 129 (1974).
4. H1 Coll., F. Aaron *et al.*, *Normalised Multi-Jet Cross Sections at High Q^2 using Regularised Unfolding and Extraction of $\alpha_s(M_Z)$ in Deep-Inelastic Scattering at HERA*, preliminmary results: H1prelim-12-031 (2012).
5. S. Schmitt, arXiv:1205.6201 [physics.data-an].
6. Z. Nagy and Z. Trocsanyi, Phys. Rev. D **59**, 14020 (1999).
7. Z. Nagy and Z. Trocsanyi, Phys. Rev. Lett. **87**, 82001 (2001).
8. M. Botje, Eur. Phys. J. C **14**, 285 (2000).
9. H1 Coll., F. Aaron *et al.*, Eur.Phys.J. C **65**, 363 (2010).
10. S. Bethke, Eur. Phys. J. C **64**, 689 (2009).

LHCf: FORWARD PHYSICS AND ULTRAHIGH-ENERGY COSMIC RAY

Gaku Mitsuka
on behalf of the LHCf Collaboration

University of Florence and
JSPS Postdoctoral Fellow for Research Abroad

Abstract

The Large Hadron Collider forward experiment measured very forward neutral particle spectra in LHC proton-proton collisions in 2010 and proton-lead collisions in 2013. In this paper we will discuss the inclusive photon energy spectra and the transverse momentum spectra of neutral pion at the $\sqrt{s} =$ 7 TeV and 900 GeV proton-proton collisions. The spectra in both collision energies are compared with the predictions of several hadronic interaction models that are often used for high energy particle physics and for modeling ultrahigh-energy cosmic ray showers. Also we will present the status of the data analysis at the $\sqrt{s_{NN}} = 5.02$ TeV proton-lead collisions.

1. Introduction

The Large Hadron Collider forward (LHCf) experiment [1] has been designed to measure the hadronic production cross sections of neutral particles emitted in very forward angles in proton-proton (p-p) and proton-lead (p-Pb) collisions at the LHC, including zero degrees. The LHCf detectors have the capability for precise measurements of forward high-energy inclusive-particle-production cross sections of photons, neutrons, and possibly other neutral mesons and baryons. The analyses in this paper concentrate on obtaining (1) the inclusive production rate for neutral pions (π^0s) in the rapidity range larger than $y = 8.9$ as a function of the π^0 transverse momentum, and (2) the inclusive production rate for photons in the rapidity ranges

$\eta > 8.77$ and $\eta > 8.81$ at $\sqrt{s} = 900\,\mathrm{GeV}$ and $7\,\mathrm{TeV}$, respectively, as a function of the photon energy.

This work is motivated by an application to the understanding of ultrahigh-energy cosmic ray (UHECR) phenomena, which are sensitive to the particle productions driven by soft and semi-hard QCD at extremely high energy. Although UHECR observations have made notable advances in the last few years, critical parts of the analysis depend on Monte Carlo (MC) simulations of air shower development that are sensitive to the choice of the hadronic interaction model. The fact that the lack of knowledge about forward particle production in hadronic collisions hinders the interpretation of observations of UHECR was studied in other documents, for example see Ref. [2].

This paper is organized as follows. In Sec. 2 the LHCf detectors are described. The analyses results are then presented in Sec. 3 and Sec. 4. In Sec. 5 the current status of the data analysis on the p-Pb collisions at $\sqrt{s_{NN}} = 5.02\,\mathrm{TeV}$ is shown.

2. The LHCf Detectors

Two independent LHCf detectors, called Arm1 and Arm2, have been installed in the instrumentation slots of the target neutral absorbers (TANs) [3] located $\pm 140\,\mathrm{m}$ from the ATLAS interaction point (IP1) and at zero degree collision angle. Charged particles produced at IP1 and directed towards the TAN are swept aside by the inner beam separation dipole magnet D1 before reaching the TAN. Consequently only neutral particles produced at IP1 enter the LHCf detector. At this location the LHCf detectors cover the pseudorapidity range from 8.7 to infinity for zero degree beam crossing angle. With a maximum beam crossing angle of $140\,\mu\mathrm{rad}$, the pseudorapidity range can be extended to 8.4 to infinity. The structure and performance of the LHCf detectors are explained in Ref. [4].

3. Results of π^0 Analysis at $\sqrt{s} = 7\,\mathrm{TeV}$

The combined p_T spectra of the Arm1 and Arm2 detectors are presented in Fig. 1 for six ranges of rapidity y: 8.9 to 9.0, 9.0 to 9.2, 9.2 to 9.4, 9.4 to 9.6, 9.6 to 10.0, and 10.0 to 11.0. σ_inel is the in-

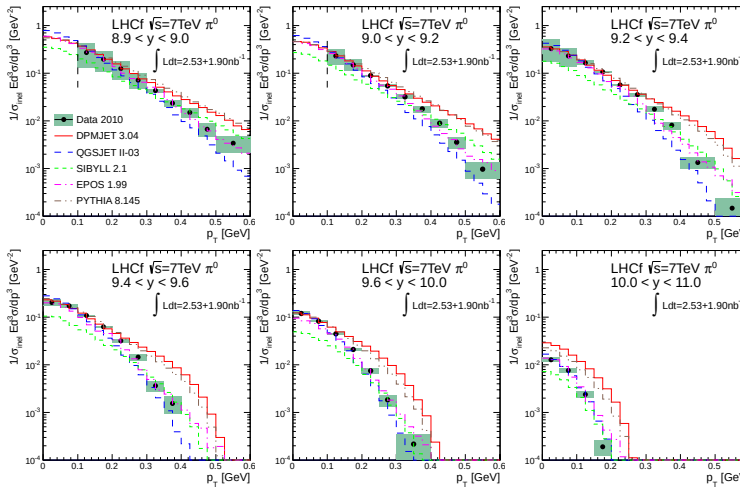

Fig. 1: Combined p_{T} spectra of the Arm1 and Arm2 detectors (black dots) and the total uncertainties (shaded rectangles) compared with the predicted spectra by hadronic interaction models

elastic cross section for p-p collisions at $\sqrt{s} = 7\,\mathrm{TeV}$. $Ed^3\sigma/dp^3$ is the inclusive cross section of π^0 production. For comparison, the p_{T} spectra predicted by various hadronic interaction models are also shown. The hadronic interaction models that have been used in the comparison are DPMJET 3.04 [8] (solid, red), QGSJET II-03 [9] (dashed, blue), SIBYLL 2.1 [10] (dotted, green), EPOS 1.99 [11] (dashed dotted, magenta), and PYTHIA 8.145 [12,13] (default parameter set, dashed double-dotted, brown). Among hadronic interaction models tested in this analysis, EPOS 1.99 shows the best overall agreement with the LHCf data. However EPOS 1.99 behaves softer than the data in the low p_{T} region, $p_{\mathrm{T}} \lesssim 0.4\,\mathrm{GeV}$ in $9.0 < y < 9.4$ and $p_{\mathrm{T}} \lesssim 0.3\,\mathrm{GeV}$ in $9.4 < y < 9.6$, and behaves harder in the large p_{T} region. Detailed discussion on the analysis is found in the other document [5].

4. Results of Photon Analysis at $\sqrt{s} = 900\,\mathrm{GeV}$ and 7 TeV

The photon energy spectra at the p-p collisions at $\sqrt{s} = 900\,\mathrm{GeV}$ are shown in Fig. 2. The Arm1 and Arm2 results are combined as

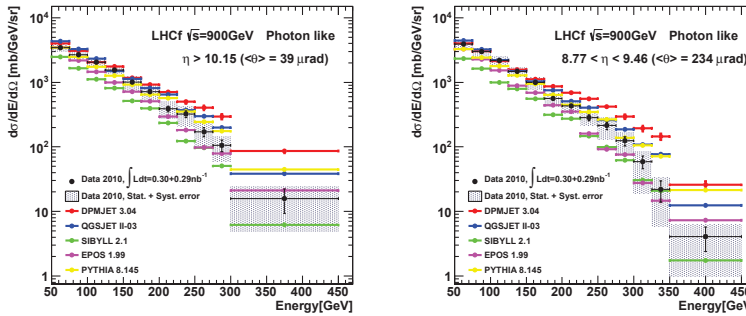

Fig. 2: Combined Arm1 and Arm2 photon energy spectra compared with MC predictions. The left and the right panels are the results of the small and the large towers, respectively

weighted averages with the weights taken to be the square of the inverse of the errors in each energy bin. The error bars of the data (black points) represent the statistical error; the hatches in the spectra represent the total uncertainty (quadratic summation of the statistical and the systematic errors). In Fig. 2, the predictions of the hadronic interaction models, QGSJET II-03, PYTHIA 8.145, SIBYLL 2.1, EPOS 1.99 and DPMJET 3.04, are also shown. The same analysis processes were applied to the MC simulations as to the experimental data except for the particle identification and its correction. For the analysis of the MC simulations, the known particle type was used. For better visibility, only the statistical errors for DPMJET 3.04 (red points) are shown by the error bars. Details of the analysis are found in Ref. [6], and the same analysis at $\sqrt{s} = 7\,\mathrm{TeV}$ is presented in Ref. [7].

5. Status of the Analysis on the p-Pb Collisions

Data taking of LHCf at the p-Pb collisions at the LHC is motivated by the fact that precise understanding of nuclear effects is crucial to adapt the measurement at the p-p collisions to the interpretation of high energy cosmic ray physics, since a target particle in cosmic ray induced hadronic intearctions is nucleus. LHCf have successfully taken the data at the p-Pb collisions at $\sqrt{s_{NN}} = 5.02\,\mathrm{TeV}$ from January to February in 2013. In this operation the Arm2 detector was

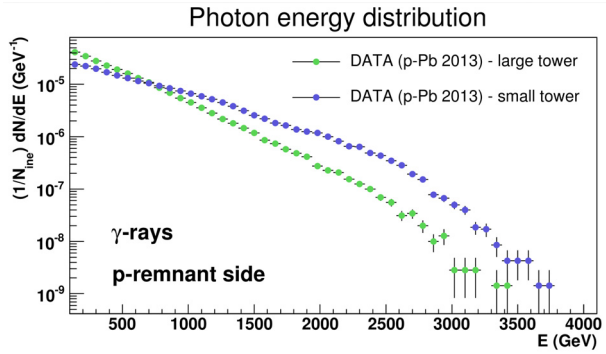

Fig. 3: Photon energy spectra at the p-Pb collisions at $\sqrt{s_{NN}} = 5.02$ TeV. Small and Large tower approximately cover $\eta > 10.0$ and $\eta > 8.7$, respectively

only used. Owing to the swap of the p and Pb beams durint the operation, the data on the both p-remnant and Pb-remnant sides are collected. The preliminary photon energy spectrum is shown in Fig. 3.

1. LHCf Technical Design Report, CERN-LHCC-2006-004
2. R. Ulrich, R. Engel and M. Unger, Phys. Rev. D **83**, 054026 (2011).
3. W.C. Turner, E.H. Hoyer and N.V. Mokhov, Proc. of EPAC98, Stockholm, 368 (1998). LBNL Rept. LBNL-41964 (1998).
4. O. Adriani *et al.*, Int. J. Mod. Phys. A 28, 1330036 (2013).
5. O. Adriani *et al.*, Phys. Rev. D **86**, 092001 (2012).
6. O. Adriani *et al.*, Phys. Lett. B **715**, 298-303 (2012).
7. O. Adriani *et al.*, Phys. Lett. B **703**, 128-134 (2011).
8. F.W. Bopp, J. Ranft, R. Engel and S. Roesler, Phys. Rev. C **77**, 014904 (2008).
9. S. Ostapchenko, Nucl. Phys. Proc. Suppl. **151**, 143 (2006).
10. E.-J. Ahn, R. Engel, T.K. Gaisser, P. Lipari and T. Stanev, Phys. Rev. D **80**, 094003 (2009).
11. K. Werner, F.-M. Liu and T. Pierog, Phys. Rev. C **74**, 044902 (2006).
12. T. Sjöstand, S. Mrenna and P. Skands, JHEP **05**, 026 (2006).
13. T. Sjöstand, S. Mrenna and P. Skands, Comput. Phys. Comm. **178**, 852 (2008).

ISOLATED PHOTONS IN PHOTOPRODUCTION AT HERA

Volodymyr Myronenko
on behalf of the ZEUS Collaboration

Deutsches Elektronen-Synchrotron,
e-mail: volodymyr.myronenko@desy.de

Abstract

Isolated photons, inclusive and with accompanying hadronic jet, have been measured by the ZEUS detector at HERA collider, using an integrated luminosity of 374 pb^{-1}. Differential cross sections as a function of photon transverse energy and pseudorapidity are presented in ranges of $6 < E_T^\gamma < 15$ GeV and $-0.7 < \eta^\gamma < 0.9$ for inclusive production. Differential cross sections for photons with jets are measured as a function of jet transverse energy and pseudorapidity in ranges of $4 < E_T^{jet} < 35$ GeV and $-1.5 < \eta^{jet} < 1.8$. The comparison of the experimental results to theoretical predictions is shown.

1. Introduction

Isolated photons with high transverse energy, E_T^γ, can be produced in a hard partonic scattering ("prompt" photons), being radiated from an outgoing high-E_T parton from a proton, or appear in neutral mesons decays. Prompt photon photoproduction can occur in two ways: direct production, where a parton from a proton interacts with a photon radiated by a lepton, and resolved production, where a parton from a proton interacts with a parton from the photon. The prompt photons are usually isolated from other particles as they are not the result of fragmentation. Thus the isolation provides a good possibility to distinguish between real prompt photon and background events.

These processes provide a possibility to test QCD models. The resolved production allows exploration of the hadronic behaviour of photons.

Theoretical predictions for isolated photon production were calculated to next-to-leading order by Fontannaz, Guillet and Heinrich (FGH) [1]. The calculations based on the k_T-factorisation approach were provided by Lipatov, Malyshev and Zotov (LMZ) [2]. Both predictions were compared to the experimental measurements.

2. Experimental Set-Up and Measurement

The measurement [3] was performed using the experimental data of 374 ± 7 pb^{-1} collected by the ZEUS detector at HERA collider, improving the precision of the previous measurements [4,5]. The lepton beam energy was 27.5 GeV and proton beam energy was 920 GeV in the analysed period of HERA operation. A detailed description of the ZEUS detector can be found elsewhere. [6]

A photon candidate was reconstructed as a narrow jet-like object by energy deposit in electromagnetic calorimeter and no-track requirement using k_T-clustering algorithm. [7] The photon energy deposit of $6 < E_T^\gamma < 15$ GeV was required in the barrel calorimeter ($-0.7 < \eta^\gamma < 0.9$). The photon candidate had to carry at least 90% of the energy of the jet. If a hadronic jet was required, it was reconstructed using the k_T-clustering algorithm in the region of $4 < E_T^{jet} < 35$ GeV and $-1.5 < \eta^{jet} < 1.8$. The DIS background was rejected by requiring no scattered lepton detected in calorimeter (typical for photoproduction).

To estimate the amount of background from neutral meson decays ($\pi^0 \to \gamma\gamma$ and $\eta \to \pi^0\pi^0\pi^0 \to \gamma\gamma\gamma\gamma\gamma\gamma$), a $\langle \delta Z \rangle$ variable was defined as

$$\langle \delta Z \rangle = \frac{\sum_i E_i |Z_i - \overline{Z_{cluster}}|}{w_{cell} \sum_i E_i}. \qquad (1)$$

The variable Z_i is Z position of center of ith cell, $\overline{Z_{cluster}}$ is the energy-weighted centriod of the energetic cluster in the calorimeter, w_{cell} is a width of the cell in the Z direction and E_i is the energy detected in the cell. The sum runs over all barrel calorimeter cells in the cluster. Figure 1 shows a two-peaked $\langle \delta Z \rangle$ distribution, where

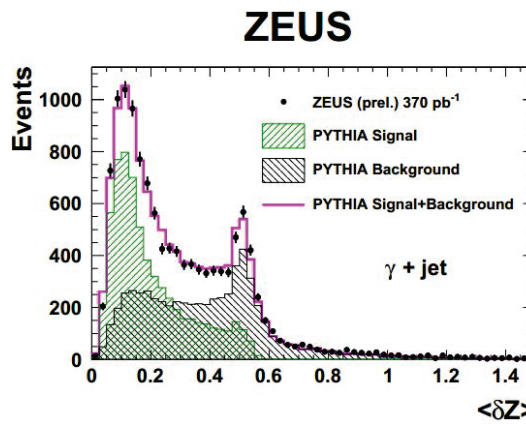

Fig. 1: Distribution of the mean width $\langle \delta Z \rangle$, fitted to a combination of Monte-Carlo modelled background from neutral meson decays and signal from isolated photons

the peak at 0.1 represents the signal from isolated photons and the peak at 0.5 stands for signal from neutral meson decays as the decay products usually hit more than one cell in contrast to the prompt photons. The amount of background was estimated by fitting the experimental distribution to a combination of Monte-Carlo modelled signal and background contributions (PYTHIA 6.416 [8]).

3. Results

To measure the differential cross sections the $\langle \delta Z \rangle$ fit was performed separately in all bins of the cross sections in the kinematic region of $6 < E_T^{\gamma} < 15$ GeV, $-0.7 < \eta^{\gamma} < 0.9$, $4 < E_T^{jet} < 35$ GeV and $-1.5 < \eta^{jet} < 1.8$. The differential cross sections were measured as a function of E_T^{γ}, η^{γ} in the inclusive measurement. For isolated photons accompanied by hadronic jets the differential cross sections were measured as a function of E_T^{γ}, η^{γ}, E_T^{jet} and η^{jet}. The most significant source of the systematic uncertainty was the uncertainties in the simulation of jet hadronisation (estimated using HERWIG 6.510 [9]) and photon energy scale uncertainty. Figure 2 shows the comparison of the experimental measurements to the theoretical NLO calculations

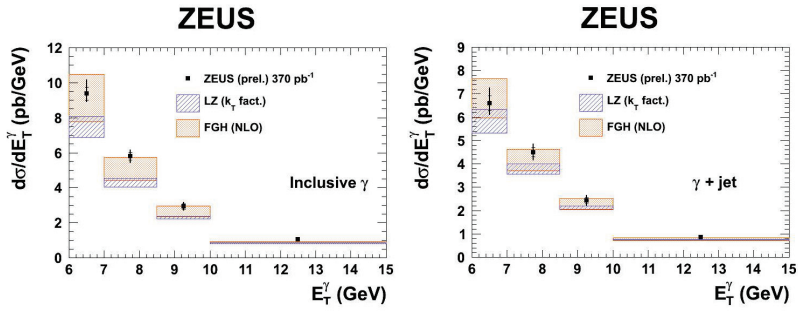

Fig. 2: Differential cross sections as functions of E_T^γ for the inclusive measurements and E_T^γ for photons accompanied by hadronic jets

and calculations based on the k_T-factorisation approach. The FGH calculations agree well with the experimental measurements.

1. M. Fontannaz, G. Heinrich, Eur. Phys. J. C **34**, 191 (2004).
2. A.V. Lipatov, N.P. Zotov, Phys. Rev. D **72**, 054002 (2005).
3. ZEUS preliminary result, ZEUS-prel-13-001 (2013).
4. ZEUS Collaboration, S.Chekanov *et al.*, Eur. Phys. J. C **49**, 511 (2007).
5. ZEUS Collaboration, H.Abramowicz *et al.*, Phys. Lett. B **88**, 715 (2012).
6. ZEUS Collaboration, U.Holm *et al.*, *The ZEUS detector*, http://www-zeus.desy.de/bluebook/bluebook.html (1993).
7. S. Catani *et al.*, Nucl Phys. B **406**, 187 (1993).
8. T. Sjöstrand, Comp. Phys. Comm. **39**, 347 (1986).
9. G. Marchesini, Comp. Phys. Comm. **67**, 465 (1992).

HIGGS RESULTS FROM CMS

Marco Pieri
for the CMS Collaborations

University of California San Diego,
La Jolla, CA, U.S.A

Abstract

The recent Higgs results from CMS based on the data collected in 2011 and 2012 at 7 and 8 TeV centre-of-mass energy, corresponding to integrated luminosities of 5 and 20 fb^{-1}, are described. The observed new boson with a measured mass of about $125.7 \pm 0.3(\text{stat.}) \pm 0.3(\text{syst.})$ GeV is found to be consistent with the Standard Model Higgs boson in all investigated properties.

1. Introduction

In the Standard Model [1,2] (SM) one scalar Higgs boson is predicted to exist [3, 4]. In July 2012, combining the 7 TeV data with the first 5 fb^{-1} collected at 8 TeV centre-of-mass (CM) energy, ATLAS and CMS discovered a new boson with a mass around 126 GeV [5, 6]. CMS [7] has now analyzed the full dataset collected in 2012 that amounts to 19.6 fb^{-1}. The analyses in the most important channels are briefly described in section 2, the combined results based on all channels are described in section 3 and finally the summary is given in section 4. The Higgs boson is expected to be produced at LHC through different processes. The dominant one is the gluon fusion followed by vector boson fusion (VBF), associated production with vector bosons (VH) and associated production with a $\text{t}\bar{\text{t}}$ pair (ttH).

2. Search Channels

The five most sensitive channels contributing to the discovery of the Higgs boson with mass of approximately 126 GeV are listed in Table 1

T a b l e 1: The five most sensitive low mass Higgs boson search channels. The most relevant information is indicated for each of them

Channel H $\rightarrow$	IntL 7+8 TeV (fb^{-1})	m_H resol.	Expected disc. sens.	Observed error on σ/σ_{SM}
$\gamma\gamma$	5.1 + 19.6	1%	4.2σ	0.27
$ZZ^{(*)} \rightarrow 4\ell$	5.1 + 19.6	1.5%	6.9σ	0.26
$WW^{(*)} \rightarrow 2\ell 2\nu$	4.9 + 19.5	20%	5.1σ	0.21
$\tau\tau$	4.9 + 19.6	15%	2.6σ	0.4
bb	5.0 + 19.0	10%	2.1σ	0.5

along with the integrated luminosities used, the mass resolution, the expected discovery sensitivity and the observed error on the signal strength, defined as $\mu = \sigma/\sigma_{SM}$.

The branching ratio (BR) of the Higgs boson decay into a diphoton pair is approximately 2×10^{-3}, corresponding to a number of expected events of almost 1000 in the full data taking period. The efficiency of the search is approximately 40%. On the other hand the background, constituted by irreducible diphoton QCD production and other reducible backgrounds in which at least one reconstructed photon comes from the mis-reconstruction of a jet (fake), is very large. The sensitivity of the analysis is increased by separating the selected events in different categories with different signal to background ratios. Among these categories some are aimed at selecting exclusive signatures corresponding to the VBF and VH production modes [1]. Figure 1 left shows the p-value as function of the Higgs mass in the studied mass range 110–150 GeV. The maximum observed p-value is 3.2σ (for 4.2σ expected), found at a mass of 125 GeV, and corresponds to a signal strength of 0.78 ± 0.27 [8].

The $H \rightarrow ZZ \rightarrow 4\ell$, Higgs decay into four charged leptons, is usually referred to as the golden channel for the detection of the Higgs boson at LHC. The BR is very small, of the order of 10^{-4} but the background is smaller still and the signal can be clearly seen as a peak in the invariant mass of the four charged leptons. Figure 1 right shows the invariant mass spectrum of all selected candidates in the full mass range. Three distinct features are visible in the plot: at low mass the Z peak corresponding to the Z into four lepton decay, at high mass the SM ZZ continuum production and in the intermediate

[1] ttH has also been studied but it is not yet part of the combined $\gamma\gamma$ analysis.

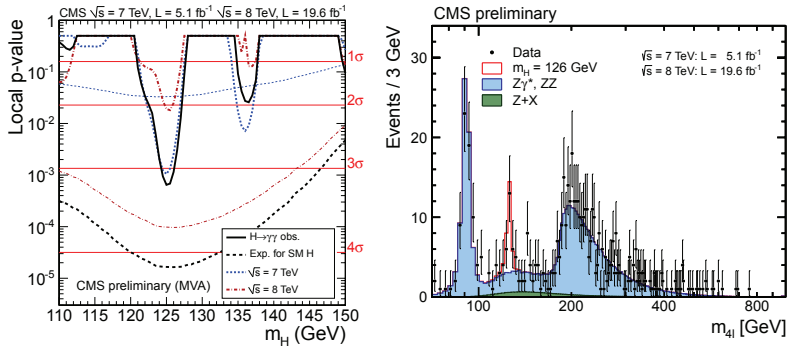

Fig. 1: Left: local p-value as function of mass for the $H \to \gamma\gamma$ channel. The dashed lines indicate the expected p-value in the hypothesis of the existence af a standard model Higgs boson while the solid lines show the observed p-value. Right: invariant mass spectrum of all candidates of the $H \to ZZ \to 4\ell$ search in the full mass range

region, at about 125 GeV, the excess corresponding to the discovered Higgs boson. To derive the final results the information from all measured angles is combined into a kinematic discriminant that is used together with the mass and another discriminant addressing the VBF production channel. At 125 GeV an excess of 6.7σ is observed for an expected of 7.3σ and the measured signal strength is $0.9^{+0.30}_{-0.24}$ [9].

The $H \to WW \to 2\ell 2\nu$ channel has comparable sensitivity to the $\gamma\gamma$ and ZZ channels at a mass of 125 GeV. The signature is two high p_T leptons plus missing transverse energy (MET) originating from the undetected neutrinos from the W decays. The missing neutrinos also limit the precision of the mass determination that is approximately 20%. The signal shows up in this channel as an excess of data over the expected background that is estimated using data whenever possible. The analysis is carried out in different categories depending on the number of jets present in the events and on the flavour of the leptons. Same-flavour leptons, ee and $\mu\mu$, and different-flavour events, eμ, are analyzed separately. The most sensitive channels are the 0-jet and 1-jet different-flavour and they are exploited using an optimized 2D analysis based on the dilepton mass and the transverse mass constructed with the dilepton system and the MET. Combining all channels an excess of 4.0σ is observed at 125 GeV for an expected of 5.1σ and the measured signal strength is found to be 0.76 ± 0.21 [10].

The H $\rightarrow \tau\tau$ analysis is carried out in many different channels, split using the Higgs production signature, 0-jet, 1-jet, 2 VBF jets, and VH production, and the combination of the two τ-leptons decay modes: electron, muon or hadronic. The most important aspects of the analysis are the mass reconstruction that uses a full kinematic fit, and the background estimation, that is obtained by fitting all channels simultaneously. The 0-jet channels have large statistics and help constraining the different nuisances that control the background rates and shapes. The combination of all channels gives an observed excess of 2.85σ a 125 GeV for an expected of 2.62σ and a measured signal strength of 1.1 ± 0.4 [11].

As the background in the gluon fusion production channel is too large, the H $\rightarrow$ bb channel exploits the VH mode [12], with leptonic decays of the W and Z bosons, the VBF [13] and ttH [14] production channels. The analysis is optimized using an MVA discriminant that encapsulates the discrimination power of all most sensitive variables. The shape of this discriminant is fitted in a similar way as in the H $\rightarrow \tau\tau$ channel. The $b\bar{b}$ invariant mass is reconstructed using a multivariate regression that yields a mass resolution of 8-9%. Combining all channels an excess of 2.1σ is observed at 125 GeV for an expected of 2.1σ and the measured signal strength is 1.0 ± 0.5. The combination of this channel with the H $\rightarrow \tau\tau$ gives an excess greater than 3σ at 125 GeV that constitutes direct evidence of the Higgs boson decays into fermions.

Recently a search for invisible decays in the VBF and ZH production modes has been carried out. The expected BR into invisible modes is tiny in the standard model. No signal has been observed and 95% C.L. limits have been derived on the invisible branching ratio of the Higgs boson of 0.69 and 0.75 for the two channels [16, 17].

Finally the search for the Higgs boson decays into Zγ is also performed [15]. The sensitivity of this channel is much lower than others and a 95% C.L. limit on μ of approximately ten times the SM is obtained.

3. Combination of Results

All channels are combined and the final results on signal strengths, couplings and mass are derived. From the high mass resolution $\gamma\gamma$

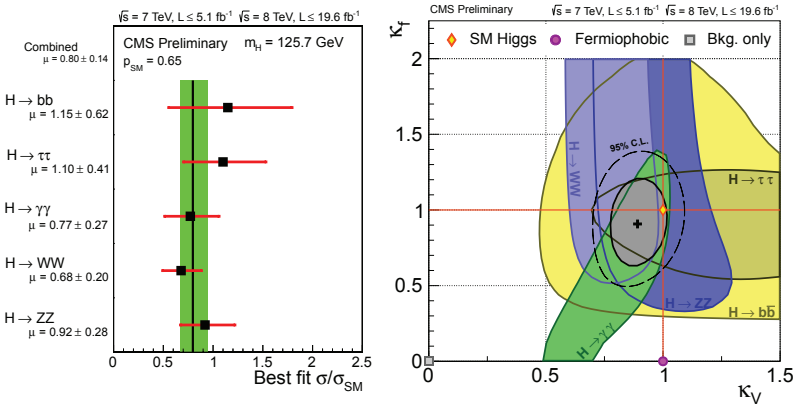

Fig. 2: Left: Higgs boson signal strength measured in the five most sensitive channels. The line and the band indicate the overall fitted μ and its uncertainty. Right: Confidence level contours of the scaling factors of the fermion couplings and the vector couplings of the Higgs boson. The contributions from the five different channels are also indicated

and ZZ channels the mass of the Higgs boson can be measured and is found to be $M_{\mathrm{H}} = 125.7 \pm 0.3(\mathrm{stat.}) \pm 0.3(\mathrm{syst.})\,\mathrm{GeV}$. Figure 2 left shows a summary of the measured signal strengths in the five most sensitive search channels [18], evaluated at the measured mass of 125.7 GeV. All channels present some excess and are consistent with the SM expectations. The overall signal strength is found to be $\mu = 0.80 \pm 0.14$, again consistent with the standard model. From the combined fit of all channels it is also possible to measure various couplings of the Higgs boson to the fermions and to the vector bosons. Figure 2 right shows the constraints that are obtained on the two parameters κ_f and κ_V that are used to scale all couplings to the fermions and to the vector bosons respectively. The measured angles between the final products and the beam axis contain information on the spin and parity of the new boson. The best channel for this analysis is the ZZ channel where all angles can be measured. Different models have been tested and all tested spin-parity J^P hypotheses 0^-, 1^+, 1^- and graviton-like 2^+ models are excluded at a confidence level larger than 95%. In summary data suggest a strong preference for the 0^+ nature of the discovered Higgs boson.

4. Summary

Preliminary results of the analysis of the full dataset collected at LHC in 2011 and 2012 at 7 and 8 TeV centre-of-mass energy and corresponding to integrated luminosities of 5 and 20 fb^{-1} have been reported. The observed new boson with a measured mass of about $125.7 \pm 0.3(\text{stat.}) \pm 0.3(\text{syst.})$ GeV is found to be consistent with the Standard Model Higgs boson in all investigated properties. Many different searches for beyond the SM Higgs bosons have also been carried out and improved exclusion limits have been obtained.

1. S. Weinberg, *A Model of Leptons*, Phys. Rev. Lett. **19**, 1264 (1967).
2. A. Salam, *Elementary Particle Theory* (Almquist and Wiksells, Stockholm, 1968), p. 367.
3. F. Englert and R. Brout, Phys. Rev. Lett. **13**, 321 (1964).
4. P.W. Higgs, Phys. Rev. Lett. **13**, 508 (1964).
5. G. Aad *et al.* [ATLAS Collaboration], Phys. Lett. B **716**, 1 (2012).
6. S. Chatrchyan *et al.* [CMS Collaboration], Phys. Lett. B **716**, 30 (2012).
7. CMS Collaboration, JINST **3**, S08004 (2008).
8. CMS Collaboration, CMS Phys. Anal. Summ. CMS-PAS-HIG-13-001 (2013).
9. CMS Collaboration, CMS Phys. Anal. Summ. CMS-PAS-HIG-13-002 (2013).
10. CMS Collaboration, CMS Phys. Anal. Summ. CMS-PAS-HIG-13-003 (2013).
11. CMS Collaboration, CMS Phys. Anal. Summ. CMS-PAS-HIG-13-004 (2013).
12. CMS Collaboration, CMS Phys. Anal. Summ. CMS-PAS-HIG-13-012 (2013).
13. CMS Collaboration, CMS Phys. Anal. Summ. CMS-PAS-HIG-13-011 (2013).
14. CMS Collaboration, CMS Phys. Anal. Summ. CMS-PAS-HIG-13-019 (2013).
15. CMS Collaboration, CMS Phys. Anal. Summ. CMS-PAS-HIG-13-006 (2013) [arXiv:1307:5515 [hep-ex]].
16. CMS Collaboration, CMS Phys. Anal. Summ. CMS-PAS-HIG-13-013 (2013).
17. CMS Collaboration, CMS Phys. Anal. Summ. CMS-PAS-HIG-13-018 (2013).
18. CMS Collaboration, CMS Phys. Anal. Summ. CMS-PAS-HIG-13-005 (2013).

THE INCLUSIVE PRODUCTION OF THE MESON RESONANCES IN NEUTRINO-NUCLEON INTERACTIONS

A.Yu. Polyarush

Institute for Nuclear Research, RAS

Abstract

The inclusive production of the meson resonances $\rho^0(770)$, $f_0(980)$, $f_2(1270)$, $K^{*+}(892)$ in neutrino-nucleon interactions has been studied with the NOMAD detector. The detector was exposed to the wide band neutrino beam generated by 450-GeV protons at CERN-SPS. For the first time the $f_0(980)$ meson is observed in neutrino interactions. The significance of its observation is 6 standard deviations. The presence of $f_2(1270)$ in the neutrino interactions is reliably established. The average multiplicity of these three resonances is measured as a function of several kinematic variables. The experimental results are compared to the multiplicities obtained from a simulation based on the Lund model. Matrix element of spin density matrix for $K^{*+}(892)$ meson have been measured.

1. Introduction

The study of inclusive meson and baryon resonances is believed to reveal more directly the primary interaction mechanism than the studies of stable particles (like pions and kaons) since many of the latter are produced in the decays.

The role of the orbitally excited mesons, for example $f_0(980)$ ($J^{PC} = 0^{++}$) and $f_2(1270)$ ($J^{PC} = 2^{++}$), is of special interest in view of possible different dynamics of their production. Compared to other mesons within its mass region the $f_0(980)$ has a small total

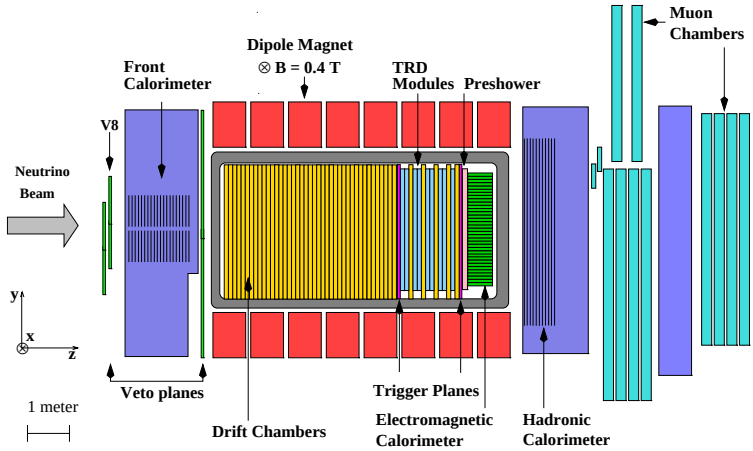

Fig. 1: A sideview of the NOMAD detector

width and a low partial width to $\gamma\gamma$. A number of nonstandard interpretations of the $f_0(980)$ state were suggested: one approach regards the $f_0(980)$ as four quark bound state [1], others as KK molecule states [2]. Robson [3] proposed an interpretation of the $f_0(980)$ as scalar glueball.

2. The NOMAD Detector

NOMAD (see Fig. 2) is described in [4]. It consists of a number of subdetectors most of which are located inside a 0.4 T dipole magnet with an inner volume of $7.5\times3.5\times3.5$ m^3: an active target made of drift chambers (DC) with a mass of 2.7 tons (mainly carbon – 78.87%), an average density of 0.1 g/cm^3 and a total length of about one radiation length ($\sim 1.0X_0$), followed by a transition radiation detector (TRD), a preshower detector (PS) and a lead glass electromagnetic calorimeter (ECAL). The low density and the good instrumentation of the active target (there is less than 1% of a radiation length between two consecutive measurements) make possible to obtain the detailed information about the final state of neutrino interactions.

3. Extraction of the Resonance Signal

The resonance signal is determined by fitting the invariant mass distribution of all possible $\pi^+\pi^-$ combinations dN/dm with the reflections subtracted by an expression containing a relativistic Breit-Wigner function $BW(m)$ for the signal and a parameterization $BG(m)$ for the background:

$$\frac{dN}{dm} = [1 + a_1 BW_\rho(m) + a_2 BW_{f_0}(m) + a_3 BW_{f_2}(m)]BG(m). \quad (1)$$

The Breit-Wigner function is

$$BW = \frac{m}{k} \frac{m_R \Gamma'_R}{(m^2 - m_R^2)^2 + m_R^2 \Gamma'^2_R}, \quad (2)$$

where

$$\Gamma'_R = \Gamma_R \left(\frac{k}{k_R}\right)^{2L+1} \frac{m_R}{m}. \quad (3)$$

Here m_R and Γ_R are central mass and width of the resonance R; L is the relative orbital angular momentum of the two pions (equal to the spin of the resonance): $L = 0$ for $f_0(980)$, $L = 1$ for $\rho^0(770)$, and $L = 2$ for $f_2(1270)$; k is the pion momentum in the resonance rest frame; k_R is the value of k when $m = m_R$ (central mass). The background was assumed to have the following shape

$$BG = a_4(m - 2m_\pi)^{a_5} \exp(a_6 m + a_7 m^2 + a_8 m^3) \quad (4)$$

which takes into account the threshold effect and exponential fall-off of the distribution at high values of m.

4. Results

After correcting the result of the fit for the efficiencies determined from the MC (about 0.77 for all the studied resonances) and for the branching ratios $BR(R \to \pi^+\pi^-)$ we obtain the results [5] shown in Table 1. The average multiplicity of these three resonances was measured as a function of several kinematic variables. Fig. 2 shows the average multiplicities of each of the studied resonances as a function of W^2. From Fig. 3 we see that the forward production of $\rho^0(770)$ is

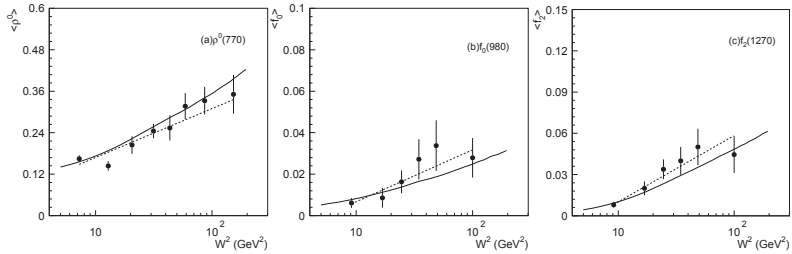

Fig. 2: Average $\rho^0(770)$ (a), $f_0(980)$ (b), $f_2(1270)$ (c) multiplicity as a function of W^2. The solid line represents the result of the Lund simulation. The dashed line represents a fitted function $N_R = a + b \times \ln W^2$. The errors are statistical only

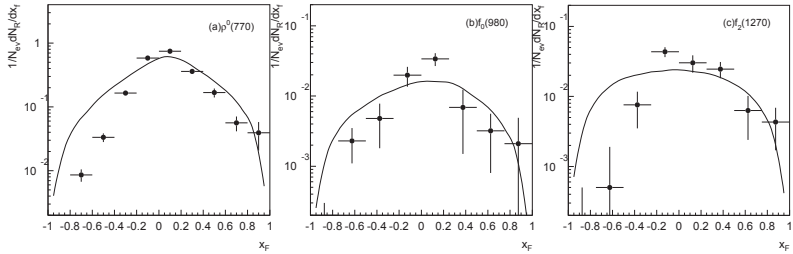

Fig. 3: Average $\rho^0(770)$(a), $f_0(980)$(b), $f_2(1270)$(c) multiplicity as a function of x_F. The solid line represents the result of the Lund simulation

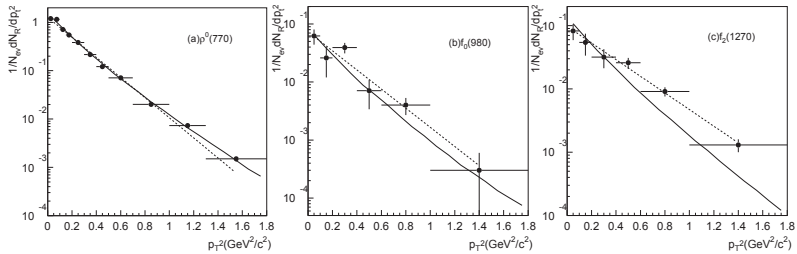

Fig. 4: Average $\rho^0(770)$ (a), $f_0(980)$ (b), $f_2(1270)$ (c) multiplicity as a function of p_T^2. The solid line represents the result of the Lund simulation. The dashed straight line represents the result of the fit by the function $ae^{-bp_T^2}$

stronger than the backward production. The fall of the $\rho^0(770)$ p_T^2 dependence appears steeper than previously measured in neutrino experiments. The p_T^2 distributions for $f_2(1270)$ are harder than simulated by JETSET.

T a b l e 1: Corrected numbers of mesons, their masses and widths

Resonance	Number of mesons	Average Multiplicity	Mass MeV	Γ (MeV)
$\rho^0(770)$	130368±4336	0.195±0.007	768±2	151±7
$f_0(980)$	11809±1965	0.018±0.003	963±5	35±10
$f_2(1270)$	25189±3958	0.038±0.006	1286±9	198±30

Matrix element of spin density matrix for $K^{*+}(892)$ meson have been measured [6]

$$\rho_{00} = 0.40 \pm 0.06(\text{stat.}) \pm 0.03(\text{syst.}). \quad (5)$$

Result are in agreement within errors with the $\rho_{00} = 1/3$, which corresponds to no spin alignment for this meson. For $K^{*+}(892)$ mesons produced in νNC interactions the measured parameter is $\rho_{00} = 0.66 \pm 0.10(\text{stat.}) \pm 0.05(\text{syst.})$.

1. R.L. Jaffe and K. Johnson, Phys. Lett. B **60**, 201 (1976); R.L. Jaffe Phys. Rev. D **15**, 267 (1977) and Phys. Rev. D **15**, 269 (1977).
2. J. Weinstein and N. Isgur, Phys. Rev. D **41**, 2236 (1990).
3. D. Robson, N. Phys. B **130**, 328 (1977).
4. J. Altegoer *et al.*, NOMAD Collaboration, Nucl. Instr. and Meth. A **404**, 96 (1998).
5. P. Astier *et al.*, Nucl. Phys. B **601**, 3-23 (2001).
6. A. Chukanov, D. Naumov, B. Popov *et al.*, Eur. Phys. J. C **46**, 69-79 (2006).

LHCb OVERVIEW

V.M. Pugatch
on behalf of the LHCb Collaboration

Institute for Nuclear Research,
National Academy of Science,
Kyiv, Ukraine

Abstract

An overview of selected results obtained by the LHCb Collaboration on heavy flavored hadrons spectroscopy, lifetimes, CP symmetries as well as rare decays is presented.

1. Introduction

Since 2011, the Large Hadron Collider has extended the research area for interactions in energy scale up to 10^{13} eV where quark-gluon degrees of freedom determine the properties of collisions. The recent discovery of the light Higgs boson at CERN also implies that new physics may exist in contribution of super-partners in loops. Thus, rare decays precisely described in the framework of the Standard Model (SM) are good candidates for probing New Physics measuring angular distributions, branching ratios etc. CP symmetry Violation (CPV) is another potential source of New Physics since SM evaluations are by far lower than needed to explain the baryon asymmetry in the Universe. New Physics may modify measured features of CP-violation and rare decays via its contribution in loop diagrams. Selected results of the LHCb measurements of CP violating as well as rare decays observables are discussed for the 2011 data set obtained in pp collisions at a center of mass energy of 7 TeV and integrated luminosity of 1 fb^{-1} (if not otherwise indicated).

2. LHCb Detector and Its Performance

LHCb detector [1] is built mainly for the CP-violation as well as rare decay studies. It is a forward spectrometer (10–300 mrad) measuring forward produced b-hadrons (B^0, B^+, B_s, B_c, b-baryons) as well as many other species. The LHC delivers luminosity at the LHCb interaction point IP-8 of about $(2\text{–}4)\times10^{32}$ cm^{-2}s^{-1} for proton-proton energies up to 8 TeV. The $b\bar{b}$ cross-section measured by LHCb at 7 TeV constitutes 79 µb [2] in LHCb acceptance, implying $\sim 100\,000$ $b\bar{b}$ pairs produced every second. In each p-p collision about 1500 charged particles are produced resulting in a necessity of multi-level triggering for preselection of Beauty and Charm events and loading challenging radiation on detectors and readout electronics. The LHCb detector has performed excellently in this environment:

- Acceptance $2 < \eta < 5$.
- Momentum resolution about 0.5%.
- Track reconstruction efficiency $> 96\%$.
- Impact parameter resolution: ~ 20 µm.
- Decay time resolution: ~ 45 fs.
- Invariant mass resolution: $\sim$ (10–20) MeV/c^2.
- Particle identification with efficiency exceeding 90% by Ring-Imaging Cherenkov Detectors and Muon System.

The data accumulated so far correspond to the integrated luminosities in the years:

- 2010—37 pb^{-1},
- 2011—1.0 fb^{-1} at $\sqrt{s} = 7$ TeV,
- 2012—2.0 fb^{-1} at $\sqrt{s} = 8$ TeV.

A highly efficient trigger provides selection of B-hadrons decay products with perfect separation of the secondary vertex allowing to

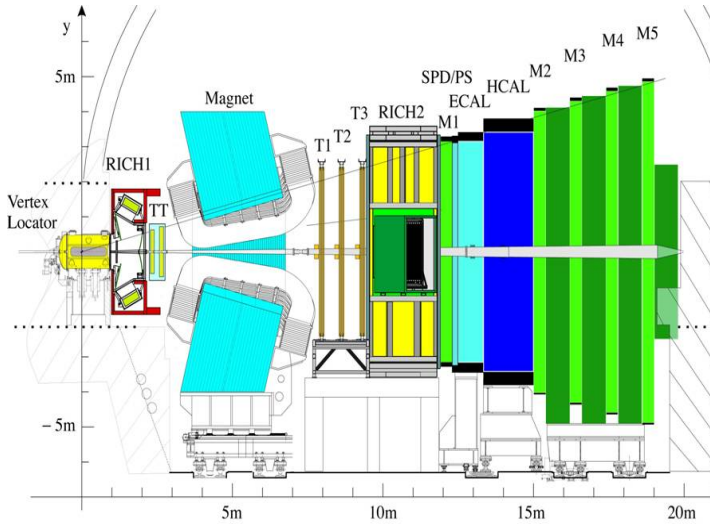

Fig. 1: The LHCb detector

study B hadron oscillations with minimal period of 45 fs. Substantial background suppression is realized due to high invariant mass-resolution (~ 14 MeV/c^2), excellent particle identification and magnetic field flipping up-and-down for artificial asymmetries removal. The scheme of the LHCb detector is shown in Fig. 1.

Tracks and vertices of charged particles are reconstructed by the Vertex Locator (VELO), tracking stations T1–T3 (Silicon Tracker, ST). The VELO uses silicon r/ϕ microstrip detectors with 180k readout channels. With a resolution of 44 µm along the Z-direction and 8 µm perpendicular to Z (beam direction) plane (20 µm precision of the impact parameter determination) it provides time resolution of ~ 45 fs properly suited for the studies of B-meson oscillations. The Turicensis Tracker micro-strip detectors cover 8 m^2 with 144k readout channels. T1–T3 stations have in their Inner Part (IT) silicon micro-strip detectors with 129k readout channels, while for Outer Part (OT) straw tube chambers measure tracks information via 54k readout channels. The tracker has $\sim 0.5\%$ momentum resolution with 96% efficiency for tracks with p higher than 10 GeV/c. The radiation load onto the silicon microstrip sensors is measured by the Radiation

Monitoring System [3] located at the Inner Tracker Station IT-2. Fluences of charged particles measured during years 2011-2012 are in good agreement with Monte-Carlo evaluations and are in the range of $(2\text{–}6)\times10^{12}$ MIP/cm^2 depending upon the sensor location. The Calorimeter (ECAL) measures photons and π^0 mesons, while photon/electron/hadron identification is provided by preshower detector (PS), electromagnetic (ECAL) and hadron (HCAL) calorimeters (invariant mass-resolution $\sim$ 14 MeV/c^2). The K/π separation is provided by Cherenkov detectors (RICH1 and RICH2) exploring $\sim$500 Hybrid Photo Diodes. Muon stations (M1–M5, equipped by 1400 multi-wire proportional chambers) are used for muon identification ($\sim$95% efficiency).

3. Spectroscopy and Lifetime Measurements at LHCb

The high energy of collisions at the LHC raises production rates by many orders of magnitude in comparison with e^+e^- B-factories. All b-hadron species have been identified by LHCb. Fig. 2 illustrates the LHCb spectroscopy performance with invariant mass resolution (10–20) MeV/c^2 (depending upon the particle momentum). Two excited states of Λ_b-baryon (at 5911.95 and 5919.76 MeV/c^2) were observed for the first time in the $\Lambda_b\pi^+\pi^-$ mass-spectrum. Overall errors do not exceed 1 MeV/c^2 while discrepancies with theories reach 20–30 MeV/c^2 [4] indicating room for further studies.

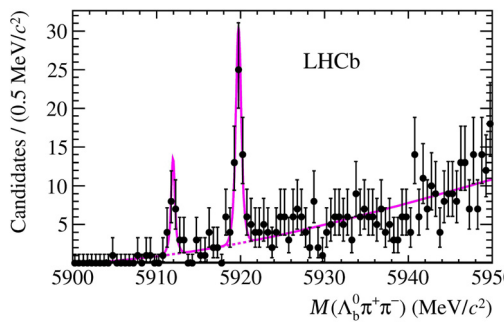

Fig. 2: Excited states of Λ_b-baryon in the $\Lambda_b\pi^+\pi^-$ mass-spectrum

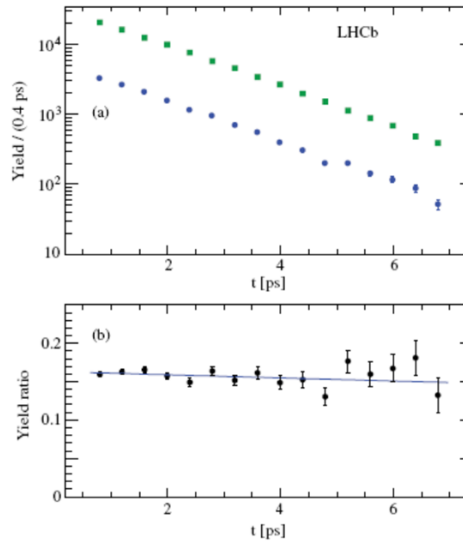

Fig. 3: Top: Evolution of the decay rates for B^0-meson (squares) and Λ_b-baryon (circles). Bottom: Ratio of two rates as a function of time

Lifetime measurements for various b-hadron species have been performed at LHCb. An example of such measurements is shown in Fig. 3 where the lifetime of the B-meson is compared with the lifetime of Λ_b-baryon. These studies have been carried out in view of discrepancies of the Λ_b baryon lifetime values measured in some experiments with theoretical calculation based on the heavy quark expansion. The ratio of the Λ_b baryon lifetime to that of the B^0 meson measured by LHCb using 1.0 fb^{-1} of integrated luminosity in 7 TeV center-of-mass energy pp-collisions is $0.976 \pm 0.012 \pm 0.006$ indicating good agreement with above mentioned theory. Using the known B^0 meson lifetime, the Λ_b lifetime is found to be $1.482 \pm 0.018 \pm 0.012$ ps. In both cases the first uncertainty is statistical and the second systematic [5].

4. B-mesons Oscillations

LHCb measures flavor evolution (mixing or oscillations) with an accuracy of 45 fs due to displaced vertex reconstruction with an accuracy

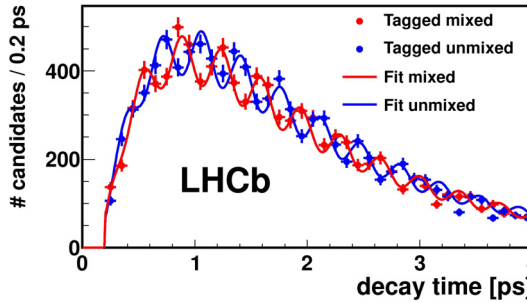

Fig. 4: Time evolution of the mixing asymmetry for B_s^0-$\bar{B}_s^0$ decays

of about 30 µm from the VELO. Such features of mixing as mass difference Δm (related to the frequency of mixing), width difference and the $\Delta\Gamma$ phase between the decay and mixing amplitudes ϕ_s define the observable evolution of the corresponding rates. ϕ_s is sensitive to physics beyond the Standard Model that affects the loops in mixing and/or decay.

A neutral meson mixing with its own antiparticle is well described in the SM which predicts oscillation frequencies for different hadrons ranging over few orders of magnitude. LHCb has performed the world's most precise measurements of the B_d^0 and B_s^0 oscillation frequencies. Fig. 4 shows the measured B_s^0-$\bar{B}_s^0$ oscillations. Clearly seen are contributions of heavy and light B_s^0 and $\bar{B}_s^0$ eigenstates which modulate an exponential decay pattern.

The frequency of oscillations extracted from combined studies of $B_d^0 \to D^-\pi^+$ and $B_d^0 \to J/\psi K^{0*}$) decays is $\Delta m_d = 0.5156 \pm 0.0051_{stat} \pm 0.0033_{syst}$ ps^{-1} [6], while the corresponding value for the B_s decay is $\Delta m_s = 17.768 \pm 0.023_{stat} \pm 0.006_{syst}$ ps^{-1} [7]. The statistical precision of these data (1.0 fb^{-1}) will be improved when the whole set of data (3.0 fb^{-1}) is analyzed.

5. CP Symmetry Violation

5.1. CP violation from time dependent analysis of B-mesons decay

CP symmetry violation in the B^0 decays is treated with the framework of the SM as a result of interference between amplitudes of the

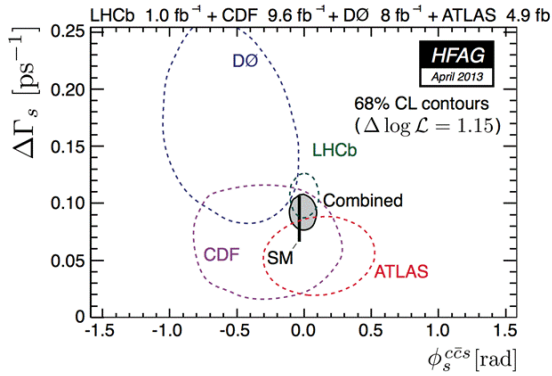

Fig. 5: CP violating phase ϕ_s and differences in decay widths of the B_s^0 mass eigenstates in resonant and non-resonant decays measured by different experiments. The solid line – combination of all measurements. Thick line – SM prediction

neutral meson mixing and direct decay into the final state. The B_s^0 decay is sensitive also to mixing-induced CP violation where the CP-violating phase accordingly to the SM is very small ($\phi_s = -0.0363 \pm 0.0017$ rad). New physics contributing via box diagrams could modify this phase. Time dependent decay studies for measuring CP violating parameters in B_s mixing have been performed for $B_s^0 \to J/\psi K^+K^-$ and $B_s^0 \to J/\psi \pi^+\pi^-$. The combined results are compatible with SM: $\phi_s = 0.01 \pm 0.07_{stat} \pm 0.01_{syst}$ rad [8]. The measurement results of the ϕ_s by LHCb shown in Fig. 5 along with measurements by the CDF and D0 collaborations as well as ATLAS demonstrate agreement with the SM prediction reducing the window for new physics contributions at the current level of the experimental and theoretical precision.

5.2. CP violation and CKM angle γ

The Unitarity Triangle (UT) is one of the powerful tools of the SM treating CP-violation in weak interactions in the framework of the Cabibbo-Kobayashi-Maskawa (CKM) mixing matrix. The angle γ was the least experimentally studied angle of the UT. Here we present some of the results obtained recently for the CKM angle γ in the LHCb experiment. The measurements of γ have been performed

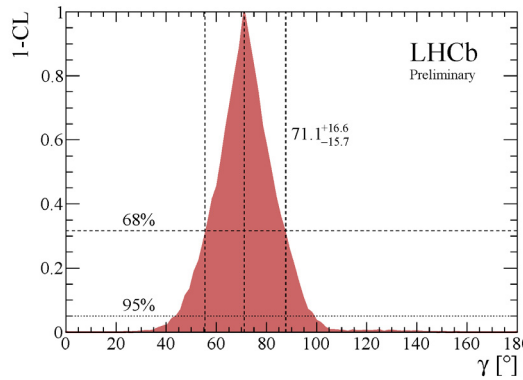

Fig. 6: UT γ angle from the $B^{\pm} \to DK^{\pm}$ decay

exploring 1 fb^{-1} dataset from $B^{\pm} \to Dh^{\pm}$ decays. Fig. 6 shows example [9] of the γ extraction from the tree-level processes $B^{\pm} \to DK^{\pm}$: $\gamma = (71.1^{+16.6}_{-15.7})^{\circ}$ at 68% confidence level (CL). The accuracy of γ determination will be improved when the full available dataset of 3 fb^{-1} is analyzed providing a base for comparison of the results from tree-level and loop-level processes which may result in indication of New Physics contribution.

6. Rare Decays

Experimental studies of rare decays that proceed in the SM by electroweak box or penguin diagrams and are mediated by Flavour Changing Neutral Current (FCNC) are motivated by an expectation that they could reveal physics beyond the Standard Model in modified branching ratios and/or angular distributions of decay products. The SM prediction for branching ratio of $B^0_s \to \mu^+\mu^-$ decay (helicity and FCNC suppressed process with pure leptonic final state) is well defined with very low value of $(3.56 \pm 0.30) \times 10^{-9}$. It is even lower for the $B^0 \to \mu^+\mu^-$ decay: $(1.07 \pm 0.10) \times 10^{-10}$ [10]. The LHCb $B^0_s \to \mu^+\mu^-$ results [11] for the whole data set accumulated in 2011 and 2012 years (3 fb^{-1}) are shown in Fig. 7 together with other experimental results and SM prediction.

The LHCb and CMS combined average results are BR($B^0_s \to \mu^+\mu^-$) $= (2.9 \pm 0.7) \times 10^{-9}$, BR($B^0 \to \mu^+\mu^-$) $= (3.6 \pm 1.6_{stat} \pm$

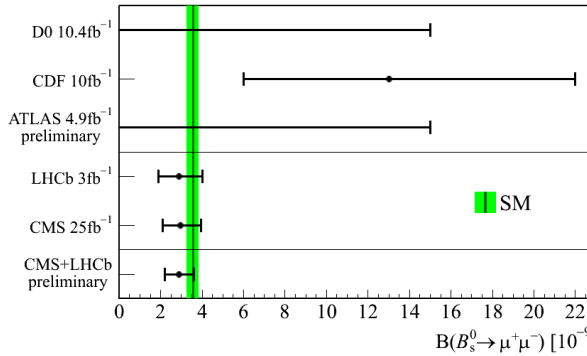

Fig. 7: Branching ratio of $B_s^0 \to \mu^+\mu^-$ decay measured by different experiments. SM prediction is shown by vertical band

$1.4_{syst}) \times 10^{-10}$, which are well consistent with the SM expectations. New Physics might appear in the next digit of the theory and data accuracies.

7. Summary and Outlook

The LHCb experiment has successfully completed the first phase of studies at the LHC in the new energy region of collisions up to 8 TeV having accumulated data with 3 fb^{-1} integrated luminosity. Physics goals aimed at heavy flavor studies (CP violation and rare decays) have been accessed. Most of results obtained so far ($\sim 1/3$ of data analyzed, over 150 publications) are consistent with the Standard Model predictions. Many SM parameters were measured with the highest precision in the sector of CP violation as well as rare decays. Some observations are made for the first time (e.g. $B_s^0 \to \mu^+\mu^-$ decay, CP violation in B_s^0, etc.).

LHCb will continue data taking in 2015–2017 planning the upgrade for running in 2019 at luminosity up to 2×10^{33} cm^{-2}s^{-1}. After the upgrade, LHCb will collect 50 fb^{-1} of integrated luminosity which will allow precision measurements of CP-violating phases, CKM angles, branching ratios of the rare decays as well as other features of physics also beyond the SM.

Acknowledgments

We express our gratitude to our colleagues in the CERN accelerator departments for the excellent performance of the LHC. We thank the technical and administrative staff at the LH Cb institutes. We acknowledge support from CERN and from the national agencies.

1. LHCb Collaboration, R. Aaij *et al.*, Journal of Instrumentation **3**, SO8005 (2008).
2. LHCb Collaboration, R. Aaij *et al.*, Phys. Lett. B **694**, 209 (2010).
3. V. Pugatch *et al.*, Radiation Monitoring System for the LHCb Inner Tracker *LHCb Note* **2002-067**.
4. LHCb Collaboration, R. Aaij *et al.*, Phys. Rev Lett. **109**, 172003 (2012).
5. LHCb Collaboration, R. Aaij *et al.*, Phys. Rev. Lett. **111**, 102003 (2013).
6. LHCb Collaboration, R. Aaij *et al.*, Phys. Lett. B **719**, 318 (2013).
7. LHCb Collaboration, R. Aaij *et al.*, New J. Phys. **15**, 053021 (2013).
8. LHCb Collaboration, R. Aaij *et al.*, Phys. Rev. D **87**, 112010 (2013).
9. LHCb Collaboration, R. Aaij *et al.*, Phys. Lett. B **726**, 151 (2013).
10. A.J. Buras, J. Girrbach, D. Guadagnoli and G. Isidori, Eur. Phys. J. C **72**, 2172 (2012).
11. LHCb Collaboration, R. Aaij *et al.*, Phys. Rev. Lett. **111**, 101805 (2013).

RECENT RESULTS FROM THE PIERRE AUGER OBSERVATORY

J. Ridky[1]
for the Pierre Auger Collaboration[2]

[1] *Institute of Physics, AS CR, Praha, Czech Republic*
[2] *Observatorio Pierre Auger, Malargüe, Argentina*
Full author list:
http://www.auger.org/archive/authors_2013_06.html

Abstract

The Pierre Auger Observatory is about to complete 5 years of operation of its full array. From the very beginning the Observatory was constructed as a dual detector based on fluorescence and surface detectors. All measurements are supplemented by an extensive system of atmospheric monitoring and detector calibration. As a result the Observatory provides a wealth of high quality data which bring interesting information on hadron collisions at energies beyond the reach of terrestrial accelerators.

1. Introduction

The idea of the Pierre Auger ultra high energy cosmic ray (UHECR) observatory, based on dual detection technique, was elaborated in the '90s [1]. The surface detector (SD) [2] is based on Cherenkov tanks with water level 1.2 m high which provides a uniform exposure even for large zenith angles. Each station works autonomously. The fluorescence detector (FD) [3] is segmented into 24 telescopes – Schmidt cameras, overlooking the whole SD area of 3,000 km^2. The prototypes of both SD and FD were successfully tested in 2001–2002 and since 2004 the detector has been in standard operation though the

full detection area and all fluorescence detectors were completed in 2008. Since then the basic design has been supplemented by equipping an area of 25 km^2 with stations spaced at 750 m [4], half the spacing in the main array, overlooked by three additional fluorescence detectors with total field of view 180° in azimuth and 30°–60° in the elevation angle [5]. This area is also being enhanced with muon detectors [6]. This allows a smooth overlap with data of the experiments sensitive to lower energy CR. The stable and reliable operation of the Pierre Auger Observatory (Auger) allows to test other detection techniques and concepts like radio and microwave detection of UHECR showers [7]. The Observatory provides also a facility for specific atmospheric phenomena studies, environmental studies etc. [8].

2. Calibration and Monitoring

The concept of dual detection connects the almost permanent uptime and well defined detection area of the surface detector with the calorimetric measurements of the shower energy provided by the fluorescence detector. To maximize the synergy of the two detectors a thorough calibration is indispensable. The surface detector is calibrated on-line by the flux of atmospheric muons and the whole system is monitored to ensure maximum properly working stations [9].

The FD measurements entail both detector calibration and atmosphere monitoring. Auger uses several schemes to calibrate parts of the detectors each measured night and in longer periods end-to-end calibrations of the whole optical system [10]. The state of the atmosphere is monitored by active means (lidars and laser shots [11]) and by passive ones (cloud monitoring [12], star monitoring [13] and satellite pictures [14]). Auger has also built a local atmosphere model based on several years of atmospheric sounding. The system works regularly each measured night and it is designed to record the state of the atmosphere after each UHECR shower in the respective direction [15].

3. Selected Results

The above described system gives the unique opportunity to obtain currently the most detailed information on the hadron interactions

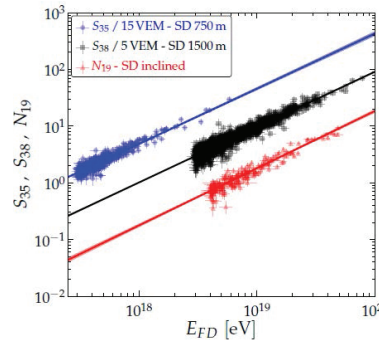

Fig. 1: SD signals versus FD measured energy

at highest possible energies. The calorimetric FD measurements are the key to set the energy scale to all SD measurements, thus almost eliminating any significant role of Monte Carlo (MC) simulations as the light profile of the shower is a robust quantity [16]. Only the missing energy is currently estimated by MC. However, the recent studies show that even this can be estimated from the muon content of the shower [17].

The exposure of Auger is increasing by 5,000 km^2 sr every year and the integrated exposure is currently 32,000 km^2 sr yr. There are 81,568 events with zenith below 60° registered with full exposure ($E > 3$ EeV) by the 1.5 km spaced SD, 11,940 inclined showers (zenith $> 60°$), 25,676 events detected above 0.3 EeV by the 0.75 km spaced SD, and 11,172 hybrid showers measured both by SD and FD above 1 EeV. The energy calibration of the SD signal of the three above mentioned event classes by the FD energy measurement is shown in Fig. 1 [18]. The reliable knowledge of energy allows more detailed studies of hadronic interactions. Auger measured $\sigma_{\rm inel}(pp) = 92 \pm 7({\rm stat})^{+9}_{-11}({\rm syst}) \pm 7({\rm Glauber})$ mb at cms energy equivalent to $57 \pm 0.3({\rm stat}) \pm 6({\rm syst})$ TeV [19]. The result is derived from a measurement of the tail in the distribution of maxima of shower depth, $X_{\rm max}$. At higher energies the uncertainties due to a possibly mixed mass composition become larger. Chemical composition is determined from the measurement of the average of maximum shower depth, ($\langle X_{\rm max} \rangle$) and the dispersion of this quantity ($\sigma(X_{\rm max})$) [20,21] (Fig. 2 left and right respectively [22]).

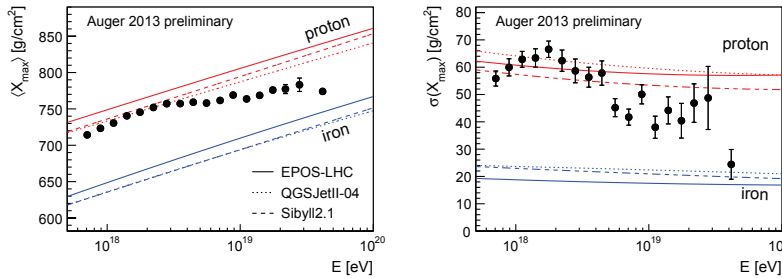

Fig. 2: Mean values of shower maxima (left) and dispersion of the shower maxima (right)

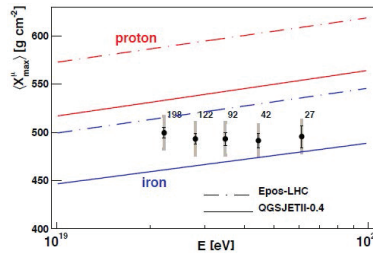

Fig. 3: Mean values of muon production maxima

An important feature of the cosmic ray showers is their muon content [23–25]. It also characterises the type of the primary. A dedicated analysis allows to reconstruct the production depth of the muons in the UHECR showers [26]. The average maxima of the distributions are shown in Fig. 3. These measurements, along with those in Fig. 2, may be used to assess the validity of hadronic interaction models at ultra-high energies. This is important as the magnitude of the cross section depends both on the energy and the type of the primary and the models are indispensable for the chemical composition analysis.

4. Conclusions

The high quality data provided by Auger shed new light on hadronic interactions at highest possible energies. So far we are not able to

distinguish individual types of primary particles but even so the measurements provide important information on hadronic interactions.

The author is grateful to all his collaborators who contributed to this talk. This contribution was supported by MSMT CR, project LG13007.

1. J. Abraham *et al.* (The Pierre Auger Collaboration), Nucl. Inst. Meth. A **523**, 50 (2004).
2. J. Abraham *et al.* (The Pierre Auger Collaboration), Nucl. Inst. Meth. A **613**, 29-39 (2010).
3. J. Abraham *et al.* (The Pierre Auger Collaboration), Nucl. Inst. Meth. A **620**, 227-251 (2010).
4. F. Sanchez for the Pierre Auger Collaboration, 32nd ICRC proceedings, arXiv:1107.480.
5. T. H.-J. Mathes for the Pierre Auger Collaboration, 32nd ICRC proceedings, arXiv:1107.480.
6. F. Suarez for the Pierre Auger Collaboration, 33rd International Cosmic Ray Conference (ICRC 2013), arXiv:1307.5059 [astro-ph.HE], page 80.
7. P. Abreu *et al.* (The Pierre Auger Collaboration), JINST, **7**, P11023 (2012).
8. L. Wiencke for the Pierre Auger Collaboration, Eur. Phys. J. Plus, **127**, 98 (2012).
9. X. Bertou for the Pierre Auger Collaboration, Proceedings of the 28th ICRC, p. 813.
10. M. D. Roberts for the Pierre Auger Collaboration, Proceedings of the 28th ICRC, p. 453.
11. L. Valore for the Pierre Auger Collaboration, 33rd International Cosmic Ray Conference (ICRC 2013), arXiv:1307.5059 [astro-ph.HE], page 100.
12. J. Chirinos for the Pierre Auger Collaboration, 33rd International Cosmic Ray Conference (ICRC 2013), arXiv:1307.5059 [astro-ph.HE], page 108.
13. P. Travnicek el al. for the Pierre Auger Collaboration, Proceedings of the 30th ICRC, pp. 347-350.
14. P. Abreu *et al.* (The Pierre Auger Collaboration), Astroparticle Physics, in press 2013.
15. P. Abreu *et al.* (The Pierre Auger Collaboration), JINST **7**, P09001 (2012).
16. J. Abraham *et al.* (The Pierre Auger Collaboration), Phys. Rev. Lett. **101**, 061101 (2008).
17. M. J. Tueros for the Pierre Auger Collaboration, 33rd International Cosmic Ray Conference (ICRC 2013), arXiv:1307.5059 [astro-ph.HE], page 11.
18. A. Schulz for the Pierre Auger Collaboration, 33rd International Cosmic Ray Conference (ICRC 2013), arXiv:1307.5059 [astro-ph.HE], page 27.

19. P. Abreu *et al.* (The Pierre Auger Collaboration), Phys. Rev. Lett. **109**, 062002 (2012).

20. P. Abreu *et al.* (The Pierre Auger Collaboration), Phys. Rev. Lett. **104**, 091101 (2010).

21. V. de Souza for the Pierre Auger Collaboration, 33rd International Cosmic Ray Conference (ICRC 2013), arXiv:1307.5059 [astro-ph.HE], page 35.

22. A. Letessier-Selvon for the Pierre Auger Collaboration, 33rd International Cosmic Ray Conference (ICRC 2013), arXiv:1310.4620 [astro-ph.HE].

23. I. Valiño for the Pierre Auger Collaboration, 33rd International Cosmic Ray Conference (ICRC 2013), arXiv:1307.5059 [astro-ph.HE], page 44.

24. B. Kegl for the Pierre Auger Collaboration, 33rd International Cosmic Ray Conference (ICRC 2013), arXiv:1307.5059 [astro-ph.HE], page 48.

25. G.R. Farrar for the Pierre Auger Collaboration, 33rd International Cosmic Ray Conference (ICRC 2013), arXiv:1307.5059 [astro-ph.HE], page 52.

26. D. Garcia-Gamez for the Pierre Auger Collaboration, 33rd International Cosmic Ray Conference (ICRC 2013), arXiv:1307.5059 [astro-ph.HE], page 40.

DIFFRACTIVE AND PHOTON EXCHANGE PROCESSES WITH TAGGED PROTONS AT THE LHC

Christophe Royon

IRFU-SPP, CEA Saclay,
F91 191 Gif-sur-Yvette cedex, France

Abstract

We describe different diffractive and photon induced processes which can be studied at the LHC using tagged intact protons, leading to a better understanding of the Pomeron structure in terms of quarks and gluons, and better sensitivity to quartic anomalous couplings between photons and W, Z bosons and photons.

1. Inclusive Diffraction Measurement at the LHC

In this section, we discuss potential measurements at the LHC that can constrain the Pomeron structure in terms of quarks and gluons that has been derived from QCD fits at HERA and at the Tevatron. It is possible to probe this structure and the QCD evolution at the LHC in a completely new kinematical domain.

1.1. Dijet production in double Pomeron exchanges processes

One can first probe if the Pomeron is universal between ep and pp colliders using LHC data, or in other words, if we are sensitive to the same object at HERA and the LHC. The different diagrams of the processes that can be studied at the LHC are namely double pomeron exchange (DPE) production of dijets, of γ+jet, sensitive respectively

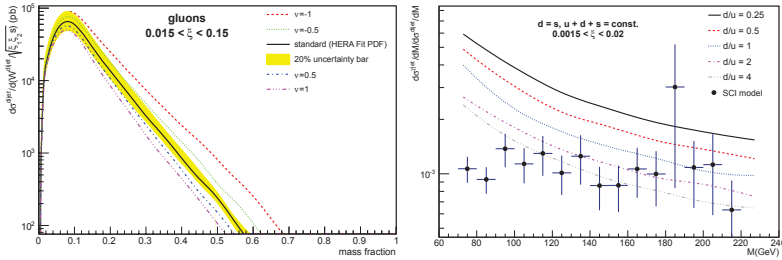

Fig. 1: Left: DPE di-jet mass fraction distribution. The different curves correspond to different modifications of the Pomeron gluon density extracted from HERA data (see text). Right: DPE $\gamma+$ jet to di-jet differential cross section ratio, for the acceptance of the 210m proton detectors as a function of the diffractive mass

to the gluon and quark contents of the Pomeron, and the jet gap jet events ssnsitive to BFKL [1] resummation effects. All diagrams were included in the FPMC [2] generator that was used for this analysis.

The dijet production in DPE events at the LHC is sensitive to the gluon density in the Pomeron. In order to quantify the sensitivity to the Pomeron structure in terms of gluon density at the LHC, we display in Fig. 1, left, the dijet cross section as a function of the dijet mass fraction [3], assuming the protons to be tagged in the AFP [4] proton detectors at 210 m. The central black line displays the cross section value for the gluon density in the Pomeron measured at HERA including an additional survival probability of 0.03. The yellow band shows the effect of the 20% uncertainty on the gluon density taking into account the normalisation uncertainties. The dashed curves display the sensitivity to the gluon density distribution at high β by multiplying the gluon density in the Pomeron from HERA by $(1-\beta)^{\nu}$ where ν varies between –1 and 1. When ν is equal to –1 (resp. 1), the gluon density is enhanced (resp, decreased) at high β. From Fig. 1, we notice that the dijet mass cross section is indeed sensitive to the gluon density in the Pomeron ans its shape, and we can definitely check if the Pomeron model from HERA and its structure in terms of gluons is compatible between HERA and the LHC. This will be an important test of the Pomeron universality. This measurement can be performed for a luminosity as low as 10 pb^{-1} since the cross section is very large (typically, one day at low luminosity without pile up at the LHC).

1.2. Sensitivity to the Pomeron structure in quarks using γ + jet events

Fig. 1, right, displays a possible observable at the LHC that can probe the quark content in the Pomeron, namely the γ+jet to the dijet cross section ratio [3] as a function of diffractive mass ($\sqrt{\xi_1 \xi 2S}$) for different assumptions on the quark content of the Pomeron, d/u varying between 0.25 and 4 in steps of 0.25. We notice that the cross section ratio varies by a factor 2.5 for different values of u/d. The QCD diffractive fits at HERA assumed that $u = d = s = \bar{u} = \bar{d} = \bar{s}$, since data were not sensitive to the difference between the different quark component in the Pomeron. The LHC data will allow us to determine for instance which value of d/u is favoured by data. Let us assume that $d/u = 0.25$ is favoured. If this is the case, it will be needed to go back to the HERA QCD diffractive fits and check if the fit results at HERA can be modified to take into account this assumption. If the fits to HERA data lead to a large χ^2, it would indicate that the Pomeron is not the same object at HERA and the LHC. On the other hand, if the HERA fits work under this new assumption, the quark content in the Pomeron will be further constrained. The advantage of measuring the cross section ratio as a function of diffractive mass is that most of the systematic uncertainties will cancel.

Soft color interaction models (SCI) are alternative models to explain diffraction at hadronic colliders [5]. In Fig. 1, right, we notice that the distribution of the γ+jet to dijet ratio as a function of the total diffractive mass distributions may allow to distinguish between the Herwig/DPE and Pythia/SCI models because the latter leads to a flatter dependence on the total diffractive mass, giving further insight into soft QCD.

1.3. Jet gap jet production in double Pomeron exchanges processes

In this process, both protons are intact after the interaction and detected in AFP at 210 m, two jets are measured in the ATLAS/CMS central detector and a gap devoid of any energy is present between the two jets [6]. This kind of event is important since it is sensitive to QCD resummation dynamics given by the BFKL [1, 7] evolution

equation. This process has never been measured to date and will be one of the best methods to probe these resummation effects, benefitting from the fact that one can perform the measurement for jets separated by a large angle (there is no remnants which 'pollute' the event). As an example, the cross section ratio for events with gaps to events with or without gaps as a function of the leading jet p_T is of the order of 20% which is much higher than the expectations for non-diffractive events. This is due to the fact that the survival probability of 0.03 at the LHC does not need to be applied for diffractive events. The inconvenient aspect of this measurement is obviously that it depends on the weak unknown dependency of the survival probability on the diffrative processes (DPE jets and jet gap jet events for instance).

2. Exclusive WW and ZZ Production

In the Standard Model (SM) of particle physics, the couplings of fermions and gauge bosons are constrained by the gauge symmetries of the Lagrangian. The measurement of W and Z boson pair productions via the exchange of two photons allows to provide directly stringent tests of one of the most important and least understood mechanism in particle physics, namely the electroweak symmetry breaking [8].

We use the parameterization of the quartic couplings defined in [9]. The cuts to select quartic anomalous gauge coupling WW events are the following, namely $0.0015 < \xi < 0.15$ for the tagged protons corresponding to the AFP forward proton detectors at 210 and 420 m, $\not{E}_T > 20$ GeV, $\Delta\phi < 3.13$ between the two leptons. In addition, a cut on the p_T of the leading lepton $p_T > 160$ GeV and on the diffractive mass $W > 800$ GeV are requested since anomalous coupling events appear at high mass. After these requirements, we expect about 0.7 background events for an expected signal of 17 events if the anomalous coupling is about four orders of magnitude lower than the present LEP limit [10] ($|a_0^W/\Lambda^2| = 5.4\ 10^{-6}$) for a luminosity of 30 fb^{-1}, and about two orders of magnitude better than the present CMS limits [11].

The search for quartic anomalous couplings between γ and W bosons was performed again after a full simulation of the ATLAS

detector including pile up [4] assuming the protons to be tagged in AFP at 210 m only. Integrated luminosities of 40 and 300 fb^{-1} with, respectively, 23 or 46 average pile-up events per beam crossing have been considered. In order to reduce the background, each W is assumed to decay leptonically (note that the semi-leptonic case in under study). The full list of background processes used for the ATLAS measurement of Standard Model WW cross-section was simulated, namely $t\bar{t}$, WW, WZ, ZZ, W+jets, Drell-Yan and single top events. In addition, the additional diffractive backgrounds were also simulated, Since only leptonic decays of the W bosons are considered, we require in addition less than 3 tracks associated to the primary vertex, which allows us to reject a large fraction of the non-diffractive backgrounds (e.g. $t\bar{t}$, diboson productions, W+jet, etc.) since they show much higher track multiplicities. Remaining Drell-Yan and QED backgrounds are suppressed by requiring the difference in azimuthal angle between the two leptons $\Delta\phi < 3.1$. After these requirements, a similar sensitivity with respect to fast simulation without pile up was obtained.

Of special interest will be also the search for anomalous quartic $\gamma\gamma\gamma\gamma$ anomalous couplings which is now being implemented in the FPMC generator [12]. Let us notice that there is no present existing limit on such coupling and the sensitivity using the forward proton detectors is expected to be similar as the one for $\gamma\gamma WW$ or $\gamma\gamma ZZ$

T a b l e 1: Reach on anomalous couplings obtained in γ induced processes after tagging the protons in AFP compared to the present OPAL limits. The 5σ discovery and 95% C.L. limits are given for a luminosity of 30 and 200 fb^{-1}

Couplings	OPAL limits [GeV^{-2}]	Sensitivity @ $\mathcal{L} = 30$ (200) fb^{-1}	
		5σ	95% CL
a_0^W/Λ^2	[–0.020, 0.020]	5.4 10^{-6} (2.7 10^{-6})	2.6 10^{-6} (1.4 10^{-6})
a_C^W/Λ^2	[–0.052, 0.037]	2.0 10^{-5} (9.6 10^{-6})	9.4 10^{-6} (5.2 10^{-6})
a_0^Z/Λ^2	[–0.007, 0.023]	1.4 10^{-5} (5.5 10^{-6})	6.4 10^{-6} (2.5 10^{-6})
a_C^Z/Λ^2	[–0.029, 0.029]	5.2 10^{-5} (2.0 10^{-5})	2.4 10^{-5} (9.2 10^{-6})

anomalous couplings. If discovered at the LHC, $\gamma\gamma\gamma\gamma$ quartic anomalous couplings might be related to the existence of extra-dimensions in the universe, which might lead to a reinterpretation of some experiments in atomic physics. As an example, the Aspect photon correlation experiments [13] might be interpreted via the existence of extra-dimensions. Photons could communicate through extra-dimensions and the deterministic interpretation of Einstein for these experiments might be true if such anomalous couplings exist. From the point of view of atomic physics, the results of the Aspect experiments would depend on the distance of the two photon sources.

1. V.S. Fadin, E.A. Kuraev, L.N. Lipatov, Phys. Lett. B **60**, 50 (1975); I.I. Balitsky, L.N. Lipatov, Sov. J. Nucl. Phys. **28**, 822 (1978).
2. M. Boonekamp, A. Dechambre, V. Juranek, O. Kepka, M. Rangel, C. Royon, R. Staszewski, e-Print: arXiv:1102.2531; M. Boonekamp, V. Juranek, O. Kepka, C. Royon, *Forward Physics Monte Carlo*, Proceedings of the workshop: HERA and the LHC workshop series on the implications of HERA for LHC physics, arXiv:0903.3861 [hep-ph].
3. C, Marquet, C. Royon, M. Saimpert, D. Werder, arXiv:1306.4901.
4. ATLAS Coll., CERN-LHCC-2011-012.
5. A. Edin, G. Ingelman and J. Rathsman, Phys. Lett. B **366**, 371 (1996); Z. Phys. C **75**, 57 (1997); J. Rathsman, Phys. Lett. B **452**, 364 (1999).
6. C. Marquet, C. Royon, M. Trzebinski, R. Zlebcik, Phys. Rev. D **87**, 3, 034010 (2013); O. Kepka, C. Marquet, C. Royon, Phys. Rev. D **83**, 034036 (2011).
7. C. Marquet, C. Royon, Phys. Rev. D **79**, 034028 (2009); O. Kepka, C. Royon, C. Marquet, R. Peschanski, Eur. Phys. J. C **55**, 259-272 (2008); Phys. Lett. B **655**, 236-240 (2007); H. Navelet, R. Peschanski, C. Royon, S. Wallon, Phys. Lett. B **385**, 357 (1996); H. Navelet, R. Peschanski, C. Royon, Phys. Lett. B **366**, 329 (1996).
8. E. Chapon, O. Kepka, C. Royon, Phys. Rev. D **81**, 074003 (2010); O. Kepka and C. Royon, Phys. Rev. D **78**, 073005 (2008); J. de. Favereau *et al.*, preprint arXiv:0908.2020.
9. G. Belanger and F. Boudjema, Phys. Lett. B **288**, 201 (1992).
10. G. Abbiendi *et al.* [OPAL Collaboration], Phys. Rev. D **70**, 032005 (2004) [arXiv:hep-ex/0402021].
11. CMS Coll., JHEP **07**, 116 (2013).
12. O. Kepka, B. Lenzi, C. Royon, M. Saimpert, in preparation.
13. A. Aspect, P. Grangier, G. Roger, Phys. Rev. Lett. **49**, no. 2, 91-94 (1982); A. Aspect, J. Dalibard, G. Roger, Phys. Rev. Lett. **49**, Iss. 25, 1804 (1982).

SEARCHES FOR PHYSICS BEYOND THE STANDARD MODEL WITH THE ATLAS DETECTOR

V. Solovyev
On behalf of the ATLAS Collaboration

Petersburg Nuclear Physics Institute,
Gatchina, 188300, Russia

Abstract

Searches for physics beyond the Standard Model with the ATLAS detector at the LHC are presented. The focus is on the most recent results obtained with the data collected during 2012 data taking at $\sqrt{s} = 8$ TeV center-of-mass energy. No evidence for physics beyond the Standard Model is found.

1. Introduction

The Standard Model (SM) provides an extremely good description of experimental data. However, there are still several unanswered questions, e.g. the hierarchy problem, the dark matter description etc. Therefore searches for physics beyond the SM (BSM) need to be performed.

Excellent performance of the LHC (Large Hardon Collider) and the ATLAS detector [1] in 2012 provides great opportunity for BSM searches. More than 20 fb^{-1} of data were delivered to ATLAS during proton-proton collisions at $\sqrt{s} = 8$ TeV center-of-mass energy.

BSM analyses in ATLAS are divided into searches for Supersymmetry and Exotic searches. These proceedings describe only the selected and the most recent results from Exotics analyses.

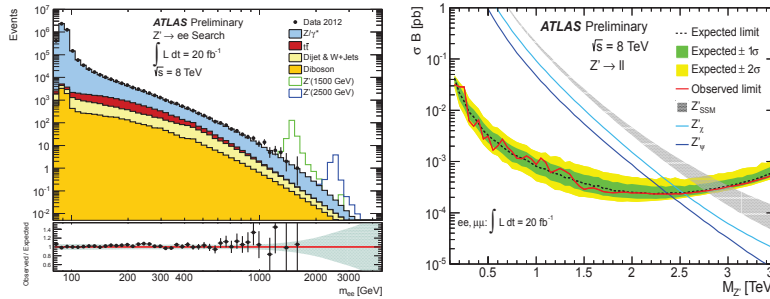

Fig. 1: Left: Dielectron invariant mass spectrum, compared to the stacked sum of all expected backgrounds, with two selected Z' signals overlaid. The ratio of observed to expected events with statistical uncertainty is shown below, the shaded band indicates the mass-dependent systematic uncertainty. Right: Median expected (dashed line) and observed (solid red line) 95% C.L. limits on σB and expected σB for Z' production and the two E6-motivated Z' models for the combination of the dielectron and dimuon channels. The thickness of the Z' SSM theory curve represents all theoretical uncertainties

2. Selected Exotics Results

2.1. Searches for heavy resonances

Heavy resonances are predicted in many models beyond the SM, e.g. Grand Unified Theories, extra dimensions, Technicolor etc.

One of the important results is the search for dilepton resonances. Results for the dielectron and dimuon channels are based on 20 fb^{-1} of data [2]. As a benchmark model the Sequential Standard model (SSM) Z' is used. Additionally E6-motivated models and Randall-Sundrum gravitons (G^*) are considered. Selected events should have at least two high-p_{T} electron (or muon) candidates. Leading (subleading) electron must have $p_{\mathrm{T}} > 40$ GeV ($p_{\mathrm{T}} > 30$ GeV), while both muons are required to have $p_{\mathrm{T}} > 25$ GeV. The observable is the invariant mass of dilepton pair, which is shown for the dielectron channel on the left of Fig. 1. Dominated background is Z/γ^* decaying to two leptons.

No significant excess is found and 95% C.L. limits on cross-section times branching ratio ($\sigma \times B$) are set. The plot on the right of Fig. 1 shows the expected and observed limits for SSM Z' for the combination of the electron and muon channels. Masses below 2.86 (2.47) TeV are excluded for SSM Z' (G^*) models.

The ditau channel is covered in a separate analysis [3]. It is less sensitive than the dielectron and dimuon channels but important since the new physics may couple preferentially to third generation. In this search fully hadronic decays of tau leptons are considered. The SSM Z' is used as a benchmark. No significant excess above SM predictions is found and masses of SSM Z' below 1.9 TeV are excluded using 19.5 fb^{-1} of data.

Searches for photon-jet resonances [4] and dijet resonances produced in association with a leptonically decaying W or Z bosons [5] also show no deviations from SM predictions using 20.3 fb^{-1} of data.

2.2. Searches for vector-like quarks

Vector-like quarks (VLQ) appear in many extensions of the SM. They are defined as quarks for which both chiralities have the same transformation properties under the electroweak gauge group. VLQs are assumed to couple preferentially to third generation quarks. The GIM mechanism does not apply to VLQs and hence tree-level neutral-current decays are possible. Weak-isospin singlet and doublet hypothesis are considered in the searches described below.

The search for neutral-current decaying VLQs ($T \to Zt$ and $B \to Zb$) using 14.3 fb^{-1} of data is described in Ref. [6]. Selected events should contain high transverse momentum ($p_{\mathrm{T}} > 150$ GeV) Z boson candidate reconstructed with oppositely charged same flavor leptons, at least 2 b-tagged jets with total transverse momentum $H_{\mathrm{T}} > 600$ GeV. The observable is the invariant mass of the Z boson candidate and highest-p_{T} b-tagged jet, $m(Zb)$, which is shown on the left of Fig. 2. Dominant background is $Z + jets$ production.

No significant excess above SM predictions is found and 95% C.L. limits are set on VLQ pair production cross-section. The plot on the right of Fig. 2 shows the expected and observed limits for the singlet hypothesis of vector-like T quark. Masses of vector-like T (B) quarks below 585 (645) GeV and 680 (725) GeV are excluded for the singlet and doublet hypothesis respectively.

The search for charged-current decaying vector-like T quarks ($T \to Wb$) described in Ref. [7] also does not show any excess above SM predictions. Masses of T quarks below 505 GeV are excluded for the singlet hypothesis using 14.3 fb^{-1} of data.

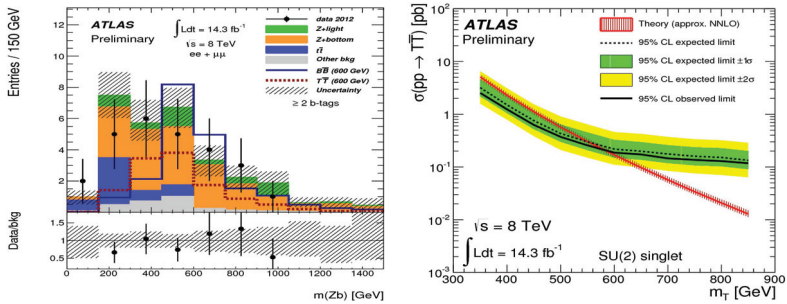

Fig. 2: Left: The $m(Zb)$ distribution after the $p_{\mathrm{T}}(Z)$ and H_{T}(jets) requirements, in Z candidate events containing at least two b-tagged jets. The hatched bands in the upper and lower panels represent the total background uncertainty. Right: Pair production cross section limit (95% C.L.) versus mass for a SU(2) singlet vector-like T quark

2.3. Search for Dark Matter Pair Production

Searches are also performed for pair production of weakly interacting massive particles ($pp \to \chi\bar{\chi}$) via some unknown intermediate state. The final state is invisible to the detector but the events can be detected if there is associated initial-state radiation of SM particle. The strongest limits come from mono-jet analyses, due to the large rate of quark or gluon radiation. However, theories predict that due to constructive interference mono-W production can be the dominant process.

The search for dark matter pair production in association with a W or Z boson using 20.3 fb^{-1} of data is described in Ref. [8]. In this analysis hadronically decaying W or Z bosons, reconstructed as a single massive jet, are considered. Events must have at least one such jet with $p_{\mathrm{T}} > 250$ GeV, pseudorapidity $|\eta| < 1.2$ and mass between 50-120 GeV. Selected events are expected to have large missing transverse energy ($E_{\mathrm{T}}^{\mathrm{miss}}$) from the undetected $\chi\bar{\chi}$ particles. The observable in this analysis is the mass of the large-radius jet which is shown on the left of Fig. 3.

In the absence of signal-like excess above SM background predictions 90% C.L. limits are set on the effective field mass scale, M_*, for different dark matter operators. Limits are shown on the right of Fig. 3.

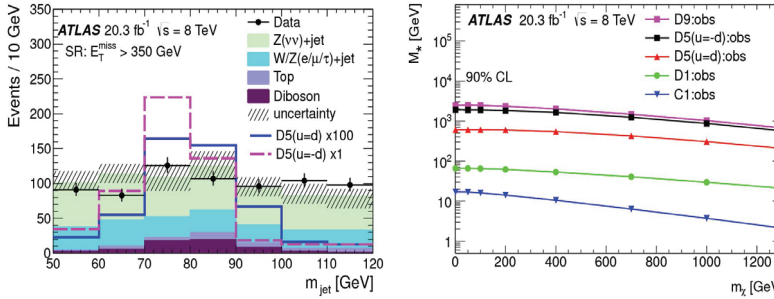

Fig. 3: Left: Data and predicted background in the signal region $E_{\mathrm{T}}^{\mathrm{miss}} > 350$ GeV. Combined single W/Z boson signal distributions of the D5 operator in the destructive and constructive cases with dark matter mass of 1 GeVand $M_* = 1$ TeV are drawn as well. Uncertainties include statistical and systematic contributions. Right: Summary of observed limits on the effective theory mass scale M_* at 90% C.L. for various operators from combined single W/Z boson signals. M_* values below these lines are excluded

3. Conclusions

There is a wide variety of searches beyond the SM in ATLAS. Despite the lack of evidence for new physics, BSM results with 2012 data are impressive since they cover the TeV mass scale. ATLAS is well prepared for the next run of the LHC with increased beam energy and intensity, when the great opportunity to discover new physics will be offered.

1. ATLAS Collaboration, JINST **3**, S08003 (2008).
2. ATLAS Collaboration, ATLAS-CONF-2013-017 https://cds.cern.ch/record/1525524.
3. ATLAS Collaboration, ATLAS-CONF-2013-066 https://cds.cern.ch/record/1562841.
4. ATLAS Collaboration, arXiv:1309.3230, submitted to Phys. Lett. B.
5. ATLAS Collaboration, ATLAS-CONF-2013-074 https://cds.cern.ch/record/1562930.
6. ATLAS Collaboration, ATLAS-CONF-2013-056 https://cds.cern.ch/record/1557773.
7. ATLAS Collaboration, ATLAS-CONF-2013-060 https://cds.cern.ch/record/1557777.
8. ATLAS Collaboration, arXiv:1309.4017, submitted to Phys. Rev. Lett.

RECENT RESULTS OF SEARCH FOR $2K$ CAPTURE IN Kr-78

M.V. Stepaniuk[1], Yu.M. Gavrilyuk[2], A.M. Gangapshev[2], V.V. Kazalov[2], V.V. Kuzminov[2], S.I. Panasenko[1], S.S. Ratkevich[1]

[1] *V.N. Karazin Kharkiv National University, Ukraine,*
[2] *Baksan Neutrino Observatory INR RAS, Russia*

Abstract

Recent results of search for $2K$ capture in ^{78}Kr at the Baksan Neutrino Observatory INR RAS are presented. Experimental technique was based on detecting the characteristic radiation of the daughter nucleus ^{78}Se by large low-background copper proportional counter. Total exposure of the experiment was 0.343 kg×y. Counting rate of $2\nu 2K$ capture events in ^{78}Kr was $12.8^{+5.2}_{-4.8}$ y^{-1} and background was $13.2^{+3.6}_{-3.2}$ y^{-1}. It gave the half-life estimation of $T_{1/2} = [9.2^{+5.5}_{-2.6}(stat) \pm 1.3(syst)] \times 10^{21}$ y. The value was in agreement with theoretical models. Because of small significance level (2.5σ) evidence could not be claimed, but it was a good indication of $2\nu 2K$ capture in ^{78}Kr.

1. Introduction

Double beta decay investigation is a straight way to determine neutrino nature (whether it is a Majorana or Dirac particle) and to get absolute neutrino mass scale and hierarchy. Besides that it helps to improve nuclear matrix elements. The data obtained for 2ν mode offer a chance to directly compare different models of the nuclear structure, which form the basis for calculations of nuclear matrix elements $|M^{2\nu}|$, and to select the optimal one. Though direct correlation between the values of nuclear matrix elements for the two-neutrino and neutrinoless modes of double β decay is absent, the methods for calculating $|M^{2\nu}|$ and $|M^{0\nu}|$ are very similar.

Positive results on 2β decay are detected up to now for 12 isotopes. Among them only ^{130}Ba decays through double electron capture, but this result is obtained in geochemical experiment. Double beta plus decay haven't been detected in direct experiment yet. $2\nu\beta^+\beta^+$ and $2\nu\beta^+$EC types are much suppressed with respect to 2νECEC because of lower Q value. For instance the ratio of probabilities for different types of ^{78}Kr decay is W(2νECEC) : W($2\nu\beta^+$EC) : W($2\nu\beta^+\beta^+$) = 1900 : 580 : 1. Hence it is likely to detect 2νECEC process firstly. Theoretical predictions for its half-life are of the order of 10^{21} years [1].

2. Experimental Technique

The experimental search for $2K$ capture in ^{78}Kr has been carried out at the Baksan Neutrino Observatory INR RAS (Russia) in one of the chambers of the underground laboratory of the Gallium Germanium Neutrino Telescope experiment during 2005 – 2012 [2]. It is located at the depth of 4700 m.w.e., where cosmic ray flux is lowered by $\sim 10^7$ times down to the level of $(3.03\pm0.10)\times10^{-9}$ cm^{-2}s^{-1} [3].

2νECEC decay is hard to study as there are no charged particles emitted. It can be detected only through characteristic radiation. When two K-electrons are captured by ^{78}Kr nucleus, two neutrinos are carrying away the Q value. As a result an excited atomic shell of ^{78}Se is generated, which deenergizes by emitting X-rays and Auger electrons. There is theoretical uncertainty in energies of characteristic photons and probability of their emission when a double vacancy in ^{78}Se is filled. The fraction of $2\nu2K$ capture events in ^{78}Kr with respect to the total number of 2νECEC events is 78.6% [4].

Large low-background copper proportional counter filled with two samples of krypton (enriched or depleted) was used in the experiment. Detector was placed inside the shielding of 18-cm-thick copper, 15-cm-thick lead, and 8-cm-thick borated polyethylene layers. The krypton served both as radiation source and working gas. Isotopic composition of two experimental samples and natural krypton (for comparison) is listed in Table 1. Krypton had no quenching or accelerating gaseous additions and was purified through a Ni/SiO_2 absorber from electronegative admixtures every $\sim$ 2000 h. Both sam-

T a b l e 1: Isotopic compositions of the krypton samples

Samples \ Isotopes	78	80	82	83	84	86
Enriched Kr	99.81	0.17	0.005	0.005	0.005	0.005
Depleted Kr	0.002	0.41	41.36	58.23	0.003	–
Natural Kr	0.354	2.27	11.56	11.55	56.9	17.37

ples have been specially cleared from radioactive isotope ^{85}Kr present in atmosphere. Every ~ 2 weeks detector was calibrated with an isotope gamma source of ^{109}Cd ($E_\gamma = 88$ keV). Main background sources were uranium and thorium radioactive chains (from surrounding material), ^{14}C (probably from cleaning inner surface with an ethanol) and cosmogenic radioactive krypton present in the samples [5].

The casing of the counter represented a radiopure copper cylinder with inner and outer diameters of 140 and 150 mm respectively. A gold-plated tungsten anode wire of 10 μm in diameter was stretched along the detector axis. A potential of +2400 V was applied to the anode, and the casing (the cathode) was grounded. To reduce edge-effects, end segments of the wire were passed through the copper tubes (3 mm in diameter and 38.5 mm in length) electrically connected to the anode. Gas amplification was absent on these segments, and charge was collected in the ionization mode. The length of the counter operating volume was 595 mm (the distance between the butt ends of the tubes), flange-flange distance was 704 mm and total length was 1160 mm. Total counter volume was 10.3 L and the operating volume was 9.159 L. The pressure was equal to 4.6 bar. The total capacity was 30.6 pF and anode resistance was 613 Ohm [6].

Two stages of measurements were carried out with different radioactive background: first stage enriched ^{78}Kr – 8400 h, depleted ^{78}Kr – 5000 h; second stage enriched ^{78}Kr – 9457 h, depleted ^{78}Kr – 6243 h. The background in the second stage was suppressed by ~ 7 times with respect to the first stage level. The reason is that inner surface of the counter's casing was shielded with 1.5 mm of pure M0k-grade copper.

The detector signals were read-out from one end of the anode wire by a charge-sensitive amplifier. The CSA parameters were optimized for transmission of a signal with minimum distortions, and information on the primary ionization charge spatial distribution in its projection to the counter radius was fully represented in the pulse

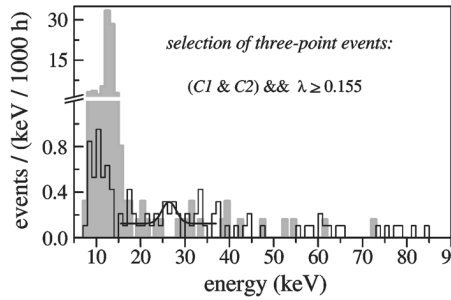

Fig. 1: The three-point spectra of the second stage selected under the conditions ("*C1*" & "*C2*") and $\lambda \geq 0.155$: krypton enriched in ^{78}Kr (black bars), depleted krypton (grey bars) and model calculation spectrum for $2K$ capture

shape. After amplification in an auxiliary amplifier the pulses were collected by the LA-n20-12PCI digital oscilloscope. The oscilloscope, integrated with a personal computer, recorded the pulse waveform digitized with a frequency of 6.25 MHz.

Data were analyzed for a signal of a so-called three-point event in which two X-rays (e.g. K_{α_1}, K_{α_2}) and Auger electrons are emitted with the overall energy 25.3 keV. Characteristic photons can pass a long distance in the gas from the point of its origin to the point of absorption, while electrons are absorbed virtually immediately. These three-cluster events have a number of unique features and were a subject of search in the experiment.

Offline processing of the digitized pulses was performed using specially developed technique which rejects pulses of no-ionized nature. The signals were denoized with wavelet transformation and symmetrized by discarding ionic component contribution, leaving only signal of primary electrons [6, 7]. The amplitude of primary charge pulse $M1$ is proportional to the energy release in detector. $M2$ is a smaller secondary charge pulse magnitude, owing to the photoelectrons knocked out of the copper case by photons produced in electronic avalanches during gas amplification process. Parameter $\lambda = (M2 - M1)/M1$ is a relative amplitude of the afterpulse which is used to select required signals. The charge signal was differentiated to obtain current signal, which then was fitted with three Gaussians according to three-point event. If three Gaussian areas correspond

to energy depositions $E1$, $E2$ and $E3$ ($E1 \leq E2 \leq E3$), then the selection criteria are: $C1$: $0.9 \leq E1 \leq 4.5$ keV (Auger electrons), $C2 : 0.7 \leq E2/E3 \leq 1.0$ (two K-rays), $\lambda > 0.155$ (proportional mode). After selection of events the spectrum shown on Figure 1 was obtained. One can see that in the spectrum of the enriched sample there is an excess of events in the region of expected effect. The background in the spectrum of enriched and depleted krypton in the energy range from 22.8 to 28.8 keV was found to be $N_1 = 15$ for 9457 h, and $N_2 = 4$ for 6 243 h (~ 6 in 9457 h) respectively.

In order to increase the statistical significance, the results of two stages of measurements were combined. Average annual count rates have been summed and then normalized to one year.

3. Conclusions

A combination of methods of selection of useful events with a unique set of characteristics and wavelet analysis of signals reduced background in the energy region of interest by ~ 2000 times. After two stages of measurements the total exposure was 0.343 kg×y. Counting rate of $2\nu 2K$ capture events in ^{78}Kr was $12.8^{+5.2}_{-4.8}$ y^{-1} [5]. It gave the following half-life estimation:

$$T^{2\nu 2K}_{1/2}(g.s. \rightarrow g.s.) = [9.2^{+5.5}_{-2.6}(stat) \pm 1.3(syst)] \times 10^{21}\mathtt{y}\ (90\%\ \mathtt{C.L.}).$$

Previous result was [8]:

$$T^{2\nu 2K}_{1/2}(g.s. \rightarrow g.s.) \geq 2.3 \times 10^{20}\mathtt{y}\ (90\%\ \mathtt{C.L.}).$$

The value is in agreement with theoretical models. Because of small significance level (2.5σ) evidence cannot be claimed, but it is a good indication of $2\nu 2K$ capture in ^{78}Kr.

1. M. Aunola and J. Suchonen, Nucl. Phys. A **602**, 133 (1996).
2. Ju.M. Gavriljuk *et al.*, Phys. At. Nucl.**69**, 2124 (2006).
3. V.N. Gavrin *et al.*, preprint INR RAN, P-**698**, Moscow, (1991).
4. M. Doi and T. Kotani, Prog. Theor. Phys. **87**, 1207 (1992).
5. Yu.M. Gavrilyuk *et al.*, Phys. Rev. C **87**, 035501 (2013).
6. Yu.M. Gavrilyuk *et al.*, Instrum. Exp. Tech. **53**, 57 (2010).
7. S.S. Ratkevich, Vis. Khar. Nat. Univ. **746**, 23 (2006).
8. Ju.M. Gavriljuk *et al.*, Phys. Atomic Nuclei **63**, 2201 (2000).

STATUS OF THE EXCLUSIVE MSSM HIGGS PRODUCTION AT LHC AFTER THE RUN I

M. Taševský

Institute of Physics of the Academy of Sciences of the Czech Republic, Na Slovance 2, 18221 Prague, Czech Republic
e-mail: Marek.Tasevsky@cern.ch

Abstract

We investigate the prospects for Central Exclusive Diffractive (CED) production of MSSM Higgs bosons at the LHC using forward proton detectors (FPD) proposed to be installed 220 m and 420 m from ATLAS and CMS detectors. We summarize the situation after the first and very successful data taking period of the LHC. The discovery of a Higgs boson and results from searches for additional MSSM Higgs bosons from the ATLAS and CMS, have recently led to a proposal of new low-energy MSSM benchmark scenarios. The CED signal cross section for the process $H/h \to b\bar{b}$ and its backgrounds are estimated in these new scenarios. We also comment on the experimental procedure if the proposed FPDs are to be used to measure the CED signal.

1. Introduction

A brief overview of the analysis is given here, while more details can be found in [1]. The interest in the CED production of new particles is still significant over the last decade (e.g. [1–3] and references in [1]). The process is defined as $pp \to p \oplus \Phi \oplus p$ where all of the energy lost by the protons during the interaction (a few per cent) goes into the production of the central system, Φ. The final state therefore consists of a centrally produced system (e.g. dijet, heavy particle or Higgs boson) coming from a hard subprocess, two very forward protons and no other activity. The '$\oplus$' sign denotes the regions devoid of activity, often called rapidity gaps. A simultaneous detection of both forward protons and the central system opens up a window to a rich physics program covering not only exclusive but also a variety of

QCD, Electroweak and beyond Standard Model (BSM) processes (see e.g. [2, 4–7]). Such measurements can put constraints on the Higgs sector of Minimal Supersymmetric SM (MSSM) and other popular BSM scenarios [8–10].

The attractivity of the CED production stems from a precise measurement of the Higgs mass using FPDs, a possibility to measure its spin, parity and couplings to b-quarks using a few events and a good S/B ratio. These aspects together with calculations of signal and background processes are in detail discussed in [9]. Studies of the CED Higgs production contributed to the physics motivation for upgrade projects to install FPDs at 420 m [5] and 220 m from the ATLAS (AFP project [6]) and CMS (PPS project [7]) detectors. At present, only 220 m devices are being considered in ATLAS and CMS.

In MSSM [11] the Higgs sector consists of five physical states. At lowest order the MSSM Higgs sector is $\mathcal{CP}$-conserving, containing two $\mathcal{CP}$-even bosons, the lighter h and the heavier H, a $\mathcal{CP}$-odd boson, A, and the charged bosons $H^{\pm}$. It can be specified in terms of the gauge couplings, the ratio of the two vacuum expectation values, $\tan\beta \equiv v_2/v_1$, and the mass of the A boson, M_A.

Last year, the discovery of a new resonance with mass close to 125.5 GeV has been announced by ATLAS [12] and CMS [13]. Preliminary estimates of its spin-parity and couplings suggest that it behaves like a SM Higgs boson. At the same time, results from analyses searching for the MSSM signal at LHC have been published. Based on all these results i) seven new low-energy MSSM benchmark scenarios have been proposed [14] that are compatible over large parts of the (M_A, $\tan\beta$) parameter plane with the mass and production rates of the observed Higgs boson signal at 125.5 GeV, and ii) the most recent LHC exclusion regions have been evaluated using the latest version of the program `HiggsBounds` [15]. The aim of this analysis is to investigate the CED Higgs boson production in these new benchmark scenarios taking into account the recent LHC exclusion regions and the region of the allowed Higgs mass.

2. Prospects in New Benchmark MSSM Scenarios

The SM cross section used [16] for the normalization within `HiggsBounds` is evaluated using the MRST2002 NNLO PDFs. For each point in the parameter space we evaluate the relevant Higgs

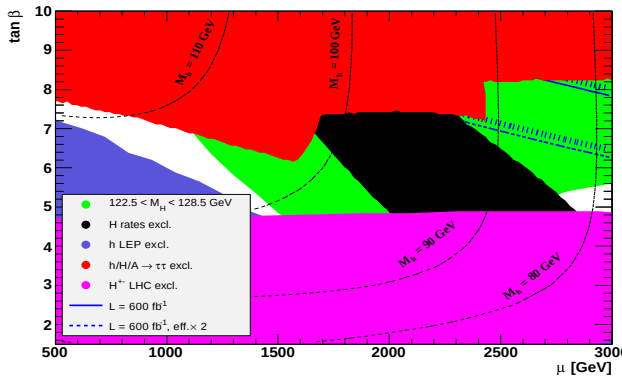

Fig. 1: Contours of $3\,\sigma$ statistical significance (solid blue lines) for the $h \to b\bar{b}$ channel in CED production at $\sqrt{s} = 14$ TeV in the $(\mu, \tan\beta)$ plane of the MSSM within the Low-MH benchmark scenario. The values of the mass of the light $\mathcal{CP}$-even Higgs boson, M_h, are indicated by dashed (black) contour lines. The dark shaded (blue) region corresponds to the parameter region that is excluded by the LEP MSSM Higgs searches, the lighter shaded (red), the lighter shaded (pink) and black areas are excluded by LHC MSSM Higgs searches in the analyses of h/H/A $\to \tau\tau$, charged Higgs and Higgs rates, respectively. The light shaded (green) area corresponds to the allowed mass region $122.5 < M_H < 128.5$ GeV

production cross section times the Higgs branching ratio for the $b\bar{b}$ decay in MSSM (BR($h \to b\bar{b}$)). The values of M_H, BRs and effective couplings in MSSM are calculated with the program `FeynHiggs` [17]. The resulting theoretical cross section is multiplied by the experimental efficiencies as described in [9]. We also show the parameter regions excluded by the LEP and LHC Higgs-boson searches as obtained with `HiggsBounds` [15] and so called region of allowed Higgs masses, i.e. $M_H = 125.5 \pm 3$ GeV (by the light gray (green)). The total uncertainty of 3 GeV represents a combination of the experimental ($\sim$0.6 GeV) and theoretical uncertainty from unknown higher-order corrections in MSSM. The prospects for observing the neutral $\mathcal{CP}$-even Higgs bosons in CED within the new MSSM benchmark scenarios are discussed in detail in [1]. In summary: available cross-sections in all scenarios are too small (smaller than 0.02 fb) to be considered seriously for further studies with the exception of the Low-MH scenario for which the contours of $3\,\sigma$ statistical significances are shown in Fig. 1 for the 420+220 FPD configuration and for two assumed effective luminosities, 600 fb^{-1} and 600 fb^{-1} eff$\times$2. The region of

interest is the area of allowed Higgs masses that is not overlaid by the LHC exclusion region. The highest achievable significances are located in the same corner of the green band as the highest S/B ratios (see [1]). We conclude that if MSSM is realized as in the Low-MH scenario, i.e. the heavy Higgs at mass of 125.5 GeV and the lighter one in the range 80–90 GeV, FPD projects could be very helpful to ATLAS and CMS in searches for such a low-mass object. Note that due to mass acceptance it can only be seen with stations at 420 m.

A few notes about experimental issues: i) the total integrated luminosity needed to observe the light Higgs boson produced in CED with mass around 80–90 GeV is of the order of 1000 fb^{-1} meaning that data from both the AFP and PPS would have to be combined, ii) putting the AFP stations at 420 m into the L1 ATLAS trigger scheme is currently impossible due to a short L1 latency, iii) the total mass acceptance decreases and the mass resolution and b-tagging efficiency worsen with decreasing mass. However, improvements are expected in the reduction of background, e.g. in reducing the misidentification of gluon to be b-quark and resolution below 10 ps in the fast timing detectors. We conclude that investigating the mass range 80–90 GeV with FPDs at LHC is more challenging than that around 120 GeV.

Acknowledgments

The work was supported by the project LG13009 of the Ministry of Education of the Czech republic. Big thanks to Sven Heinemeyer and Valery Khoze for their encouragement and assistance.

1. M. Tasevsky, arXiv:1309.7772 [hep-ph].
2. V.A. Khoze, A.D. Martin and M.G. Ryskin, Eur. Phys. J. C **23**, 311 (2002).
3. L.A. Harland-Lang *et al.*, arXiv:1301.2552 [hep-ph].
4. CMS and TOTEM forward physics group, CERN/LHCC 2006-039/G-124.
5. M. Albrow *et al.*, JINST **4**, T10001 (2009).
6. The AFP project in ATLAS, `http://cdsweb.cern.ch/record/1402470`.
7. The PPS project in CMS, M. Albrow, AIP Conf. Proc. **1523**, 320 (2012).
8. A. Kaidalov et al., Eur. Phys. J. C **33**, 261 (2004).
9. S. Heinemeyer et al., Eur. Phys. J. C **53**, 231 (2008); C **71**, 1649 (2011).
10. B. Cox, F. Loebinger and A. Pilkington, JHEP **0710**, 090 (2007).

11. H. Nilles, Phys. Rept. **110**, 1 (1984); H. Haber, G. Kane, Phys. Rept. **117**, 75 (1985).

12. G. Aad *et al.* (ATLAS Collab.), Phys. Lett. B **716**, 1 (2012).

13. S. Chatrchyan *et al.* (CMS Collab.), Phys. Lett. B **716**, 30 (2012).

14. M. Carena *et al.*, arXiv:1302.7033 [hep-ph].

15. P. Bechtle *et al.*, Comp. Phys. Comm. **181**, 138 (2010); Comp. Phys. Comm. **182**, 2605 (2011); arXiv:1301.2345 [hep-ph].

16. R Harlander and W. Kilgore, Phys. Rev. D **68**, 013001 (2003).

17. S. Heinemeyer *et al.*, Comp. Phys. Comm. **124**, 76 (2000); **180**, 1426 (2009).

JINR ASTROPHYSICAL STUDIES IN THE NUCLEON AND TUS SPACE EXPERIMENTS

L. Tkachev, V. Boreiko, N. Gorbunov, A. Grinyuk,
V. Grebenyuk, A. Kalinin, S. Porokhovoy, B. Sabirov,
A. Sadovsky, M. Slunecka, A. Tkachenko
on behalf of NUCLEON and TUS callaborations

Abstract

The JINR team participates in the preparation of the two space experiments: NUCLEON and TUS, together with SINP MSU that is principal investigator and the other institutions.The main aim of the NUCLEON space experiment is the measurement of the cosmic rays flux, composition and anisotropy in the energy range 10^{11}–5×10^{14} eV. The TUS space experiment is aimed to study energy spectrum, composition and arrival distribution of the Ultra High Energy Cosmic Rays (UHECR) at $E \sim 10^{20}$ eV.

1. Introduction

The **NUCLEON** project main idea is to develop a method and to design a scientific instrument being able to measure the Cosmic Ray (CR) flux, composition and a possible anisotropy in the energy range 10^{11}–5×10^{14} eV with the high precision of the charge resolution measurement [1]. At the same time this instrument should be light (~ 350 kg) and small (~ 1.0 m^3) to be used on regular serial Russian satellites as an additional payload. That makes possible 5 year flight and provides the low price of the apparatus.

The NUCLEON charge range sensitivity is up to $Z \sim 30$. Such measurements are motivated by the "knee" problems: change of the slope and composition in the CR energy spectrum at $\sim 10^{15}$ eV. Besides the CR anisotropy measurements will be done as it was fullfilled

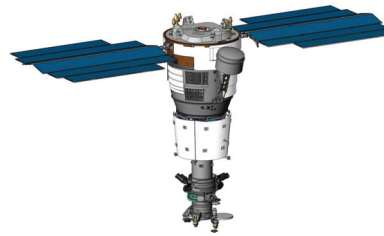

Fig. 1: Scheme of NUCLEON detector at the RESURS P No. 2 satellite

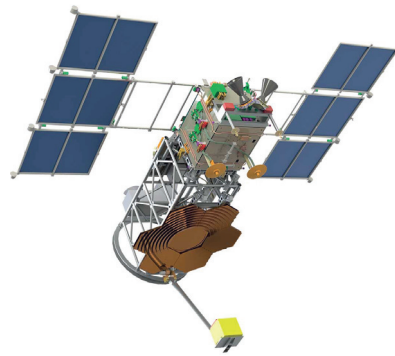

Fig. 2: Detector TUS on-board Lomonosov satellite

in MILAGRO, ARGO-YBJ, TIBET and IceCube experiments [2] at the 10–100 TeV energy. The NUCLEON instrument is planned to be launched by the RESURS-P No. 2 satellite (Fig. 1) in 2014 with exposure time in orbit of about 5 years.

The **TUS** space experiment is aimed to study energy spectrum, composition and angular distribution of the Ultra High Energy Cosmic Rays (UHECR) at $E \sim 10^{20}$ eV that is beyond the GZK energy limit. The TUS detector will measure the fluorescence and Cherenkov light radiated by EAS of the UHECR at night side of the Earth atmosphere from the space platform at heights 400–550 km. There are two main parts of this detector: a modular Fresnel mirror and a 16×16 matrix of PMTs with corresponding DAQ electronics. The TUS mission is now planned for operation at the dedicated "Mikhail Lomonosov" satellite [3] shown in Fig. 2.

2. The NUCLEON Space Experiment Preparation

The NUCLEON detector (Fig. 3) consists of 4 silicon layers of the Charge Measuring System (CMS), 6 layers of the silicon tracker used as an energy measuring system, and the Electromagnetic Calorimeter (ECAL) together with a scintillator trigger system and a control electronics.

The combine tests of the all NUCLEON flight model detectors has been done at CERN SPS test beams in 2012 and 2013. It was taken more than 400.000 ion beam events in 2013 test at different trigger hardness conditions. The goals of that tests were:

– to confirm and check a possibility of the different nucleus separation up to $Z = 30$ in silicon 12×12 mm^2 pads of the CMS,

– to check new chips of special multichannel charge sensitive amplifiers with wide dynamic range and nonlinear gain characteristic that are using in the readout electronic of ECAL.

To check the angular resolution, the NUCLEON detector was turned with respect to the pion beam direction. As can be seen in Fig. 4 the measured angular resolution value is about 2° that is good enough for the NUCLEON tasks.

The CMS charge resolution was measured in 2013 with ion beam and is presented in the top part of the Fig. 5. One can see a good separation of peaks from different nucleus up to $Z = 30$.

The second goal is to check and calibrate the new readout electronic chips of ECAL. The bottom part of the Fig. 5 illustrates the ion beam structure that was measured by silicon sensors of ECAL.

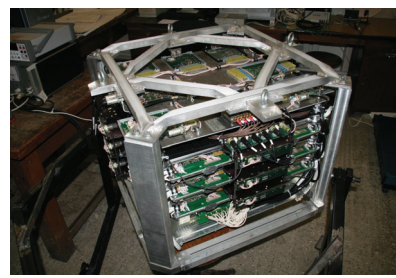

Fig. 3: The NUCLEON apparatus prepared for combine tests

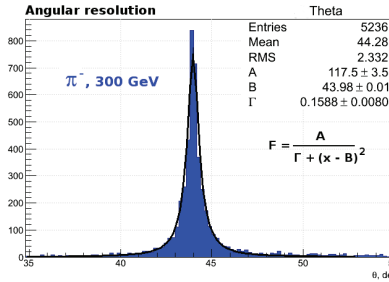

Fig. 4: The NUCLEON detector angular resolution

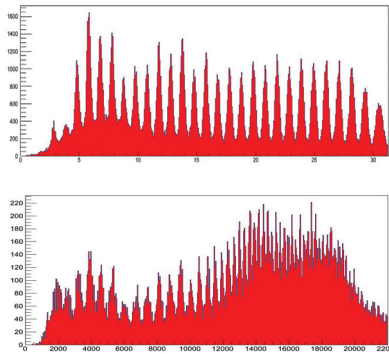

Fig. 5: The NUCLEON detector charge resolution

The ECAL detectors and readout electronics allows to separate the different nucleus peaks up to $Z = 50$ that is in the wider interval than was expected before.

3. Status of the TUS Detector Tests

The TUS photo detector and trigger electronics consists of 256 PMT pixels with the time resolution 0.8 μs and the spatial pixel resolution of 5×5 km. The digital integrators allow to use the same photo detector to study different phenomena in the atmosphere: from ~ 100 μs (EAS) to 1–100 ms (TLE) and up to 1 s (micrometeors).

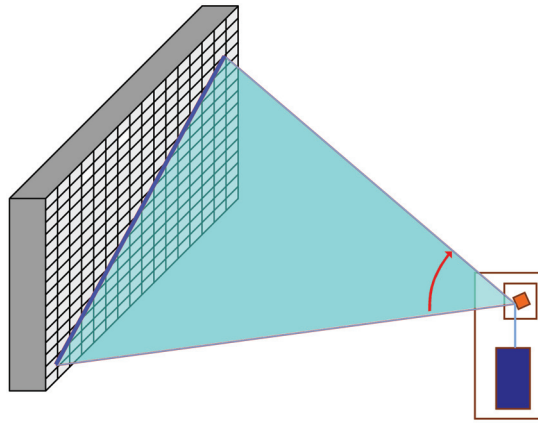

Fig. 6: The scheme of the photo detector preflight test with the EAS simulator

A special optical simulator of EAS with rapidly moving laser beam was produced at JINR for preflight tests of the TUS photo detector and trigger electronics (Fig. 6). The light beam is falling onto the rotated mirror. The mirror rotation speed may be changed to simulate trigger conditions. The satellite installation on the space platform and the elaboration of the TUS calibration system in flight are in progress.

4. Conclusion

The **NUCLEON** space qualification tests were fulfilled at the space center ARSENAL of St.Petersburg and the beam tests at the SPS CERN. The NUCLEON detector is ready for a launch at the RESURS-P No. 2 satellite and to data taking from orbit in 2014.

The **TUS** mission is planned for operation in 2014 at the dedicated "Mikhail Lomonosov" satellite for 3 years of data taking. It will be the first orbital UHECR detector which will test this technique of measurements and give important information for future projects (JEM-EUSO, KLYPVE). In 3 years of operation in space TUS exposure will be ~ 12000 km^2 year sr – comparable with the exposure of the largest ground-based detectors.

1. D. Podorozhnyiet *et al.*, NIM in press.

2. MILAGRO collaboration. 32^{nd} ICRC Proc., Aug. 11-18, Beijing, China; ARGO_YBJ collaboration. 32^{nd} ICRC Proc., Aug. 11-18, Beijing, China. ID-0507; TIBET ASy collaboration. 32^{nd} ICRC Proc., Aug. 11-18, Beijing, China. ID-0379, ID-1167; IceCube collaboration. 32^{nd} ICRC Proc., Aug. 11-18, Beijing, China. ID-0305, 0306.

3. M.I. Panasyuk *et al.*, 32d ICRC Proc. Beijing (2011) ID-1261.

MEASUREMENTS OF THE HIGGS BOSON PROPERTIES WITH THE ATLAS DETECTOR

Makoto Tomoto
On behalf of the ATLAS Collaboration

Graduate School of Science and Kobayashi-Maskawa Institute, Nagoya University, Japan

Abstract

The measurements of the properties of a new boson discovered by the ATLAS experiment at the LHC are presented, based on proton-proton collision data collected in 2011 and 2012. The production strengths and the couplings are measured using decays of the new boson into $\gamma\gamma$, $ZZ^* \to 4\ell$, and $WW^* \to \ell\nu\ell\nu$. The spin-0 and CP-even ($J^P = 0^+$) hypothesis of the standard model (SM) Higgs boson is compared to several alternative hypotheses with $J^P = 0^-$, 1^+, 1^-, 2^+ using decays of the new boson into $\gamma\gamma$, $ZZ^* \to 4\ell$, and $WW^* \to e\nu\mu\nu$. The measured properties are compatible with the SM Higgs boson.

1. Introduction

One year has passed since a new boson with a mass of $m_H \simeq 125.5\,\mathrm{GeV}$ was discovered by the ATLAS and the CMS Collaborations [1, 2]. Since then our interests have been focused on whether it provides masses to the fermions and bosons and whether it is a Higgs boson of $J^P = 0^+$ as predicted by the standard model (SM). They are addressed experimentally by measuring its properties such as the production strengths, the couplings and the spin-parity. We also search for signs of physics beyond the SM (BSM) by studying its properties.

At the LHC, the Higgs boson is produced via gluon fusion (ggF), vector boson fusion (VBF), associated production with W or Z (VH),

and associated production with a top quark pair (ttH). In these mechanisms, VBF and VH provide a direct probe of the vector boson coupling while ggF provides an indirect probe of the Higgs-fermion coupling. The Higgs boson with a mass of $m_H \simeq 125.5$ GeV is detectable at LHC experiments using the $H \to \gamma\gamma$ via a W boson or a top quark loop, $H \to ZZ^*$, $H \to WW^*$, $H \to \tau\tau$, and $H \to b\bar{b}$ decay channels.

The expected number of signal events in the studies of the $H \to \gamma\gamma$, $H \to ZZ^*$, and $H \to WW^*$ decay channels are around 370, 15, and 150 respectively, for the $\sqrt{s} = 8$ TeV data collected by the ATLAS experiment [3] in 2012 (for the study of $H \to ZZ^*$ the $\sqrt{s}$ =7 TeV data collected in 2011 is also included). This article presents measurements of the properties of the new boson such as the signal strengths, the couplings, and the spin-parity in the analyses of these three channels based on the 7 TeV and 8 TeV data [4, 5].

2. Production Strength and Coupling Measurements

The Higgs boson production strengths μ normalized to the SM expectation (so that $\mu = 1$ corresponds to the SM Higgs boson hypothesis and $\mu = 0$ to the background-only hypothesis) are measured using the $H \to \gamma\gamma$, $H \to ZZ^*$, and $H \to WW^*$ final states. The parameter μ is determined from a fit to the data using the profile likelihood ratio for a fixed mass hypothesis corresponding to the measured value $m_H = 125.5$ GeV. The left-hand figure of Fig. 1 shows the production strengths for three channels and their combination. The production strengths are categorized by the vector-boson mediated processes, VBF and VH, and the gluon mediated processes, ggF and ttH ($\mu_{\mathrm{VBF+VH}} = \mu_{\mathrm{VBF}} = \mu_{\mathrm{VH}}$, $\mu_{\mathrm{ggF+ttH}} = \mu_{\mathrm{ggF}} = \mu_{\mathrm{ttH}}$). To test the sensitivity to VBF production alone, the data are fitted with the ratio $\mu_{\mathrm{VBF}}/\mu_{\mathrm{ggF+ttH}}$. A value $\mu_{\mathrm{VBF}}/\mu_{\mathrm{ggF+ttH}} = 1.4^{+0.4}_{-0.3}(\mathrm{stat})^{+0.6}_{-0.4}(\mathrm{sys})$ is obtained from the combination of the three channels. This result provides evidence at the 3.3 σ level that a fraction of Higgs boson production occurs through the VBF.

Following the approach and benchmarks recommended in [6], the coupling scaling factors κ_j are defined in such a way that the cross

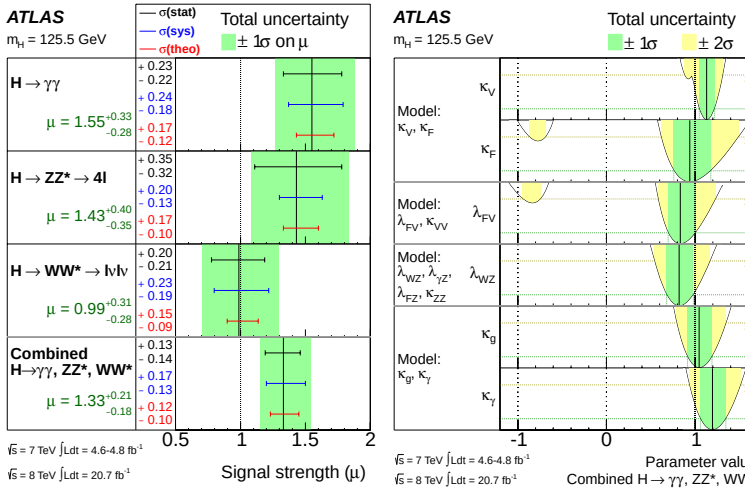

Fig. 1: Left: The measured production strengths for a Higgs boson with mass $m_H = 125.5$ GeV, normalized to the SM expectations, for diboson final states and their combination [4]. The best-fit values are shown by the solid vertical lines. The total $\pm 1\sigma$ uncertainty is indicated by the shaded band, with the individual contributions from the statistical uncertainty (top), the total systematic uncertainty (middle), and the theory uncertainty (bottom) on the signal cross-section shown as superimposed error bands. Right: Summary of the measurements of the coupling scale factors (the measurements of κ_V v.s. κ_F and κ_g v.s. κ_γ described in the text together with the ratio of couplings to fermions and vector bosons and the ratio of couplings to W and Z) for a Higgs boson with mass $m_H = 125.5$ GeV [4]. The best-fit values are represented by the solid vertical lines with the $\pm 1\sigma$ and $\pm 2\sigma$ uncertainties given by the dark- and light-shaded bands, respectively

sections σ_j and the partial decay width Γ_j associated with the SM particle j scale with κ_j^2 compared to the SM prediction. The results are extracted from fits to the data using the profile likelihood ratio, where the κ_j couplings are treated either as parameters of interest or as nuisance parameters, depending on the measurement. A number of assumptions are made, as described below.

The first benchmark considered assumes one coupling scale factor for fermions (κ_F) and one for vector bosons (κ_V). The effective scale factors in loop-induced processes (i.e. κ_γ and κ_g) and the total Higgs boson width scale factor κ_H are expressed as a function of the SM coupling scale factors and depend only on κ_F and κ_V. κ_F

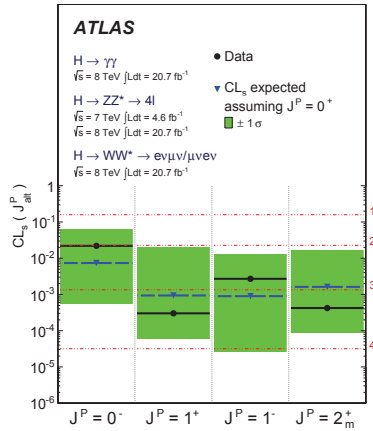

Fig. 2: Expected (triangles/dashed lines) and observed (circles/solid lines) $\mathrm{CL_S}$ for alternative spin-parity hypotheses assuming a $J^P = 0^+$ [5]. The bands represent the 68% $\mathrm{CL_S}(\mathrm{J^P_{alt}})$ expected exlusion range for a signal with assumed $J^P = 0^+$

and κ_V are measured using the data for the three channels and their combination, assuming $\kappa_V > 0$ (only the relative sign of κ_F and κ_V is physical). Because of the negative interference between the W-boson loop and the top-quark loop in $H \to \gamma\gamma$ decay, κ_F prefers the positive relative sign. The 68% confidence level (CL) intervals of κ_F and κ_V are $\kappa_F \in [0.76, 1.18]$ and $\kappa_V \in [1.05, 1.22]$, respectively. The second benchmark considered probes the BSM contributions in the κ_g and κ_γ assuming the couplings of the known particles to the Higgs boson and κ_H equal to 1. The best-fit values are $\kappa_g = 1.04 \pm 0.14$ and $\kappa_\gamma = 1.20 \pm 0.15$.

The right-hand figure of Fig. 1 shows the summary of the measurements of the coupling scale factors for a Higgs boson with $m_H = 125.5$ GeV. The compatibility of the best-fit values and SM predictions is between 12% to 20%.

3. Spin-Parity Measurements

Several alternative specific models, J^P=0^-, 1^+, 1^-, 2^+, are tested against the SM Higgs boson $J^P = 0^+$ hypothesis, using angular and kinematic distributions in $H \to \gamma\gamma$, $H \to ZZ^* \to 4\ell$, and $H \to$

$WW^* \to e\nu\mu\nu$ decays. The $J = 1$ particle decaying to $\gamma\gamma$ is ruled out because of Landau-Yang theorem [7, 8]. For $J^P = 2^+$, the graviton-inspired model with minimal coupling to SM particles (2^+_m model) is chosen as a benchmark [9]. Fig. 2 shows expected and observed CL_s for alternative spin-parity hypotheses assuming a $J^P = 0^+$ signal. For the spin-2 hypothesis, the result for the specific 2^+_m model is shown. $J^P = 0^-$, 1^+, 1^-, and 2^+ are excluded against $J^P = 0^+$ at more than 97.8% CL.

4. Conclusion

ATLAS Run-1 ends with a great success. Since the discovery of a new boson, its properties have been measured by the ATLAS experiment with increasing precision. All measured properties are compatible with the SM Higgs boson so far. LHC will increase the energy and integrated luminosity in the upcoming runs. More precise measurements will be achieved to challenge the SM predictions and will give us hints of the BSM. The "Higgs physics" has just begun.

1. ATLAS Collaboration, Phys. Lett. B **716**, 1-29 (2012).
2. CMS Collaboration, Phys. Lett. B **716**, 30-61 (2012).
3. ATLAS Collaboration, 2008 JINST 3 S08003.
4. ATLAS Collaboration, Phys. Lett. B **726**, 88-119 (2013).
5. ATLAS Collaboration, Phys. Lett. B **726**, 120-144 (2013).
6. LHC Higgs Cross Section Working Group, arXiv:1209.0040 [hep-ex].
7. L. D. Landau, Dokl. Akad. Nauk Ser. Fiz. **60**, 207 (1948).
8. C.-N. Yang, Phys. Rev. **77**, 242 (1950).
9. Y. Gao, A.V. Gritsan, Z. Guo, K. Melnikov, M. Schulze, and N.V. Tran, Phys. Rev. D **81**, 075022 (2010).

THE QUARKONIUM SAGA IN HEAVY ION COLLISIONS

Itzhak Tserruya
Weizmann Institute of Science, Rehovot, Israel
e-mail: Itzhak.Tserruya@weizmann.ac.il

Abstract

J/ψ suppression was proposed more than 25 years ago as an unambiguous signature for the formation of the Quark Gluon Plasma in relativistic heavy ion collisions. After intensive efforts, both experimental and theoretical, the quarkonium saga remains exciting, producing surprising results and not fully understood. This talk focuses on recent results on quarkonium production at RHIC and the LHC.

1. Introduction

More than 25 years ago, Matsui and Satz published their by now classic paper where they proposed J/ψ suppression as an unambiguous signature of quark deconfinement in the Quark Gluon Plasma (QGP) [1]. At high color density the confining potential becomes color screened, (the QCD equivalent of the QED Debye screening of electrical charges) effectively limiting the range of the strong interaction. As a consequence, when the screening radius becomes smaller than the $c\bar{c}$ binding radius, the c and $\bar{c}$ cannot bind together any longer, leading to suppression of the J/ψ yield in nuclear collisions.

One of the first observations made by the NA38/NA50 experiment in the framework of the CERN SPS heavy ion program, was indeed the suppression of J/ψ production in S+U collisions at 200 A GeV [2]. However, this suppression was found to follow the same systematic trend observed in proton-nucleus collisions and in collisions involving light nuclei like O+Cu and O+U. The J/ψ suppression in all these systems was properly accounted for by a final state absorption cross section of $\sigma_{abs} \sim 4$ mb of the charmonium state in nuclear matter [3]. An anomalous J/ψ suppression, stronger than expected from this absorption cross section, was observed in semi-central and central

Pb+Pb collisions at 158 A GeV suggesting the onset of an additional suppression mechanism, possibly the production of a deconfined state of matter [4]. Consistent results were later obtained by the NA60 experiment in In+In collisions at 158 A GeV [5].

Experimental results from RHIC and more recently from LHC, unveiled a much richer physics landscape with a variety of competing effects that can potentially affect the charmonium production in nuclear collisions. These include nuclear modifications of the gluon distribution functions (shadowing or anti-shadowing), gluon saturation, initial and final state k_T scattering, initial and final state parton energy loss, nuclear absorption, co-mover breakup and recombination.

This paper focuses on some of the most recents quarkonium results obtained at RHIC and the LHC.

2. RHIC Results

The first charmonia measurements performed by the PHENIX experiment at RHIC in Au+Au collisions at $\sqrt{s_{NN}} = 200$ GeV yielded two surprising results. First, at mid-rapidity, the level of J/ψ suppression, quantified by the the nuclear modification factor R_{AA} (defined as the ratio of the yield per binary nucleon-nucleon collision, N_{coll}, in A+A collisions to the yield in p+p collisions), is very similar to the one observed at the SPS (see left panel of Fig. 1) [6, 7]. This is contrary to the stronger suppression anticipated at RHIC due to the increase of more than one order of magnitude in collision energy. The sec-

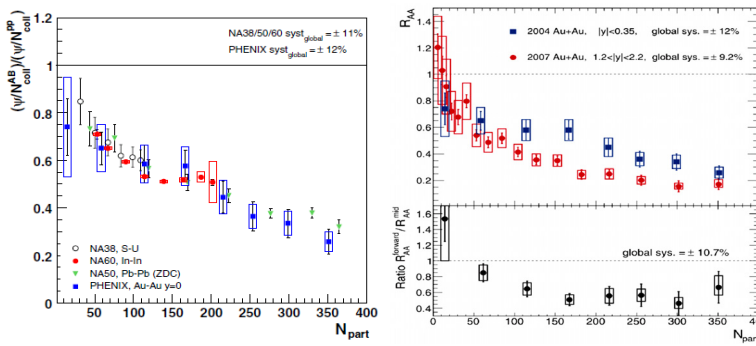

Fig. 1: Left: The J/ψ nuclear modification factor, R_{AA}, measured at mid-rapidity by PHENIX at $\sqrt{s_{NN}} = 200$ GeV [6] and by NA38, NA50 and NA60 at SPS energies [7]. Right: J/ψ R_{AA} measured by PHENIX at forward and mid-rapidity at $\sqrt{s_{NN}} = 200$ GeV [6]

ond surprising result is that J/ψ is more suppressed at forward than at mid-rapidity by about a factor of two, in spite of the fact that the energy density at forward rapidity is presumably smaller than at mid-rapidity (see right panel of Fig. 1) [6].

PHENIX has also measured the J/ψ R_{AA} at intermediate energies of 62 and 39 GeV (see Fig. 2) [8]. Within the experimental uncertainties, no significant change is observed in R_{AA}.

The almost constant level of suppression observed at mid-rapidity, from the SPS energy of $\sqrt{s_{NN}} = 17.3$ GeV up to the top RHIC energy of $\sqrt{s_{NN}} = 200$ GeV, can be explained by the interplay between direct J/ψ suppression and coalescence or recombination of c and $\overline{c}$ quarks. As the collision energy increases the direct suppression due to color screening in the QGP increases. But at the same time, over this energy range, the $c\overline{c}$ production cross section increases by almost two orders of magnitude increasing the probability of charmonium production by recombination of c and $\overline{c}$ quarks. In some models, like the statistical hadronization model, recombination takes place at the hadronization stage [9]. In others, like in the rate equation approach, recombination occurs continuously through the entire evolution of the collision [10]. As an example, calculations based on the rate equation approach are shown in Fig. 2. Accidentally, the larger direct suppression almost compensates the larger recombination rate yielding

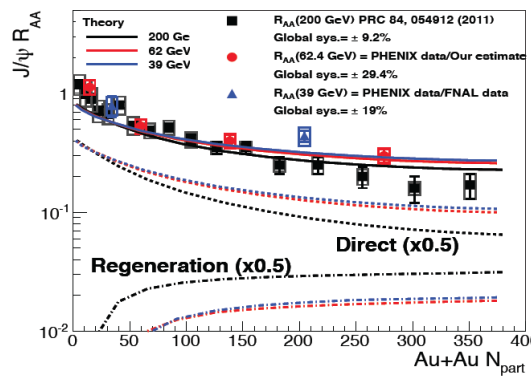

Fig. 2: J/ψ R_{AA} measured by PHENIX at mid-rapidity at $\sqrt{s_{NN}} = 200$, 62 and 39 GeV [8] together with calculations including suppression and recombination [10]

an almost constant R_{AA} over this broad energy range, in reasonable agreement with the mid-rapidity PHENIX data. However, this model has difficulties in reproducing the stronger suppression observed at forward rapidity. In order to do that, it requires a smaller open charm production and a stronger cold nuclear matter suppression [10].

If a significant fraction of J/ψ is formed by recombination of charm quarks, the J/ψ should inherit elliptic flow, v_2, from the charm quarks. The measurement of J/ψ flow thus provides an independent and additional support to the recombination scenario. At RHIC, the J/ψ v_2 measured by STAR in Au+Au collisions was found to be consistent with zero [11]. But one should note that the predicted v_2 is very small (of the order of 2-3%) [12] and data of much higher precision are needed before a definite statement can be made. At the LHC, where recombination is expected to play a larger role, the predicted values are somewhat larger (of the order of 5%) and the ALICE experiment recently reported a non-zero v_2 of J/ψ in semi-central Pb+Pb collisions which is consistent with calculations [13].

The PHENIX experiment has studied the J/ψ production dependence on the system size by varying the colliding nuclei. In Cu+Cu collisions the J/ψ R_{AA} shows a similar behavior to that of Au+Au collisions when both are compared at the same number of participating nucleons N_{part} [14]. A real benefit in the study of light systems is that they provide higher precision in the determination of N_{part} for $N_{part} \leq 100$. Recently, PHENIX measured J/ψ production in Cu+Au and U+U collisions at $\sqrt{s_{NN}} = 200$ GeV [15]. In these systems J/ψ production is tested under different initial geometries and thus gives additional constraints to theoretical models.

The observed J/ψ yield can be affected by a variety of cold nuclear matter (CNM) effects including nuclear modifications of the gluon distribution function (shadowing and anti-shadowing), gluon saturation, intial state parton scattering and nuclear absorption (for a review see [16]). The measurement of J/ψ in a small size system such as d+Au is considered the most appropriate way to quantitatively study these CNM effects[1]. PHENIX has measured J/ψ production in d+Au collisions at $\sqrt{s_{NN}} = 200$ GeV in three rapididty intervals:

[1] This working hypothesis might be challenged by recent results suggesting that effects of hydrodynamic origin occur in d+Au and p+Pb collisions [17] – [20].

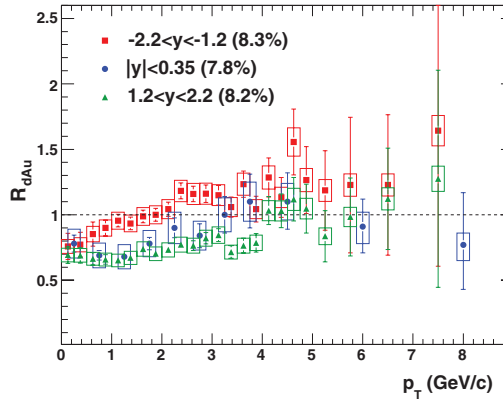

Fig. 3: Centrality integrated J/ψ R_{dAu} vs p_T measured by PHENIX in d+Au collisions at $\sqrt{s_{NN}} = 200$ GeV [21]

mid-rapidity ($|y| < 0.35$), forward rapidity ($1.2 < y < 2.2$) and backward rapidty ($-2.2 < y < -1.2$) [21]. The centrality integrated R_{dAu} vs. p_T is shown in Fig. 3 for the three rapidity intervals overlaid. A small but significant suppression is seen in the three cases. Whereas at backward rapidity (the Au-going direction) the suppression is seen at low $p_T < 2$ GeV/c, the mid- and forward rapidity intervals show a remarkably similar behavior with a suppression extending up to $p_T \sim 4$ GeV/c. For all three intervals, R_{AA} is consistent with 1 at $p_T > 4$ GeV/c, suggesting no sizable CNM effects at high p_T. Model calculations including a mixture of CNM effects, such as shadowing, nuclear absorption and Cronin effect, have difficulties in reproducing all the d+Au results [21]. On the other hand, recent calculations including only parton p_T broadening and energy loss in the nuclear medium show remarkable agreement with the p_T and centrality dependence of the J/ψ R_{dAu} data at the three rapidity intervals [22].

3. LHC Results

The charmonium results obtained at the LHC are rather different from those obtained at RHIC. Figure 4 shows the J/ψ R_{AA} vs. N_{part} measured by ALICE in Pb+Pb collisions at $\sqrt{s_{NN}} = 2.76$ TeV [23,24]. The large difference between forward and mid-rapidity observed at

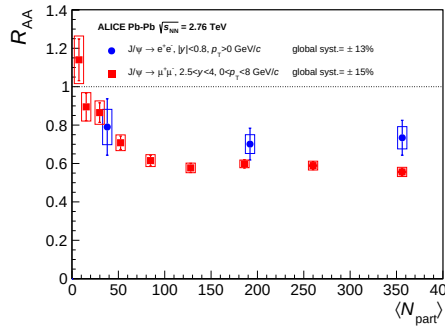

Fig. 4: J/ψ R_{AA} vs N_{part} measured by ALICE in Pb+Pb collisions at $\sqrt{s_{NN}}$ = 2.76 TeV [23, 24]

RHIC (shown in Fig. 1) does not seem to be present in the ALICE data. Furthermore, at forward rapidity, the level of suppression in semi-central or central collisions reaches a value of ~0.6, smaller than the suppression of ~0.2 observed at RHIC (cf. Fig. 1).

A large difference is also observed in the p_T dependence of R_{AA}. The left panel of Fig. 5 compares the R_{AA} p_T dependence measured by ALICE at the LHC [24] and by PHENIX at RHIC [6] at similar rapidities in central Pb+Pb and Au+Au collisions, respectively. At low p_T ($p_T \lesssim 4$ GeV/c), a stronger suppression is observed at RHIC than at LHC, probably reflecting the larger recombination contribution at the LHC. At high p_T, the opposite might be true although the p_T reach of the PHENIX data is not sufficient for a definite statement. The J/ψ R_{AA} at high p_T is of particular interest because it

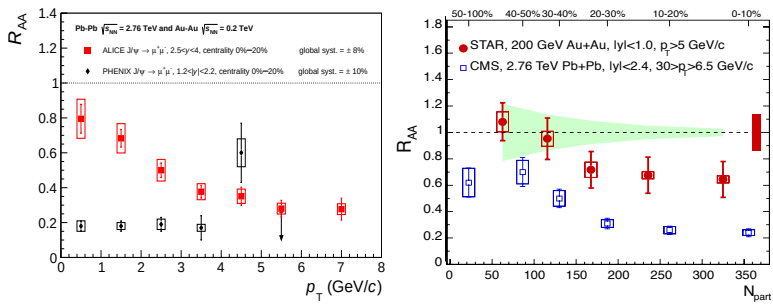

Fig. 5: Left: J/ψ R_{AA} p_T dependence measured by ALICE at LHC [24] and by PHENIX at RHIC [6]. Right: R_{AA} centrality dependence of high p_T J/ψ measured by CMS [25] and STAR [26]

might be more sensitive to color screening effects (CNM effects are measured to be low at high p_T as shown in Fig. 3 and also recombination is expected to be low at high p_T [10]). The right panel of Fig. 5 compares the R_{AA} centrality dependence for high p_T J/ψ measured by CMS [25] and STAR [26]. A stronger suppression is seen at LHC than at RHIC. However, one should note that the CMS data refer to prompt J/ψ whereas the STAR data are for inclusive J/ψ and thus this comparison might be affected by the R_{AA} of the B mesons feed-down contribution to the J/ψ yield from STAR.

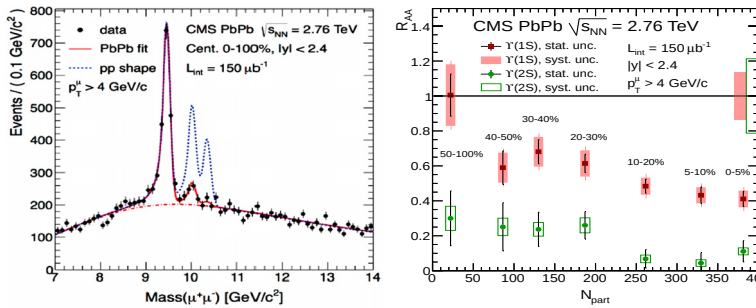

Fig. 6: Left: Υ states measured by CMS in minimum bias Pb+Pb collisions at $\sqrt{s_{NN}}$ = 2.76 TeV. The p+p mass spectrum shape, normalized to the Υ(1s) peak, is also shown [27]

CMS pioneered the study of bottomonium states at LHC [27] as an additional probe to unveil color screening effects in the QGP[2]. The left panel of Fig. 6 shows the invariant mass spectrum of $\mu^+\mu^-$ pairs in the Υ mass region in minimum bias Pb+Pb collisions at $\sqrt{s_{NN}}$ = 2.76 TeV [27]. The figure also shows the mass spectrum shape measured in p+p collisions at the same energy normalized to the peak of the Υ(1s) state. The p+p spectrum shows clear separation of the three states Υ(1S, 2S, 3S) demonstrating the excellent mass resolution of the CMS detector. The comparison of the p+p and Pb+Pb spectra already reveals a clear suppression pattern with the Υ(2S) state strongly suppressed and the Υ(3S) state hardly visible. The suppression pattern is shown in a quantitative manner in the right panel of Fig. 6 that displays the Υ R_{AA} centrality dependence.

[2]STAR has preliminary results on the production of the non-resolved Υ states (1S + 2S +3S) in Au+Au collisions at $\sqrt{s_{NN}}$ = 200 GeV [28].

Υ(1S) is suppressed by a factor of $\sim$2 in central collisions. This is consistent with the assumption that the feed-down states (that account for $\sim$50% of the Υ(1S) yield [29]) are fully suppressed. Υ(2S) shows a stronger suppression. The Υ(3S) state is so suppressed that only an upper limit of $R_{AA} = 0.10$ (with a confidence level of 95%) is reported for minimum bias Pb+Pb collisions. This ordering follows the expected sequential melting of the resonances as their binding energy increases, with the lowest binding energy state, Υ(3S), melting first. This appealing interpretation needs to be reconsidered after measuring possible nuclear effects in p+Pb collisions. It will also be interesting to compare to similar data of resolved Υ states at RHIC energies.

4. Conclusions

After more than 25 years of intensive experimental and theoretical effort, the quarkonium saga is still evolving, producing exciting and surprising results but not fully understood at the quantitative level. The ongoing systematic study of quarkonia states over a broad energy range and using several collision systems shall ultimately allow disentangling the melting of the resonances in the QGP from recombination, cold nuclear matter and other competing effects.

1. T. Matsui and H. Satz, Phys. Lett. B **178**, 416 (1986).
2. M.C. Abreu *et al.* (NA38 Collaboration), Phys. Lett. B **449**, 128 (1999).
3. B. Alessandro *et al.* (NA50 Collaboration), Phys. Lett. B **553**, 167 (2003).
4. M.C. Abreu *et al.* (NA50 Collaboration), Phys. Lett. B **477**, 28 (2000), B. Alessandro *et al.* (NA50 Collaboration), Eur. Phys. J. C **39**, 335 (2005).
5. R. Arnaldi *et al.* (NA60 Collaboration), Phys. Rev. Lett. **99**, 132302 (2007).
6. A. Adare *et al.* (PHENIX Collaboration), Phys. Rev. Lett. **98**, 232301 (2007) and Phys. Rev. C **84**, 054912 (2011).
7. E. Scomparin *et al.* (NA60 Collaboration), J. Phys G **34**, S463 (2007).
8. A. Adare *et al.* (PHENIX Collaboration), Phys. Rev. C **86**, 064901 (2012).
9. A. Andronic, P. Braun-Munzinger, K. Redlich and J. Stachel, Nucl. Phys. A **789**, 334 (2007).
10. X. Zhao and R. Rapp, Phys. Rev. C **82**, 064905 (2010).
11. L. Adamczyk *et al.* (STAR Collaboration), Phys. Rev. Lett. **111**, 052301 (2013).

12. X. Zhao, A. Emerick and R. Rapp, Nucl. Phys. A **904-905**, 611c (2013); Y. Liu, N. Xu and P. Zhuang, Nucl. Phys. A **834**, 317c (2010).
13. E. Abbas *et al.* (ALICE Collaboration), arXiv:1303.5880.
14. A.Adare *et al.* (PHENIX Collaboration), Phys. Rev. Lett. **101**, 122301 (2008).
15. T. Sakaguchi for the PHENIX Collaboration, Nucl. Phys. A **904**, 11c (2013).
16. N. Brambilla, S. Eidelman, B. Heltsley, R. Vogt *et al.*, Eur. Phys. J. C **71**, 1534 (2011).
17. A. Adare *et al.* (PHENIX Collaboration), arXiv:1303.1794.
18. G. Aad *et al.* (ATLAS Collaboration), Phys. Rev. Lett. **110**, 182302 (2013).
19. B. Abelev *et al.* (ALICE Collaboration), Phys. Lett. B **719**, 29 (2013).
20. S. Chatrchyan *et al.* (CMS Collaboration), Phys. Lett. B **718**, 795 (2013).
21. A. Adare *et al.* (PHENIX Collaboration), Phys. Rev. C **87**, 034904 (2013).
22. F. Arleo, R. Kolevatov, S. Peigne and M. Rustamova, JHEP **1305**, 155 (2013).
23. B. Abelev *et al.* (ALICE Collaboration), Phys. Rev. Lett. **109**, 072301 (2012).
24. B. Abelev *et al.* (ALICE Collaboration), arXiv:1311.0214.
25. S. Chatrchyan *et al.* (CMS Collaboration), JHEP **05**, 063 (2012).
26. L. Adamczyk *et al.* (STAR Collaboration), Phys. Lett. B **722**, 55 (2013).
27. S. Chatrchyan *et al.* (CMS Collaboration), Phys. Rev. Lett. **109**, 222301 (2012).
28. W. Xie for the STAR Collaboration, Nucl. Phys. A **904-905**, 170c (2013).
29. R. Aaij *et al.* (LHCb Collaboration), JHEP **02**, 014 (2012).

DEVELOPMENT OF A PROTON COMPUTED TOMOGRAPHY (pCT) SCANNER AT NIU

S.A. Uzunyan[1], G. Blazey[1], S. Boi[1], G. Coutrakon[1], A. Dychkant[1], B. Erdelyi[1], A. Gearhart[1], D. Hedin[1], E. Johnson[1], J. Krider[1], V. Zutshi[1], R. Ford[2], T. Fitzpatrick[2], G. Sellberg[2], J.E. Rauch[2], M. Roman[2], P. Rubinov[2], P. Wilson[2], K. Lalwani[3], M. Naimuddin[3]

[1]*Department of Physics, Northern Illinois University, DeKalb, IL 60115, USA*
[2]*Fermi National Accelerator Laboratory, Batavia, IL 60510, USA*
[3]*Delhi University, 110007, India*

Abstract

We describe the development of a proton Computed Tomography (pCT) scanner at Northern Illinois University (NIU) in collaboration with Fermilab and Delhi University. This paper provides an overview of major components of the scanner and a detailed description of the data acquisition system (DAQ).

1. Introduction

Images with protons provide electron density along the proton path in the body of a patient. The electron density determines the penetration range for a proton of a certain energy, thereby allowing accurate location of the Bragg peak inside a tumor volume. Proton imaging can provide range uncertainties of about 1% compared to 3-4% achievable via traditional X-ray computed tomography, while

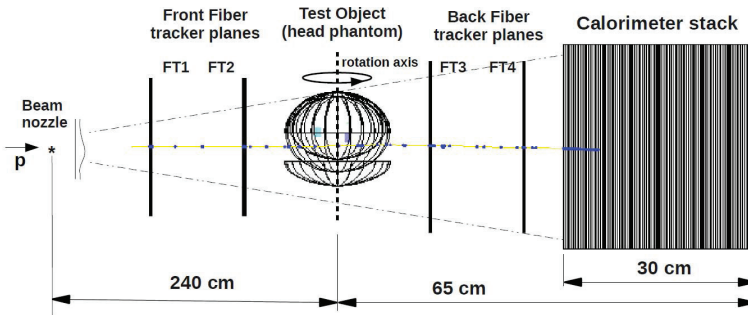

Fig. 1: A schematic of the NIU Phase II pCT detector

also inducing a lower dose for image production [1]. To date a prototype scanner capable of producing images of the required quality was built at Loma Linda University Medical Center (LLUMC) in 2010 [2]. The pCT Phase II scanner constructed at Northern Illinois University (NIU) is a successor of this device. It is designed to demonstrate pCT can be used in a clinical environment and has the ability to collect data required for 2D or 3D image reconstruction in less than 10 min. We concentrate here on the data acquisition system. The detailed description of the scanner hardware components is given in [3], and the image reconstruction hardware and software are described in [4].

2. The Scanner Design Overview

The scanner side view is shown in Figure 1, corresponding to the geometry used for the detector simulation in GEANT [5]. The key elements are the fiber tracker (FT) consisting of four X-Y stations (spatial resolution of $\sim$1 mm/$\sqrt{12}$) before and after a rotating Head Phantom, and the range detector, a calorimeter stack consisting of 96, 3.2 mm thick, scintillating tiles. The signal readout in both detectors ($\sim$2400 channels) is perfomed with CPTA 151-30 [6] silicon photomultipliers (SiPM). For each incident proton the detector measures the proton track (X,Y) positions in the tracker stations and the residual proton energy deposited in the calorimeter stack. The detector acceptance allows scanning of volumes of approximately 24 cm wide and 36 cm high. The system is designed to collect $\approx 2\times10^9$ pro-

ton histories for one 3D image of a human head at a data collection rate of 2 MHz or faster.

3. The Front-End Data Formats

The SiPMs signals from the fiber tracker planes and from the calorimeter stack are collected and digitized by the 16 or 32 channel FPGA-based front-end electronics boards. The boards send digitized data to the DAQ system through 20 UDP streams (eight are reserved for the fiber tracker and 12 for the calorimeter stack) over 1 Gbit/s ethernet connections. There is no an external trigger: each board reads out all of its channels if at least one of them has a signal above a threshhold. The data are shipped in the following formats:

• fiber tracker RAW data. The fibers in the fiber tracker planes are bundled in groups of three neighbor fibers. This design allows the incident proton to simultaneously hit two adjacent bundles and thus the front-end reports paired hits: the local bundle number (lbn) of the first bundle in a pair and the state (fired or not) of the $(lbn + 1)$ neighbor. The timestamp (ts) is added to distinguish hits of different proton histories.

• calorimeter stack RAW data. The scintillator planes in the calorimeter stack are grouped in eight. For each group the front-end reports: the plane number LP_{max} with the maximum energy deposition, the amplitude A_{max} of this maximum energy deposition, the fractional (to the A_{max}) amplitudes in the remaining seven planes, and the timestamp.

The size of the fiber tracker and calorimeter hits in the described design is three and six bytes, respectively. At the readout rate of 2 MHz this requires 6 MB/s transfer rates for the fiber tracker data channels (assuming that the level of noise in the fiber tracker planes will be low) and 12 MB/s for the calorimeter data channels. For the 2×10^9 histories we expect a 208 GB RAW data sample.

4. The DAQ System

The complete DAQ system, shown in Figure 3, was assembled and commissioned in January-March 2013. The six worker nodes and the

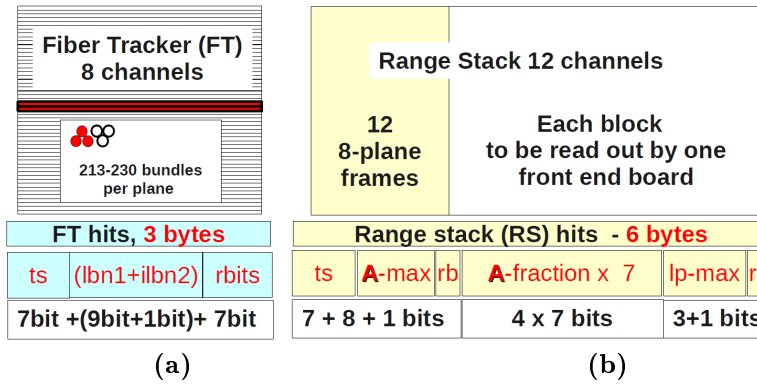

Fig. 2: The bit content of RAW (input) events from the (a) fiber tracker and (b) calorimeter front-end channels

head node form a cluster that provides 24 input channels to collect front-end data, 72 CPU cores (running at 2.6 GHz) for the data processing, and 9 TB disk storage space. The head node runs cluster management software and is remotely accessible from an operator desktop. All nodes are interconnected with a 2 Gbit/s internal network. The DAQ software uses the free Scientific Linux 6.2 operating system, with the event collector and processing modules developed based on the ROOT [7] data analysis tools. As tested, this system is capable of accepting data at a rate up to 50 MB/s per input stream with an error rate less than 0.06%. The maximum amount of RAW data that can be acquired by the cluster during one image scan is 336 GB (56 GB per worker node). In the output stream, the DAQ system reconstructs and records each proton track (the eight hits in the fiber planes), the rotation angle of the detector, and the energy deposited in the calorimeter stack. For 2×10^9 proton histories the 48 GB data file will be stored for subsequent image reconstruction at the NIU Compute Cluster.

4.1. Test beam results

In the Fall of 2012, the DAQ reconstruction software was used for the data taking control and for the data analysis in tests of the fiber tracker and calorimeter prototypes at LLUMC. After assembling the

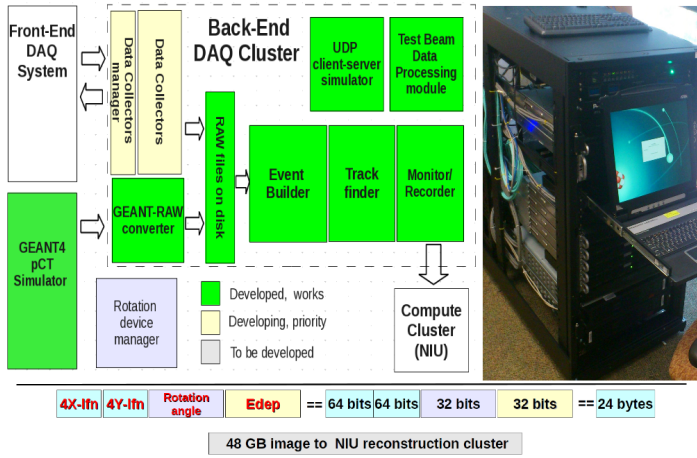

Fig. 3: A diagram of the DAQ software modules, the assembled DAQ cluster, and the bit content of the output event

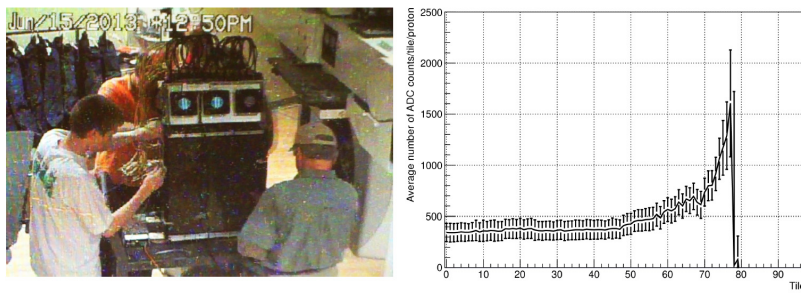

(a) (b)

Fig. 4: a) The assembled calorimeter stack at ProCure Proton center in Warrenville, Illinois; b) the average maximum of the calorimeter stack tile signals (in ADC counts) versus tile number collected from 9000 200 MeV protons

calorimeter this software was again used for analysis of tests conducted at the ProCure Proton center in Warrenville, Illinois. Figure 4 shows the first results of the Bragg peak measurement for a 200 MeV proton beam.

5. The Project Status

The major components of the NIU Phase II pCT scanner (the calorimeter, the fiber tracker and the DAQ system) were assembled by November 2013 and are being commissioned. The complete system will be tested in 2014. The detailed project documentation can be found at [8].

Acknowledgements

We thank the staffs at Fermilab and collaborating institutions, and acknowledge support from the US Department of Defense.

1. Z. Liang *et al. Proton Computed Tomography*, in M.A. Hayat, Ed., Cancer Imaging-Instrumentation and Applications, **2**, 99-120 (2007).
2. H.F.-W. Sadrozinski *et al.*, IEEE NSS-MIC Conference, 4457-4461 (2011).
3. G. Coutrakon *et al.*, Proceedings AccApp 2013, Bruges, Belgium.
4. N. T. Karonis *et al.* J. Parallel Distrib. Comput. (2013). http://dx.doi.org/10.1016/j.jpdc.2013.07.016
5. A. Agostinelli *et al.*, NIM A **506**, 250-303 (2003).
6. CPTA Ltd., www.cpta-apd.ru, Moscow, Russia.
7. R. Brun, F. Rademakers, Proceedings AIHENP96 Workshop, Lausanne, Sep. 1996, Nucl. Inst. Meth. in Phys. Res. A **389**, 81-86 (1997).
8. http://www.niu.edu/nicadd/research/medical.

2. PHENOMENOLOGY AND THEORY

CRITICAL DIMENSIONS OF STRONGLY INTERACTING ANISOTROPIC SYSTEMS

A. Babich

Institute of Electrophysics and Radiation Technologies
NAS of Ukraine
e-mail: avbabich@yahoo.com

Abstract

Investigation of properties of anisotropic systems of arbitrary dimensions is an important problem in modern cosmology and particle physics. The physical properties of these systems strongly depend on the space dimension. The important characteristics of systems are the upper and the lower critical (borderline) dimensions that determine the degree of influence of fluctuations in a vicinity of critical points. We have introduced a model that allows describing phase transitions in systems with the points that combine the properties of multicritical and Lifshitz points. We have calculated the upper and the lower critical dimension for such systems. The properties of systems in spaces of critical dimensions have been investigated.

1. Introduction

One of the effects of the progress of physic during XX century is the revision of the physical space dimension conception. One of the most important steps on this way was an invention of general relativity. The clear "picture" of 3-dimensional Euclidian space and 1-dimensional time changed to 4-dimensional Riemannian space-time. Further progress of physics, especially in such fields as particle physics, quantum gravity and cosmology led to necessity of considering the spaces with different numbers of dimensions.

Other example of changing of the conception of the space dimension one can see in theory of critical phenomena. The progress of

the theory of phase transitions led to essential revision of function of space dimension in thermodynamic. Space dimensionality appears in thermodynamic equations equally with other model parameters [1]. And it should be considered as continuous real value. One of the most important properties of the systems in vicinity of a point of phase transitions (critical point) is a strong increase of fluctuations influence. The influence of the fluctuations strongly depends on spatial dimension. One of the effects of this dependence is an existence of 2 critical (or borderline) dimensions. Lower critical dimension determines the range of the existence of the ordering states: there are no phase transitions with nonzero temperature if the space dimensionality is less than the lower critical dimension (or in other words at the lower critical dimension goldstone bosons start to interact strongly) [3]. The upper critical dimension determines a range of the mean field based theories applicability in describing of critical phenomena.

In the simplest model that allows one to describe the phase transition the lower and upper critical dimensions equal 2 and 4 correspondingly. In more complicated models that allow the Lifshitz (anisotropic systems) or the multicritical (higher order parameters nonlinearities) points the critical dimensions depend on the model parameters.

Initially the basics objects the of phase transition theory application were various condensed matter systems. But different quantum theories with anisotropic space time scaling (i.e. with Lifshitz points) have recently been considered as possible candidates for describing the quantum gravity [2]. In this paper we want to generalize already existing models and find the critical dimensions of such models. In [4] the model that allow one to study critical phenomena in the system with joint multicritical and lifshitz-point-like behavior was introduced. In the vicinity of the critical point Hamiltonian (we use the thermodynamic terminology, but it is easy to modify our results in terms of quantum field theory) of such system can be written as follows:

$$H = \int d^m x_i d^{d-m} x_c \Big\{ \frac{r}{2}\varphi^2 + \frac{\gamma}{2}\left(\Delta_i^{\frac{1}{2}}\varphi\right)^2 + \\ + \frac{\delta}{2}\left(\Delta_c^{\frac{1}{2}}\varphi\right)^2 + \frac{\beta}{2}\left(\Delta_i^{\frac{p}{2}}\varphi\right)^2 + u\varphi^{N+1}\Big\}, \qquad (1)$$

where φ is a one-component order parameter, d is the space dimension and $r, \gamma, \delta, \beta, u$ are the model parameters. We assume that the space can be divided into two subspaces of dimensions m and $d-m$ denoted by i and c respectively. There are wave modulation vectors in the first subspace and none in the second one. Let us assume d and m to be continuous variables and $d > m$. Δ_c and Δ_i are the Laplacian operators available in the corresponding subspaces. In this case the operators Δ^l are defined as $\Delta^l = \Delta\left(\Delta^{l-1}\right)$. For non-integer values of l and m the corresponding operators are determined using the inverse Fourier transformation. At the critical point $r = \gamma = 0$, and the other parameters in (1) are positive quantities.

We want to generalize model (1) in following way. Lets assume that a space with a dimensionality d is divided into k subspaces. Each of them has a dimensionality m_α, $\alpha = 1, ..., k$. An order of the highest derivative in the subspace labeled by α is p_α. The hamiltonian of such model is:

$$\mathcal{H} = \int \left\{ \sum_{i=1}^{k} \left[a_i (\Delta^{\frac{1}{2}} \varphi)^2 + b_i (\Delta^{\frac{p_i}{2}} \varphi)^2 \right] + \right.$$

$$\left. + \alpha\tau\varphi^2 + u\varphi^{N+1} \right\} \prod_{i=1}^{k} d^{m_i} x_i, \qquad (2)$$

Corresponding hamiltonian in the momentum space:

$$H = \frac{1}{2} \int d^d q \nu(q) \eta(q) \eta(-q) +$$

$$+ u \int d^d q_1 \cdot ... \cdot d^d q_{N+1} \delta(q_1 + ... q_{N+1}) (\eta(q_1) ... \eta(q_{N+1})). \qquad (3)$$

Here $\nu(q) = \alpha\tau + \sum_{i=1}^{k} q_i^{2p_i}$, q_i are the absolute value of the wave vector $\overrightarrow{q}$ being in the sector i, and $q_i^2 = \sum_{æ=1}^{m_i} q_j^2$.

2. Critical Dimensions

The lower critical dimension d_l is defined by the following condition: there are no ordering states in a space with $d < d_l$ under condition

of nonzero temperature. From the thermodynamic point of view it means that fluctuation contribution to the entropy is a divergent function of temperature. The fluctuation contribution to entropy looks as follows [5]:

$$S_{fl} = s\tau^{\sigma(d)}, \tag{4}$$

here $\tau = (T - T_c)/T_c$ is the reduced temperature, $\sigma(d)$ is a function of space dimensionality and does not depend on T. We are interested in the critical behavior of S_{fl}, so:

$$\lim_{\tau \to 0} S_{fl} = \begin{cases} 0, & \sigma(d) < 0, \\ \infty, & \sigma(d) > 0. \end{cases} \tag{5}$$

One can see that under condition $T_c \neq 0$ the fluctuation contribution to the entropy is a divergent function if $\sigma(d) > 0$ otherwise it goes to zero. Thus one can find the lower critical dimension from the following condition:

$$\sigma(d_l) = 0. \tag{6}$$

And final expression for d_l:

$$d_l = \sum_{i=1}^{k-1} m_i \left(1 - \frac{1}{p_i}\right) + 2. \tag{7}$$

There are several ways of calculating the upper critical dimension. First is similar to way we calculated d_l: comparing the first fluctuation contribution to entropy with its equilibrium value. Second is to find d_u from the stability condition of the fixed point of corresponding renomgroup transformation. In this paper we are going to calculate d_u from the condition of scale variation invariance of the model (2). We demand the invariance of the hamiltonian under the following scale transformation:$x_i \to \mu_i \cdot x_i; \varphi \to \nu \cdot \varphi$.

All these ways lead to the following expression for upper CD:

$$d_u = 2\frac{N+1}{N-1} + \sum_{i=1}^{k-1} m_i \left(1 - \frac{1}{p_i}\right). \tag{8}$$

Let us find the range of the fluctuation region:

$$\Delta d \equiv d_u - d_l = \frac{4}{N-1}. \tag{9}$$

Easy to find that:

$$\lim_{N\to\infty}(d_u - d_l) = 0. \tag{10}$$

So, the fluctuation region decreases as a function of power of nonlinearity. This fact is physically reasonable. Strong coupling supresses the fluctuations. As it is expected, the lower critical dimension of any systems is not less then 2. The obtained results are correct for classical PTs. As we know, in the theory of quantum PTs the effective dimension of a system in the vicinity of the quantum critical point is higher than a dimension of space. So it is apparent that there are more possible types of PTs in a quantum case. In particular, our results do not contradict a possibility of quantum PTs in 2-dimensional systems.

1. Shang-keng Ma, *Modern Theory of Critical Phenomena* (Perseus Books, U.S., 1976).
2. Petr Horava, Phys. Rev. D **79**, 084008 (2009).
3. A.M. Polyakov, *Gauge Fields and Strings* (Harwood Academic Publishers, Switzerland, 1987).
4. A.V. Babich, S.V. Berezovsky, V.F. Klepikov, Int. J. Mod. Phys. B **22**, 851-857 (2008).
5. A.V. Babich, L.N. Kitcenko, V.F. Klepikov, Mod. Phys. Lett. B **25**, 1839-1845 (2011).

COMMENTS ON BLOW-UPS

Dmitri Bykov[1,2,3]

[1] *Steklov Mathematical Institute of Russ. Acad. Sci., Gubkina str. 8, 119991 Moscow, Russia*
[2] *Nordita, KTH Royal Institute of Technology and Stockholm University, Roslagstullsbacken 23, 106 91 Stockholm, Sweden*
[3] *Max-Planck-Institut für Gravitationsphysik, Albert-Einstein-Institut, Am Mühlenberg 1, D-14476 Potsdam-Golm, Germany*
e-mail: dbykov@mi.ras.ru

Abstract

We review the geometric notion of blow-up and describe some of its applications in the physics of gauge-theoretic and gravitational instantons.

Blow-ups are a ubiquitous phenomenon in geometry. Intuitively speaking, a blow-up is a sphere $\mathbb{CP}^1$ embedded holomorphically 'at a point' of a complex surface X, though the setup is also generalizable to higher dimensional varieties. Blow-ups are perhaps somewhat less known in physics, but we will argue here, using two examples, that there are physical situations where they are indispensable.

For an extended account of some of the topics covered here see [1].

1. What is a Blow-Up?

Consider two-dimensional complex space $\mathbb{C}^2$ with coordinates (z_1, z_2). The blow-up is a replacement of one of the points in $\mathbb{C}^2$, say, the origin $(0,0)$ by a 'sphere' $\mathbb{CP}^1$. This $\mathbb{CP}^1$ encodes the angle at which we approach the point.

Formally speaking, the blown-up manifold $\mathbb{C}^2$, denoted $\widetilde{\mathbb{C}^2}$, may be defined by means of the equation

$$\widetilde{\mathbb{C}^2} = \{z_1 w_2 = z_2 w_1 \subset \mathbb{C}^2 \times \mathbb{CP}^1\}, \tag{1}$$

where $(w_1 : w_2)$ are the homogeneous coordinates on the $\mathbb{CP}^1$. Clearly, there is a projection map $\pi : \widetilde{\mathbb{C}^2} \to \mathbb{C}^2$, which is singular at the point $z_1 = z_2 = 0$ – its Jacobian is zero at this point. However, the manifold $\widetilde{\mathbb{C}^2}$ is nonsingular. It is evident from (1) that the paths in $\mathbb{C}^2$, which approach the origin at distinct angles, end up at distinct points of the $\mathbb{CP}^1$.

At first it may seem like an artificial construction, but the examples below will serve to convince the reader that this is not so.

2. The Deformed ADHM Equations

It has been an observation of [3] that blown-up spacetime $\widetilde{\mathbb{C}^2}$ appears inevitably if one considers a natural deformation of the ADHM equations [2] — the equations that describe the moduli space of instantons (gauge connections with self-dual field strength) on $\mathbb{R}^4$.

The simplest way to describe the moduli space $\mathcal{M}_{n,k}$ of instantons for gauge group $U(n)$ and instanton charge k is to regard it as a hyper-Kähler quotient $\mathbb{C}^{2k(n+k)} /\!/_H U(k)$. We will view $\mathbb{C}^{2k(n+k)}$ as a collection of two $k \times k$ matrices B_0, B_1 and two matrices I, J of sizes $k \times n$ and $n \times k$, respectively. Then the action of $U(k)$ on these matrices can be described as follows:

$$B_{0,1} \to g B_{0,1} g^\dagger, \quad I \to gI, \quad J \to Jg^\dagger, \quad \text{where} \quad g \in U(k). \tag{2}$$

Upon defining the moment maps for the $U(k)$ action, $\mu_\mathbb{R}$ and $\mu_\mathbb{C}$, one can write down the ADHM [2] equations:

$$\text{ADHM}: \qquad \mu_\mathbb{R} = \mu_\mathbb{C} = 0. \tag{3}$$

From a mathematical standpoint, they are not completely natural. Indeed, nothing prohibits a 'central' term in the r.h.s.: $\mu_\mathbb{R} = \xi_1 \mathbb{1}_k$, $\mu_\mathbb{C} = (\xi_2 + i\xi_3)\,\mathbb{1}_k$, and, therefore, generically it is natural to include it. For $\xi \neq 0$ these equations, however, no longer describe the moduli space of instantons on $\mathbb{R}^4$ (the curvature is no longer self-dual). One possible physical interpretation of the deformed equations, due to [3], is that they decribe instantons on a new manifold $Y \neq \mathbb{R}^4$.

For $\xi \neq 0$ the problem turns out to be nontrivial even for abelian $U(1)$ instantons. In the case $n = k = 1$ one can build, however, the gauge potential explicitly and check that the corresponding field strength is self-dual on a manifold $\widetilde{\mathbb{C}^2}$ described by (1), with the metric simply being the metric induced by the embedding (1) in $\mathbb{C}^2 \times \mathbb{CP}^1$. The physical reason for the appearance of the blow-up is that the $U(1)$ instanton carries not just the instanton charge, but also a monopole charge, whose magnetic flux 'inflates' the sphere $\mathbb{CP}^1$ around itself.

For what follows we document that the Kähler potential of the induced metric is

$$K = \log x + x, \tag{4}$$

where

$$x := |z_1|^2 + |z_2|^2 \tag{5}$$

is a $U(2)$-invariant combination that we will encounter frequently.

3. Effective Actions, ADE Singularities and ALE Spaces

Another physics realm where the blow-up appears naturally is in the framework of effective supersymmetric field theories on D-branes placed at singularities of Calabi-Yau manifolds. In this section we describe $\mathcal{N} = (1,0)$ supersymmetric theories in 6D, which arise as effective theories for the fluctuations of six-simensional D-branes located at ADE-singularities of a transverse $K3$-surface (Calabi-Yau space) [4]. The so-called Higgs branch of such theories naturally leads to manifolds (the so-called 'gravitational instantons') which include copies of $\mathbb{CP}^1$ glued in with normal bundle $\mathcal{O}(-2)$.

In six dimensions the gauge field strength superfield $(W_a)_A$ is of opposite chirality to the supercharge and may be expanded in elementary fields as follows, up to linear order in the Grassmann coordinates $(\theta_a)_A$[1]:

$$W^a_A = \lambda^a_A + F^{ab}\theta^b_A + (D_i\sigma_i)_{AB}C^{ab}\theta^b_B + \dots, \tag{6}$$

and the matrix of fields F^{ab} is 'traceless': $C_{ab}F^{ab} = 0$ (C is a non-degenerate charge conjugation matrix). The reality property for the

[1]Here $a = 1,2,3,4$ is the $SU(4)$ index, $A = 1,2$ is the $SU(2)$ R-symmetry index.

symplectic-Majorana spinor W_A^a translates into the reality properties of the component fields. In particular, λ_A^a is a symplectic-Majorana spinor as well, $(F_{ab})^*$ is linearly related to F_{ab}, hence it has only 15 real components, which can be packed into a skew-symmetric real-valued tensor $F_{\mu\nu}$, and D_i are a triplet of real auxiliary fields.

It is precisely the appearance of this triplet, in place of a singlet D, that is important for us here. Assuming that the theory includes M hypermultiplets with scalar components ${}_m\phi_A^a$, where a is an $U(N)$ gauge index and m labels the hypermultiplet ($m = 1 \dots M$), let us now write out the part of the supersymmetric Lagrangian, where the D_i fields enter:

$$\mathfrak{L} \sim \frac{1}{2} D_i^2 + D_i \big[\sum_{m=1}^{M} ({}_m\phi_A^a)^* (\sigma_i)_{AB}\ {}_m\phi_B^a + \zeta_i \big], \tag{7}$$

where ζ_i is a triplet of Fayet-Iliopoulos terms. The fields D_i are auxiliary, in the sense that they have no kinetic terms, so they can be integrated out of (7) to produce

$$\mathfrak{L} \sim \frac{1}{2} \big[\sum_{m=1}^{M} ({}_m\phi_A^a)^* (\sigma_i)_{AB}\ {}_m\phi_B^a + \zeta_i \big]^2. \tag{8}$$

The locus of points in field space where this function reaches a (zero) minimum is given by the hyper-Kähler moment map equations $\mu_i = 0$, $i = 1, 2, 3$. Since field configurations related by gauge transformations are equivalent, we need to take the quotient with respect to the gauge group $U(N)$, hence the space of physical field configurations saturating the minimum of the potential is the hyper-Kähler quotient $\{\ \mu_i^{-1}(0),\ i = 1, 2, 3\ \}/U(N)$. These hyper-Kähler quotients are Ricci-flat asymptotically locally Euclidean (ALE) spaces, which have 'blown-up' spheres embedded in them.

The physical interpretation of the situation elaborated in this section is quite remarkable: the smooth ALE metrics provided by the hyper-Kähler quotients are in fact metrics on the resolutions of the ADE-singularities at which we place our D-branes!

The Eguchi-Hanson space is a special case when $N = 1, M = 2$. It is described by a Kähler potential that, in principle, is known explicitly, but for us the only important thing will be its expansion around the origin:

$$K = \log x + x^2 + \dots, \qquad \text{as} \quad x \to 0. \tag{9}$$

The important difference between (4) and (9) is the x vs. x^2 terms in the expansions of the Kähler potentials. Our point is that they are different because the $\mathbb{CP}^1$'s in the two cases are embedded with different normal bundles: $\mathcal{O}(-1)$ and $\mathcal{O}(-2)$, respectively.

4. Einstein Metrics on Blown-Up Spaces

A natural question, which arises from the above analysis, is what happens in the case of a sphere $\mathbb{CP}^1$ embedded with a normal bundle $\mathcal{O}(-m)$ for higher m, i.e. $m \geq 3$. From the adjunction formula it follows that this can only happen for a $\mathbb{CP}^1$ in a surface Y of 'negative curvature', i.e. $c_1(Y) < 0$, — this is in contrast to the $\mathcal{O}(-1)$ case (in a surface of 'positive curvature') and the $\mathcal{O}(-2)$ case (Calabi-Yau).

It is interesting to note that in the negative-curvature case it is possible to build Kähler-Einstein metrics on the total spaces of the $\mathcal{O}(-m)$, $m \geq 3$ line bundles over $\mathbb{CP}^1$. Indeed, we look for the metrics $g_{i\bar{j}}$ satisfying

$$R_{i\bar{j}} = -g_{i\bar{j}}. \tag{10}$$

The metric is assumed to be $U(2)$-invariant and originating from a Kähler potential: $g_{i\bar{j}} = \frac{\partial^2 K}{\partial z^i \partial \bar{z}^j}$ with $K = K(x)$. For such an ansatz the equation (10) with the boundary condition (chosen by analogy with (4) and (9))

$$K(x) = \log x + a\, x^m + \ldots \qquad \text{as} \quad x \to 0 \tag{11}$$

may be solved explicitly. Introducing a new function $Q := xK'$, we can write the solution as follows:

$$Y_m : \quad \begin{cases} m > 3 : & x = \prod_{i=1}^{3} (Q - y_i)^{\frac{1}{2+y_i}}, \\ & \text{where } \; y_i^3 + 3y_i^2 - (m-2)^2(m+1) = 0 \\ m = 3 : & x = e^{-\frac{2}{Q+2}} \left(\frac{Q-1}{Q+2}\right)^{1/3}. \end{cases}$$

The interesting fact is that, for $m \geq 3$, the Kähler potential tends to infinity as $|z_1|^2 + |z_2|^2 \to 1$. Moreover, asymptotically near $|z_1|^2 + |z_2|^2 \simeq 1$ the metric behaves as the Lobachevsky space H_4 metric near the boundary. However, the requirement that the topological characteristics of this space — the Euler characteristic and signature —

are integers, implies[2] that the boundary cannot be $S^3 = \partial \mathrm{H}_4$, but it rather has to be a quotient thereof, more precisely the lens space $L(m,1) = S^3/\mathbb{Z}_m$. Requiring that the boundary is the appropriate lens space, we find that Y_m has the topological numbers of a line bundle over $\mathbb{CP}^1$.

To summarize, we have described the neighborhood of a sphere $\mathbb{CP}^1$ embedded with an arbitrary negative normal bundle $\mathcal{O}(-m)$, $m > 0$. The $m = 1$ case corresponds to the classical 'blow-up' (1).

Acknowledgements

I am grateful to I.Ya. Aref'eva, P. Di Vecchia, S. Gorchinskiy, V. Przhiyalkovskiy, K. Zarembo for discussions and to N.A.Nekrasov for bringing to my attention the reference [3]. I am indebted to Prof. A.A. Slavnov and to my parents for constant support and encouragement. I would also like to thank L. Jenkovszky for the invitation to participate in the conference "New Trends in High Energy Physics" in the Crimea. My work was supported in part by grants RFBR 11-01-00296-a, 13-01-12405 ofi-m2, 12-01-31298-mol-a and the grant for the Support of Leading Scientific Schools of Russia NSh-4612.2012.1.

1. D. Bykov, *The Kähler metric of a blow-up*, arXiv:1307.2816
2. M.F. Atiyah, N.J. Hitchin, V.G. Drinfeld and Y.I. Manin, *Construction of Instantons*, Phys. Lett. A **65**, 185 (1978).
3. H.W. Braden and N.A. Nekrasov, *Space-time foam from noncommutative instantons*, Commun. Math. Phys. **249**, 431 (2004).
4. M.R. Douglas and G.W. Moore, *D-branes, quivers, and ALE instantons*, hep-th/9603167.

[2]For more details, including the calculation of the topological characteristics of the above manifolds Y_m using Chern-Weil formulas, see our paper [1].

ISOTROPIZATION OF THE QUARK GLUON PLASMA

T. Epelbaum, F. Gelis

Institut de Physique Theorique (URA 2306 du CNRS)
CEA/DSM/Saclay 91191, Gif-sur-Yvette Cedex, France

Abstract

We report here recent analytical and numerical improvements made on the theoretical treatment of the early stages of heavy ion collisions, that amounts to solve classically the Yang-Mills equations with the inclusion of quantum corrections via the initial field configurations. We show that, in contrast with the purely Leading Order (LO) result, our simulation tends toward the fast isotropization of the pressure tensor of the system. This trend appears for already small values of the coupling constant α_s. In addition, the system exhibits an anomalously small shear viscosity.

1. Introduction

The heavy ion collisions performed at the Large Hadron Collider (LHC) and the Relativistic Heavy Ion Collider (RHIC) are among the most impressive experimental achievements ever performed in physics. In those two rings, heavy ions (led, gold...) are smashed on one another at a speed that almost reaches the one of light. The analysis carried on the product of these collisions can hopefully clarify some inflation scenarios, but they are of greater interest for understanding Quantum Chromodynamics (QCD) at very high energies.

During the past ten years or so, the RHIC and the LHC have more of less established a striking feature of the collision products. These latter – referred as the Quark Gluon Plasma, or QGP – seem to behave like a nearly perfect fluid, and do so after a very short transient time: less than 1 fm/c [1]. This is assumed to be the case because relativistic hydrodynamics with very small value of the shear viscosity can successfully describe the experimental data [2].

In the meantime, theoretical models based on QCD have so far failed to predict such an early onset of hydrodynamical behavior. The one that we will come to use – the Color Glass Condensate (CGC) effective theory [3] – even predict at its Leading Order (LO) a negative longitudinal pressure P_L of the system at the initial time, with a value opposite to the energy density ϵ and the transverse pressure P_T [4]. By contrast, hydrodynamics has among its postulates a small anisotropy of the system. This apparent paradox between theory and experiment has yet to receive a satisfying answer.

Improvement of the CGC are therefore needed. One can try for instance to take into account its next to leading order (NLO), but the results are even worse [5]: because of the presence of Weibel instabilities in the theory [6], the pressures of the system increase exponentially and diverge as time goes to infinity. A big step forward was achieved in [7] where it was shown that one can resumm all the fastest growing terms at each order of the perturbative expansion by just evolving classically an initial condition formed by the superposition of the LO and the NLO, this latter being weighted by random gaussian numbers and computed thanks to a 1-loop calculation. The classical evolution with this fluctuating initial condition can be performed numerically with the help of a Monte-Carlo (MC) method, and is referred to as the classical statistical method. As a proof of concept, this theory was successfully tested for scalar models in [8–10]. The only theoretical ingredient missing up to now in the CGC framework was the correct NLO spectrum.

In this proceeding, we present the spectrum correctly derived in [11] for the first time, and use it as an input of the classical statistical method in order to compute the time evolution of the energy-momentum tensor $T^{\mu\nu}$, to see whether or not the system isotropizes [12]. In section 2 we will detail the initial condition used, while the section 3 is devoted to the numerical results.

2. Initial Conditions in the CGC Model

2.1. LO

In all the following, we will take the usual Fock–Scwhinger gauge choice $A^\tau = 0$. a, b, c stand for color indices, while i, j, k denote

transverse spatial indices. Let's recall the central result of [13] that gives in the CGC framework and in the (τ, η, x, y) coordinate system the gauge fields at LO just above the light cone ($\tau = 0^+$)

$$\mathcal{A}^{ia}(\boldsymbol{x}_\perp) = \alpha_1^{ia}(\boldsymbol{x}_\perp) + \alpha_2^{ia}(\boldsymbol{x}_\perp),$$

$$\mathcal{A}^{\eta a}(\boldsymbol{x}_\perp) = \frac{ig}{2}\alpha_1^{iab}(\boldsymbol{x}_\perp)\alpha_2^{ib}(\boldsymbol{x}_\perp),$$

where the fields $\alpha^a_{\lambda=1,2}$ that a priori depend on $(x^\pm, \boldsymbol{x}_\perp)$ are pure gauges formed by the Wilson lines $\mathcal{U}_\lambda$

$$\alpha_\lambda^{iab}(\boldsymbol{x}_\perp) = \frac{i}{g}\mathcal{U}_\lambda^{ac\dagger}(\boldsymbol{x}_\perp)\partial^i\mathcal{U}_\lambda^{cb}(\boldsymbol{x}_\perp),$$

$$\mathcal{U}_\lambda(\boldsymbol{x}_\perp) = \exp\left(-ig\frac{1}{\nabla_\perp^2}\rho_\lambda(\boldsymbol{x}_\perp)\right), \tag{1}$$

Q_s being the saturation scale, and the $\rho \sim \frac{Q^2}{g}$ being random color sources described by a probability distribution function[1].

2.2. NLO

Taking small fluctuations as plane waves in the remote past with quantum indices $(\boldsymbol{k}_\perp, \nu)$, polarization λ and color c: $a^{\mu a}_{\boldsymbol{k}_\perp\nu\lambda c} = \delta^a_c\epsilon^\mu_{\boldsymbol{k}\lambda}e^{ikx}$ with the polarization vector $\epsilon^\mu_{\boldsymbol{k}\lambda}$ satisfying $k_\mu\epsilon^\mu_{\boldsymbol{k}\lambda} = 0$ and $\epsilon^i_{\boldsymbol{k}\lambda}\epsilon^i_{\boldsymbol{k}\lambda'} = \delta_{\lambda\lambda'}$, the recent result obtained in [11] give these small fluctuations at $\tau = 0^+$, after they have propagated on top of the two nuclei.

$$a^{ia}_{\boldsymbol{k}_\perp\nu\lambda c} = F^{+,ia}_{\boldsymbol{k}_\perp\nu\lambda c} + F^{-,ia}_{\boldsymbol{k}_\perp\nu\lambda c}\,, \quad a^{\eta a}_{\boldsymbol{k}_\perp\nu\lambda c} = \mathcal{D}^{iab}\left(\frac{F^{+,ib}_{\boldsymbol{k}_\perp\nu\lambda c}}{2+i\nu} - \frac{F^{-,ib}_{\boldsymbol{k}_\perp\nu\lambda c}}{2-i\nu}\right). \tag{2}$$

with

$$F^{\pm,ia}_{\boldsymbol{k}_\perp\nu\lambda c}(\tau,\eta,\boldsymbol{x}_\perp) = \Gamma(\mp i\nu)\,e^{\pm\frac{\nu\pi}{2}}e^{i\nu\eta}\,\mathcal{U}^{ab\dagger}_{1,2}(\boldsymbol{x}_\perp)\left[\delta^{jk} - \frac{2k^j_\perp k^k_\perp}{k^2_\perp}\right]\epsilon^k_{\boldsymbol{k}\lambda}\times$$

$$\times\int\frac{\mathrm{d}^2\boldsymbol{p}_\perp}{(2\pi)^2}\,e^{i\boldsymbol{p}_\perp\cdot\boldsymbol{x}_\perp}\,\widetilde{\mathcal{U}}^{bc}_{2,1}(\boldsymbol{p}_\perp+\boldsymbol{k}_\perp)\left(\frac{p^2_\perp\tau}{2k_\perp}\right)^{\pm i\nu}\left[\delta^{ij} - \frac{2p^i_\perp p^j_\perp}{p^2_\perp}\right]. \tag{3}$$

[1] This latter depends on the energy scale through the JIMWLK equation [14]. The correct implementation of the energy dependence via the JIMWLK equation is beyond the scope of this paper, and is therefore left for a further study.

Those formulas take into account the whole evolution of the fluctuations through the past light cone, and give the correct NLO spectrum at positive but small proper time $\tau = 0^+$.

2.3. Resummation

In classical Yang-Mills (YM) simulations, it was advocated in [5] that secular divergences can plague the numerical results if one adds rapidity dependent fluctuations on top of (1). One way to circumvent this problem was found in [7], where the authors defined a resummed energy-momentum tensor as

$$T^{\mu\nu}_{\text{resum}} = \int \big[\mathcal{D}a\big]\, F_0\big[a\big]\; T^{\mu\nu}_{\text{LO}}[\mathcal{A}+a](x), \tag{4}$$

with $F_0\big[a\big]$ being a Gaussian distribution of variance dictated by the spectrum of fluctuations (2). This $T^{\mu\nu}_{\text{resum}}$ takes fully into account the first order of quantum corrections, and a subset of every higher order corrections. When applied to scalar models [8–10], this formula was able to account for all the macroscopic manifestations of a possible thermalization of the system: the formation of an equation of state, and an isotropization of the pressures. We will therefore apply (4) to the YM case.

3. Numerical Results

3.1. Numerical implementation

It was shown in [7] that evaluating numerically (4) amounts to do a Monte-Carlo sampling of the initial condition formed by the sum of the classical background field (1) and the NLO spectrum (2) weighted by random gaussian coefficients

$$A^{\mu a} = \mathcal{A}^{\mu a} + \sqrt{\frac{1}{2\pi V}}\text{Re}\int_{\boldsymbol{k}_\perp \nu} \sum_{\lambda c} a^{\mu a}_{\nu \boldsymbol{k}_\perp \lambda c} c^{c\lambda}_{\nu \boldsymbol{k}_\perp}, \tag{5}$$

V being the lattice volume and $c^c_{\nu \boldsymbol{k}_\perp \lambda}$ being random complex gaussian numbers of variance one

$$\left\langle c^{c\lambda}_{\nu \boldsymbol{k}_\perp} c^{d\lambda' *}_{\nu' \boldsymbol{k}'_\perp} \right\rangle = \delta_{\nu\nu'}\delta_{\boldsymbol{k}_\perp \boldsymbol{k}'_\perp}\delta^{\lambda\lambda'}\delta^{cd}. \tag{6}$$

One then just perform the time evolution of (5) through the classical Yang-Mills equations used in Hamiltonian formulation

$$\mathcal{E}^{\mu a} = -\tau g^{\mu\nu}\partial_\tau \mathcal{A}_{\nu a}, \qquad \partial_\tau \mathcal{E}^{\mu a} = \tau\, g^{\mu\nu}\mathcal{D}^{\rho ab}\mathcal{F}^b_{\rho\nu}, \tag{7}$$

with the GAUSS's law constraint $\mathcal{D}^{ab}_\mu \mathcal{E}^\mu_b = 0$. In the process, one has to exchange the use of the A with link variables $U_\mu = e^{-iga_\mu A_\mu}$ in order to exactly preserve gauge invariance on the lattice. The a_μ are the lattice spacings in the μ direction.

4. Numerical Results

In figure 1 we summarize what is performed numerically.

What we compute at positive times is the ratio $P_{T,L}/\epsilon$, the different components of $T^{\mu\nu}_{\text{resum}}$ being averaged over the lattice volume and the MC method. Here is what we find numerically for $g = 0.1$ and $g = 0.5$.

What we see is that for $g = 0.1$, the resummed result extracted from (4) is very close from the pure LO simulation. This suggests that the instabilities have not yet played their role at very early times for such a small value of the coupling. By contrast, $g = 0.5$ sees an important qualitative change: the longitudinal pressure increases

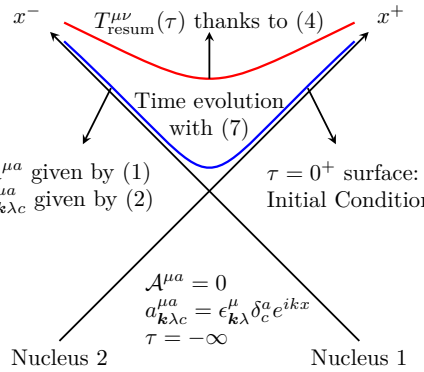

Fig. 1: Schematic picture in light cone coordinate system of a heavy ion collision. We perform a classical statistical Yang-Mill simulation with the correct initial condition on the blue surface $\tau = 0^+$ in order to obtain $T^{\mu\nu}_{\text{resum}}$ at later times

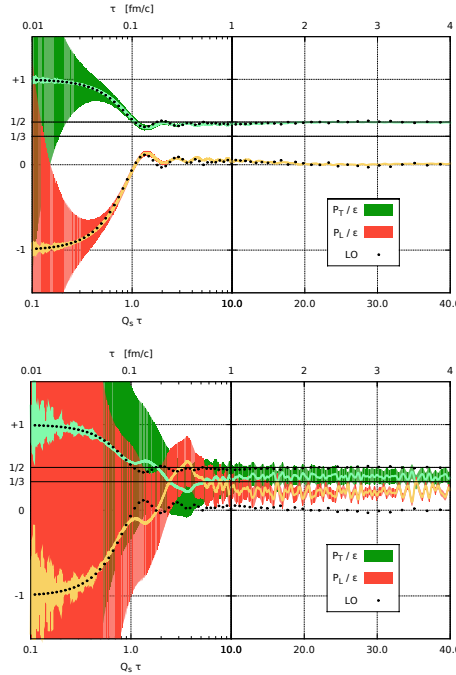

Fig. 2: $P_{T,L}/\epsilon(\tau)$ for $g = 0.1$ ($\alpha_s = 8 \times 10^{-4}$, upper plot) and $g = 0.5$ ($\alpha_s = 2 \times 10^{-2}$, lower plot). The bands indicate statistical errors. The dotted curves represent the LO result

rapidly and the system experiences a fixed anisotropy (of the order of 40%) after a very short transient time of the order of 1 fm/c. This is compatible with the very early onset of viscous hydrodynamics that was so far postulated, and observed here for the first time in a weak coupling QCD framework. In addition, a very small value of the dimensionless ratio $\eta\epsilon^{-3/4} \sim 1$ –almost compatible with the values used in viscous hydrodynamical simulations– can be obtained for $g = 0.5$, by fitting the energy density with the help of a first order viscous hydrodynamical model $\epsilon = \epsilon_0\tau^{-4/3} - 2\eta\tau^{-1}$. This has to be compared with the LO value of 300. The conclusion is therefore that one does not need strong coupling techniques nor to obtain small value of the dimensionless shear viscosity neither to observe a fast isotropization of the QGP.

Acknowledgement

This work is supported by the Agence Nationale de la Recherche project 11-BS04-015-01. Some of the computations were performed with the resources provided by GENCI-CCRT (project t2013056929).

1. P. Romatschke, Int. J. Mod. Phys. E **19**, 1 (2010).
2. M. Luzum, P. Romatschke, Phys. Rev. C **78**, 034915 (2008).
3. F. Gelis, E. Iancu, J. Jalilian-Marian, R. Venugopalan, Ann. Rev. Part. Nucl. Sci. **60**, 463 (2010).
4. T. Lappi, L.D. McLerran, Nucl. Phys. A **772**, 200 (2006).
5. P. Romatschke, R. Venugopalan, Phys. Rev. Lett. **96**, 062302 (2006); P. Romatschke, R. Venugopalan, Phys. Rev. D **74**, 045011 (2006).
6. S.Mrowczynski, Phys. Lett. B **314**, 118 (1993).
7. F. Gelis, T. Lappi, R. Venugopalan, Phys. Rev. D **78**, 054019 (2008).
8. K. Dusling, T. Epelbaum, F. Gelis, R. Venugopalan, Nucl. Phys. A **850**, 69 (2011).
9. T. Epelbaum, F. Gelis, Nucl. Phys. A **872**, 210 (2011).
10. K. Dusling, T. Epelbaum, F. Gelis, R. Venugopalan, Phys. Rev. D **86**, 085040 (2012).
11. T. Epelbaum, F. Gelis, Phys. Rev. D **88**, 085015 (2013).
12. T. Epelbaum, F. Gelis, arXiv:1307.2214.
13. A. Kovner, L.D. McLerran, H. Weigert, Phys. Rev. D **49**, 3352 (1994).
14. E. Iancu, A. Leonidov, L.D. McLerran, hep-ph/0202270; E. Iancu, R. Venugopalan, hep-ph/0303204; F. Gelis, E. Iancu, J. Jalilian-Marian, R. Venugopalan, Ann. Rev. Part. Nucl. Sci. **60**, 463 (2010).

IMPACT FACTORS FOR REGGEON-GLUON TRANSITION IN $N = 4$ SYM[†]

V.S. Fadin

Budker Institute of Nuclear Physics of SD RAS,
630090 Novosibirsk Russia
and Novosibirsk State University,
630090 Novosibirsk, Russia

Abstract

I present results of calculations of the impact factors for reggeon-gluon transition in the maximally extended supersymmetric Yang-Mills theory ($N = 4$ SYM) with large number of colours. These impact factors are indispensable constituents in the proof of the multi-Regge form of amplitudes with gluon exchanges and in calculation of the remainder function to the Bern–Dixon–Smirnov (BDS) ansatz for scattering amplitudes with maximal helicity violation (MHV).

1. Introduction

Impact factors for reggeon-gluon transition play an important role in the BFKL (Balitsky–Fadin–Kuraev–Lipatov) approach [1]. This approach is based on the remarkable property of non-Abelian gauge theories – reggeization of gauge bosons. The idea of reggeization appeared as the result of the fixed order calculations. Evidently it must be proved. It can be done, both in the leading logarithmic aproximation(LLA) [2] in and in next-to-leading one (NLA) [3] in

[†]Work supported in part by the Ministry of Education and Science of Russian Federation and in part by RFBR, grant 13-02-01023.

all orders of perturbation theory, using bootstrap relations, which follow from requirement of compatibility of the multi-Regge form of scattering amplitudes with s-channel unitarity. It was proved [3] that fulfillment of an infinite set of these relations guarantees the multi-Regge form of scattering amplitudes and that all bootstrap relations are fulfilled if several conditions imposed on the Reggeon vertices and the trajectory (bootstrap conditions) hold true. The most complicated condition, which includes the impact factors for reggeon-gluon transition, was proved recently, both in QCD [4, 6] and in its supersymmetric generalisations [7].

In $N = 4$ SYM there is an additional interest to the impact factors. Recently, the BFKL approach was extensively used for verification of the BDS ansatz [8] for multi-particle MHV amplitudes and for calculation of the remainder factor to this ansatz [9]. It was demonstrated that in so called Mandelstam kinematical region the BDS amplitude $M_{2\to 4}^{BDS}$ should be multiplied by the factor containing contribution of the Mandelstam cut, and this contribution was found in the LLA and in the NLA [10].

In the NLA this contribution was found assuming existence of conformal invariant (in momentum space) representations of the BFKL kernel and the impact factors. Herewith, the convolution of the impact factors calculated with some conjecture was used instead of the impact factors themselves. Later it was shown [11] that indeed the BFKL kernel has the conformal invariant representation. But for conformal invariance of the remainder factor, which is generally supposed (but not strictly proved) the impact factors for reggeon-gluon transition also must have such representation. It makes direct calculation of the impact factors and investigation of their properties very important.

2. Calculation of the Impact Factor

We start from the result obtained in [3–7]. Note however that we use here the planar approximation and don't perform signaturization, therefore only s-channel parts of the impact factors considered in above-mentioned papers are retained. In the Born approximation, the impact factor for transition of a reggeon R with transverse

(to the plane of initial momenta p_A, p_B) momentum $\vec{q}_1$ into a gluon with transverse momentum $\vec{k}$ and positive helicity in interaction with reggeized gluons $\mathcal{G}_1$ and $\mathcal{G}_2$ is written as

$$\langle GR_1|\mathcal{G}_1\mathcal{G}_2\rangle^{(B)} = -\sqrt{2}\, g^2 \delta(\vec{q}_1 - \vec{k} - \vec{r}_1 - \vec{r}_2) \left(T^a T^b\right)_{c_1 c_2} \frac{q_1^- r_1^+}{(q_1^+ - r_1^+)}, \tag{1}$$

where g is the coupling constant, T^i are the colour group generators, $\vec{r}_1$, $\vec{r}_2$ and c_1, c_2 are transverse momenta and colour indices of the reggeized gluons $\mathcal{G}_1$ and $\mathcal{G}_2$ correspondingly, a and b are colours of the reggeon R and the gluon G, and we use "helical" vector components $\pm$ instead of the Cartesian ones x, y; $a^{\pm} = a_x \pm i a_y$.

One-loop correction to (1) containing gluon, fermion and scalar contributions, which were found in Refs. [6], [4] and [7] correspondingly. For $N = 4$ SYM in the planar approximation, when only Born colour structure remains, total correction can be written as the Born term (1) multiplied by the factor

$$\begin{aligned}
\Phi^{\mathcal{G}\mathcal{G}_2}_{GR_1*} = \frac{\bar{g}^2}{2} \Bigg\{ & \frac{q_2^+(q_1^+ - r_1^+)}{k^+ r_1^+} \left(\ln\left(\frac{\vec{k}^{\,2}}{\vec{r}_2^{\,2}}\right) \ln\left(\frac{(\vec{q}_1 - \vec{r}_1)^2}{\vec{r}_2^{\,2}}\right) + \right. \\
& + \ln\left(\frac{\vec{q}_2^{\,2}}{\vec{q}_1^{\,2}}\right) \ln\left(\frac{\vec{k}^{\,2}}{\vec{q}_2^{\,2}}\right) \Bigg) + \ln\left(\frac{(\vec{q}_1 - \vec{r}_1)^2}{\vec{k}^{\,2}}\right) \ln\left(\frac{\vec{r}_2^{\,2}}{\vec{k}^{\,2}}\right) + \\
& + \ln\left(\frac{(\vec{q}_1 - \vec{r}_1)^2 \vec{q}_1^{\,2}}{\vec{k}^{\,4}}\right) \ln\left(\frac{\vec{r}_1^{\,2}}{\vec{q}_1^{\,2}}\right) - 4\frac{(\vec{k}^{\,2})^{\epsilon}}{\epsilon^2} + 6\zeta(2) + \\
& + \frac{q_2^+(q_1^+ - r_1^+)}{k^+ r_1^+} \Big(\big[k, r_2\big] I_{\vec{k}, \vec{r}_2} + \big[q_1, k\big] I_{\vec{q}_1, -\vec{k}} \Big) - \\
& - \big[k, r_2\big] I_{\vec{k}, \vec{r}_2} + \big[q_1, r_1\big] I_{\vec{q}_1, -\vec{r}_1} \Bigg\},
\end{aligned} \tag{2}$$

where $\bar{g}^2 = g^2 \Gamma(1-\epsilon)/(4\pi)^{2+\epsilon}$, $\Gamma(x)$ is the Euler gamma-function, $\zeta(n)$ is the Riman zeta-function ($\zeta(2) = \pi^2/6$), $\big[a, b\big] = a^- b^+ - a^+ b^-$,

$$I_{\vec{p}, \vec{q}} = \int\limits_0^1 \frac{dx}{(\vec{p} + x\vec{q})^2} \ln\left(\frac{\vec{p}^{\,2}}{x^2 \vec{q}^{\,2}}\right) \ , \quad I_{\vec{p}, \vec{q}} = I_{-\vec{p}, -\vec{q}} = I_{\vec{q}, \vec{p}} = I_{\vec{p}, -\vec{p} - \vec{q}}. \tag{3}$$

Here one has to call to mind that NLO impact factors are not unically defined, and to recognize that (2) is not the correction which we need. Moreover, the impact factor calculated in [4]– [7] is not the impact factor defined in [3] (we call it standard). The former was adjusted for simplification of verification of the bootstrap condition and is related with the latter by the transformation $\langle GR_1|_* = \langle GR_1|_{(s)} - \langle GR_1|^{(B)}\widehat{\mathcal{U}}_k$, with the operator $\widehat{\mathcal{U}}_k$ defined by the matrix elements

$$\langle \mathcal{G}_1'\mathcal{G}_2'|\widehat{\mathcal{U}}_k|\mathcal{G}_1\mathcal{G}_2\rangle = \frac{1}{2}\ln\Big(\frac{\vec{k}^{\,2}}{(\vec{r}_1-\vec{r}_1')^2}\Big)\langle \mathcal{G}_1'\mathcal{G}_2'|\widehat{\mathcal{K}}_r^B|\mathcal{G}_1\mathcal{G}_2\rangle, \qquad (4)$$

where $\widehat{\mathcal{K}}_r^B$ is the LO BFKL kernel related with real gluon production. Using the matrix elements

$$\begin{aligned}\langle GR_1|^{(B)}\widehat{\mathcal{U}}_k|\mathcal{G}_1\mathcal{G}_2\rangle = \langle GR_1|\mathcal{G}_1\mathcal{G}_2\rangle^{(B)}\,\frac{\bar{g}^2}{4}\Bigg\{-\frac{q_2^+(q_1^+-r_1^+)}{k^+r_1^+}\Bigg[\ln\left(\frac{\vec{q}_2^{\,2}}{\vec{r}_2^{\,2}}\right)\times\\ \times\ln\left(\frac{\vec{k}^{\,4}}{\vec{r}_1^{\,2}\vec{r}_2^{\,2}}\right)+\ln\left(\frac{(\vec{q}_1-\vec{r}_1)^2}{\vec{q}_1^{\,2}}\right)\ln\left(\frac{\vec{k}^{\,4}}{\vec{r}_1^{\,2}(\vec{q}_1-\vec{r}_1)^2}\right)\Bigg]+\\ +\ln\left(\frac{\vec{r}_2^{\,2}}{\vec{k}^{\,2}}\right)\ln\left(\frac{\vec{k}^{\,4}}{(\vec{q}_1-\vec{r}_1)^2\vec{r}_2^{\,2}}\right)+\ln\left(\frac{\vec{r}_1^{\,2}}{\vec{k}^{\,2}}\right)\ln\left(\frac{\vec{k}^{\,2}\vec{q}_1^{\,2}}{(\vec{q}_1-\vec{r}_1)^2\vec{r}_1^{\,2}}\right)-\\ -\ln\left(\frac{\vec{k}^{\,2}}{(\vec{q}_1-\vec{r}_1)^2}\right)\ln\left(\frac{\vec{k}^{\,2}\vec{q}_1^{\,2}}{(\vec{q}_1-\vec{r}_1)^4}\right)+4\frac{(\vec{k}^{\,2})^\epsilon}{\epsilon^2}-4\zeta(2)+\\ +\frac{q_2^+(q_1^+-r_1^+)}{k^+r_1^+}\Big(\big[r_1,r_2\big]I_{\vec{r}_1,\vec{r}_2}+\big[q_1,r_1\big]\big]I_{\vec{q}_1,-\vec{r}_1}\Big)+\\ +\big[k,r_2]I_{\vec{k},\vec{r}_2}-\big[q_1,r_1\big]\big]I_{\vec{q}_1,-\vec{r}_1}\Bigg\}, \qquad (5)\end{aligned}$$

we obtain for the one-loop correction to the standard impact factor

$$\begin{aligned}\Phi_{GR_1(s)}^{\mathcal{G}_1\mathcal{G}_2}=\frac{\bar{g}^2}{4}\Bigg\{\frac{q_2^+(q_1^+-r_1^+)}{k^+r_1^+}\Bigg[\ln\left(\frac{\vec{q}_2^{\,2}}{\vec{q}_1^{\,2}}\right)\ln\left(\frac{\vec{r}_1^{\,2}\vec{r}_2^{\,2}}{\vec{q}_2^{\,4}}\right)+\\ +\ln\left(\frac{\vec{r}_2^{\,2}}{(\vec{q}_1-\vec{r}_1)^2}\right)\ln\left(\frac{\vec{r}_2^{\,2}\vec{q}_1^{\,2}}{\vec{r}_1^{\,2}(\vec{q}_1-\vec{r}_1)^2}\right)\Bigg]+\ln\left(\frac{\vec{q}_1^{\,2}}{\vec{r}_1^{\,2}}\right)\ln\left(\frac{\vec{k}^{\,2}\vec{r}_1^{\,2}}{\vec{q}_1^{\,4}}\right)+\\ +\ln\left(\frac{(\vec{q}_1-\vec{r}_1)^2}{\vec{k}^{\,2}}\right)\ln\left(\frac{\vec{k}^{\,4}\vec{r}_1^{\,2}}{(\vec{q}_1-\vec{r}_1)^4\vec{q}_1^{\,2}}\right)+\ln\left(\frac{\vec{r}_2^{\,2}}{\vec{k}^{\,2}}\right)\ln\left(\frac{(\vec{q}_1-\vec{r}_1)^2}{\vec{r}_2^{\,2}}\right)-\end{aligned}$$

$$-4\frac{(\vec{k}^{\,2})^{\epsilon}}{\epsilon^2}+8\zeta(2)+\big[q_1,r_1\big]I_{\vec{q}_1,-\vec{r}_1}-[k,r_2]I_{\vec{k},\vec{r}_2}+$$
$$+\frac{q_2^+(q_1^+-r_1^+)}{k^+r_1^+}\Bigg(\big[r_1,r_2\big]I_{\vec{r}_1,\vec{r}_2}+\big[q_1,r_1\big]I_{\vec{q}_1,-\vec{r}_1}+$$
$$+2\big[k,r_2\big]I_{\vec{k},\vec{r}_2}+2\big[q_1,k\big]I_{\vec{q}_1,-\vec{k}}\Bigg)\Bigg\}. \tag{6}$$

This correction corresponds to the standard kernel, related with the kernel used for calculation of the remainder factor by the simularity transformation [11]. Corresponding transformation for the impact factor is

$$\langle GR_1|\to\langle GR_1|-\frac{1}{4}\langle GR_1|^{(B)}\left[\ln\left(\hat{\vec{q}}_1^{\,2}\hat{\vec{q}}_2^{\,2}\right),\hat{\mathcal{K}}_{rem}^{(B)}\right], \tag{7}$$

where $\hat{\mathcal{K}}_{rem}^{(B)}$ is the kernel, used for calculation of the remainder factor in the LO. Using the result of integration

$$-\frac{1}{4}\langle GR_1|^{(B)}\left[\ln\left(\hat{\vec{q}}_1^{\,2}\hat{\vec{q}}_2^{\,2}\right),\hat{\mathcal{K}}_{rem}^{(B)}\right]|\mathcal{G}_1\mathcal{G}_2\rangle=$$
$$=\langle GR_1|\mathcal{G}_1\mathcal{G}_2\rangle^{(B)}\,\frac{\bar{g}^2}{8}\Bigg\{\frac{q_2^+(q_1^+-r_1^+)}{k^+r_1^+}\left[\ln\left(\frac{\vec{q}_2^{\,2}}{\vec{r}_2^{\,2}}\right)\ln\left(\frac{\vec{q}_2^{\,4}}{\vec{r}_1^{\,2}\vec{r}_2^{\,2}}\right)+\right.$$
$$\left.+\ln\left(\frac{\vec{q}_1^{\,2}}{\vec{k}^{\,2}}\right)\ln\left(\frac{\vec{r}_2^{\,2}}{\vec{q}_2^{\,2}}\right)+\ln\left(\frac{(\vec{q}_1-\vec{r}_1)^2}{\vec{q}_1^{\,2}}\right)\ln\left(\frac{\vec{k}^{\,2}\vec{q}_1^{\,2}}{\vec{r}_1^{\,2}\vec{r}_2^{\,2}}\right)\right]-$$
$$-\ln\left(\frac{\vec{r}_1^{\,2}}{\vec{r}_2^{\,2}}\right)\ln\left(\frac{\vec{k}^{\,2}\vec{r}_1^{\,2}}{\vec{q}_1^{\,2}\vec{r}_2^{\,2}}\right)-\ln\left(\frac{\vec{k}^{\,2}\vec{q}_1^{\,2}}{\vec{r}_1^{\,2}\vec{r}_2^{\,2}}\right)\ln\left(\frac{(\vec{q}_1-\vec{r}_1)^4}{\vec{k}^{\,2}\vec{q}_1^{\,2}}\right)+2\big[k,r_2\big]I_{\vec{k},\vec{r}_2}-$$
$$-2\big[q_1,r_1\big]I_{\vec{q}_1,-\vec{r}_1}+\frac{q_2^+(q_1^+-r_1^+)}{k^+r_1^+}\Bigg(\big[r_1,r_2\big]I_{\vec{r}_1,\vec{r}_2}+\big[q_1,r_1\big]I_{\vec{q}_1,-\vec{r}_1}-$$
$$-\big[k,r_2\big]I_{\vec{k},\vec{r}_2}-\big[q_1,k\big]I_{\vec{q}_1,-\vec{k}}\Bigg)\Bigg\}, \tag{8}$$

we obtain correction to the transformed impact factor

$$\Phi_{GR_1(t)}^{\mathcal{G}_1\mathcal{G}_2}=\frac{\bar{g}^2}{8}\Bigg\{\frac{q_2^+(q_1^+-r_1^+)}{k^+r_1^+}\ln\left(\frac{\vec{q}_2^{\,2}(\vec{q}_1-\vec{r}_1)^2}{\vec{q}_1^{\,2}\vec{r}_2^{\,2}}\right)\ln\left(\frac{(\vec{q}_1-\vec{r}_1)^4\vec{q}_1^{\,2}\vec{k}^{\,2}\vec{r}_1^{\,2}}{\vec{r}_2^{\,6}\vec{q}_2^{\,4}}\right)-$$

$$-3\ln^2\left(\frac{\vec{k}^{\,2}\vec{r}_1^{\,2}}{\vec{q}_1^{\,2}\vec{r}_2^{\,2}}\right)+4\ln\left(\frac{\vec{q}_2^{\,2}}{\vec{q}_1^{\,2}}\right)\ln\left(\frac{\vec{q}_2^{\,4}(\vec{q}_1-\vec{r}_1)^4}{\vec{q}_1^{\,2}\vec{r}_2^{\,2}\vec{k}^{\,2}\vec{r}_1^{\,2}}\right)-$$
$$-4\ln\left(\frac{\vec{q}_2^{\,2}(\vec{q}_1-\vec{r}_1)^2}{\vec{q}_1^{\,2}\vec{r}_2^{\,2}}\right)\ln\left(\frac{\vec{q}_2^{\,2}(\vec{q}_1-\vec{r}_1)^2}{\vec{k}^{\,2}\vec{r}_1^{\,2}}\right)-4\ln^2\left(\frac{\vec{q}_1^{\,2}}{\vec{q}_2^{\,2}}\right)-$$
$$-8\frac{(\vec{k}^{\,2})^\epsilon}{\epsilon^2}+16\zeta(2)+3\frac{q_2^+(q_1^+-r_1^+)}{k^+r_1^+}\times$$
$$\times\left(\Big[r_1,r_2\Big]I_{\vec{r}_1,\vec{r}_2}+\Big[q_1,r_1\Big]I_{\vec{q}_1,-\vec{r}_1}+\Big[k,r_2\Big]I_{\vec{k},\vec{r}_2}+\Big[q_1,k\Big]I_{\vec{q}_1,-\vec{k}}\right)\Bigg\}. \quad (9)$$

But it is not the end of the story. As it is known, definition of NLO impact factors depends on an energy scale which is used. The energy scale used at definition of the impact factor (6) (see [3]) differs from the energy scale used for calculation of the remainder factor [10]. To adjust the impact factor (6) to the energy scale used in [10], we need to add to (9) the term

$$-\frac{1}{2}\ln\left(\frac{\vec{q}_2^{\,2}}{\vec{q}_1^{\,2}}\right)\langle GR_1|^{(B)}\hat{\mathcal{K}}^{(B)}_{rem}|\mathcal{G}_1\mathcal{G}_2\rangle=\langle GR_1|\mathcal{G}_1\mathcal{G}_2\rangle^{(B)}\frac{\bar{g}^2}{2}\ln\left(\frac{\vec{q}_2^{\,2}}{\vec{q}_1^{\,2}}\right)\times$$
$$\times\left\{\frac{q_2^+(q_1^+-r_1^+)}{k^+r_1^+}\ln\left(\frac{\vec{q}_2^{\,2}(\vec{q}_1-\vec{r}_1)^2}{\vec{q}_1^{\,2}\vec{r}_2^{\,2}}\right)-\ln\left(\frac{\vec{q}_2^{\,4}(\vec{q}_1-\vec{r}_1)^4}{\vec{q}_1^{\,2}\vec{r}_2^{\,2}\vec{k}^{\,2}\vec{r}_1^{\,2}}\right)\right\}. \quad (10)$$

After this, using properties of functions $I_{\vec{a},\vec{b}}$, we obtain

$$\Phi^{\mathcal{G}_1\mathcal{G}_2(1)}_{GR_1}=\frac{\bar{g}^2}{8}\Bigg\{(1-z)\left[\ln\left(\frac{|1-z|^2}{|z|^2}\right)\ln\left(\frac{|1-z|^4}{|z|^6}\right)-\right.$$
$$\left.-3Li_2(z)+3Li_2(z^*)-\frac{3}{2}\ln|z|^2\ln\frac{1-z}{1-z^*}\right]-4\ln|1-z|^2\ln\frac{|1-z|^2}{|z|^2}-$$
$$-3\ln^2|z|^2-4\ln^2\left(\frac{\vec{q}_1^{\,2}}{\vec{q}_2^{\,2}}\right)-8\frac{(\vec{k}^{\,2})^\epsilon}{\epsilon^2}+16\zeta(2)\Bigg\}, \quad (11)$$

where the ratio $z=-q_1^+r_2^+/(k^+r_1^+)$ is conformal invariant. Finally, in order to move to the impact factor for calculation of the reminder function, one has to discard the terms $\bar{g}^2\big(-(1/2)\ln^2(\vec{q}_1^{\,2}/\vec{q}_2^{\,2})-(\vec{k}^{\,2})^\epsilon/\epsilon^2+3\zeta(2)\big)$ in (11), since they are already taken into account in the BDS ansatz.

3. Summary

We calculated the impact factors for reggeon-gluon transition in the maximally extended supersymmetric Yang-Mills theory ($N = 4$ SYM) with large number of colours. Starting from rather cumbersome results obtained in [4]- [7] for check of the bootstrap condition, we get, after several transformations, quite simple and conformal invariant expression for the one-loop correction to the impact factor for calculation of the remainder factor.

1. V.S. Fadin, E.A. Kuraev and L.N. Lipatov, Phys. Lett. B **60**, 50 (1975); E.A. Kuraev, L.N. Lipatov and V.S. Fadin, Sov. Phys. JETP **44**, 443 (1976), *ibid.* **45**, 199 (1977); I.I. Balitsky and L.N. Lipatov, Sov. J. Nucl. Phys. **28**, 822 (1978).
2. Ya.Ya. Balitskii, L.N. Lipatov and V.S. Fadin, in *Materials of IV Winter School of LNPI* (Leningrad, 1979), 109.
3. V.S. Fadin, R. Fiore, M.G. Kozlov and A.V. Reznichenko, Phys. Lett. B **639**, 74 (2006) [arXiv:hep-ph/0602006].
4. M.G. Kozlov, A.V. Reznichenko and V.S. Fadin, Phys. Atom. Nucl. **74**, 758 (2011) [Yad. Fiz. **74**, 784 (2011)].
5. M.G. Kozlov, A.V. Reznichenko and V.S. Fadin, Phys. Atom. Nucl. **75**, 493 (2012).
6. M.G. Kozlov, A.V. Reznichenko and V.S. Fadin, Phys. Atom. Nucl. **75**, 850 (2012).
7. M.G. Kozlov, A.V. Reznichenko and V.S. Fadin, preprint BINP 2012-32, to be published in Phys. Atom. Nucl.
8. Z. Bern, L.J. Dixon and V.A. Smirnov, Phys. Rev. D **72**, 085001 (2005) [hep-th/0505205].
9. J. Bartels, L.N. Lipatov and A. Sabio Vera, Phys. Rev. D **80**, 045002 (2009) [arXiv:0802.2065 [hep-th]]; Eur. Phys. J. C **65** , 587 (2010) [arXiv:0807.0894 [hep-th]]; L.N. Lipatov and A. Prygarin, Phys. Rev. D **83**, 045020 (2011) [arXiv:1008.1016 [hep-th]]; Phys. Rev. D **83**, 125001 (2011) [arXiv:1011.2673 [hep-th]]; J. Bartels, L.N. Lipatov and A. Prygarin, Phys. Lett. B **705**, 507 (2011) [arXiv:1012.3178 [hep-th]].
10. V.S. Fadin and L.N. Lipatov, Phys. Lett. B **706**, 470 (2012) [arXiv:1111.0782 [hep-th]].
11. V.S. Fadin, R. Fiore, L.N. Lipatov and A. Papa, Nucl. Phys. B **874**, 230 (2013).

ELECTROWEAK MODEL AT ZERO ENERGY

N.A. Gromov

November 12, 2013

Department of Mathematics, Komi Science Center UrD RAS, Syktyvkar, Russia
e-mail: gromov@dm.komisc.ru

Abstract

The zero energy limit of the modified Electroweak Model with the contracted gauge group is regarded at the level of classical gauge fields. The Lagrangian of the model is split at zero energy on two parts: one in the base and other in the fiber. Both Lagrangians are explicitly obtained.

1. Introduction

The modern theory of electroweak processes is the Electroweak Model, which is in good agreement with experimental dates, including the latest ones from LHC. This model is a gauge theory based on the gauge group $SU(2) \times U(1)$, which is the direct product of two simple groups. The operation of group contraction [1] transforms a simple or semisimple group to a nonsemisimple one. For better understanding of a complicated physical system it is useful to investigate its limits for limiting values of its physical parameters. In this paper we discuss at the level of classical gauge fields the modified Electroweak Model with the contracted gauge group $SU(2;j) \times U(1)$. It was shown [2–4] that the contraction parameter depend on the energy s in center-of-mass system $j^2(s) = \frac{g}{m_W}\sqrt{s}$, so the contracted gauge group correspond to the zero energy limit of the Electroweak

Model. According to the general theory of semi-Riemannian geometry [5, 6] Riemannian field space of the Electroweak Model is split in the limit $j^2 \to 0 (s \to 0)$ on the base space and the fiber spaces. The Lagrangian of the Electroweak Model is split in the zero energy limit on two parts: Lagrangian in the base and Lagrangian in the fiber. We obtain both these Lagrangians.

2. Modified Electroweak Model

We consider the Electroweak Model where the contracted gauge group $SU(2;j) \times U(1)$ acts in the boson, lepton and quark sectors. The contracted group $SU(2;j)$ and its fundamental representation space $C_2(j)$ are obtained by the **consistent rescaling** of the group $SU(2)$ and the space C_2

$$z'(j) = \begin{pmatrix} jz_1' \\ z_2' \end{pmatrix} = \begin{pmatrix} \alpha & j\beta \\ -j\bar{\beta} & \bar{\alpha} \end{pmatrix} \begin{pmatrix} jz_1 \\ z_2 \end{pmatrix} = u(j)z(j),$$

$$\det u(j) = |\alpha|^2 + j^2|\beta|^2 = 1, \quad u(j)u^\dagger(j) = 1 \tag{1}$$

when contraction parameter tends to zero $j \to 0$ or is equal to the nilpotent unit $j = \iota$, $\iota^2 = 0$. The contracted group $SU(2;\iota)$ is isomorphic to Euclid group $E(2)$ and the space $C_2(\iota)$ is the fiber space with the one-dimension base $\{z_2\}$ and the one-dimension fiber $\{z_1\}$. The actions of the unitary group $U(1)$ and the electromagnetic subgroup $U(1)_{em}$ in the space $C_2(j)$ are given by the same matrices as in C_2.

The space $C_2(j)$ can be obtained from C_2 by the substitution $z_1 \to jz_1$, which induces the substitution of Lie algebra generators: $T_1 \to jT_1$, $T_2 \to jT_2$, $T_3 \to T_3$. As far as the gauge fields take their values in Lie algebra, we can substitute the gauge fields instead of transforming the generators, namely: $A^1_\mu \to jA^1_\mu$, $A^2_\mu \to jA^2_\mu$, $A^3_\mu \to A^3_\mu$, $B_\mu \to B_\mu$. For the standard gauge boson fields these substitutions are as follows:

$$W^\pm_\mu \to jW^\pm_\mu, \quad Z_\mu \to Z_\mu, \quad A_\mu \to A_\mu. \tag{2}$$

The fields $L_l = \begin{pmatrix} \nu_l \\ e_l \end{pmatrix}$, $Q_l = \begin{pmatrix} u_l \\ d_l \end{pmatrix}$ are $SU(2)$-doublets, i.e. vectors in the space C_2, so their components are transformed similar to

the components of z, namely:

$$\nu_l \to j\nu_l, \quad e_l \to e_l, \quad u_l \to ju_l, \quad d_l \to d_l. \tag{3}$$

The right lepton and quark fields are $SU(2)$-singlets, i.e. scalars, and therefore are not transformed.

After transformations (2), (3) the boson Lagrangian of the Electroweak Model can be represented in the form

$$L_B(j) = L_B^{(2)}(j) + L_B^{int}(j) =$$

$$= \frac{1}{2}\left(\partial_\mu\chi\right)^2 - \frac{1}{2}m_\chi^2\chi^2 - \frac{1}{4}\mathcal{Z}_{\mu\nu}\mathcal{Z}_{\mu\nu} + \frac{1}{2}m_Z^2 Z_\mu Z_\mu - \frac{1}{4}\mathcal{F}_{\mu\nu}\mathcal{F}_{\mu\nu} +$$

$$+j^2\left\{-\frac{1}{2}\mathcal{W}_{\mu\nu}^+\mathcal{W}_{\mu\nu}^- + m_W^2 W_\mu^+ W_\mu^-\right\} + L_B^{int}(j) = L_{B,b} + j^2 L_{B,f}, \tag{4}$$

where as usual the second order terms describe the boson particles content of the model and higher order terms L_B^{int} are regarded as their interactions. So Lagrangian (4) includes charded W-bosons with identical mass $m_W = \frac{1}{2}gv$, massless photon A_μ, neutral Z-boson with mass $m_Z = \frac{v}{2}\sqrt{g^2+g'^2}$ and Higgs boson χ, $m_\chi = \sqrt{2\lambda}v$. In the limit $j \to 0$ boson Lagrangian is split in two parts: Lagrangian $L_{B,b}$ of the base fields

$$L_{B,b} = \frac{1}{2}\left(\partial_\mu\chi\right)^2 - \frac{1}{2}m_\chi^2\chi^2 - \frac{1}{4}\mathcal{Z}_{\mu\nu}^2 + \frac{1}{2}m_Z^2\left(Z_\mu\right)^2 - \frac{1}{4}\mathcal{F}_{\mu\nu}^2 +$$

$$+\frac{gm_z}{2\cos\theta_W}\left(Z_\mu\right)^2\chi - \lambda v\chi^3 + \frac{g^2}{8\cos^2\theta_W}\left(Z_\mu\right)^2\chi^2 - \frac{\lambda}{4}\chi^4 \tag{5}$$

and Lagrangian $L_{B,f}$ of the fields, which are in the fiber

$$L_{B,f} = -\frac{1}{2}\mathcal{W}_{\mu\nu}^+\mathcal{W}_{\mu\nu}^- + m_W^2 W_\mu^+ W_\mu^- -$$

$$-2ig\left(W_\mu^+ W_\nu^- - W_\mu^- W_\nu^+\right)\left(\mathcal{F}_{\mu\nu}\sin\theta_W + \mathcal{Z}_{\mu\nu}\cos\theta_W\right) + gW_\mu^+ W_\mu^-\chi -$$

$$-\frac{i}{2}e\left[A_\mu\left(\mathcal{W}_{\mu\nu}^+ W_\nu^- - \mathcal{W}_{\mu\nu}^- W_\nu^+\right) - A_\nu\left(\mathcal{W}_{\mu\nu}^+ W_\mu^- - \mathcal{W}_{\mu\nu}^- W_\mu^+\right)\right] -$$

$$-\frac{i}{2}g\cos\theta_W\left[Z_\mu\left(\mathcal{W}_{\mu\nu}^+ W_\nu^- - \mathcal{W}_{\mu\nu}^- W_\nu^+\right) - Z_\nu\left(\mathcal{W}_{\mu\nu}^+ W_\mu^- - \mathcal{W}_{\mu\nu}^- W_\mu^+\right)\right] +$$

$$+\frac{g^2}{4}\left(W_\mu^+W_\nu^- - W_\mu^-W_\nu^+\right)^2 + \frac{g^2}{4}W_\mu^+W_\nu^-\chi^2 -$$

$$-\frac{e^2}{4}\left\{\left[\left(W_\mu^+\right)^2 + \left(W_\mu^-\right)^2\right](A_\nu)^2 - 2\left(W_\mu^+W_\nu^+ + W_\mu^-W_\nu^-\right)A_\mu A_\nu +\right.$$

$$\left. + \left[\left(W_\nu^+\right)^2 + \left(W_\nu^-\right)^2\right](A_\mu)^2\right\} - \frac{g^2}{4}\cos\theta_W\left\{\left[\left(W_\mu^+\right)^2 + \left(W_\mu^-\right)^2\right](Z_\nu)^2 -\right.$$

$$\left. -2\left(W_\mu^+W_\nu^+ + W_\mu^-W_\nu^-\right)Z_\mu Z_\nu + \left[\left(W_\nu^+\right)^2 + \left(W_\nu^-\right)^2\right](Z_\mu)^2\right\} -$$

$$-eg\cos\theta_W\left\{W_\mu^+W_\mu^-A_\nu Z_\nu + W_\nu^+W_\nu^-A_\mu Z_\mu -\right.$$

$$\left. -\frac{1}{2}\left(W_\mu^+W_\nu^- + W_\nu^+W_\mu^-\right)\left(A_\mu Z_\nu + A_\nu Z_\mu\right)\right\}. \qquad (6)$$

The lepton Lagrangian in terms of electron and neutrino fields takes the form

$$L_L(j) = e_l^\dagger i\tilde{\tau}_\mu\partial_\mu e_l + e_r^\dagger i\tau_\mu\partial_\mu e_r - m_e(e_r^\dagger e_l + e_l^\dagger e_r) +$$

$$+\frac{g\cos 2\theta_w}{2\cos\theta_w}e_l^\dagger\tilde{\tau}_\mu Z_\mu e_l - ee_l^\dagger\tilde{\tau}_\mu A_\mu e_l - g'\cos\theta_w e_r^\dagger\tau_\mu A_\mu e_r +$$

$$+g'\sin\theta_w e_r^\dagger\tau_\mu Z_\mu e_r + j^2\left\{\nu_l^\dagger i\tilde{\tau}_\mu\partial_\mu\nu_l + \frac{g}{2\cos\theta_w}\nu_l^\dagger\tilde{\tau}_\mu Z_\mu\nu_l +\right.$$

$$\left. +\frac{g}{\sqrt{2}}\left[\nu_l^\dagger\tilde{\tau}_\mu W_\mu^+ e_l + e_l^\dagger\tilde{\tau}_\mu W_\mu^-\nu_l\right]\right\} = L_{L,b} + j^2 L_{L,f}. \qquad (7)$$

The quark Lagrangian in terms of u- and d-quarks fields can be written as

$$L_Q(j) = d_l^\dagger i\tilde{\tau}_\mu\partial_\mu d_l + d_r^\dagger i\tau_\mu\partial_\mu d_r - m_d(d_r^\dagger d_l + d_l^\dagger d_r) - \frac{e}{3}d_l^\dagger\tilde{\tau}_\mu A_\mu d_l -$$

$$-\frac{g}{\cos\theta_w}\left(\frac{1}{2} - \frac{2}{3}\sin^2\theta_w\right)d_l^\dagger\tilde{\tau}_\mu Z_\mu d_l - \frac{1}{3}g'\cos\theta_w d_r^\dagger\tau_\mu A_\mu d_r + \frac{1}{3}g'\sin\theta_w d_r^\dagger\tau_\mu Z_\mu d_r -$$

$$+j^2\left\{u_l^\dagger i\tilde{\tau}_\mu\partial_\mu u_l + u_r^\dagger i\tau_\mu\partial_\mu u_r - m_u(u_r^\dagger u_l + u_l^\dagger u_r) + \frac{g}{\cos\theta_w}\left(\frac{1}{2} - \frac{2}{3}\sin^2\theta_w\right)u_l^\dagger\tilde{\tau}_\mu Z_\mu u_l +\right.$$

$$+\frac{2e}{3}u_l^\dagger\tilde{\tau}_\mu A_\mu u_l + \frac{g}{\sqrt{2}}\left[u_l^\dagger\tilde{\tau}_\mu W_\mu^+ d_l + d_l^\dagger\tilde{\tau}_\mu W_\mu^- u_l\right] + \frac{2}{3}g'\cos\theta_w u_r^\dagger\tau_\mu A_\mu u_r -$$

$$\left. -\frac{2}{3}g'\sin\theta_w u_r^\dagger\tau_\mu Z_\mu u_r\right\} = L_{Q,b} + j^2 L_{Q,f}. \qquad (8)$$

Constants $m_e = h_e v/\sqrt{2}$, $m_u = h_u v/\sqrt{2}$, $m_d = h_d v/\sqrt{2}$ represents electron and quark masses.

The complete Lagrangian of the modified model is given by the sum

$$L(j) = L_B(j) + L_Q(j) + L_L(j) =$$

$$= L_{B,b} + L_{L,b} + L_{Q,b} + j^2 \{L_{B,f} + L_{L,f} + L_{Q,f}\} = L_b + j^2 L_f. \quad (9)$$

3. Description of Physical Systems with Contracted Symmetry Group

The standard way of describing a physical system in field theory is its decomposition on independent more or less simple the subsystems and then introduction of interactions between them. In Lagrangian formalism this implies that some terms describe independent subsystems (free fields) and the rest of the terms correspond to interactions between the fields.

The operation of group contraction transforms a simple or semisimple group G to a nonsemisimple one with the structure of a semidirect product $G = A(\times G_1$, where A is Abelian and $G_1 \subset G$ is an untouched subgroup. At the same time the space of the fundamental representation of the group G is split under the contraction in such a way that the subgroup G_1 acts in the fiber. the gauge theory with a contracted gauge group describes a physical system, which is divided on two subsystems S_b and S_f. One subsystem S_b includes all fields from the base and the other subsystem S_f is built from fiber fields. S_b forms a closed system since according to semi-Riemannian geometry [5, 6] the properties of the base do not depend on the points of the fiber, which physically means that the fields from the fiber do not interact with the fields from the base. On the contrary the properties of the fiber depend on the points of the base, therefore the subsystem S_b exert influence upon S_f. More precisely, the fields from the base are outer (or background) fields for the subsystem S_f and specify outer conditions in every fiber.

In particular, the simple group $SU(2)$ is contracted to the nonsemisimple one, which is isomorphic to the Euclid group $E(2) = A_2(\times SO(1)$, where Abelian subgroup A_2 is generated by the translations [7]. The fields space of the Electroweak Model is split in the

limit case of the zero energy in such a way that photon, Higgs boson, Z-boson, electron and d-quark fields are in the base, whereas W-boson, neutrino and u-quark fields are in the fiber. The base subsystem is the closed physical system which Lagrangian L_b involves in addition to the free base particle their interactions and self-actions. It is remarkable that L_b does not included charded weak current interactions, which are switch off at zero energy. Indeed, W-bosons are the only gauge bosons in the fiber therefore their does not influences on fields in the base. Lagrangian L_f of the fiber subsystem includes W-bosons, neutrino, u-quark fields, their electromagnetic and weak (neutral and charded currents) interactions. Higgs boson, photon, Z-boson, electron and d-quark fields in L_f are regarded as the outer parameters which specify conditions in every fiber.

In order to avoid terminological misunderstanding let us stress that we regard locally trivial fibering, which is defined by the projection in the field space. This fibering is understood in the context of semi-Riemannian geometry [5,6] and has nothing to do with the principal fiber bundle. The simple and the best known example of fiber space is the nonrelativistic space-time with one dimensional base, which is interpreted as time, and three dimensional fiber, which is interpreted as proper space. It is well known, that in nonrelativistic physics the time does not depend on the space coordinates, while the space properties can be changed in time. Galilei transformation $t' = t,\ x' = x + vt$ is the simplest demonstration of this fact.

Acknowledgements

I thank A.A. Slavnov for helpful discussions and the organizers of the conference, especially L.L. Jenkovszky, for hospitality. This work was supported by Program of UrD RAS, project No 12-P-1-1013.

1. E. Inönü, E.P. Wigner, Proc. Nat. Acad. Sci. USA **39**, 510 (1953).
2. N.A. Gromov, in *New Trends in High-Energy Physics* (Kiev, 2011), p. 296
3. N.A. Gromov, Phys. Part. Nucl. **43**, 723 (2012).
4. N.A. Gromov, Phys. Atom. Nucl., **76**, 1144 (2013).
5. R.I. Pimenov, Vestnik Leningrad Univ. **1**, 137 (1965) (in Russian).
6. N.A. Gromov, Phys. At. Nucl. **72**, 794 (2009).
7. N.A. Gromov, Phys. Atom. Nucl. **73**, 326 (2010)

HIGGS BOSON DECAY TO PHOTON AND Z BOSON: A WINDOW TO PHYSICS BEYOND THE STANDARD MODEL

A.Yu. Korchin[1,2], V.A. Kovalchuk[1]

[1] *NSC 'Kharkov Institute of Physics and Technology', 61108 Kharkiv, Ukraine*
[2] *V.N. Karazin Kharkiv National University, 61022 Kharkiv, Ukraine*

Abstract

Polarization characteristics of γZ state in the Higgs boson decay $h \to \gamma Z$ are discussed. A nonzero value of the photon circular polarization arises due to presence of CP-even and CP-odd parts in the $h\gamma Z$ effective Lagrangian and its non-Hermiticity. Measurement of the circular polarization through forward-backward asymmetry of fermions in the decay $h \to \gamma Z \to \gamma f \bar{f}$ will allow one to search for deviation from the standard model.

1. Introduction

The ATLAS and CMS collaborations at the LHC observed a boson h with mass around 126 GeV. Though the data are more consistent with the pure scalar boson hypothesis than the pure pseudoscalar one, there are many extensions of the standard model (SM) with a more complicated Higgs sector, in which some of the Higgs bosons may not have definite CP parity [1].

We suggest to study CP and possible CPT violation in the decay

$$h \to \gamma Z \to \gamma f \bar{f}, \tag{1}$$

with $f = \ell, q$, where ℓ (q) denote leptons (quarks).

In the SM the decay amplitude in the lowest order is determined by the loop contributions [2] which have nonzero imaginary part due to rescattering effects $h \to f\bar{f} \to \gamma Z$ (f are fermions with masses $m_f \leq m_h/2$). The effective $h\gamma Z$ interaction Lagrangian $\mathcal{L}_{\rm eff}^{h\gamma Z}$ is thus non-Hermitian. This non-Hermiticity leads to a nonzero value of the the photon circular polarization in decay (1) once we assume a mixture of CP violating term in $\mathcal{L}_{\rm eff}^{h\gamma Z}$. In the SM and theories beyond the SM which are CPT symmetric, there are no sources of non-Hermiticity of $\mathcal{L}_{\rm eff}^{h\gamma Z}$ apart from rescattering effects.

The CPT theorem is a consequence of Lorentz invariance, locality, connection between spin and statistics, and a Hermitian Hamiltonian [3]. However there are many extensions of the SM in which CPT violation appears due to nonlocality in the string theory, or violation of Lorentz symmetry in the extra dimensional models [4]. One can also mention possible deviations from the standard quantum mechanical evolution of states in some models of quantum gravity (see, e.g., investigation [5] of CPT violation in neutral-meson systems). The CPT violating effects in some of these underlying theories, in principle, can be additional sources of non-Hermiticity of effective Lagrangian $\mathcal{L}_{\rm eff}^{h\gamma Z}$ and hence contribute to photon circular polarization.

2. Effective Lagrangian and Decay $h \to \gamma Z \to \gamma f \bar{f}$

The effective Lagrangian for the $h\gamma Z$ interaction can be written as

$$\mathcal{L}_{\rm eff}^{h\gamma Z} = \frac{e\,g}{16\,\pi^2\,v}\Big(c_{1Z}\,Z_{\mu\nu}F^{\mu\nu}h - \\ -c_{2Z}\,(\partial_\mu h\,Z_\nu - \partial_\nu h\,Z_\mu)\,F^{\mu\nu} - \tilde{c}_Z\,Z_{\mu\nu}\widetilde{F}^{\mu\nu}h\Big), \qquad (2)$$

where e is the positron electric charge, g is the $SU(2)_L$ coupling constant and $v = \left(\sqrt{2}G_{\rm F}\right)^{-1/2} \approx 246$ GeV, $F_{\mu\nu}$ and $Z_{\mu\nu}$ are the field strengths for the electromagnetic and Z field, $\widetilde{F}_{\mu\nu} = \varepsilon_{\mu\nu\alpha\beta}F^{\alpha\beta}/2$, c_{1Z}, c_{2Z} and $\tilde{c}_Z$ are dimensionless effective coupling constants.

The terms proportional to c_{1Z} and c_{2Z} correspond to a CP-even scalar h, while the term proportional to $\tilde{c}_Z$ indicates a CP-odd pseudoscalar h. The presence of both sets means that h is not a CP eigenstate and interference of these terms lead to CP violating effects which reveal in polarization states of the photon.

One can write c_{1Z} as the sum of terms in the SM and new physics (NP) beyond the SM: $c_{1Z} = c_Z^{\rm SM} + c_{1Z}^{\rm NP}$. In the SM, $c_{2Z} = \tilde{c}_Z = 0$ and their nonzero values come from effects of NP. The coupling $c_Z^{\rm SM}$ has small imaginary part arising due to the intermediate on-mass-shell $\ell^+\,\ell^-$ and $q\bar{q}$ states in the one-loop contributions [$\ell = e,\ \mu,\ \tau$, and $q = u,\ d,\ s,\ c,\ b$ (excluding top quark)].

For decay of the zero-spin Higgs h boson into γ and Z boson we find in Ref. [6] the helicity amplitudes and polarization parameters $\xi_1,\ \xi_2,\ \xi_3$.

Due to the zero-spin nature of the Higgs boson, the photon and Z boson have equal helicities. This allows for measurement of the photon circular polarization, described by the parameter ξ_2,

$$\xi_2 = \frac{|H_+|^2 - |H_-|^2}{|H_+|^2 + |H_-|^2} = \frac{2\,{\rm Im}((c_{1Z} + c_{2Z})\tilde{c}_Z^*)}{|c_{1Z} + c_{2Z}|^2 + |\tilde{c}_Z|^2}, \qquad (3)$$

in the decay $h \to \gamma Z \to \gamma f\bar{f}$. Indeed, we derive the following angular distribution in the polar angle θ between the momentum of the fermion f in the Z boson rest frame and the direction of the Z boson motion in the h boson rest frame,

$$\frac{1}{\Gamma}\frac{d\Gamma(h \to \gamma\,Z \to \gamma\,f\bar{f})}{d\cos\theta} = \frac{3}{8}\Big(1 + \cos^2\theta - 2\,A^{(f)}\,\xi_2\,\cos\theta\Big), \qquad (4)$$

where $A^{(f)} \equiv 2\,g_V^f g_A^f\ [(g_V^f)^2 + (g_A^f)^2]^{-1}$ with vector, g_V^f, and axial-vector, g_A^f constants for $Zf\bar{f}$ coupling.

Measurement of the forward-backward asymmetry $A_{\rm FB}$ relative to the direction of Z boson motion in the h boson rest frame for the f fermions produced in decay (1) allows one to find polarization parameter ξ_2 [6].

3. Values of Parameters and Discussion

In the SM the parameters take values $\xi_1^{SM} = \xi_2^{SM} = 0$, $\xi_3^{SM} = -1$, and deviations of the measured values of ξ_i from ξ_i^{SM} $(i = 1, 2, 3)$ will point to effects of NP.

In order to estimate magnitude of effects of NP, we consider a model with the scalar and pseudoscalar couplings of fermions to the

Higgs boson. The calculated in this model parameters are

$$\xi_1 = \pm 0.121, \qquad \xi_2 = \mp 0.001, \qquad \xi_3 = -0.993. \tag{5}$$

In Ref. [6] we also used effective field-theory approach [7] in which NP is described by the dimension-6 operators in the fields of the SM.

It turns out that the rescattering effects on the one-loop level result in values of ξ_2 in the $h \to \gamma Z$ decay about 10^{-3}. It would be of interest to check in the experimental analysis of the distribution (4) if the parameter ξ_2 is very small indeed. If the analysis yielded sizable values of ξ_2, this would mean the presence of additional sources of non-Hermiticity of effective Lagrangian. The latter may arise, for example, due to the breaking of Hermiticity in an underlying (fundamental) theory at very small distances. Thus measurement of the photon circular polarization in the $h \to \gamma Z \to \gamma \bar{f} f$ decay through the forward-backward asymmetry $A_{\rm FB}$ can be useful for searching for deviations from the SM and possible effects of CPT violation.

The parameters ξ_1, ξ_3 can be extracted from the azimuthal angle distribution in the process $h \to \gamma^* Z \to \ell^+\ell^- Z$ with decay $Z \to \bar{f} f$ on mass shell [6]. These parameters carry information on the CP properties of the Higgs boson, and their experimental determination can put constraints on models of physics beyond the SM.

Acknowledgements

A.Yu.K. thanks the Organizers of the Conference 'New trends in high-energy physics', Alushta, Ukraine, September 23-29, 2013, for invitation to present the talk. This work was supported by the National Academy of Sciences of Ukraine (project no. ЦО-12-1).

1. G.C. Branco, P.M. Ferreira, L. Lavoura *et al.*, Phys. Rep. **516**, 1 (2012).
2. L. Bergström and G. Hulth, Nucl. Phys. B **259**, 137 (1985); B **276**, 744(E) (1986).
3. R.F. Streater and A.S. Wightman, *PCT, Spin and Statistics and All That* (W.A. Benjamin, Inc. New York-Amsterdam, 1964).
4. A. Kostelecky, arXiv:0802.0581v1.
5. J. Bernabeu, N.E. Mavromatos and J. Papavassiliou, Phys. Rev. Lett. **92**, 131601 (2004).
6. A.Yu. Korchin and V.A. Kovalchuk, Phys. Rev. D **88**, 036009 (2013).
7. B. Grzadkowski, M. Iskrzynski, M. Misiak, and J. Rosiek, J. High Energy Phys. **10**, 085 (2010).

QUANTUM CHROMODYNAMICS WITH MASSIVE GLUONS

S.A. Larin

Institute for Nuclear Research of the Russian Academy of Sciences, 60th October Anniversary Prospect 7a, Moscow 117312, Russia

Abstract

It is shown that the Lagrangian of Quantum Chromodynamics should be modified by the adding gluon masses to ensure that QCD does not contradict to experiments. On mass-shell renormalizability of the resulting theory is discussed.

1. The discovery [1] of asymptotic freedom in Quantum Chromodynamics (QCD) has lead to the establishment of QCD as the theory of strong interactions. The gauge bosons of the theory, the gluons, are considered to be massless to have gauge invariance and correspondingly renormalizability. In the present paper it is shown that the QCD Lagrangian should be modified by the adding gluon masses to ensure that QCD does not contradict to experiments. On mass-shell renormalizability of the resulting theory is discussed.

2. The Lagrangian of QCD is

$$L_{QCD} = -\frac{1}{4}F^a_{\mu\nu}F^a_{\mu\nu} + i\overline{\psi}_f\gamma_\mu D_\mu\psi_f - m_f\overline{\psi}_f\psi_f -$$

$$-\frac{1}{\xi}(\partial^\mu A^a_\mu)^2 + \partial^\mu\overline{c}^a(\partial_\mu c^a - gf^{abc}c^bA^c_\mu) + counterterms, \qquad (1)$$

where $F^a_{\mu\nu} = \partial_\mu A^a_\nu - \partial_\nu A^a_\mu + gf^{abc}A^b_\mu A^c_\nu$ is the gluon field strength tensor, $D_\mu = \partial_\mu - igA^a_\mu T^a$ is the covariant derivative. The quark fields ψ_f transform as the fundamental representation of the colour group $SU(3)$, $f = u, d, s, c, b, t$ is the flavour index. The gluons A^a_μ

transform as the adjoint representation of this group. c^a are the ghost fields, ξ is the gauge parameter of the usually chosen general covariant gauge, f^{abc} are the structure constants of the group, T^a are the generators of the fundamental representation. $g = g(\mu)$ is the renormalized strong coupling constant, $g^2/(16\pi^2) \equiv a_s$, $m_f = m_f(\mu)$ is the Lagrangian (renormalized) mass of a quark with a flavor f, and μ is the renormalization point. The summations over repeated indexes are assumed.

3. Let us consider the vacuum polarization function $\Pi(q^2)$

$$(-q^2 g_{\mu\nu} + q_\mu q_\nu)\Pi(q^2) = i \int \mathrm{d}x e^{iqx} \langle 0|\ T\ j_\mu(x) j_\nu(0)\ |0\rangle, \qquad (2)$$

where $j_\mu = \sum_f q_f \overline{\psi}_f \gamma_\mu \psi_f$ is the electromagnetic quark current and $q_f = 2/3, -1/3, ...$ is the electromagnetic charge of the quark with a flavor f.

According to general principles of local quantum field theory the function $\Pi(q^2)$ satisfies the Källen-Lehmann [2] spectral representation

$$\Pi(q^2) = \frac{1}{12\pi^2} \int\limits_{4m_\pi^2}^{\infty} ds\ \frac{R(s)}{s - q^2 - i0}, \qquad (3)$$

where the ratio $R(s) = \sigma_{tot}(e^+e^- \to hadrons)/\sigma(e^+e^- \to \mu^+\mu^-)$ is the normalized total cross-section of electron-positron annihilation into hadrons, m_π is a pion mass.

The Källen-Lehmann representation determines the analytic properties of $\Pi(q^2)$ which should be an analytic function in the complex q^2-plane with the cut starting from the first physical threshold, i.e. as it is dictated by experiments from the two-pion threshold $q^2 = 4m_\pi^2$. In particular, one gets for the discontinuity of $\Pi(q^2)$ on the cut

$$\Delta\Pi(q^2) \equiv \Pi(q^2 + i0) - \Pi(q^2 - i0) = \begin{cases} i\ R(q^2)/(6\pi) & \text{at}\ \ s > 4m_\pi^2, \\ 0 & \text{at}\ \ s < 4m_\pi^2. \end{cases} \qquad (4)$$

Perturbative QCD produces the following expression for the discontinuity

$$\Delta\Pi(q^2)_{pQCD} = \theta(q^2)\ \rho_{gluon}(q^2) + \theta(q^2 - 4M_u^2)\ \rho_{quark}(q^2). \qquad (5)$$

The gluon spectral density $\rho_{gluon}(q^2)$ contributes for $q^2 > 0$ as it is indicated by the theta-function $\theta(q^2)$. This is the known zero threshold. It arises from those absorptive parts of Feynman diagrams of $\Pi(q^2)$ which are produced by purely gluonic cuts of the diagrams (i.e. by the Cutcosky cuts which cross only gluon propagators of diagrams). As it is well known such diagrams appear for the first time at the four-loop level in the order a_s^3 (corresponding cuts cross 3 gluon propagators).

The quark spectral density $\rho_{quark}(q^2)$ arises from the quark cuts of the diagrams (i.e. from the cuts which cross two or more quark propagators of the diagrams). It contributes for $q^2 > 4M_u^2$ where M_u is the perturbative pole mass of the lightest u-quark, defined as the pole of the quark propagator within perturbation theory. A perturbative quark pole mass

$$M_f = m_f(\mu) + O(a_s) \tag{6}$$

appears after summation of perturbative corrections to a quark propagator. It is a renormalization group invariant quantity, i.e. independent on the renormalization point μ and on the choice of the subtraction scheme. In this sense it behaves as a physical object and that is why it is natural to use this definition of a quark mass to parametrize the theory.

We will not discuss here the important by themselves questions of convergence or divergence of corresponding perturbative QCD series at low or at high energies. Here we will just accept that our conventional perturbation theory is adequate to the exact solution of the theory, i.e. it correctly reproduces the perturbative expansion of the exact solution.

Hence one gets within QCD that $\Delta\Pi(q^2)$ is non-zero in the energy interval $0 < q^2 < 4m_\pi^2$ since the perturbative contribution $\Delta\Pi(q^2)_{pQCD}$ is non-zero in this interval. And we would like to stress here that one should get in QCD an exact zero below the two-pion threshold as it is dictated by experiments. There are of course also non-perturbative contributions, i.e. contributions of the type of e^{-1/a_s} which are invisible in the perturbative expansion at $a_s = 0_+$

$$e^{-1/a_s} = 0 \cdot a_s + 0 \cdot a_s^2 + ...$$

But non-perturbative contributions can not exactly cancel the perturbative contribution in the continuous interval $0 < q^2 < 4m_\pi^2$ because of the different dependence on a_s. To get that $\Delta\Pi(q^2) = 0$ at $0 < q^2 < 4m_\pi^2$ in agreement with experiments one should move perturbative gluon and quark thresholds above $q^2 = 4m_\pi^2$. That is why we should introduce the non-zero Lagrangian gluon masses.

The first naive objection here is that nobody trusts perturbation theory below the two-pion threshold, i.e. that the corresponding perturbative series is heavily divergent in this energy region. But for us here only the principal existence of the pertubative series with finite coefficients below the two-pion threshold is of importance independently on the question of its divergence.

Thus one obtains the following restrictions on the (perturbative pole) masses of gluons and quarks

$$(3M_{gl})^2 > 4m_\pi^2, \quad 4M_u^2 > 4m_\pi^2. \tag{7}$$

Although the restriction on M_u seems to be quite strong for the lightest u-quark it is not excluded from the first principles.

4. To construct QCD with massive gluons we will follow the approach of [3]. Presently this is the only known way to get (on mass-shell) renormalizable theory of massive gluons without color scalars (color scalars are rejected by experiments). Within this approach one starts from a renormalizable theory with scalar fields using the Englert-Brout-Higgs mechanism of spontaneous symmetry breaking [4] and after transition to the unitary gauge removes remaining massive scalar fields. Thus we add to the massless QCD Lagrangian (1) the scalar part to begin with the following general Lagrangian

$$L_{QCD+scalars} = -\frac{1}{4}F^a_{\mu\nu}F^a_{\mu\nu} + i\overline{\psi}_f\gamma_\mu D_\mu\psi_f - m_f\overline{\psi}_f\psi_f +$$

$$+ (D_\mu\Phi)^+ D_\mu\Phi + (D_\mu\Sigma)^+ D_\mu\Sigma - \lambda_1\left(\Phi^+\Phi - v_1^2\right)^2 - \lambda_2\left(\Sigma^+\Sigma - v_2^2\right)^2 -$$

$$-\lambda_3\left(\Phi^+\Phi + \Sigma^+\Sigma - v_1^2 - v_2^2\right)^2 - \lambda_4\left(\Phi^+\Sigma\right)\left(\Sigma^+\Phi\right) +$$

$$+L_{gf} + L_{gc} + counterterms, \tag{8}$$

where we introduced two triplets $\Phi(x)$ and $\Sigma(x)$ of complex scalar fields in the fundamental representation of the $SU(3)$ color group to

get all gluon massive. L_{gf} is the gauge fixing part of the Lagrangian in some chosen gauge and L_{gc} is the corresponding gauge compensating part with the Faddeev-Popov ghost fields.

We can choose the following shifts of scalar fields by the quantities v_1 and v_2 to generate masses of all eight gluons

$$\Phi(x) = \begin{pmatrix} \phi_1(x) + i\phi_2(x) + v_1 \\ \phi_3(x) + i\phi_4(x) \\ \phi_5(x) + i\phi_6(x) \end{pmatrix}, \quad \Sigma(x) = \begin{pmatrix} \sigma_1(x) + i\sigma_2(x) \\ \sigma_3(x) + i\sigma_4(x) + v_2 \\ \sigma_5(x) + i\sigma_6(x) \end{pmatrix}. \tag{9}$$

Choosing for simplicity $v_1 = v_2 \equiv v$ one obtains the following massive terms for gluons in the Lagrangian

$$L_M = M^2 \left[(A^1)^2 + (A^2)^2 + (A^3)^2 + \frac{1}{2}(A^4)^2 + \right.$$
$$\left. + \frac{1}{2}(A^5)^2 + \frac{1}{2}(A^6)^2 + \frac{1}{2}(A^7)^2 + \frac{1}{3}(A^8)^2 \right], \tag{10}$$

where $M^2 \equiv g^2 v^2$ is the gluon mass parameter of the theory.

After the chosen shifts the following four combinations of scalar fields

$$\phi_1 + \frac{\lambda_3}{\lambda_1 + \lambda_3}\sigma_3, \quad \sigma_3, \quad \sigma_1 + \phi_3, \quad \sigma_2 - \phi_4 \tag{11}$$

become massive Higgs particles.

The following eight combinations

$$\sigma_1 - \phi_3, \quad \phi_4 + \sigma_2, \quad \phi_2 - \sigma_4, \quad \phi_2 + \sigma_4, \quad \phi_5, \quad \phi_6, \quad \sigma_5, \quad \sigma_6 \tag{12}$$

become massless Goldstone ghosts.

Now one can make transition to the unitary gauge. All ghost fields as usual disappear from the Lagrangian. Following the approach of [3] one can remove in the unitary gauge all Higgs fields from the Lagrangian preserving on mass-shell renormalizability of the theory. The Lagrangian of the resulting theory is

$$L_{massive\ QCD} = L_M - \frac{1}{4}F^a_{\mu\nu}F^a_{\mu\nu} + i\overline{\psi}_f\gamma_\mu D_\mu\psi_f -$$
$$- m_f\overline{\psi}_f\psi_f + counterterms, \tag{13}$$

where L_M is given in eq.(10).

Let us note that on mass-shell renormalizability does not mean that one should consider quarks and gluons as free external particles. It means that in the $SU(3) \times SU(2) \times U(1)$ theory the S-matrix elements with the physical external particles will be finite.

One can calculate the one-loop β-function in this theory to obtain for a massless renormalization scheme (i.e. a scheme where renormalization group functions do not depend on masses) the following result

$$\beta(a_s) = \mu^2 \frac{\partial a_s}{\partial \mu^2} = \sum_{i \geq 0} \beta_i a_s^{i+2},$$

$$\beta_0 = -\frac{7}{2} C_A + \frac{4}{3} T_F n_f, \tag{14}$$

here $C_A = 3$ is the Casimir operator of the adjoint representation of the $SU(3)$ color group, $T_F = 1/2$ is the trace normalization of the fundamental representation, n_f is the number of active quark flavors.

Thus asymptotic freedom remains valid in the considered theory with massive gluons.

Acknowledgements

The author is grateful to collaborators of the Theory division of INR for helpful discussions. The work is supported in part by the grant for the Leading Scientific Schools NS-5590.2012.2.

1. D.J. Gross, F. Wilczek, Phys. Rev. Lett. **30**, 1343 (1973); H.D. Politzer, Phys. Rev. Lett. **30**, 1346 (1973); G. 't Hooft, report at the Marseille Conference on Yang-Mills Fields, 1972.
2. G. Källen, Helv. Phys. Acta **25**, 417 (1952); H. Lehmann, Nuovo Cim. **11**, 342 (1954).
3. S.A. Larin, e-Print: hep-ph/0503198; Phys. Part. Nucl. **44**, 386 (2013).
4. P.W. Higgs, Phys. Lett. **12**, 132 (1964); F. Englert and R. Brout, Phys. Rev. Lett. **13**, 321 (1964).

ANALYTIC PROPERTIES OF PRODUCTION AMPLITUDES IN $N = 4$ SUSY

L.N. Lipatov

St. Petersburg State University,
Petersburg Nuclear Physics Institute
Gatchina, Orlova Roshcha, 188300, St. Petersburg, Russia
e-mail: lipatov@thd.pnpi.spb.ru

Abstract

The BFKL approach is based on a theory formulated in terms of reggeized gluons and their interactions. The corresponding effective action is derived from QCD and is local in the particle rapidities. In particular, Pomeron and Odderon are composite states of two and three reggeized gluons, respectively. In the planar limit of $N = 4$ SUSY the scattering amplitudes for the multi-Regge kinematics of produced gluons contain in some regions apart from the Regge poles also the Mandelstam cut contributions. In these regions they obey the kinematical constraints in the form of the Steinmann relations leading to the dispersion-like representations. We study them for amplitudes with 6 and 7 external particles.

1. Reggeized Gluons and Their Composite States

The essential contribution to the elastic cross-section at large energies $\sqrt{s}$ and fixed momentum transfers $|q|$ appears from the Regge kinematics

$$s = 4E^2 \gg -t = \vec{q}^2. \tag{1}$$

In this region it is convenient to use the t-channel partial wave representation for the scattering amplitude with a definite signature $p = \pm 1$

$$A^p(s,t) = s \int\limits_{a-i\infty}^{a+i\infty} \frac{d\omega}{2\pi i} \left((-s)^\omega - p s^\omega\right) f^p_\omega(t). \tag{2}$$

In the case, when the leading singularity of $f^p_\omega(t)$ is the Regge pole

$$f^p_\omega(t) = \frac{\gamma^2(t)}{\omega - \omega_p(t)}, \ \omega_p(t) = \Delta - \alpha' \vec{q}^2 \tag{3}$$

the amplitude has the power-like behavior [1]

$$A^p_{\text{Regge}}(s,t) = \xi_p(t)\, s^{1+\omega_p(t)}\, \gamma^2(t), \ \xi_p(t) = e^{-i\pi\omega_p(t)} - p. \tag{4}$$

The Regge poles generate the cut singularities in the ω-plane [2]. For example, in the simple case of the two reggeon exchange this Mandelstam contribution can be written as follows

$$A^p_{\text{Mand}}(s,t) = \xi_p s \int \frac{d^2k}{(2\pi)^2} \Phi^2(k, q-k) s^{\omega_{p_1}(-k^2)} s^{\omega_{p_2}(-(q-k)^2)}, \ p = p_1 p_2. \tag{5}$$

The Mandelstam cuts appear as a result of an analytic continuation of the multi-particle t-channel unitarity relation [3]

$$\Im_t f_\omega(t) \sim \sum_n \int d\Omega_n |f^{(n)}_\omega|^2. \tag{6}$$

To describe an approximately constant behavior of the total cross-sections σ a special j-plane singularity - Pomeron with vacuum quantum numbers is introduced

$$\sigma = \frac{1}{s} \Im A(s.0), \ A(s,t) \approx i s\, s^{\Delta - \alpha'_P q^2}, \tag{7}$$

where the Pomeron intercept Δ and its slope α'_P are small according to the experimental data. All Pomeron interactions are taken into account in the 2+1 dimensional effective field theory [4].

In the leading logarithmic approximation (LLA)

$$\alpha_s \ln s \sim 1, \ \alpha_s = \frac{g^2}{4\pi} \ll 1 \tag{8}$$

the Born scattering amplitude in QCD is multiplied by the Regge factor

$$M_{AB}^{A'B'}(s,t) = M_{AB}^{A'B'}(s,t)|_{\rm Born}\, s^{\omega(t)}, \tag{9}$$

where the gluon Regge trajectory in LLA is given below

$$\omega(-|q|^2) = -\frac{\alpha_s N_c}{4\pi^2}\int d^2k\,\frac{|q|^2}{|k|^2|q-k|^2} \approx -\frac{\alpha_s N_c}{2\pi}\,\ln\frac{|q^2|}{\lambda^2}. \tag{10}$$

In the inelastic processes the most essential contribution to the total cross-section appears from the multi-Regge kinematics corresponding to the large pair energies $\sqrt{s_k}$ of produced gluons in comparison with momentum transfers q_i and transverse components $k_{r\perp}$ of the particle momenta. The corresponding amplitude has the factorized form [5]

$$M_{2\to 2+n} \sim \frac{s_1^{\omega_1}}{|q_1|^2}\, gT^{d_1}_{c_2c_1} C(q_2,q_1)\,\frac{s_2^{\omega_2}}{|q_2|^2}...gT^{d_n}_{c_{n+1}c_n}\, C(q_{n+1},q_n)\,\frac{s_{n+1}^{\omega_{n+1}}}{|q_{n+1}|^2}, \tag{11}$$

where ω_r are the Regge trajectories and $C(q_i,q_{i-1})$ are the Reggeon-Reggeon-gluon vertices. In LLA they are

$$\omega_r = -\frac{\alpha_s N_c}{2\pi}\left(\ln\frac{|q_r^2|}{\mu^2} - \frac{1}{\epsilon}\right),\ C(q_2,q_1) = \frac{q_2\, q_1^*}{q_2^* - q_1^*}, \tag{12}$$

where the produced gluons are assumed to have definite helicities.

The knowledge of quantities $M_{2\to 2+n}$ gives a possibility to construct the total cross-section and the scattering amplitude with color singlet quantum numbers in the crossing channel. This amplitude can be expressed in terms of the Pomeron wave function satisfying the BFKL equation [5]

$$E\,\Psi(\vec\rho_1,\vec\rho_2) = H_{12}\,\Psi(\vec\rho_1,\vec\rho_2),\ \sigma_t \sim s^{\Delta},\ \Delta = -\frac{\alpha_s N_c}{2\pi}\,E_0. \tag{13}$$

The operator H_{12} is the BFKL Hamiltonian and Δ is the Pomeron intercept. In the impact parameter representation the hamiltonian can be written as follows [6]

$$H_{12} = \frac{1}{p_1p_2^*}(\ln|\rho_{12}|^2)p_1p_2^* + \frac{1}{p_1^*p_2}(\ln|\rho_{12}|^2)p_1^*p_2 + \ln\,|p_1p_2|^2 - 4\psi(1)\,, \tag{14}$$

where

$$\rho_{12} = \rho_1 - \rho_2,\ \rho_r = x_r + iy_r,\ \Delta = 4\alpha N_c \ln 2/\pi. \tag{15}$$

The Schrödinger equation is invariant under the Möbius transformations [7]

$$\rho_k \to \frac{a\rho_k + b}{c\rho_k + d} \tag{16}$$

and, as a result, the eigenfunctions and eigenvalues of H_{12} are classified by the conformal weights

$$m = \gamma + n/2,\ \widetilde{m} = \gamma - n/2, \tag{17}$$

depending on the anomalous dimension $\gamma = 1/2 + i\nu$ of twist-2 operators and integer conformal spin n. The energies have the property of the holomorphic separability and are expressed in terms of the logarithmic derivative $\psi(x)$ of the gamma function

$$E = 2\chi(n,\gamma) = \psi(m) + \psi(1-m) + \psi(\widetilde{m}) + \psi(1-\widetilde{m}) - 4\psi(1). \tag{18}$$

These properties lead to the integrability of the BFKL dynamics in the multi-color limit [8,9].

2. Effective Action for Reggeized Gluons

Generally the BFKL approach to high energy QCD is based on an effective field theory for the reggeized gluons similar to the Gribov Pomeron calculus. The gluon Regge trajectory and various reggeon couplings in this theory can be calculated from the gauge invariant effective lagrangian written for a cluster of quarks and gluons interacting with the reggeized gluons and having their rapidities y in some interval η

$$y = \frac{1}{2}\ln\frac{\epsilon_k + |k|}{\epsilon_k - |k|},\ |y - y_0| < \eta,\ \eta \ll \ln s. \tag{19}$$

We introduce the anti-hermitian fields v_μ describing the usual gluons and the gauge invariant fields $A_\pm$ describing the production and annihilation of the reggeized gluons

$$v_\mu(x) = -iT^a v^a_\mu(x),\ A_\pm(x) = -iT^a A^a_\pm(x),\ \delta A_\pm(x) = 0. \tag{20}$$

The fields $A_\pm$ satisfy the kinematical constraints

$$\partial_- A_+ = \partial_+ A_- = 0, \tag{21}$$

corresponding to the fact, that the Sudakov variables of momenta of various clusters of particles are strongly ordered in their rapidities y_i in an accordance with the quasi-multi-Regge kinematics.

The effective action for particles inside a cluster with a given rapidity value has the form [10]

$$S = \int d^4x \left(L_{QCD} + Tr(V_+ \partial_\mu^2 A_- + V_- \partial_\mu^2 A_+) \right), \tag{22}$$

where L_{QCD} is the usual QCD action and the effective currents $V_\pm$ are given below

$$V_+ = -\frac{1}{g}\partial_+ P \exp\left(-\frac{g}{2} \int_{-\infty}^{x^+} v_+(x') d(x')^+ \right) = v_+ - g v_+ \frac{1}{\partial_+} v_+ + \dots . \tag{23}$$

The Feynman rules for this action are derived in ref. [11]. The effective action approach gives a possibility to construct various reggeon vertices needed to calculate next-to-leading order (NLO) corrections to the BFKL kernel in the color singlet [12, 13] and adjoint [14, 15] representations.

The NLO correction to the BFKL kernel in QCD was calculated in ref. [12]. In the case of the $N = 4$ extended super-symmetric gauge theory the two loop result has the property of the hermitian separability [13]. Moreover, in this model the eigenvalue contains only the special functions having the maximal transcendentality possible in the given order [17]. The maximal transcendentality property in $N = 4$ SUSY is valid in each order of perturbation theory also for the anomalous dimensions of the twist 2 operators [17], which allowed to calculate them up to the fifth order [18–20]. Its singular behavior at $j \to 1$, obtained from the BFKL equation in Ref. [17], is in an agreement with the direct calculation with the use of the integrability of the theory.

It is well known, that the $N = 4$ four-dimensional conformal field theory according to the Maldacena guess is equivalent to the superstrings living on the anti-de-Sitter 10-dimensional space [21–23]. As

a result, the Pomeron in this model is dual to the reggeized graviton in the anti-de-Sitter space. On can write the kernel of the BFKL equation for N=4 SUSY in a diffusion approximation in the form

$$j = 2 - \Delta - D\,\nu^2,\ \gamma = 1 + \frac{j-2}{2} + i\nu, \tag{24}$$

where the parameters Δ and D depend on the gauge coupling constant. According to the energy-momentum conservation we have $D = \Delta$.

It turns out, that due to the AdS/CFT correspondence [21–23] the diffusion approximation for the BFKL equation corresponds to the linear Regge trajectory

$$j = 2 + \frac{\alpha'}{2}\,t,\ t = E^2/R^2,\ \alpha' = \frac{R^2}{2}\,\Delta. \tag{25}$$

of the graviton living in the 10-dimensional anti-de-Sitter space.

Because the behavior of the anomalous dimension at large coupling constants is known, one can calculate the Pomeron intercept in the strong coupling limit [18,24]

The duality between the BFKL Pomeron and reggeized graviton means, that the Pomeron calculus could be formulated in the framework of the approach based on an effective action for the reggeized graviton interactions (see Ref. [25]).

3. Production Amplitudes in the Multi-Regge Kinematics

Several years ago Z. Bern, L.Dixon and V.Smirnov suggested an explicit expression at $N_c \to \infty$ for multi-gluon production amplitude in $N = 4$ SUSY with the maximal helicity violation [26]. It turned out, that this amplitude is not correct already in two loops [27]. The reason is that the BDS amplitude does not satisfy the Steinmann requirement of absence of simultaneous singularities in the overlapping channels [28]

$$\Delta_{s_r}\Delta_{s_{r+1}} M_{2\to 2+n} = 0. \tag{26}$$

Moreover, it does not contain the Mandelstam cut contributions [29]. These contributions appear in the planar amplitudes starting from 6

external legs [30]. The correct amplitude differs from the BDS expression by a factor - so-called remainder function R. This function should be conformal invariant in the momentum space [31]. In LLA R can be calculated in the multi-Regge kinematics from the BFKL and BKP equations because its hamiltonian coincides with the local hamiltonian of the open integrable spin chain [32]. We consider below the analytic properties of the planar gluon production amplitudes in $N = 4$ SUSY at the multi-Regge kinematics. For 6-point amplitude such study was done in Ref. [33]). In an accordance with the Steinmann constraint for one gluon production the amplitude has the form (cf. [34])

$$\frac{M_{2\to 3}}{\Gamma(t_1)\Gamma(t_2)|\Gamma_a|} = c_R^a(-\widetilde{s})^{j_2}(-s_1)^{j_1-j_2} + c_L^a(-\widetilde{s})^{j_1}(-s_2)^{j_2-j_1},\ \widetilde{s} = s|k_\perp^a|^2 \tag{27}$$

where $\Gamma(t_r)$ are reggeon residues, c_R^a and c_L^a are two real vertices for the gluon a with the transverse momentum $k_\perp^a$ produced from the reggeized gluon [27]

$$c_R^a = \frac{\sin\pi\omega_{1a}}{\sin\pi\omega_{12}},\ c_L^a = \frac{\sin\pi\omega_{2a}}{\sin\pi\omega_{21}} \tag{28}$$

and ω_a is the phase of the complex production vertex [27]

$$\Gamma_a(\ln|k_\perp^a|^2 - i\pi) = |\Gamma_a|\, e^{i\pi\omega_a}. \tag{29}$$

In the case of production of two particles a and b the expression for the multi-Regge amplitude consists of five terms

$$\begin{aligned}\frac{M_{2\to 4}}{\Gamma(t_1)\Gamma(t_2)|\Gamma_a||\Gamma_b|} &= c_R^a c_L^b(-\widetilde{s})^{j_2}(-s_1)^{j_1-j_2}(-s_3)^{j_3-j_2} + \\ &+ c_R^a c_R^b(-\widetilde{s})^{j_3}(-\widetilde{s}_{012})^{j_2-j_3}(-s_1)^{j_1-j_2} + \\ &+ c_L^a c_L^b(-\widetilde{s})^{j_1}(-\widetilde{s}_{123})^{j_2-j_1}(-s_3)^{j_3-j_2} \\ &+ c_L^a c_R^b\Big(k(-\widetilde{s})^{j_3}(-\widetilde{s}_{012})^{j_1-j_3}(-s_2)^{j_2-j_1} + \\ &+ l(-\widetilde{s})^{j_1}(-\widetilde{s}_{123})^{j_3-j_1}(-s_2)^{j_2-j_3}\Big),\end{aligned} \tag{30}$$

where the invariants $\widetilde{s}$ contain the corresponding factors depending on the transverse momenta. The quantities k and l

$$k = \frac{\sin\pi\omega_1}{\sin\pi\omega_2}\,\frac{\sin\pi\omega_{23}}{\sin\pi\omega_{13}},\ l = \frac{\sin\pi\omega_3}{\sin\pi\omega_2}\,\frac{\sin\pi\omega_{21}}{\sin\pi\omega_{31}},\ k+l=1 \qquad (31)$$

are fixed from the factorization relations for the Regge poles [34]. To formulate these factorization relations it is needed to introduce the signatures $\tau_r = \pm 1$ for reggeons in t_r-channels. Then for the planar case the generating function for amplitudes $2 \to n+1$ in all physical regions related by twists in the corresponding t-channel lines can be written as follows

$$A^{\tau_1\ldots\tau_n}_{2\to n+1} = A + \sum_{r=1}^{n}\tau_r\,A_r + \sum_{r_1<r_2}\tau_{r_1}\tau_{r_2}\,A_{r_1r_2} + \ldots + \tau_1\tau_2\ldots\tau_n\,A_{1\ldots n}. \qquad (32)$$

The factorized Weis expression for this expression has the following complex form [34]

$$\frac{A^{\tau_1\ldots\tau_n}_{2\to n+1}}{s\Gamma(t_1)\Gamma(t_2)|\Gamma_a||\Gamma_b|\ldots} = |s_1|^{\omega_1}\xi_1 V^{1,2}|s_2|^{\omega_2}\xi_2 V^{2,3}\ldots V^{n-1,n}|s_n|^{\omega_n}\xi_n, \qquad (33)$$

where

$$\xi_r = e^{-i\pi\omega_r} - \tau_r,\ \xi_{12} = e^{-i\pi\omega_{12}} + \tau_1\tau_2,\ V^{1,2} = \frac{\xi_{12}}{\xi_1}c^a_R + \frac{\xi_{21}}{\xi_2}c^a_L. \qquad (34)$$

For the case of the transition $2 \to 4$ we obtain the amplitude in two physical regions, where the BDS expression is not correct,

$$\frac{A^{\tau_1\ldots\tau_3}_{2\to 4}}{s|s_1|^{\omega_1}|s_2|^{\omega_2}|s_3|^{\omega_3}\Gamma(t_1)\Gamma(t_2)|\Gamma_a||\Gamma_b|} = \ldots + \left(\tau_1\tau_3 e^{-i\pi\omega_2} + \tau_1\tau_2\tau_3\right)A + \ldots. \qquad (35)$$

Here

$$A = \frac{2\cos\pi\omega_2\,\sin\pi\omega_a\,\sin\pi\omega_b}{i\sin\pi\omega_2} + i\sin\pi(\omega_a+\omega_b) + \cos\pi\omega_{ab} \qquad (36)$$

contains the non-physical pole $1/\sin\pi\omega_2$. But just in these physical regions there is a contribution of the Mandelstam cuts [27]. For

example at $s, s_2 > 0, s_1, s_3 < 0$ we obtain the following complex structure of the cut

$$A_{cut} = i \int \frac{d\omega_2'}{2\pi i} (-s_2)^{\omega_2'} f_{\omega_2'} \tag{37}$$

with a real function $f_{\omega_2'}$. Therefore we can redefine the expression for the Regge pole contribution by subtracting from its expression two first term and including them in the redefined cut contribution [33]. In such manner we have

$$A_{pole}^{2\to 4} = \cos \pi\omega_{ab}. \tag{38}$$

As a result, in the region $s, s_2 > 0,\ s_1, s_3 < 0$ we obtain the following dispersion representation for the remainder function [33,35]

$$R\, e^{i\pi\delta} = \cos\, \pi\omega_{ab} + i\, \frac{a}{2} \sum_{n=-\infty}^{\infty} (-1)^n e^{i\phi n} \times$$
$$\times \int_{-\infty}^{\infty} \frac{|w|^{2i\nu} d\nu}{\nu^2 + \frac{n^2}{4}}\, \Phi(\nu, n) \left(\frac{-1}{\sqrt{u_2 u_3}} \right)^{\omega(\nu,n)}, \tag{39}$$

where the anharmonic ratios in the momentum space are

$$u_1 = \frac{s s_2}{s_{012} s_{123}},\ u_2 = \frac{s_1 t_3}{s_{012} t_2},\ u_3 = \frac{s_3 t_1}{s_{123} t_2},$$
$$|w|^2 = \frac{u_2}{u_3},\ \cos\phi = \frac{1 - u_1 - u_2 - u_3}{2\sqrt{u_2 u_3}}, \tag{40}$$

the BDS phases

$$\delta = \frac{\gamma_K}{8}\, \ln \frac{|w|^2}{|1+w|^4},\ \omega_{ab} = \frac{\gamma_K}{8}\, \ln |w|^2, \tag{41}$$

the impact factor product [36]

$$\Phi = 1 - a \left(\frac{E_{\nu n}^2}{2} + \frac{3}{8}\, n^2/(\nu^2 + \frac{n^2}{4})^2 + \zeta(2) \right), \tag{42}$$

and the BFKL kernel eigenvalue

$$\omega(\nu, n) = -a E_{\nu,n} - a^2(\epsilon_{\nu n}^{FL} + 3\zeta(3)) \tag{43}$$

in leading [30]

$$E_{\nu n} = -\frac{|n|/2}{\nu^2+\frac{n^2}{4}} + 2\Re\psi(1+i\nu+\frac{|n|}{2}) - 2\psi(1), \qquad (44)$$

and next-to-leading [35] approximations

$$\epsilon^{FL}_{\nu n} = -\frac{\Re}{2}\left(\psi''(1+i\nu+\frac{|n|}{2}) - \frac{2i\nu\psi'(1+i\nu+\frac{|n|}{2})}{\nu^2+\frac{n^2}{4}}\right) -$$
$$-\zeta(2)\,E_{\nu n} - \frac{1}{4}\,\frac{|n|\left(\nu^2-\frac{n^2}{4}\right)}{\left(\nu^2+\frac{n^2}{4}\right)^3}. \qquad (45)$$

The analogous dispersion relations are obtained for the 7-point amplitude in all physical regions having the Mandelstam cut contributions [37].

Acknowledgments

I thank the Hamburg University for hospitality and my collaborators J. Bartels, V.S. Fadin, A. Kormilitzin, A. Prygarin and A. Sabio Vera for helpful discussions. This work was supported by the RFFI grant.

1. V.N. Gribov, Sov. Phys. JETP **14**, 478 (1962).
2. S. Mandelstam, Nuovo Cim. **30**, 1148 (1963).
3. V.N. Gribov, I.Ya. Pomeranchuk and K.A. Ter-Martirosyan, Phys. Rev. B **139**, 184 (1965).
4. V.N. Gribov, Sov. Phys. JETP **26**, 414 (1968).
5. L.N. Lipatov, Sov. J. Nucl. Phys. **23**, 338 (1976); V.S. Fadin, E.A. Kuraev, L.N. Lipatov, Phys. Lett. B **60**, 50 (1975); E.A. Kuraev, L.N. Lipatov, V.S. Fadin, Sov. Phys. JETP **44**, 443 (1976).
6. L.N. Lipatov, Phys. Lett. B **309**, 394 (1993).
7. L.N. Lipatov, Sov. Phys. JETP **63**, 904 (1986).
8. L.N. Lipatov *High energy asymptotics of multi-colour QCD and exactly solvable lattice models*, hep-th/9311037, unpublished.
9. L.N. Lipatov, Nucl. Phys. B **548**, 328 (1999).
10. L.N. Lipatov, Nucl. Phys. B **452**, 369 (1995); Phys. Rept. **286**, 131 (1997).
11. E.N. Antonov, L.N. Lipatov, E.A. Kuraev, I.O. Cherednikov, Nucl. Phys. B **721**, 111 (2005).

12. V.S. Fadin, L.N. Lipatov, Phys. Lett. B **429**, 127 (1998); M. Ciafaloni and G. Camici, Phys. Lett. B **430**, 349 (1998).

13. A.V. Kotikov, L.N. Lipatov, Nucl. Phys. B **582**, 19 (2000).

14. V.S. Fadin, L.N. Lipatov, Phys. Lett. B **706**, 470 (2012).

15. J. Bartels, V.S. Fadin, L.N. Lipatov, G.P. Vacca, arXiv: 1210.0797 [hep-ph].

16. L.N. Lipatov, J. Phys. A **42**, 304020 (2009).

17. A.V. Kotikov, L.N. Lipatov, Nucl. Phys. B **661**, 19 (2003).

18. A.V. Kotikov, L.N. Lipatov, A.I. Onishchenko, V.N. Velizhanin, Phys. Lett. B **595**, 521 (2004); [Erratum-ibid. B **632**, 754 (2006)].

19. A.V. Kotikov, L.N. Lipatov, A.Rej, M. Staudacher, V.N. Velizhanin, J. Stat. Mech. **0710**, P10003 (2007).

20. T. Lukowski, A. Rei, V.N. Velizhanin, Nucl. Phys. B **831**, 105 (2010).

21. J.M. Maldacena, Adv. Theor. Math. Phys. **2**, 231 (1998).

22. S.S. Gubser, I.R. Klebanov, A.M. Polyakov, Phys. Lett. B **428** 105 (1998).

23. E. Witten, Adv. Theor. Math. Phys. **2**, 253 (1998).

24. R.C. Brower, J. Polchinsky, M.J. Strassler, C.I. Tan, JHEP **0712**, 005 (2007).

25. L.N. Lipatov, Physics of Particles and Fields **44**, 391 (2013), arXiv: 1105.31277 [hep-ph].

26. Z. Bern, L.J. Dixon, V.A. Smirnov, Phys. Rev. D **72**, 085001 (2005).

27. J. Bartels, L.N. Lipatov, A. Sabio Vera, Phys. Rev. D **80**, 045002 (2009).

28. O. Steinmann, Helv. Physica Acta **33**, 257, 349 (1960).

29. S. Mandelstam, Nuovo Cim. **30**, 1148 (1963).

30. J. Bartels, L.N. Lipatov, A. Sabio Vera, Eur. Phys. J. C **65**, 587-605 (2010).

31. J.M. Drummond, J. Henn, V.A. Smirnov, E. Sokatchev, JHEP **0701**, 064 (2007); J.M. Drummond, G.P. Korchemsky, E. Sokatchev, Nucl. Phys. B **795**, 385 (2008).

32. L.N. Lipatov, J. Phys. A **42**, 304020 (2009).

33. L.N. Lipatov, Theor. Math. Phys. **170**, 166 (2012), hep-th 1008.1015.

34. I.T. Drummond, P.V. Landshoff, W.J. Zakrzewski, Nucl. Phys. B **11**, 383 (1969); J.H. Weis, Phys. Rev. D **4**, 1777 (1971).

35. V.S. Fadin, L.N. Lipatov, Physics Letters B **706**, 470-476 (2012), hep-th 1111.0782.

36. L.N. Lipatov and A. Prygarin, Phys. Rev. D **83**, 125001 (2011), hep-th 1011.2673.

37. J. Bartels, A. Kormilitzin, L.N. Lipatov, *Analytic structure of the $n = 7$ scattering amplitude in $N = 4$ SYM theory at multi-Regge kinematics: Conformal Regge pole contribution*, preprint DESY 13-209.

EFFECTS OF THE NEXT-TO-LEADING ORDER TERMS IN THE CHIRAL SU(3) LAGRANGIAN ON THE STRANGENESS –1 s-WAVE MESON-BARYON INTERACTIONS

V.K. Magas[1,2], A. Feijoo[1], A. Ramos[1,2]

[1]*Dept. d'Estructura i Constituents de la Matèria, Universitat de Barcelona, Martí Franquès 1, E08028 Barcelona, Spain*
[2]*Institut de Ciéncies del Cosmos, Universitat de Barcelona, Martí Franquès 1, E08028 Barcelona, Spain*

Abstract

The meson-baryon interactions in s-wave in strangeness S=-1 sector are studied using chiral unitarity approach based on next-to-leading order chiral SU(3) Lagrangian. The model is fitted to the large set of experimental data in different two-body channels. The particular attention is paid to the Ξ hyperon production reaction, $\bar{K}N \to K\Xi$, where the effect of the next-to-leading order terms in the Lagrangian play crucial role, since at tree level the cross section of this reaction is zero.

It is well known that the proper theory of strong interaction – Quantum Chromodynamics (QCD) – is not suitable to study low energy hadron dynamics. For such studies the effective theories should be used, and the SU(3) Chiral Perturbation Theory (χPT) is a classical example. This theory is based on the effective Lagrangian with hadron degrees of freedom, which respects the symmetries of QCD, in particular the chiral symmetry $SU(3)_R \times SU(3)_L$. χPT has many

succesful applications, however it fails to describe the hadron dynamics in the vicinity of dynamically generated resonances. The good example of such situation is the kaon-nucleon interaction at low momenta, where the perturbation scheme is violated by the presence of $\Lambda(1405)$ resonance, located only 27 MeV below the KN threshold. In this case the use of some non-perturbative techniques is mandatory. In particular such a situation can be successfully studied within a unitary extension of Chiral Perturbation Theory (UχPT), originally proposed in [1], where the unitarization is implemented in coupled channels.

The $\Lambda(1405)$ resonance is not only a reason to use UχPT theory, but also a good test of the predictive power of this approach. The point is that $\Lambda(1405)$ is a dynamically generated resonance. For the first time this was predicted in 1977, see Ref. [2], and later detailed calculations performed in the framework of UχPT have shown that $\Lambda(1405)$ is actually a superposition of two close dynamically generated states: one at lower energy $\approx$1390 MeV with larger width $\approx$130 MeV, which couples most strongly to $\Sigma\pi$ channels; and the other one at higher energy $\approx$ 1420 MeV and with a much narrower width $\approx$30 MeV, which couples most strongly to $\bar{K}N$ channels. Thus, the experimental shape of $\Lambda(1405)$ resonance depends on the details of the given experiment, namely on the relative weight of the $\Sigma\pi$ and $\bar{K}N$ channels in the given reaction. This rather nontrivial prediction has been finally confirmed experimentally, see Ref. [3] for more details.

The UχPT method consist in solving the Lippmann-Schwinger equations in coupled channels, which is reduced to a system of the algebraic equations [4]:

$$T_{ij} = V_{ij} + V_{il} G_l T_{lj}, \tag{1}$$

where T_{ij} is the scattering amplitude for the transition from channel "i" to channel "j"; the subscripts i, j, l run over all the possible channels. In particular, for the meson-baryon interaction in $S = -1$ sector, which is of prime interest for us, there are following 10 channels: $K^- p$, $\bar{K}^0 n$, $\pi^0\Lambda$, $\pi^0\Sigma^0$, $\pi^+\Sigma^-$, $\pi^-\Sigma^+$, $\eta\Lambda$, $\eta\Sigma^0$, $K^+\Xi^-$, $K^0\Xi^0$.

In our study we calculate the loop function, G_l, using dimensional regularization scheme:

$$G_l = \frac{2M_l}{(4\pi)^2}\left\{a_l + \ln\frac{M_l^2}{\mu^2} + \frac{m_l^2 - M_l^2 + s}{2s}\ln\frac{m_l^2}{M_l^2} + \right.$$

$$\left. + \frac{q_{cm}}{\sqrt{s}}\ln\left[\frac{(s+2\sqrt{s}q_{cm})^2 - (M_l^2 - m_l^2)^2}{(s-2\sqrt{s}q_{cm})^2 - (M_l^2 - m_l^2)^2}\right]\right\}, \quad (2)$$

where M_l and m_l are the baryon and meson masses of the "l" channel correspondingly, and a_l are the so called subtraction constants, which are used as free parameters and fitted to the experimental data. Taking into account the isospin symmetry there are only 6 independent subtraction constants. See Ref. [4] for more details.

The V_{ij} is the interaction kernel for (i,j) channels, which is calculated from the chiral Lagrangian up to the corresponding order in momentum over baryon mass. For meson-baryon interaction the lowest order in momentum term, i.e. leading order (LO) term, is the so called Weimberg-Tomozawa (WT) term:

$$V_{ij}^{WT} = -C_{ij}\frac{1}{4f^2}(k^0 + k'^0), \quad (3)$$

which depends only on the one parameter – the pion decay constant f. C_{ij} is a matrix of coefficients; k^μ and k'^μ are the four-moments for the incoming and outgoing mesons in the process. The pion decay constant is well known experimentally, $f_{\rm exp} = 93.4$ MeV, however in LO UχPT calculations this parameters is usually taken to be $f = 1.15 - 1.2 f_{\rm exp}$, in order to partly simulate effect of the higher order corrections.

The interaction kernel up to next-to-leading order (NLO) is also known, however it is only very recently it started to used in real calculations and data fitting [5–9]. The reason is rather straightforward – NLO terms in chiral Lagrangian depend on 7 new parameters, which were not known, and thus the predictive power of the NLO UχPT calculations was rather questionable.

$$V_{ij}^{NLO} = V_{ij}^{WT} + \frac{1}{f^2}\left(D_{ij} - 2(k_\mu k'^\mu)L_{ij}\right)\sqrt{\frac{M_i + E_i}{2M_i}}\sqrt{\frac{M_j + E_j}{2M_j}}, \quad (4)$$

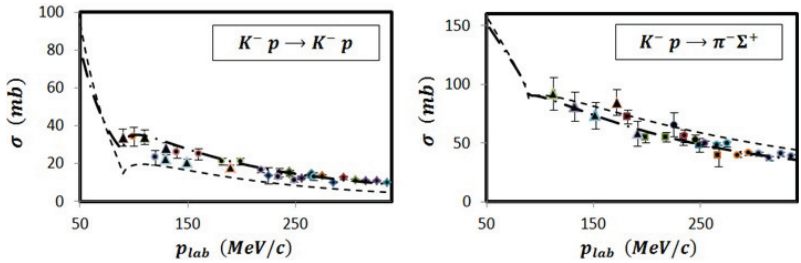

Fig. 1: The total cross section of the $K^- p$ scattering to the indicated channels. WT fit is presented by dashed line; NLO fit – by dot-dashed line. Experimental data are from [11] (diamonds), [12] (circles), [13] (squares), [14] (triangles)

where D_{ij} and L_{ij} are the coefficient matrixes, which depend on the new parameters: b_0, b_D, b_F, d_1, d_2, d_3, d_4 (see [5–9] for more details).

Thanks to great experimental advances of the last years, like for example CLAS photoproduction experiment [10], we have accumulated a sufficient amount of a good quality data to attempt to fit these new parameters. Also due to the large amount of the theoretical studies based on WT interaction we know where this approach fails to describe the data. In particular, in our study we concentrate on the Ξ hyperon production reactions: $K^- p \to K^+ \Xi^-$, $K^0 \Xi^0$, where the effect of the NLO terms in the Lagrangian play crucial role, since at tree level the cross section of this reaction is zero. These reactions are also particularly interesting, because they were not considered in the works of the other groups [5–7, 9].

Having calculated the T-matrix, by solving system of equations (1), we can then calculate the corresponding cross section for $i \to f$ reaction in the following way:

$$\sigma_{if} = \frac{1}{4\pi} \frac{M_i M_f}{s} \frac{k_f}{k_i} |T_{if}|^2 .$$

To simulate the available experimental data we calculate the transitions from $K^- p$ initial state to different final states and study the $\sqrt{s}$ dependence of the corresponding cross sections, some examples are presented in Figs. 1 and 2, and three branching ratios are compared to the experimental data in Table 1. We perform 7 and 14 parameters fits: pion decay constant and 6 subtraction constants in the case of

WT interaction kernel (WT fit), and 7 additional NLO parameters for the NLO kernel (NLO fit).

Looking at Figs. 1, 2 and Table 1 we can conclude that the inclusion of the NLO terms into interaction kernel improves the agreement with data. This has also been shown in more details in Refs. [5–9].

Fig. 2 shows the Ξ hyperon production reactions, which are the key point of this work, as well as of the previous study [8]. Note that these channels are extremely sensitive to the NLO corrections and therefore may play a crucial role in determining the NLO parameters. However, before coming up with the final result of the fit we have to make sure that we have taken into account all the physical processes, significant for these reactions. We can see that although the overall agreement is quite good, still there are some resonance-like shapes in the experimental data, which are not reflected in our smooth curves. In our opinion, which is based on the phenomenological study [22], this indicates the necessity to take into consideration the $\bar{K}N \to Y \to K\Xi$ reactions, where Y stands for some high spin resonances, which couple to these channels. Based on our results, Fig. 2, it seems that $\Sigma(2030)$ and $\Sigma(2250)$ would be good candidates for "Y", what coincides with finding of [22]. These resonances have spins $5/2^-$ and $7/2^+$ respectively, and therefore require a special treatment, analogous to that performed in [23, 24]. This work is in progress now.

The final goal of our study is to find trustable restrictions on the 7 NLO parameters of the chiral Lagrangian. We would like to stress that technically to change in the calculations the WT interaction, eq. (3), to NLO interaction, eq. (4), is rather straightforward. The problem comes from the fact that 7 new parameters of NLO interaction are not well controlled at the moment. Once the stable values for these parameters will be obtained, all the groups doing simulations

T a b l e 1: This table shows the branching ratios at threshold for the best χ^2 fit at tree level (WT) and for NLO calculations, to be compared with experimental values

	$\gamma = \frac{\Gamma(K^-p\to\pi^+\Sigma^-)}{\Gamma(K^-p\to\pi^-\Sigma^+)}$	$R_n = \frac{\Gamma(K^-p\to\pi^0\Lambda)}{\Gamma(K^-p\to neutral\,states)}$	$R_c = \frac{\Gamma(K^-p\to\pi^+\Sigma^-,\pi^-\Sigma^+)}{\Gamma(K^-p\to inelastic\,channels)}$
WT	2.25	0.196	0.636
NLO	2.36	0.197	0.659
Exp.	2.36 ± 0.04	0.189 ± 0.015	0.664 ± 0.011

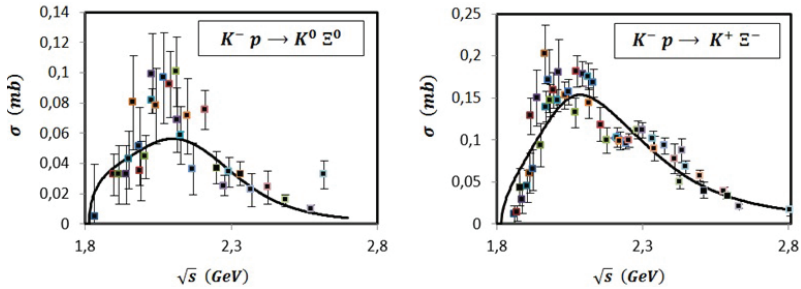

Fig. 2: The total cross section of the $K^- p$ scattering to the indicated channels. Solid line represents results of NLO fit (WT interaction is 0). Experimental data are from [15–21]

based on chiral Lagrangian will be able to increase the accuracy of their calculations to the next order with a rather little effort.

Acknowledgements

This work is supported by the European Community – Research Infrastructure Integrating Activity Study of Strongly Interacting Matter (HadronPhysics3, Grant Agreement Nr 283286) under the 7th Framework Programme, by the contract FIS2011-24154 from MICINN (Spain), and by the Generalitat de Catalunya, contract 2009SGR-1289.

1. N. Kaiser, P. B. Siegel, W. Weise, Nucl. Phys. A **594**, 325 (1995).
2. M. Jones, R.H. Dalitz and R.R. Horgan, Nucl. Phys. B **129**, 45 (1977).
3. V.K. Magas, E. Oset, A. Ramos, Phys. Rev. Lett. **95**, 052301 (2005).
4. E. Oset, A. Ramos, Nucl. Phys. A **636**, 99 (1998).
5. B. Borasoy, R. Niβler, W. Wiese, Eur. Phys. J. A **25**, 79 (2005).
6. Y. Ikeda, T. Hyodo, W. Wiese, Nucl. Phys. A **881**, 98 (2012).
7. T. Hyodo, D. Jido, Progress in Particle and Nuclear Physics **67**, 55 (2012).
8. A. Feijoo, Master Thesis (Master Interuniversitario de Fisica Nuclear), Universidad de Barcelona, Spain, 2012.
9. Zhi-Hui Guo, J.A. Oller, Phys. Rev. C **87**, 035202 (2013).
10. K. Moriya *et al.* [CLAS Collaboration], Phys. Rev. C **87**, 035206 (2013).
11. R. O. Bangerter *et al.*, Phys. Rev. D **23**, 1484 (1981).

12. J. Ciborowski *et al.*, J. Phys. G **8**, 13 (1982).
13. T.S. Mast *et al.*, Phys. Rev. D **14**, 13 (1976).
14. J.K. Kim, Phys. Rev. Lett. **14**, 89 (1965).
15. G. Burgun *et al.*, Nucl. Phys. B **8**, 447 (1968).
16. J.R. Carlson *et al.*, Phys. Rev. D **7**, 2533 (1973).
17. P.M. Dauber *et al.*, Phys. Rev. **179**, 1262 (1969).
18. M. Haque *et al.*, Phys. Rev. **152**, 1148 (1966).
19. G.W. London *et al.*, Phys. Rev. **143**, 1034 (1966).
20. T.G. Trippe, P. E. Schlein, Phys. Rev. **158**, 1334 (1967).
21. W.P. Trower *et al.*, Phys. Rev. **170**, 1207 (1968).
22. D.A. Sharov, V.L. Korotkikh, D.E. Lanskoy, Eur. Phys. J. A **109**, 47 (2011).
23. K. Nakayama, Y. Oh and H. Habertzettl, Phys. Rev. C **74**, 035205 (2006).
24. K. Shing Man, Y. Oh and K. Nakayama,, Phys. Rev. C **83**, 055201 (2011).

GENERALIZED LOOP SPACE AND TMDS

T. Mertens

Departement Fysica, Universiteit Antwerpen,
B-2020 Antwerpen, Belgium

Abstract

Recast of a gauge theory in the Wilson loop space representation, where the degrees of freedom are absorbed in the path/loop dependence, allows one, in principle, to relate observables (field correlators) with fully gauge invariant fundamental variables. Over-completeness of this space requires the introduction of an equivalence relation which is provided by Wilson loop functionals operating on piecewise regular paths. On the other hand, certain classes of the Wilson loops possess the same singularity structure as some Transverse Momentum Dependent PDFs (TMDs), which are not renormalizable by the common methods due to exactly this singularity structure. By introducing geometrical operators, like the area-derivative, we derive an evolution equation for these Wilson loops and propose to develop further this method to construct appropriate renormalization scheme and full set of evolution equations for the TMDs.

1. Introduction

Wilson lines (also called gauge links or eikonal lines) emerge naturally in gauge theory as the parallel transporter or holonomy of the gauge connection. This can be easily seen from the directional derivative:

$$\lim_{\epsilon \to 0} \frac{1}{\epsilon} \left(\psi(x + \epsilon n) - \psi(x)\right), \tag{1}$$

of a Dirac field $\psi(x)$. Written in the form (1) this derivative is not well defined due to the fact that gauge fields are local and this is not

taken into account. This is solved by parallel transporting one of the fields by use of the parallel transporter (2):

$$U(y,x;\Gamma) = \exp\left(\frac{i}{\hbar}g\int_{\Gamma} A_\mu \mathrm{d}x^\mu\right), \tag{2}$$

which is *path dependent*. Applying this operator to parallel transport the Dirac field $\psi(x)$ to $x+\epsilon n$, and expanding to first order in ϵ results in:

$$\psi(x+\epsilon n) = \psi(x) + \epsilon n^\mu \partial_\mu \psi(x) + \mathcal{O}(\epsilon^2), \tag{3}$$

$$D_\mu \psi(x) = \partial_\mu \psi(x) + igA_\mu(x)\psi(x), \tag{4}$$

the usual covariant derivative.

Eq. (5) shows the definition of the hadronic tensor, written in function of the correlator $\Phi^\Gamma_{ss'}(x,\vec{k}_\perp)$ which is shown in (6). Here we have explicitly written the spin and transverse momentum dependence, which give rise to the polarization dependent and transverse momentum distribution (TMDs) functions for (SI)DIS.

$$W_{\mu\nu} = e_q^2 \int \frac{d^4k}{(2\pi)^4} \mathrm{Tr}\left(\gamma^\nu (\not{k} + \not{q})\gamma^\mu \Phi^\Gamma_{ss'}(x,\vec{k}_\perp)\right)\delta\left((k+q)^2\right), \tag{5}$$

$$\Phi^\Gamma_{ss'}(x,\vec{k}_\perp) = \int d^4x\; e^{-ikx}\langle P,s\left|\bar{\psi}(x)\;\Gamma\;\psi(0)\right|P,s'\rangle. \tag{6}$$

It should be clear from (6) that this correlator is not gauge invariant as it depends on fields at two different space-time points. By introducing a Wilson line $\mathcal{W}_{\mathrm{TMD}} = U(x,0;\Gamma)$ one is able to construct a gauge-invariant correlator $\Phi^\Gamma_{ss'}(x,\vec{k}_\perp)$ shown in (7). For a discussion on the physical interpretation and structure of this gauge link and a general introduction to TMDs I refer to [1–3].

$$\Phi^\Gamma_{ss'}(x,\vec{k}_\perp) = \frac{1}{2}\int \frac{dz^- d^2z_\perp}{(2\pi)(2\pi^2)} e^{ik\cdot z}\left\langle P,s\left|\overline{\psi}(x)\Gamma\mathcal{W}_{\mathrm{TMD}}\;\psi(0)\right|P,s'\right\rangle_{z^+=0}. \tag{7}$$

2. Generalized Loop Space

The Ambrose-Singer theorem allows the rewriting of a gauge theory in function of the holonomy of the gauge connection 1-forms, which

depends on the loop over which this holonomy is calculated, and thus naturally introduces a loop space [4–6]. One of the issues with this approach is that a naive loop space is over-complete, which can be solved by the introduction of an equivalence relation that in our case will be the Wilson Loop Functional (WLF), the trace of the holonomy over the loop Γ, defined in (8). To consistently be able to reconstruct the gauge theory extra constraints, algebraic, unitarity and Mandelstam constraints, are necessary. They have their origin in the fact that one needs to be able to combine the loops algebraically and that it needs to be possible to write the product of two traces in the WLF as a single trace over some loop.

$$\mathcal{W}(\Gamma) = \mathrm{Tr}\ \mathcal{P} \exp\left[-ig \int_{\Gamma} dz^{\mu}\ A_{\mu}(z) \right] \in \mathbb{C}. \tag{8}$$

Expanding the exponential in (8) returns a sum over integrals (9) which were introduced by Chen [7–10] and are referred to as *Chen Iterated Integrals*. These integrals are a special example of the product integrals introduced by Volterra in 1880 [11]. They solve differential equations of the form $S'(t) = S(t) \cdot A(t)$, where the prime denotes the derivative with respect to t, that give rise to the holonomy (9) in differential geometry [6].

$$U_{\Gamma} = 1 + \int_{\Gamma} \omega + \int_{\Gamma} \omega_1 \omega_2 + \cdots \tag{9}$$

Chen Iterated Integrals are defined as an iterative extension of the usual line integrals:

$$X(\gamma) = I_{i_1 \cdots i_p}(\gamma) = \int_a^b I_{i_1 \cdots i_{p-1}}(\gamma^t)\ dx_{i_p}(t), \tag{10}$$

or after introduction of coordinates:

$$X^{\omega_1 \cdots \omega_r}(\gamma) = \int_{\gamma} \omega_1 \cdots \omega_r = \int_0^1 \left(\int_{\gamma^t} \omega_1 \cdots \omega_{r-1} \right) \omega_r(t) dt, \tag{11}$$

where $\omega_k(t) \equiv \omega_k(\gamma(t)) \cdot \dot{\gamma}(t)$ and γ^t represents the path for $t \in [0, t]$. Note that the path-ordering operator $\mathcal{P}$ is absorbed in the integrals

by the way they are defined. Motivated by (12) one introduces the shuffle product (definition 2.1) on the set of 1-forms $\Omega = \bigwedge^1 \mathcal{M}$ (Real, Complex or Lie-Algebra valued) of the base manifold $\mathcal{M}$.

$$\int_\gamma \omega_1 \cdots \omega_k \int_\gamma \omega_{k+1} \cdots \omega_{k+l} = \sum_\sigma \int_\gamma \omega_{\sigma(1)} \cdots \omega_{\sigma(k+l)}, \qquad (12)$$

where σ is running over all (k,l)-shuffles.

Definition 2.1 *Let* $\omega_1 \cdots \omega_k = \omega_1 \otimes \cdots \otimes \omega_k \in \bigotimes^k \left(\bigwedge^1 \mathcal{M} \right), k \geq 1$ *and* $\omega_1 \cdots \omega_k = 0$*, for* $k = 0$*, the shuffle multiplication is given by:*

$$\omega_1 \cdots \omega_k \bullet \omega_{k+1} \cdots \omega_{k+l} = \sum_\sigma{}' \omega_{\sigma(1)} \cdots \omega_{\sigma(k+l)}$$

with $\sum_\sigma{}'$ *the sum over all* (k,l)*-shuffles.*

Using this shuffle product Chen [7–10] introduced the notion of an algebraic path, which can be seen as a generalization of the intuitive notion of a path in a manifold in much the same way as distributions in calculus generalize functions. This shuffle algebra is Banach, Hopf, Commutative, Nuclear and Locally Multiplicative-Convex. These porperties then allow for the existence of a Gel'fand space (definition 2.2) so that we can introduce the concept of a generalized loop (definition 2.3).

Definition 2.2 *Let* A *be a commutative Banach algebra, then we write* $\triangle(A)$ *(or* $\triangle$*) for the collection of nonzero complex homomorphisms* $h : A \to \mathbb{C}$*. Elements of the Gel'fand space are called characters.*

Definition 2.3 *A Generalized Loop based at* $p \in \mathcal{M}$ *is a character of the algebra* $\mathcal{A}_p$ *or, equivalently, a continuous complex algebra homomorphism* $\tilde{\alpha} : Sh(\mathcal{M}) \to \mathbb{C}$*, that vanishes on the ideal* $\mathbf{J}_p$*. For the details on the ideal* $\mathbf{J}_p$ *I refer to [6–10].*

It should be clear from (8) and the above discussion that the Wilson Loop Functionals form such a complex algebra homomorphism $\mathcal{A}_p$ depending on the (algebraic) path/loop under consideration. The continuity follows from introducing the Gel'fand topology on the set

of Wilson Loop Functionals, which is the weak*-induced topology of these homomorphisms. This topology can be shown to be Hausdorff allowing for a consistent definition of convergence. Introducing the product $\tilde{\alpha} \star \tilde{\beta} = \widetilde{\alpha \cdot \beta}$ turns the generalized loop space in a topological group, with which one can associate an infinite dimensional Lie Algebra. The pointed differentiations (definition 2.4) form a tangent space to the generalized loop space and can be shown to be isomorphic to this Lie Algebra.

Definition 2.4 *A pointed differentiation is a pair* (d, p) *where* $d : \mathfrak{U} \to \Omega$ *is a differentiation and* $p \in Alg(\mathfrak{U}, k)$.

3. Wilson Loops on the Light-Cone – a New Derivative

As a first example we studied the vacuum expectation value of a Wilson loop quadrilateral on the light-cone (figure 1), which resulted at first order in [12]:

$$W_{\text{L.O.}}(\Gamma_\square) = 1 - \frac{\alpha_s C_F}{\pi} \left(2\pi\mu^2\right)^\epsilon \Gamma(1-\epsilon) \times$$

$$\times \left[\frac{1}{\epsilon^2} \left(-\frac{s}{2}\right)^\epsilon + \frac{1}{\epsilon^2} \left(-\frac{t}{2}\right)^\epsilon - \frac{1}{2} \left(\ln^2 \frac{s}{-t} + \pi^2 \right) \right] + \mathcal{O}(\alpha_s^2), \quad (13)$$

where $s = (v_1 + v_2)^2$ and $t = (v_2 + v_3)^2$. Although the mathematical structure introduced before allows for several differential operators such as the path-derivative and the area-derivative, they unfortunately fail to converge when applied to this specific loop [13]. We thus were forced to introduce a new differential operator (14) graphically represented in figure 2 that for the moment seems to be a special

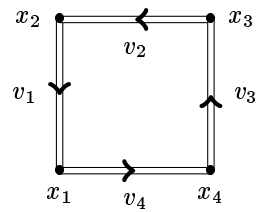

Fig. 1: Parametrisation of a rectangular Wilson loop in coordinate space

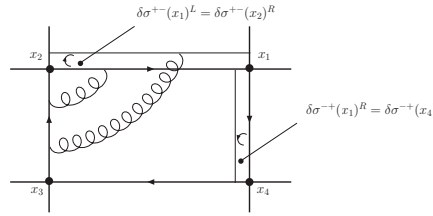

Fig. 2: Graphical representation of the new derivative [15]

case of the Fréchet derivative [14].

$$\begin{aligned}
\delta\sigma^{+-} &= N^+\delta N^- \to v_1\delta v_2 = \frac{1}{2}\delta s,\\
\delta\sigma^{-+} &= -N^-\delta N^+ \to -v_2\delta v_1 = \frac{1}{2}\delta t,\\
\frac{\delta}{\delta\ln\sigma} &\equiv \sigma_{+-}\frac{\delta}{\delta\sigma_{+-}} + \sigma_{-+}\frac{\delta}{\delta\sigma_{-+}}.
\end{aligned} \tag{14}$$

4. Conjecture

Applying this new derivative followed by the usual renormalization derivative $\frac{d}{d\ln\mu}$ to (13), and taking the large N_c limit results in:

$$\mu\frac{d}{d\mu}\frac{\delta\ \ln W(\Gamma_\square)}{\delta\ln\sigma} = -4\ \Gamma_{\rm cusp},\ \ \Gamma_{\rm cusp} = \frac{\alpha_s N_c}{2\pi} + O(\alpha_s^2), \tag{15}$$

where $\Gamma_{\rm cusp}$ is the quark cusp anomalous dimension. We then propose the generalization (16) of (15) as an evolution equation for Wilson loops on the light-cone [15–18].

$$\mu\frac{d}{d\mu}\frac{\delta\ \ln W(\Gamma_\square)}{\delta\ln\sigma} = -\sum_{\rm cusps}\Gamma_{\rm cusp}. \tag{16}$$

5. Other Example

To test our conjecture we consider as an example the Pi-shape (figure 5). Calculating the diagram to first order results in [19]:

$$\begin{aligned}
W(\Gamma_\Pi) &= 1 + \frac{\alpha_s N_c}{2\pi}\ + \left[-L^2(NN^-) + L(NN^-) - \frac{5\pi^2}{24}\right],\\
L(NN^-) &= \frac{1}{2}\left(\ln(\mu NN^- + i0) + \ln(\mu NN^- + i0)\right)^2.
\end{aligned} \tag{17}$$

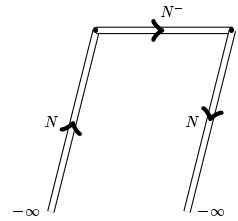

Fig. 3: Π shape

Applying our derivative, with now $\frac{d}{d\sigma} = \frac{d}{d(2NN^-)}$, and the usual energy scaling derivative $\frac{d}{d\ln\mu}$ to (17) shows that this is consistent with our conjecture [15]

$$\mu\frac{d}{d\mu}\left[\frac{d}{d\ln\sigma}\ \ln\ W(\Gamma_\Pi)\right] = -2\Gamma_{\rm cusp}. \qquad (18)$$

Aknowledgements

I would like to thank I. Cherednikov, F. Van der Veken and P. Taels for discussions and comments.

1. A.V. Belitsky, X. Ji, and F. Yuan, Nucl. Phys. B **656**, 165 (2003), arXiv:hep-ph/0208038 [hep-ph].
2. D. Boer, P. Mulders, and F. Pijlman, Nucl. Phys. B **667**, 201 (2003), arXiv:hep-ph/0303034 [hep-ph].
3. A. Belitsky and A. Radyushkin, Phys. Rept. **418**, 1 (2005), arXiv:hep-ph/0504030 [hep-ph].
4. R. Giles, Phys. Rev. D **24**, 2160 (1981).
5. R. Gambini and A. Trias, Phys. Rev. D **21**, 3413 (1980).
6. J.N. Tavares, Int. J. Mod. Phys. A **9**, 4511 (1994), arXiv:9305173 [hep-th].
7. K.T. Chen, J. Alg. **9**, 8 (1968).
8. K.T. Chen, Proc. of the London Math. Soc. **s3-4**, 502 (1954), http://plms.oxfordjournals.org/content/s3-4/1/502.full.pdf+html.
9. K.T. Chen, Tr. Am. Math. Soc. **89**, 395 (1958).
10. K.T. Chen, Tr. Am. Math. Soc. **156**, 359 (1971).
11. V. Volterra, *Sui fondamenti della teoria delle equazioni differenziali lineari.*
12. G.P. Korchemsky, J. M. Drummond, and E. Sokatchev, Nucl. Phys. B **795**, 385 (2008), arXiv:0707.0243 [hep-th].

13. I.O. Cherednikov, T. Mertens, and P. Taels, In preparation (2013).

14. I.O. Cherednikov, T. Mertens, and P. Taels, In preparation (2013).

15. I.O. Cherednikov, T. Mertens, and F.F. Van der Veken, Phys. Rev. D **86**, 085035 (2012), arXiv:1208.1631 [hep-th].

16. I.O. Cherednikov, T. Mertens, and F.F. Van der Veken, Int. J. Mod. Phys. Conf. Ser. **20**, 109 (2012), arXiv:1208.5410 [hep-th].

17. F.F. Van der Veken, I.O. Cherednikov, and T. Mertens, AIP Conf. Proc. **1523**, 272 (2012), arXiv:1212.4345 [hep-th].

18. I.O. Cherednikov, T. Mertens, and F. Van der Veken, Phys. Part. Nucl. **44**, 250 (2013), arXiv:1210.1767 [hep-ph].

19. G. Korchemsky and G. Marchesini, Nucl. Phys. B **406**, 225 (1993), arXiv:hep-ph/9210281 [hep-ph].

UNIFIED DESCRIPTION OF VMP AND DVCS

Andrii Salii

Bogolyubov Institute for Theoretical Physics,
National Academy of Sciences of Ukraine,
UA-03680 Kiev, Ukraine
e-mail: saliy.andriy@gmail.com

Abstract

A Pomeron model with two trems ("soft" and "hard") is suggested and tested on vector meson production (VMP) and deeply virtual Compton scattering (DVCS) data in both photoproduction and electroproduction regions. As the scale of the process hardness a parameter $\widetilde{Q^2} = Q^2 + M_V^2$ was used, where Q^2 is the virtuality of the incoming photon and M_V is the mass of the produced vector particle. With a small number of adjustable parameters, the model fits all available data on VMP an DVCS.

1. Introduction

According to perturbative QCD calculations, the Pomeron corresponds to the exchange of an infinite gluon ladder, producing an infinite set of moving Regge poles, the so-called BFKL Pomeron [1], whose intercept $\alpha(0)$ is near $1.3 \div 1.4$. Phenomenologically, "soft" (low virtuality Q^2) and "hard" (high virtuality Q^2) diffractive processes with Pomeron exchange are described by the exchange of two different objects in the t channel, a "soft" and a "hard" Pomeron (or their QCD gluon images) [2, 3]. This implies the existence of two (or even more) scattering amplitudes, differing by the values of the parameters of the Pomeron trajectory, their intercept $\alpha(0)$ and slope $\alpha'(t=0)$, typically $(1.08 \div 1.09)$ and (0.25), respectively for the "soft" Pomeron, and $(1.3 \div 1.4)$, and $(0.1$ or even less) for the "hard" one.

In the present approach, initiated in Refs. [4,5], we postulate that

1. Regge factorization holds, *i.e.* the dependence on the virtuality of the external particle (virtual photon) enters only the relevant vertex, not the propagator;

2. there is only one Pomeron in nature, the same in all reactions, but it may be complicated, i.e. having many, at least two, components.

2. Two-Component Model

To reproduce the observed trend of hardening as $\widetilde{Q^2}$ – increases, and following Donnachie and Landshoff [6,7], a two-term amplitude, characterized by a two-component – "soft" + "hard" – Pomeron, was suggested: $A(s,t,\widetilde{Q^2}) = A_s(s,t,\widetilde{Q^2}) + A_h(s,t,\widetilde{Q^2})$, or following [4]:

$$A(s,t,Q^2) = \widetilde{H_s}\, e^{-i\frac{\pi}{2}\alpha_s(t)} \left(\frac{s}{s_{0s}}\right)^{\alpha_s(t)} e^{b_s t} + \\ + \widetilde{H_h}\, e^{-i\frac{\pi}{2}\alpha_h(t)} \left(\frac{s}{s_{0h}}\right)^{\alpha_h(t)} e^{b_h t}, \qquad (1)$$

where $H_s = \frac{A_s}{\left(1+\frac{\widetilde{Q^2}}{Q_s^2}\right)^{n_s}}$, $H_h = \frac{A_h\left(\frac{\widetilde{Q^2}}{Q_h^2}\right)}{\left(1+\frac{\widetilde{Q^2}}{Q_h^2}\right)^{n_h+1}}$ and $\widetilde{H}_{h,s} = \frac{s_{0s,h}}{\sqrt{\pi}} H_{s,h}$. $H_{s,h}(\widetilde{Q^2})$ factors define the ralative weight of the two terms as a function of $\widetilde{Q^2} = Q^2 + M_V^2$, that define the hardness of reaction.

The parameters of Pomeron trajectories were fixed to $\alpha_s(t) = 1.08 + 0.25t$, $\alpha_h(t) = 1.40 + 0.1t$, see [8].

Using Eq. (1) we calculate the differential and integrated cross sections:

$$\frac{d\sigma_{el}}{dt} = H_s^2 e^{2\{L(\alpha_s(t)-1)+b_s t\}} + H_h^2 e^{2\{L(\alpha_h(t)-1)+b_h t\}} + \\ + 2H_s H_h e^{L(\alpha_s(t)-1)+L(\alpha_h(t)-1)+(b_s+b_h)t} \cos\Big(\frac{\pi}{2}(\alpha_s(t)-\alpha_h(t))\Big), \qquad (2)$$

$$\sigma_{el} = \frac{H_s^2 e^{2\{L(\alpha_{0s}-1)\}}}{2(\alpha_s' L + b_s)} + \frac{H_h^2 e^{2\{L(\alpha_{0h}-1)\}}}{2(\alpha_h' L + b_h)} + \\ + 2H_s H_h e^{L(\alpha_{0s}-1)+L(\alpha_{0h}-1)} \frac{\mathfrak{B}\cos\phi_0 + \mathfrak{L}\sin\phi_0}{\mathfrak{B}^2+\mathfrak{L}^2}, \qquad (3)$$

where $L = \ln(s/s_0)$, $\phi_0 = \frac{\pi}{2}(\alpha_{0s} - \alpha_{0h})$, $\mathfrak{B} = L\alpha'_s + L\alpha'_h + (b_s + b_h)$, $\mathfrak{L} = \frac{\pi}{2}(\alpha'_s - \alpha'_h)$,

Normalization of the data from different reactions.

Before fitting our model to the available HERA experimental data on $d\sigma_{el}/dt(t)$ and $\sigma_{el}(Q^2, W))$ of VMP and DVCS reactions, we need to normalize the data.

Using the following normalization parameters (see for eg. [9]):

$$f_{\rho^0} : f_\omega : f_\phi : f_{J/\psi} : f_\Upsilon = 0.68 : 0.068 : 0.155 : 1 : 0.75,$$

we obtain that the normalized data $f_i \cdot \sigma_{el}(\widetilde{Q^2})$ of different ractions ρ^0, ω, ϕ and J/ψ lie on the same $(W, \widetilde{Q^2})$ surface, see Fig. 1(left).

Fitting procedure. We performed a global fit of our model, with Eqs. (2) and (3), to all VMP (i.e. J/ψ, ϕ, ρ^0 and Υ) and DVCS HERA data [10–43], with $W > 30$ GeV^2.

For DVCS we fixed: $M^{eff}_{DVCS} = 1.8$ GeV and a normalization factor $f_{DVCS} = 0.091$.

The parameters of the fit are present in Table 1. The corresponding results of the fit are shown in Fig. 1 ($\sigma_{el}(\widetilde{Q^2})$), and Fig. 2 ($\sigma_{el}(W)$, and $d\sigma_{el}/dt(t)$).

Using Eq. (2) and the formula

$$B(\widetilde{Q^2}, W, t) = \frac{d}{dt} \ln \frac{d\sigma_{el}}{dt}, \tag{4}$$

we have calculated the forward slopes and compared them with the experimental data on VMP, within four separate t bins with the mean values of 0.12, 0.25, 0.5, and 0.6 GeV^2. The results are shown in Fig. 1 (right plot).

Table 1: Parameters of the two-component Pomeron model (Eqs. (2) and (3)) obtained from the fit to the combined VMP and DVCS data. $[A_{0s,h}] = \frac{\sqrt{nb}}{\mathrm{GeV}}$, $\left[\widetilde{Q^2_{s,h}}\right] = \mathrm{GeV}^2$, $[\alpha'_{s,h}] = [b_{s,h}] = \mathrm{GeV}^{-2}$, $[n_{s,h}] = [\alpha_{0\,s,h}] = 1$. $s_{0s,h}$ **fixed to 1 GeV^2**

	$A_{0s,h}$	$\widetilde{Q^2_{s,h}}$	$n_{s,h}$	$\alpha_{0\,s,h}$	$\alpha'_{s,h}$	$b_{s,h}$
soft	807	0.46	1.79	1.08	0.25	3.41
hard	47.9	1.30	1.33	1.20	0.01	2.15

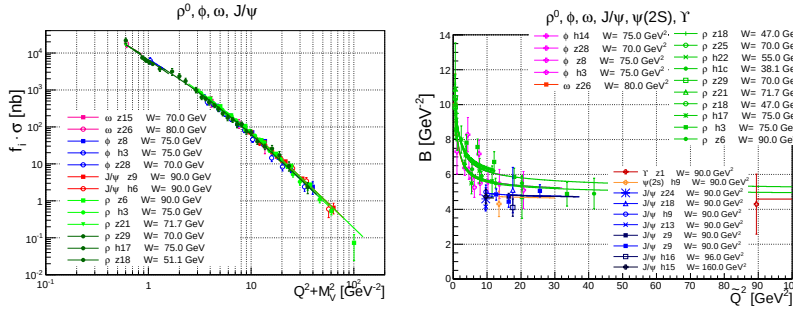

Fig. 1: Fit of Eq. (3) to data on normalized cross sections $f_i \cdot \sigma_{el}(Q^2)$ for ρ^0, ϕ, ω and J/ψ. And experimental data vs theoretical predictions on the slope Eq. (4).

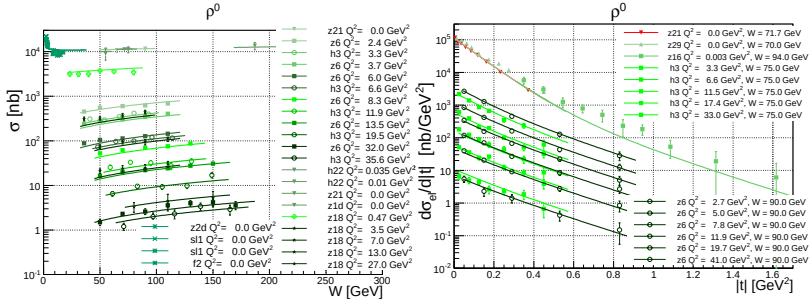

Fig. 2: Fits of the integrated cross section $\sigma_{el}(W)$ Eq. (3) and the differential cross section Eq. (2) to the ρ^0 meson data

3. Discussion of the Results and Conclusions

In this paper we have proposed a complete and economic model that describes both "soft" and "hard" exclusive production of vector particles. The Pomeron, and corresponding scattring amplitude, are composed of two terms, the "soft" and the "hard" components, the relative weight of which governs the "softness" or "hardness" of processes.

In the framework of this model we have analyzed all data on vector meson (ρ^0, ω, ϕ, J/ψ, Υ) production and DVCS obtained at HERA by the H1 and ZEUS collaborations. A global fit was performed with a small number of free parameters (i.e. 8 free parameters, 4 parameters of Pomeron trajectories and 5 parameters for the normalization of the cross sections from 6 processes), universal for all reactions. Some of

the results are present in Figs. 1-2. The values of the parameters are quoted in Table 1. Fit was preformed only for high energies (above 30 GeV).

In order to incorporate DVCS together with VMP we have assigned a non-zero value to the "mass" of the DVCS process, that can be treated as an effective mass of quark-antiquark system, $M^{eff}_{DVCS} = 1.8$ GeV;

The model reasonably well describes the dependance of the slope parameter B as a function of $\widetilde{Q^2}$ (see Figs. 1 for fixed values of t.

As have been found, the "soft" component of the Pomeron dominates in the region of small t and small $\widetilde{Q^2}$. Hence, a parameter, responsible for the "softness" and/or "hardness" of processes, can be presented as a combination of t and Q^2. A simple solution was suggested in Ref. [5] with the introduction of the variable $z = t - Q^2$. The interplay of these two variables remains an important open problem that requires further investigation.

Acknowledgments

The author thanks Laszlo Jenkovszky for ideas and discussions; Salvatore Fazio and Roberto Fiore for collaboration; Rainer Schicker and WP8 of the hadron physics program of the 8th EU program period for partial financial support.

1. V.S. Fadin, E.A. Kuraev, and L.N. Lipatov, Phys. Lett. B **60**, 50 (1975); I.I. Balitsky and L.N. Lipatov, Yad. Fizika **28**, 822 (1978).
2. V. Barone and E. Predazzi, "High-energy particle diffraction", Springer-Verlag Berlin Heidelberg NewYork, ISBN 3540421076, (2002).
3. S. Donnachie *et al.*, "Pomeron physics and QCD", Camb. Monogr. Part. Phys. Nucl. Phys. Cosmol. **19**, 1 (2002).
4. S. Fazio *et al.* Acta. Phys. Pol. B **44**, 1333 (2013), [arXiv:1304.1891].
5. M. Capua *et al.* Phys. Lett. B **645**, 161 (2007), [hep-ph/0605319].
6. P.V. Landshoff, Acta Phys. Polon. B **40**, 1967 (2009), [arXiv:0903.1523].
7. A. Donnachie and P.V. Landshoff, arXiv:0803.0686 [hep-ph].
8. A. Donnachie and P.V. Landshoff, arXiv:1112.2485 [hep-ph].
9. I.P. Ivanov *et al.*, Phys. Part. Nucl. **37**, 1 (2006), [hep-ph/0501034].
10. S. Chekanov *et al.*, Phys. Lett. B **680**, 4 (2009), [arXiv:0903.4205 [hep-ex]].

11. J. Breitweg *et al.*, Phys. Lett. B **437** (1998) 432 [hep-ex/9807020].
12. C. Adloff *et al.*, Phys. Lett. B **483**, 23 (2000) [hep-ex/0003020].
13. C. Adloff *et al.*, Phys. Lett. B **541**, 251 (2002) [hep-ex/0205107].
14. A. Aktas *et al.*, Eur. Phys. J. C **46**, 585 (2006) [hep-ex/0510016].
15. S. Chekanov *et al.*, Nucl. Phys. B **695**, 3 (2004) [hep-ex/0404008].
16. H. Abramowicz *et al.*, Phys. Lett. B **708**, 14 (2012) [arXiv:1111.2133 [hep-ex]].
17. S. Chekanov *et al.*, Eur. Phys. J. C **24**, 345 (2002) [hep-ex/0201043].
18. C. Adloff *et al.*, Eur. Phys. J. C **10**, 373 (1999) [hep-ex/9903008].
19. J. Breitweg *et al.*, Z. Phys. C **75**, 215 (1997) [hep-ex/9704013].
20. J. Breitweg *et al.*, Eur. Phys. J. C **14**, 213 (2000) [hep-ex/9910038].
21. F. D. Aaron *et al.*, JHEP **1005**, 032 (2010) [arXiv:0910.5831 [hep-ex]].
22. M. Derrick *et al.*, Z. Phys. C **73**, 73 (1996) [hep-ex/9608010].
23. J. Breitweg *et al.*, Phys. Lett. B **487**, 273 (2000) [hep-ex/0006013].
24. C. Adloff *et al.*, Phys. Lett. B **483**, 360(2000) [hep-ex/0005010].
25. M. Derrick *et al.*, Phys. Lett. B **377** (1996) 259 [hep-ex/9601009].
26. M. Derrick *et al.*, Phys. Lett. B **380**, 220 (1996) [hep-ex/9604008].
27. C. Adloff *et al.*, Z. Phys. C **75**, 607 (1997) [hep-ex/9705014].
28. S. Chekanov *et al.*, Nucl. Phys. B **718**, 3 (2005) [hep-ex/0504010].
29. J. Breitweg *et al.*, Eur. Phys. J. C **6**, 603 (1999) [hep-ex/9808020].
30. M. Derrick *et al.*, Z. Phys. C **73**, 253 (1997) [hep-ex/9609003].
31. M. Derrick *et al.*, Z. Phys. C **69**, 39 (1995) [hep-ex/9507011].
32. C. Adloff *et al.*, Eur. Phys. J. C **13**, 371 (2000) [hep-ex/9902019].
33. S. Aid *et al.*, Nucl. Phys. B **463**, 3 (1996) [hep-ex/9601004].
34. S. Chekanov *et al.*, PMC Phys. A **1**, 6 (2007) [arXiv:0708.1478 [hep-ex]].
35. J. Breitweg *et al.*, Eur. Phys. J. C **2**, 247 (1998) [hep-ex/9712020].
36. D. Westphal, DESY-F35D-97-11.
37. 31st International Conference on High Energy Physics, ICHEP02, July 24, 2002, Amsterdam, abstract 911, session 6; http://www-h1.desy.de/h1/www/publications/conf/conf_list.html
38. F. D. Aaron *et al.*, Phys. Lett. B **681**, 391 (2009) [arXiv:0907.5289 [hep-ex]].
39. F. D. Aaron *et al.*, Phys. Lett. B **659**, 796 (2008) [arXiv:0709.4114 [hep-ex]].
40. A. Aktas *et al.*, Eur. Phys. J. C **44**, 1 (2005) [hep-ex/0505061].
41. C. Adloff *et al.*, Phys. Lett. B **517**, 47 (2001) [hep-ex/0107005].
42. S. Chekanov *et al.*, JHEP **0905**, 108 (2009) [arXiv:0812.2517 [hep-ex]].
43. S. Chekanov *et al.*, Phys. Lett. B **573**, 46 (2003) [hep-ex/0305028].

CHARGE EXCHANGE REACTION AT HIGH ENERGIES

R. Schicker[1], L. Jenkovszky[2], O. Kuprash[3]

[1]*Phys. Inst., Heidelberg*
[2]*BITP, Kiev*
[3]*DESY, Hamburg*

Abstract

The charge exchange reaction pp $\rightarrow$ n Δ^{++} at high energies is examined. The cross section of this reaction is estimated for RHIC and LHC energies based on data taken at the lower energies of the Intersecting Storage Ring (ISR) at CERN. The interest of such measurements for identifying the associated electromagnetic bremsstrahlung radiation is discussed.

1. Introduction

Diffractive reaction channels contribute about 30% to the total hadronic cross section at the energies of the Large Hadron Collider LHC at CERN. A good understanding of hadronic diffraction is therefore necessary for a comprehensive understanding of proton-proton collisions. In single and double diffractive dissociation, one or both of the protons get diffractively excited, and the proton remnants are very much forward focussed [1]. In central diffraction, a hadronic system is formed at mid-rapidity by the fusion of two Pomerons. The above reactions can, however, also be initiated by the exchange of a photon or a Reggeon. Such non-diffractive exchanges represent a potential background in the analysis of diffraction at high energies. A good understanding of electromagnetic processes, as well as of Reggeon exchanges, is therefore mandatory. The analysis of reaction channels which are purely photon or Reggeon induced are therefore of interest for identifying possible background sources in diffraction.

2. Charge Exchange Reactions

The study of charge exchange mechanism is of interest for an improved understanding of purely Reggeon induced reactions. Reggeon trajectories are defined by bound states of $q\overline{q}$-pairs. The QCD content of these exchanges was studied in Ref. [2], and remains a challenge for theory. The exchange of a charged $q\overline{q}$-pair represents a sudden acceleration of electric charge, accompanied by electromagnetic bremsstrahlung radiation. The measurement of this radiation is of interest as a test of the theorem of Low for soft photon emission as discussed below.

A variety of final states is available in charge exchanges in proton-proton collisions. Charge exchange reactions can be due to the exchange of the pion-, ρ- or A_2-trajectory.

$$pp \to n + \ \Delta^{++} \to n + p\pi^+, \tag{1}$$

$$pp \to \Delta^0 \ + \ \Delta^{++} \to n\pi^0 + p\pi^+, \tag{2}$$

$$pp \to \Delta^0 \ + \ \Delta^{++} \to p\pi^- + p\pi^+. \tag{3}$$

The simplest approach for studying these charge exchange reactions is in binary kinematics.

The relevant scattering amplitude at high energies, with a single Regge exchange (pion, ρ, A_2) is

$$A^{\pm}(s,t) = A_i \xi^{\pm}(t)\beta(t)(s/s_i)^{\alpha(t)}, \tag{4}$$

with $A^{\pm}$ the amplitude for l = even and l = odd exchange, respectively. The variables $s = (p_1+p_2)^2 = (p_3+p_4)^2$, $t = (p_1-p_3)^2 = (p_4+p_2)^2$ are the usual Mandelstam invariants, $\xi^{\pm}(t)$ is the signature factor ($\xi^{\pm}(t) = 1 \pm e^{-i\pi\alpha(t)}$), and $\beta(t)$ is the residue function taken in exponential form $\beta(t) = e^{b_i t}$, where b_i is fitted to each reaction, $pp \to n\Delta^{++}$ or $pp \to \Delta^0\Delta^{++}$. In this type of reactions, the dominant exchange is the pion trajectory at low energies with the ρ-trajectory dominating at high energies. We take a linear form $\alpha(t) = 0.0 + 0.8t$ and $\alpha(t) = 0.5 + 0.9t$ for the pion and ρ-exchange, respectively [3].

Apart from the overall normalization parameter and the standard Regge scale factor s_i, that we set equal to 1 GeV^2, the model contains

only one free parameter, namely b that we find from comparison with measured data.

With the a priory unknown normalization

$$\frac{d\sigma}{dt} = \frac{\pi}{s^2}|A(s,t)|^2 \tag{5}$$

one can calculate the cross section. By a comparison with the existing data and fits, e.g. [4], one finds the differential and integrated cross section.

Measurements of the reaction shown in eq.1. above were made at the Argonne National Zero Gradient Synchrotron [5], and at the Intersecting Storage Ring at CERN [6].

The analysis of the cross section of pp $\rightarrow$ nΔ^{++} at momenta P_L up to 11 GeV/c finds good agreement with the Chew-Low one-pion-exchange mechanism taking into account form-factor models [7–9].

The analysis of the ISR data identifies the ρ- and A_2-contribution which start to dominate the cross section at energies $\sqrt{s} = 31$ GeV [10].

In order to evaluate the cross section at RHIC and LHC energies, we take the ISR data at $\sqrt{s} = 31$, 45 and 53 GeV and fit the data as outlined above.

The cross sections extrapolated to the RHIC energies of $\sqrt{s} = 100$ and 200 GeV shown in Table 1 are 48.5 and 12.2 nb, respectively. The corresponding values for the LHC energies of $\sqrt{s} = 7$ and 14 TeV are 10.0 and 2.4 pb, respectively. These values can be used for further evaluating experimental prospects of measuring the charge exchange channel pp $\rightarrow$ nΔ^{++} at these collider energies.

T a b l e 1: Cross section pp $\rightarrow$ nΔ^{++}

	$\sqrt{s}$ (GeV)	σ (nb)
ISR	31	580 $\pm$90
	45	210$\pm$40
	53	170$\pm$40
RHIC	100	48.5$\pm$5.5
	200	12.2$\pm$1.3
LHC	7×10^3	(10.0$\pm$1.1) $\times10^{-3}$
	14×10^3	(2.4$\pm$0.3) $\times10^{-3}$

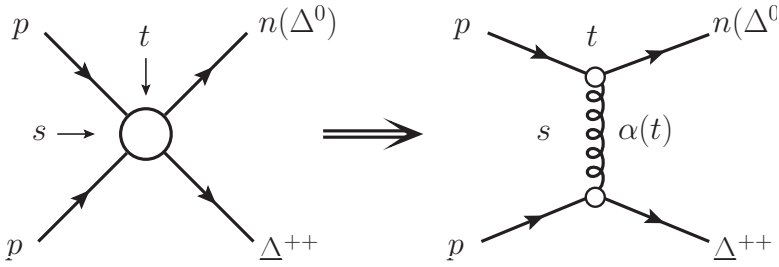

Fig. 1: Charge exchange reaction in binary kinematics

3. Electromagnetic Radiation in Charge Exchange Reactions

Accelerated electric charge emits bremsstrahlung radiation [11]. The theorem of Low relates the radiative leading and next-to-leading order in photon energy of the bremsstrahlung amplitude to the corresponding non-radiative amplitude shown in Fig. 1 [12]. The photons emitted from the external lines result in a pole term in the radiative amplitude, and generate the leading k^{-1}-dependence in the photon energy spectrum. Emission from the internal lines gives rise to the next-to-leading constant term in the energy spectrum. The theorem of Low applies to photons in the soft limit, i.e. to photon energies which are smaller than any other momentum scale in the amplitude. The emission of soft photons in the high energy limit was studied in Ref. [13]. This study finds correction in the next-to-leading radiative amplitude due to the internal structure of the external states. A generalization of the theorem of Low to the production of non-abelian gauge bosons and gravitons is presented in Ref. [14].

4. Summary and Outlook

The cross section for the charge exchange reaction pp $\rightarrow$ nΔ^{++} is extrapolated from data at the ISR to the energies of RHIC and LHC. More refined calculations are under way, and will take into account the three body nature of the final state, including the non-resonant continuum at masses beyond the Δ-resonance. The interest for mea-

suring the associated bremsstrahlung photons is outlined. Quantitative predictions for this associated radiation are under study.

Acknowledgments

We gratefully acknowledge fruitful discussions with L. Lipatov during the Crimean Conference on issues related to the subject of this paper. This work is partially supported by WP8 of the hadron physics program of the 8th EU program period.

1. L. Jenkovszky *et al.*, Mod. Phys. Lett. A **26**, 2029 (2011).
2. R. Kirschner, L.N. Lipatov and L. Szymanowski, Nucl. Phys. B **425**, 579 (1994); Phys. Rev. D **51**, 838 (1995).
3. A.B. Kaidalov and B.M. Karnakov, Sov. J. Nucl. Phys. **7**, Number 5, 685 (1968).
4. K.G. Boreskov *et al.*, Sov. J. Nucl. Phys. **15**, Number 2, 203 (1972).
5. J.D. Mountz *et al.*, Phys. Rev. D **12**, 1211 (1975).
6. H. De Kerret *et al.*, Phys. Lett. B **69**, 372 (1977).
7. G.F. Chew and F.E. Low, Phys. Rev. **113**, 1640 (1959).
8. H.P. Dürr and H. Pilkuhn, Nuovo Cimento **40A**, 899 (1965).
9. J. Benecke and H.P. Dürr, Nuovo Cimento **56A**, 269 (1968).
10. K.J.M. Moriarty and H. Navelet, Phys. Lett. B **71**, 208 (1977).
11. J.D. Jackson, Classical Electrodynamics, John Wiley & Sons.
12. F.E. Low, Phys. Rev. **110**, 974 (1958).
13. V. Del Duca, Nucl. Phys. B **345**, 369 (1990).
14. L.N. Lipatov, Nucl. Phys. B **307**, 705 (1988).

GAUGE INVARIANT INFRARED REGULARIZATION OF THE YANG-MILLS THEORY APPLICABLE BEYOND PERTURBATION THEORY

A.A. Slavnov

Steklov Mathematical Institute, Russian Academy of Sciences
Gubkina st.8, GSP-1,119991, Moscow
and Moscow State University
e-mail: slavnov@mi.ras.ru

Abstract

A gauge invariant infrared regularization of the Yang-Mills theory applicable beyond perturbation theory is constructed.

1. Introduction

In this talk I wish to make a propaganda for a class of symmetries, which were introduced in my paper rather long ago [1] , but recently were applied successfully to the nonperturbative quantization of non-Abelian gauge theories, construction of the infrared regularization, applicable beyond perturbation theory, problem of soliton exitations in Yang-Mills theory.

This symmetry is based on the equivalence theorems. It is well known that the physical content of the theory does not change under canonical transformations. The same statement with some reservations related to the renormalization properties is true also for point transformations $\varphi = \varphi' + f(\varphi')$.

One can also consider more general transformations, which contain explicitely the time derivatives of the fields. Let us transform the fields as follows

$$\varphi = \frac{\partial^n \varphi'}{\partial t^n} + f\left(\frac{\partial^{n-1}\varphi'}{\partial t^{n-1}}, \dots \frac{\partial \varphi'}{\partial t}\right) = \tilde{f}(\varphi'). \tag{1}$$

The spectrum is obviously changed under this transformation. New unphysical excitations appear. The question about the unitarity of the transformed theory arises.

Some ideas about possible violations of unitarity by this transformation are given by the path integral representation for the scattering matrix

$$S = \int \exp\left\{i \int L(\varphi) dx\right\} d\mu(\varphi); \quad \lim_{t\to\pm\infty} \varphi(x) = \varphi_{\text{out,in}}(x). \tag{2}$$

If the change (1) does not change the asymptotic conditions, then the only effect of such transformation is the appearance of a nontrivial jacobian

$$L(\varphi) \to \tilde{L}(\varphi') = L[\varphi(\varphi')] + \bar{c}^a \frac{\delta \varphi^a}{\delta \varphi'^b} c^b. \tag{3}$$

For all new excitations one should take the vacuum boundary conditions.But it is by no means obvious that such boundary conditions may be imposed. To answer this question we note that the transformed lagrangian (3) is invariant with respect to a new symmetry

$$\delta \varphi'_a = c_a, \varepsilon,$$

$$\delta c_a = 0; \quad \delta \bar{c}_a = \frac{\delta L}{\delta \varphi_a}(\varphi')\varepsilon. \tag{4}$$

In these equations ε is a constant anticommuting parameter. On mass shell these transformations are nilpotent and generate a conserved charge Q, belonging to the Grassmann algebra. In this case there exists an invariant subspace of states annihilated by Q, which has a semidefinite norm [1]. For asymptotic space this condition reduces to

$$Q_0 |\phi\rangle_{\text{as}} = 0. \tag{5}$$

The scattering matrix is unitary in the subspace which contains only excitations of the original theory. However the theories described by the L and the $\tilde{L}$ are different, and only expectation values of the gauge invariant operators coincide.

Using this method one can construct a renormalizable formulation of nonabelian gauge theories free of the Gribov ambiguity.

In fact it is not necessary to introduce higher derivatives. Necessary ingredients are new ghost excitations, and new symmetry of the Lagrangian.

These ideas were successfully implemented in the papers ([2–4,9]). A problem of unambiguos quantization of nonabelian gauge theories beyond perturbation theory originates from the classical theory: Even in classical theory the equation

$$D_\mu F_{\mu\nu} = 0 \tag{6}$$

does not determine the Cauchi problem. To deal with gauge theory one has to impose the gauge condition, selecting a unique representative in a gauge equivalent class.

Differential gauge conditions: $L(A_\mu, \varphi) = 0 \rightarrow$ which contains a differential operator as we shall see lead to appearance of Gribov ambiguity. One can try to avoid this problem by applying so called algebraic gauge conditions: $\tilde{L}(A_\mu, \varphi) = 0$. The most known condition of this kind is so called Hamiltonian gauge $A_0 = 0$. However these gauges also lead to problems. From practical point of view the most important problem is the absence of a manifest Lorentz invariance.

Let us consider the problem of Gribov ambiguity for the case of Coulomb gauge. To answer the question about ambiguity in the choice of a representative in the class of gauge invariant configurations in the case of the Coulomb gauge, we must consider a possibility of existence of several solutions of the equation $\partial_i A_i = 0$.

$$\begin{gathered} \partial_i A_i = 0, \\ A'_i = (A^\Omega)_i, \\ \triangle \alpha^a + ig\varepsilon^{abc}\partial_i(A_i^b \alpha^c) = 0. \end{gathered} \tag{7}$$

The last equation has nontrivial solutions rapidly decreasing at spatial infinity, therefore the Coulomb gauge does not select a unique

representative among gauge equivalent configurations. This fact was firstly noticed by V.N. Gribov [6] and later generalized by I. Singer [7] to arbitrary gauge. I wish to emphasize that in perturbation theory the only solution of the (eq. (7)) is $\alpha = 0$. So in perturbation theory the problem of ambiguity is absent. There are two possibilities to solve the problem of ambiguity:

1. Use of this phenomenon to try to explain confinement e.t.c. (Series of works by D. Zwanziger [8] and others.)

2. To avoid the Gribov problem by using new (equivalent) formulation of the Yang-Mills theory using more ghost fields. In the following I consider in more details the second option.

2. Formulation of the Yang-Mills Theory Free of Gribov Ambiguity

Let us consider the classical ($SU(2)$)Lagrangian

$$L = -\frac{1}{4}F^a_{\mu\nu}F^a_{\mu\nu} - m^{-2}(D^2\tilde{\phi})^*(D^2\tilde{\phi}) + (D_\mu e)^*(D_\mu b) + (D_\mu b)^*(D_\mu e) + \\ +\alpha^2(D_\mu\tilde{\phi})^*(D_\mu\tilde{\phi}) - \alpha^2 m^2(b^*e + e^*b), \tag{8}$$

where ϕ is a two component complex doublet, and

$$\tilde{\phi} = \phi - \hat{\mu}; \quad \hat{\mu} = (0, \mu\sqrt{2}g^{-1}), \tag{9}$$

μ is an arbitrary constant. D_μ denotes the usual covariant derivative. To save the place we consider here the group $SU(2)$.

In the following we shall use the parametrization of ϕ in terms of Hermitean components

$$\phi = \left(\frac{i\phi^1 + \phi^2}{\sqrt{2}}\left(1 + \frac{g}{2\mu}\phi^0\right), \frac{\phi^0 - i\phi^3(1 + g/(2\mu)\phi^0)}{\sqrt{2}}\right). \tag{10}$$

The complex anticommuting scalar fields b, e will be parameterized as follows

$$b = \left(\frac{ib^1 + b^2}{\sqrt{2}}, \frac{b^0 - ib^3}{\sqrt{2}}\right)\left(1 + \frac{g}{2\mu}\phi^0\right), \\ e = \left(\frac{ie^1 + e^2}{\sqrt{2}}, \frac{e^3}{\sqrt{2}}\right), \tag{11}$$

where the components e^α are Hermitean, and b^α are antihermitean. This particular parametrization of the classical fields is used as we want to get rid off the ambiguity in choosing the gauge for quantization completely.

In this parametrization the Lagrangian (8) is invariant with respect to "shifted" gauge transformations

$$\begin{aligned}
A^a_\mu &\to A^a_\mu + \partial_\mu \eta^a - g\epsilon^{abc} A^b_\mu \eta^c, \\
\phi^a &\to \phi^a + \frac{g^2}{4\mu}\phi^a\phi^b\eta^b + \mu\eta^a, \\
\phi^0 &\to \phi^0 - \frac{g}{2}\phi^a\eta^a\left(1 + \frac{g}{2}\phi^0\right), \\
b^a &\to b^a + \frac{g}{2}\epsilon^{abc} b^b\eta^c + \frac{g}{2}b^0\eta^a + \frac{g^2}{4\mu}b^a\phi^b\eta^b, \\
e^a &\to e^a + \frac{g}{2}\epsilon^{abc} e^b\eta^c + \frac{g}{2}e^0\eta^a, \\
b^0 &\to b^0 - \frac{g}{2}b^a\eta^a + \frac{g^2}{4\mu}(\phi^a\eta^a), \\
e^0 &\to e^0 - \frac{g}{2}e^a\eta^a.
\end{aligned} \tag{12}$$

The field ϕ^a is shifted by an arbitrary function, therefore one can put $\phi^a = 0$. Contrary to the common wisdom this gauge is algebraic, but Lorentz invariant. It may be used beyond perturbation theory as well.

This Lagrangian is also invariant with respect to the supersymmetry transformations

$$\begin{aligned}
\phi &\to \phi - b\epsilon, \\
e &\to e - \frac{D^2(\phi - \hat{\mu})}{m^2}\epsilon, \\
b &\to b,
\end{aligned} \tag{13}$$

where ϵ is a constant Hermitean anticommuting parameter. This symmetry plays a crucial role in the proof of decoupling of unphysical excitations. It holds for any α, but for $\alpha = 0$ these transformations are also nilpotent.

Note that for further discussion we need only the existence of the conserved charge Q and nilpotency of the asymptotic charge Q_0, as

the physical spectrum is determined by the asymptotic dynamics. In the case under consideration the nilpotency of the asymptotic charge requires $\alpha = 0$, and the massive theory with $\alpha \neq 0$ is gauge invariant but not unitary. It may seem strange as usually the gauge invariance is a sufficient condition of unitarity, because one can pass freely from a renormalizable gauge to the unitary one, where the spectrum includes only physical excitations. In the present case there is no "unitary" gauge. Even in the gauge $\phi^a = 0$, there are unphysical excitations.

For gauge transformations (12) the gauge $\phi^a = 0$ is admissible both in perturbation theory and beyond it. Indeed, if $\phi^a = 0$, then under the gauge transformations (12) the variables ϕ^a become

$$\delta\phi^a = \mu\eta^a \tag{14}$$

and the condition $\phi^a = 0$ implies that $\eta^a = 0$. It is also obvious that for $\alpha \neq 0$ the Lagrangian (8) describes a massive vector field and does not produce infrared singularities.

In terms of shifted variables the Lagrangian (8) looks as follows

$$\begin{aligned} L = -\frac{1}{4}F^a_{\mu\nu}F^a_{\mu\nu} - m^{-2}(D^2\phi)^*(D^2\phi) + m^{-2}(D^2\phi)^*(D^2\hat{\mu}) + \\ + m^{-2}(D^2\hat{\mu})^*(D^2\phi) - m^{-2}(D^2\hat{\mu})^*(D^2\hat{\mu}) + (D_\mu e)^*(D_\mu b) + \\ + (D_\mu b)^*(D_\mu e) + \alpha^2(D_\mu\phi)^*(D_\mu\phi) - \alpha^2(D_\mu\phi)^*(D_\mu\hat{\mu}) - \\ - \alpha^2(D_\mu\hat{\mu})^*(D_\mu\phi) + \alpha^2(D_\mu\hat{\mu})^*(D_\mu\hat{\mu}) - \alpha^2 m^2(b^*e + e^*b). \end{aligned} \tag{15}$$

The shift of the variables ϕ produces the term

$$\alpha^2(D_\mu\hat{\mu})^*(D_\mu\hat{\mu}) = \frac{\alpha^2\mu^2}{2}A^2_\mu \tag{16}$$

which gives a mass to the vector field. The term

$$m^{-2}(D^2\hat{\mu})^*(D^2\hat{\mu}) = \frac{\mu^2}{2m^2}[(\partial_\mu A_\mu)^2 + \frac{g^2}{2}(A^2)^2] \tag{17}$$

makes the theory renormalizable for any α. To avoid complications due to the presence of the Yang-Mills dipole ghosts at $\alpha = 0$ we put $\mu^2 = m^2$.

Invariance of the Lagrangian (16) with respect to the gauge transformation (12) and the supersymmetry transformations (13) makes the effective Lagrangian invariant with respect to the simultaneous BRST transformations corresponding to (12) and the supersymmetry transformations (13). The effective Lagrangian may be written in the form

$$L_{\rm ef} = L + s_1 \bar{c}^a \phi^a = L(x) + \lambda^a \phi^a - \bar{c}^a (\mu c^a - b^a). \qquad (18)$$

One can integrate over $\bar{c}, c$ in the path integral determining expectation value of any operator corresponding to observable. It leads to the change $c^a = b^a \mu^{-1}$. After such integration the effective Lagrangian becomes invariant with respect to the transformations which are the sum of the BRST transformations and the supersymmetry transformations (13) with $c^a = b^a \mu^{-1}$. These transformations look as follows

$$\begin{gathered}
\delta A^a_\mu = D_\mu b^a \mu^{-1} \epsilon, \\
\delta \phi^a = 0, \\
\delta \phi^0 = -b^0 \left(1 + \frac{g}{2\mu} \phi^0\right) \epsilon, \\
\delta e^a = \left(\frac{g}{2\mu} \epsilon^{abc} e^b b^c + \frac{g e^0 b^a}{2\mu} + i \frac{D^2 (\tilde{\phi})^a}{\mu^2}\right) \epsilon, \\
\delta e^0 = \left(-\frac{g e^a b^a}{2\mu} - \frac{D^2 (\tilde{\phi})^0}{\mu^2}\right) \epsilon, \\
\delta b^a = \frac{g}{2\mu} \epsilon^{abc} b^b b^c, \\
\delta b^0 = 0. \qquad (19)
\end{gathered}$$

For the asymptotic theory these transformations acquire the form

$$\begin{gathered}
\delta A^a_\mu = \partial_\mu b^a \mu^{-1} \epsilon, \\
\delta \phi^a = 0, \\
\delta \phi^0 = -b^0 \epsilon, \\
\delta e^a = \partial_\mu A^a_\mu \mu^{-1}, \\
\delta e^0 = -\partial^2 \phi^0 \mu^{-2}, \\
\delta b^a = 0, \\
\delta b^0 = 0. \qquad (20)
\end{gathered}$$

According to the Neuther theorem the invariance with respect to the supertransformations mentioned above generates a conserved charge Q, and the physical asymptotic states may be chosen to satisfy the equation

$$\hat{Q_0}|\psi\rangle_{\rm as} = 0, \tag{21}$$

$$Q_0 = \int d^3x[(\partial_0 A_i^a - \partial_i A_0^a)\mu^{-1}\partial_i b^a - \mu^{-1}\partial_\nu A_\nu^a \partial_0 b^a + \\ + \mu^{-2}\partial^2(\partial_0\phi^0)b^0 - \mu^{-2}\partial_0 b^0 \partial^2(\phi^0 - \mu\alpha^2 b^a A_0^a.] \tag{22}$$

Due to the conservation of the Neuther charge this condition is invariant with respect to dynamics. It was proven in the paper [9] that this symmetry guarantees the decoupling of all unphysical excitations at $\alpha = 0$ and the transitions between the states, annihilated by the charge Q include only three dimensionally transversal components of the Yang-Mills field. Therefore we succeeded to formulate the Yang-Mills theory in such a way that in a topologically trivial sector Gribov ambiguity is absent and the infrared regularization valid beyond perturbation theory is easily constructed. This approach opens also interesting possibilities to consider topologically nontrivial sectors and study the confinement problem.

3. Discussion

A renormalizable manifestly Lorentz invariant formulation of the non-Abelian gauge theories which allows a canonical quantization without Gribov ambiguity (including Higgs model) is possible.

In perturbation theory the scattering matrix and the gauge invariant correlators coincide with the standard ones.

On the basis of this approach a new gauge invariant infrared regularization of Nonabelian gauge theories is constructed.

Acknowlegements

This work was supported partially by the RFFI grant 13-01-12405 ofi-m and by the programm of Russ. Acad. Sci. "Nonlinear dynamics". I wish also to express my grattitude to L.L. Enkovsky for the hospitality extended to me during this conference.

1. A.A. Slavnov, Phys. Lett. B 391 (1991).
2. A.A. Slavnov, Theor. Math. Phys. **161**, 204-211 (2009).
3. A. Quadri, A.A. Slavnov, JHEP **07**, 087-109 (2010).
4. A. Quadri, A.A. Slavnov, Theor. Math. Phys. **166**, 291-302 (2011).
5. A.A. Slavnov, Theor. Math. Phys. **170**, 198-202 (2012).
6. V.N. Gribov, Nucl. Phys. B **139**, 1-19 (1978).
7. I.M. Singer, Comm. Math. Phys. **60**, 7-12 (1978).
8. D. Zwanziger, Nucl. Phys. B **321**, 591-604 (1989); B **323**, 513-544 (1989).
9. A.A. Slavnov, Theor. Math. Phys. **175**, 447-453 (2013).

VIRTUALLY NET SPACE-TIME MODEL AND ITS CONSEQUENCES

G.L. Stavraki

Dorodnicyn Computing Center of RAS,
Vavilov Str. 40, 119991, Moscow, Russia,
e-mail: stavraki@ccas.ru

Abstract

The space-time model is constructed as a causal virtually-field physical structure. The basic equation describes the light-like relation between two "nearest" 4-points and has the form of a noncommutative field equation. Using the correspondence principle we obtained from this equation that the gauge symmetry group is $E6$ group with three fermion multiplets of dimension (1337050) and a scalar multiplet of dimension (70070). Fixing of two group quantum numbers reduces the Fermi family (1337050) to an $SU(5)$ multiplet $(5) + (\overline{10})$ describing the observed fermion spectrum.

1. Model

1.1. Identification of space-time with the world of local Heisenberg field operators

The starting point of the space-time model under consideration is the axiomatic quantum field theory in its Wightman version [1]. In this scheme the world is described by an ensemble of local sets of Heisenberg quantum field operators parametrized by geometrical points of a four-dimensional Lorentz manifold. Attention is paid to the fact that such an array possesses a universal internal structure. This is a causal relation represented by noncommutativity of field operators at two points (in the case of two fermionic fields by a corresponding nonzero anticommutator and in the other cases by a nonzero commutator).

In the proposed model point is *defined* as a complete local set of fields and space-time is considered as the medium of such noncommuting local objects with the only a priori structure, i.e., causal ordering. (It can be noted somewhat conditionally that this construction *identifies space-time with physical vacuum*).

It is assumed that in this medium there exists the causal proximity relation between the "nearest" (by definition) elements of the medium which is described by a universal noncommutative equation relating the fields of two nearest local objects. The proximity equation is constructed using the principle of correspondence with the Lagrangian quantum field theory. The causal proximity in the medium is interpreted here as relation through the act of single-vertex field interaction realized with absolute velocity (the velocity of light). Finally, each two closest elements of the medium are assumed to be virtually distinguished by gravitational self-closure of such elementary relation which (self-closure) is due to the large virtual energy fluctuation in the interaction act region on the Planck scale.

1.2. Structure of the field supermatrix U

The local set of fields U (see [2]) involves several independent families (i) of fermionic fields $\psi_{i,\alpha,n}$ with α-spinor $\alpha = 1:4$ of representation of spin $1/2$ of the spin Lorentz group SL(2) (the metric tensor $g^{\mu\nu} = g_{\mu\nu} = g^{\mu\mu}\delta^{\mu\nu}$, $g^{\mu\mu} = (1,-1,-1,-1)$, $\mu,\nu = 0,1,2,3$ are relativistic 4-vector indices) and n-components of the multiplet of the structural Lie group Ω of the gauge symmetry group. Each of these families is a generating representation of one and the same general linear super Lie group including the group $SL(2)\otimes\Omega$. U can be considered as supertensor of this supergroup explicitly represented by a certain supermatrix [3]. The fermionic fields make up edging of the supermatrix U. r and s-components of Ω-multiplets of respectively scalar and vector fields enter in U as linear forms together with their spin-charge matrix bases in the fermion space.

The explicit expression for the supermatrix U is taken in the model as [2]

$$U = \begin{pmatrix} x_i\cdot(\delta_{ij})\times\begin{pmatrix}{\downarrow}(u_{11})^{\rightarrow} & {\downarrow}(u_{12})^{\rightarrow}\\ {\downarrow}(u_{21})^{\rightarrow} & {\downarrow}(u_{22})^{\rightarrow}\end{pmatrix} & x_i\cdot\begin{pmatrix}{\downarrow}(u_{i,13})^{\Rightarrow}\\ {\downarrow}(u_{i,23})^{\Rightarrow}\end{pmatrix}\\ x_j\cdot\begin{pmatrix}{\Downarrow}(u_{j,31})^{\rightarrow} & {\Downarrow}(u_{j,32})^{\rightarrow}\end{pmatrix} & {\Downarrow}(0)^{\Rightarrow}\end{pmatrix} \quad (1)$$

where (δ_{ij}) is a unit matrix in the numbers of fermion famlies, x_i are numerical factors dependent on the number of the family.

The elements of the fermion edging of the supermatrix U have the form

$$\begin{aligned}
{}_{\downarrow}(u_{i,13})^{\Rightarrow} &= a_{13}\cdot\underbrace{\gamma^{\lambda\Rightarrow}_{\alpha,\cdot}\cdot\psi_{i,\cdot,n}}; \; {}_{\downarrow}(u_{i,23})^{\Rightarrow} = a_{23}\cdot\bar{\psi}_{i,\cdot,n}\cdot\gamma^{\lambda\Rightarrow}_{\cdot,\alpha}; \; {}_{\Downarrow}(u_{j,31})^{\rightarrow} \\
&= -ia_{31}\cdot\bar{\psi}_{j,\lambda\Downarrow,(\alpha,n)\rightarrow} + ic_{31}\cdot(\bar{\psi}_{j,\mu}\gamma^{\mu}\gamma_{\lambda\Downarrow})_{(\alpha,n)\rightarrow}; \\
{}_{\Downarrow}(u_{j,32})^{\rightarrow} &= -ia_{32}\cdot\psi_{j,\lambda\Downarrow,(\alpha,n)\rightarrow} + ic_{32}\cdot(\gamma_{\lambda\Downarrow}\gamma^{\mu}\psi_{j,\mu})_{(\alpha,n)\rightarrow}.
\end{aligned}$$

Here λ is a relativistic index of the 4-vector.

The arrows $\rightarrow(\downarrow)$ run through the values of the joint index (α,n), the arrows $\Rightarrow(\Downarrow)$ are the values of the index of the vector λ, and a, c are the real numerical coefficients.

Within the correspondence principle, the designations ψ_λ, $\bar{\psi}_\lambda$ imply gauge Ω-derivatives of the fermionic fields ψ. The block $\begin{pmatrix} {}_{\downarrow}(u_{11})^{\rightarrow} & {}_{\downarrow}(u_{12})^{\rightarrow} \\ {}_{\downarrow}(u_{21})^{\rightarrow} & {}_{\downarrow}(u_{22})^{\rightarrow} \end{pmatrix}$ unites all the boson variables (the scalar fields φ_r, $\varphi_{\lambda,r}$, φ^+_r, $\varphi^+_{\lambda,r}$ and the vector fields $F_{\mu\nu,s}$) in the form

$$\begin{aligned}
{}_{\downarrow}(u_{11})^{\rightarrow} &= a_{11}\cdot_{\downarrow}\left(\frac{I+\gamma^5}{2}\sigma^{\lambda\mu}t_s\right)^{\rightarrow}\cdot F_{\lambda\mu,s} + \\
&\quad +_{\downarrow}\left(\frac{I+\gamma^5}{2}(y_1\cdot\delta_{r_1r_2}I + y_2\cdot q_{r_1}q^+_{r_2})\right)^{\rightarrow}\cdot\varphi_{r_1}\varphi^+_{r_2}; \\
{}_{\downarrow}(u_{22})^{\rightarrow} &= a_{22}\cdot_{\downarrow}\left(\frac{I-\gamma^5}{2}\sigma^{\lambda\mu}t_s\right)^{\rightarrow}\cdot F_{\lambda\mu,s} + \\
&\quad +_{\downarrow}\left(\frac{I-\gamma^5}{2}(z_1\cdot\delta_{r_1r_2}I + z_2\cdot q^+_{r_2}q_{r_1})\right)^{\rightarrow}\cdot\varphi_{r_1}\varphi^+_{r_2}; \\
{}_{\downarrow}(u_{21})^{\rightarrow} &= -ia_{21}\cdot_{\downarrow}\left(\frac{I-\gamma^5}{2}\gamma^{\lambda}Cq_r\right)^{\rightarrow}\cdot\varphi_{\lambda,r}; \\
{}_{\downarrow}(u_{12})^{\rightarrow} &= -ia_{12}\cdot_{\downarrow}\left(\frac{I+\gamma^5}{2}C^{-1}\gamma^{\lambda}q^+_r\right)^{\rightarrow}\cdot\varphi^+_{\lambda,r}.
\end{aligned}$$

Matrices of the form ${}_{\downarrow}(...)^{\rightarrow}$ act in the space of fermions of one family with ${}_{\downarrow}(\alpha,n)$-components, where α is a spinor relativistic index and n is the index of the fermion charge multiplet. T is transposition in the spinor space and C is the spinor matrix of charge conjugation.

Within the correspondence principle, $F_{\lambda\mu,s}$ are s-components of the gauge vector field strength $A_{\mu,s}$ and $\varphi_{\lambda,r}$, $\varphi^+_{\lambda,r}$ are gauge deriva-

tives of r-multiplets of scalar fields φ_r, φ_r^+. t_s are Hermitian generators of irreducible representation of any of the one-type fermion families in the group Ω, $t_{s_1}t_{s_2} - t_{s_2}t_{s_1} = -iE_{s_1s_2s_3}t_{s_3}$, and $E_{s_1s_2s_3}$ are real completely antisymmetric structural constants of the Lie algebra of the required group Ω. q_r are matrices in the Ω-representation of fermions that satisfy the group covariance relation $t_sq_r + q_rt_s^T = T^{\varphi}_{s,r_1r}q_{r_1}$, where T^{φ}_{s,r_1r} are matrix elements of Hermitian generators of Ω-representation of the scalar fields φ_r. The equation $q_r^T = q_r$ also holds. $a_{..}$, $y_.$, z are numerical real coefficients.

The Ω-group matrices are normalized as follows

$$E_{ss_1s_2}E_{ss_1s_3} = b_1\delta_{s_2s_3}, T^{\varphi}_{s,rr_1}q_rq^+_{r_1} = b_2t_s, (T^{\varphi}_sT^{\varphi}_s)_{r_1r_2} = b_3\delta_{r_1r_2},$$

$$(t_st_s)_{nn_1} = b_4\delta_{nn_1}, (q_rq_r^+)_{nn_1} = b_5\delta_{nn_1}, b_2 = \frac{b_3b_5}{2b_4}, b_1, b_3, b_4, b_5 > 0. \tag{2}$$

In the framework of the principle of correspondence with the conventional quantum field theory, the fields of the supermatrix U are described by the Lagrangian density in the first-order formalism in the Minkowski space

$$L = \frac{i}{2}(\bar\psi_j\gamma^\mu D_\mu\psi_j - D_\mu\bar\psi_j\gamma^\mu\psi_j) - \frac{1}{2}(\bar\psi_jq_rC\bar\psi\varphi_r - \psi_jq_r^+C^{-1}\psi_j\varphi_r^+) +$$

$$+D_\nu\varphi_r(\varphi_r^\nu)^+ + D_\nu\varphi_r^+\varphi_r^\nu - (\varphi_r^\nu)^+\varphi_{\nu,r} + X_{r_1r_2r_3r_4}\varphi_{r_1}\varphi_{r_2}\varphi^+_{r_3}\varphi^+_{r_4} -$$

$$-\frac{1}{2}F_s^{\mu\nu}(\partial_\mu A_{\nu,s} - \partial_\nu A_{\mu,s} - E_{ss_1s_2}A_{\mu,s_1}A_{\nu,s_2}), \tag{3}$$

where D_μ are gauge derivatives $D_\mu\psi = \partial_\mu\psi - it_sA_{\mu,s}\psi$, $D_\mu\varphi_r = \partial_\mu\varphi_r - iT^{\varphi}_{s,rr_1}A_{\mu,s}\varphi_{r_1}$, and $X_{...}$ is an Ω-covariant vertex matrix of scalar-field self-action.

1.3. Equation of motion of the model as an algebraic causal proximity equation in the world of local U supermatrices

In the Lagrangian quantum field theory the existence of algebraic relation between the causal shift and the field interactions is in principle well known. It consists in the fact that the result of physically graduated commutation $[A(1), B(2)]_\pm$ of Heisenberg fields entering

the vertex $\sim ABC$ at causally related points $(1) \prec (2)$ contains an operator contribution due to the field C. In some cases to the first approximation in the causal shift this contribution can even be represented directly in the form

$$[A(1), B(2)]_{\pm} \cong\sim \delta(1,2)+ \sim (C(1) + C(2)).$$

This suggests the idea that beyond the bounds of Lagrangian formalism this field interaction can be described purely algebraically in the spirit of the principle "two (causally separated) fields from a 3-vertex generate a third field": $AB \to C$, $BC \to A$, $AC \to B$. Such a description is seen to correspond schematically to the structure of a bilinear closed algebra. The main assumption there by is the possibility of an algebraic-field description of the causal proximity in which the local complex of fields U is an element of the algebraic structure of space-time.

On the basis of this consideration using the principle of correspondence with Lagrangian field theory at Planck lengths a hypothetic equation was obtained in the model (see [2, 4, 5]) which can conditionally be called the equation of limiting proximity in the set of all U. To write this equation, we preliminarily determine the bilinear antisymmetric operation $\{\,\}$ on the supertensors U which generalizes the commutation operation $[\,]_-$:

$$\{U_1, U_2\} \equiv -4ig([U_1, U_2]_- + [U_1^{\tau}, U_2^{\tau}]_-^{(\tau^{-1})}). \tag{4}$$

Here g is a dimensional constant [length] [2], which is identified with the gravitational constant, $()^{\tau}$, $()^{(\tau^{-1})}$ are direct and inverse supertranspositions of cell supermatrix $\begin{pmatrix} B_1 & F_1 \\ F_2 & B_2 \end{pmatrix}$ of the form

$$\begin{pmatrix} B_1 & F_1 \\ F_2 & B_2 \end{pmatrix}^{\tau} \equiv \begin{pmatrix} B_1^T & F_1^T \\ -F_2^T & B_2^T \end{pmatrix}, \quad \begin{pmatrix} B_1 & F_1 \\ F_2 & B_2 \end{pmatrix}^{(\tau^{-1})} \equiv \begin{pmatrix} B_1^T & -F_2^T \\ F_1^T & B_2^T \end{pmatrix},$$

where $B_i = \sum\limits_{\alpha} {}_{\leftarrow}(\Gamma_{i,\alpha}^{b})^{\rightarrow} b_{i,\alpha}$, $F_i = \sum\limits_{\beta} {}_{\leftarrow}(\Gamma_{i,\beta}^{f})^{\rightarrow} f_{i,\beta}$, $i = 1, 2$ are matrix forms with bosonic fields $b_{i,\alpha}$ and fermionic fields $f_{i,\beta}$ and $()^T$ is a usual transportion referring only to numerical matrix bases ${}_{\leftarrow}(\Gamma_{i,\alpha}^{b})^{\rightarrow}$, ${}_{\leftarrow}(\Gamma_{i,\beta}^{f})^{\rightarrow}$ of the cells B_i, F_i, not to the field operators.

Owing to the special structure of the operation $\{U_1, U_2\}$ it can identically be represented as a supermatrix with elements proportional to field (anti)commutators (antisymmetrized in $1 \leftrightarrow 2$) of the form

$$[(b_{i,\alpha})_1, (b_{j,\beta})_2]_- - (1 \leftrightarrow 2), \qquad [(b_{i,\alpha})_1, (f_{j,\beta})_2]_- - (1 \leftrightarrow 2),$$

$$[(f_{i,\alpha})_1, (f_{j,\beta})_2]_+ - (1 \leftrightarrow 2).$$

The assumed equation is called upon to describe the quntum exchange channel between the nearest elements U_1 and U_2.

We are now in a position to write the final proximity equation (see [2, 4, 5]) determining the causal structure of the set of physical field operators joined in the array of local supermatrices U, which represents here space-time identified with the world of virtual physical processes:

$$\{U_1, U_2\} = S_1(\bar{U}_1 + \bar{U}_2)^\tau S_2. \tag{5}$$

Here $\overline{(\,)}$ is a generalized Dirac conjugation operation $\bar{U} \equiv \Gamma^0 U \Gamma^0$, $\Gamma^0 = \begin{pmatrix} 0 & \gamma^0 \times \delta_{ij} & 0 \\ \gamma_0 \times \delta_{ij} & 0 & 0 \\ 0 & 0 & g^{\mu\Rightarrow}_{\lambda\Downarrow} \end{pmatrix}$. $(\,)^\tau$ is the above-defined supertransposition in the supertensor space, S_1, S_2 are numerical spin Lorentz-anisotropic factors of the form

$$S_1 = \begin{pmatrix} I \times \delta_{ij} & 0 & 0 \\ 0 & I \times \delta_{ij} & 0 \\ 0 & 0 & \frac{21}{4} g^{\varepsilon\Rightarrow}_{\lambda\Downarrow} - 3(n_{-,\lambda\Downarrow} n^{\varepsilon\Rightarrow}_{+} + n_{+,\lambda\Downarrow} n^{\varepsilon\Rightarrow}_{-}) \end{pmatrix},$$

$$S_2 = \begin{pmatrix} I \times \delta_{ij} & 0 & 0 \\ 0 & I \times \delta_{ij} & 0 \\ 0 & 0 & \frac{3}{4} g^{\varepsilon\Rightarrow}_{\lambda\Downarrow} - 3(n_{-,\lambda\Downarrow} n^{\varepsilon\Rightarrow}_{+} + n_{+,\lambda\Downarrow} n^{\varepsilon\Rightarrow}_{-}) \end{pmatrix},$$

$n^\varepsilon_\pm$ is a pair of light-like 4-vectors with the properties $n^\varepsilon_\pm n_{\pm,\varepsilon} = 0$, $n^\varepsilon_\pm n_{\pm,\varepsilon} = 1$, $n^\varepsilon_\pm = n_{\mp,\varepsilon}$.

Thus, from the point of view of the model the fields at supershort lengths form (as a result of their interactions) a local closed algebra. We also emphasize the essential character of the local unification of fields into U-supermatrix – the construction is based on the requirement of algebraic closed ness relative to precisely the U matrix as a whole.

1.4. Space-time in the model as an algebraic causal net

The obtained proximity equation in the interpretation of the correspondence principle describes locally one pair of "oncoming" directions of light. On the basis of the existence of spin-polarized structure of the relativistic vector-gauge-field strength tensor it seems natural to represent an elementary neighborhood in the net construction of space-time as three and only three light directions 3-orthogonal among themselves. An element of such a representation is a cell with corresponding three edges which are type (4) proximity equations. These equations relate one common for them original element U with three new elements corresponding to three mutually space-like ponts. The space-like relation between each two new elements U_1 and U_2 from these three is described by the equation $\{U_1, U_2\} = 0$ which generalizes the (anti)commutator relation of quantum field theory analogous in meaning. The spatial parts of the light vectors corresponding to the new elements in a particular realization describe positions of the six vertices of Euclidean 3-octahedr on with the edge length equal to 1 relative to its center of symmetry: $n^{\mu}_{\pm} \sim \left(\frac{1}{\sqrt{2}}, \mp\frac{1}{\sqrt{2}}, 0, 0\right), \left(\frac{1}{\sqrt{2}}, 0, \mp\frac{1}{\sqrt{2}}, 0\right), \left(\frac{1}{\sqrt{2}}, 0, 0, \mp\frac{1}{\sqrt{2}}\right)$.

Representing space-time conditionally as a beam of local times one can describe schematically its structure in the large as follows. The new elements that occurred from the original element-point in turn generate through new elementary causal relations the next larger layer of mutually space-like points, etc. From this point of view space-time as a whole is a noncomplanar graph of such relations between U elements. In accordance with cosmology this graph can begin with one point and then preserve the three structure (inflation period) during several point multiplication stages (which stands here for space-time expansion). However, for a space structure close to real to occur it is necessary to pass over at a certain stage from the regime of unlimited multiplication of points to the regime of their merging (Friedmann stage).

2. Corollaries

Solution of equation (5) leads within the correspondence principle to the following results.

2.1. The fermion families in the model are three

The necessary condition following from the structure of expression (1) and equation (5) is $\{U_1, U_2\}_{(33)} = 0$. Meeting this requirement, we arrive at the following result.

We have x_1, x_2, x_3 which are three different roots of the equation $x^3 = 1$ and, accordingly, exactly three one-type diagonally interacting fermion families occur automatically in the scheme, which perfectly agrees with experiment.

2.2. The characteristics of the charge symmetry group and the dimensions of particle multiplets are calculated

The solution of equation (5) is reduced to a substitution to it of the explicit expression (1) for U and a consequent operator calculation in the formalism of the light-like quantization by the correspondence principle. This results in a system of equations for the numerical coefficients in U. This system was obtained and solved in the 2008-2009 book[2] by the present author.

The solution of the equations of the model leads to the following relations between the group parameters (2)

$$\frac{b_3}{b_1} = 3; \qquad \frac{b_4}{b_1} = \frac{9}{2}.$$

From this we obtain using the group theory formulas the following. *The initially unknown group Ω appears to be the group E_6 with vector field multiplet of dimension (78). The scalar field multiplet appears to be the E_6-representation of dimension (70070) (in previous publications the value 26026 was given erroneously), and the fermionic field multiplet – a representation of dimension (1337050). This is the second corollary to the model.*

2.3. 15 observed fermions forming one family are singled out of the E_6-multiplet (1337050) by fixation of two quantum numbers

Fixing of the first quantum number reduces the group $E6$ to $SO(10)$ and singles out of the corresponding D5 decomposition of E6 fermion

multiplet (1337050) the D5 multiplets (126)+(1200)+(4125). Fixing of the second quantum number reduces the group $SO(10)$ to $SU(5)$ and in turn singles out (in a unique manner) the A4-multiplet $(5)+(\overline{10})$ from the corresponding A4 decomposition of D5 multiplets singled out by the value of the first number. This compound multiplet exactly coincides in its group quantum numbers with the observed spectrum of fermions of one family. In corollary 2.1 it is also shown that exactly three one-type fermion families occur in the model, *which suggests that from the original 3×1337050 fermions 3×15 observables are singled out in the model. This is the third corollary to the model.*

Thus, in this formally group sense the relation of the model to the observed world appears to be possible. However, it is up to dynamics to decide whether any physical meaning can be attached to this group consideration.

1. R.F. Streater, A.S. Wightman, *PCT, Spin and Statistics and All That* (W.A. Benjamin, INC, New-York-Amsterdam, 1964).

2. G.L. Stavraki, *Model of Space-Time as a Field Noncommutative Causal Structure* (Moscow, URSS, 2009).

3. B. DeWitt, *Supermanifolds* (Cambridge University Press, 1984).

4. G.L. Stavraki, Grav. & Cosmol. **12**, No. 2-3(46-47), 227-230 (2006).

5. G.L. Stavraki, arXiv: gen-ph/0907.0349.

VISUALIZATION OF COSMIC STRING MOTION IN A BACKGROUND GRAVITATIONAL FIELDS

A.V. Zhovtan[1], S.N. Roshchupkin[2]

[1] *Crimean Astrophysical Observatory,*
[2] *Taurida Vernadski V.I. National University*

Abstract

The dynamics of closed cosmic strings in background gravitational fields, using finite-difference method, has been considered. It is shown that motion of the strings is very complicated and its perform complex oscillations and deformed to form loops and cusps.

1. Introduction

Spontaneous symmetry breaking in gauge theories leads to phase transitions in the early Universe [1, 2]. In this period can appear topological structures in the Universe like strings, vacuum domain walls and monopoles. The cosmic strings are linear topological defects. Only infinitely long and closed loop strings can exist. An infinitely long cosmic string is a static cylindrically symmetric configuration of self-interacting scalar field minimally coupled to a $U(1)$ gauge field.

Circular strings in curved backgrounds have been systematically studied [3, 4], showing interesting deviations from their behavior in flat space-times. Since the equations are nonlinear, it is often quite difficult to obtain exact classical solutions in a variety of curved backgrounds [5]. In papers [6, 7] it was shown that the strings equations in the Schwarzschild black hole and Lorentz wormhole space-times are actually non-integrable and exhibit chaotic behavior. It means

that it is only possible to find the exact evolution for some special configurations or perform some numerical calculations [8].

2. Cosmic String in the Curved Background

Cosmic string is characterized by the following parameters: linear mass density μ and radius of the cross section ρ_s. For strings that arise in GUT models, this parameters related with a typical GUT mass scale m_{GUT} and the Higgs constant λ relations

$$\mu \equiv \frac{G\mu}{c^2} = \lambda^{-1}\left(\frac{m_{GUT}}{m_{pl}}\right)^2, \quad \rho_s = \frac{\hbar}{m_{GUT}c} = l_{pl}\left(\frac{m_{pl}}{m_{GUT}}\right), \quad (1)$$

where $m_{pl} = \sqrt{\frac{\hbar c}{G}}$ and $l_{pl} = \sqrt{\frac{\hbar G}{c^3}}$ – Planck mass and length.

To describe the cosmic string dynamics when ρ_s much smaller characteristic radius of curvature of the string can use an approximation in the which the location of the string in space-time is characterized by function of two variables $x^\mu(\tau,\sigma)$ ($\mu = 0,1,2,3$ σ – coordinate along the string, τ – proper time).

The Nambu-Goto string action in a curved space-time can be presented in the form [9]

$$S = \int d\tau d\sigma \left[\frac{\det(\partial_\mu x^M G_{MN}(x)\partial_\nu x^N)}{E(\tau,\sigma)} - \frac{1}{(\alpha')^2}E(\tau,\sigma)\right], \quad (2)$$

where $E(\tau,\sigma)$ is an auxiliary world-sheet density, $M,N = 0,1,\ldots,D-1$; $\mu,\nu = 0,1$ and $\partial_0 \equiv \partial/\partial\tau$, $\partial_1 \equiv \partial/\partial\sigma$. Unlike the Nambu-Goto representation, the representation (2) includes the string tension parameter $1/\alpha'$ as a constant at an additive world-sheet "cosmological" term playing the role of the potential energy. This term may be considered as a perturbative addition for the case of a weak tension [9].

In the gauge $E(\tau,\sigma) = -\gamma(x^M_{,\sigma}G_{MN}(x)x^N_{,\sigma})$ accompanied by the ortho–normality condition $x^M_{,\tau}G_{MN}(x)x^N_{,\sigma} = 0$, where $x^M_{,\tau} \equiv \partial x^M/\partial\tau$, $x^M_{,\sigma} \equiv \partial x^M/\partial\sigma$, the variational Euler–Lagrange equations of motion generated by Eq.(2) acquire the form

$$x^M_{,\tau\tau} - \varepsilon^2 x^M_{,\sigma\sigma} + \Gamma^M_{PQ}(G)[x^P_{,\tau}x^Q_{,\tau} - \varepsilon^2 x^P_{,\sigma}x^Q_{,\sigma}] = 0, \quad (3)$$

and they contain the dimensionless parameter ε. This parameter appears in another string constraint $x^M_{,\tau} G_{MN}(x) x^N_{,\tau} + \varepsilon^2 x^M_{,\sigma} G_{MN}(x) x^N_{,\sigma} = 0$, which is additional to ortho–normality condition.

3. Numerical Simulation of String Motion in Background Gravitational Fields

In recent years a large number of publications devoted to the interaction of topologically non-trivial objects [2, 5], but the question of the influence of gravitational fields on the motion of cosmic strings is still far from being solved. This is due to the fact that the dynamics of cosmic strings in the gravitational fields is described by a complicated system of the nonlinear differential equations, exact solutions are found for a special type of metrics [3, 4]. It should be noted that these studies found only partial solutions that do not allow to give a complete picture of the motion of cosmic strings. More information about the dynamics of cosmic strings can currently be obtained only by numerical experiments, which are now almost absent [10, 11].

The initial boundary value problem for the relativistic string is as follows. We must find a solution $x^M(\tau, \sigma)$ of Eq.(3) that is doubly differentiable in the domain $\Omega = \{(\tau, \sigma) : 0 \leqslant \tau \leqslant \tau_{max}, 0 \leqslant \sigma < 2\pi\}$, is continuously differentiable on the boundary Ω, and satisfies string constraints, the periodicity conditions $x^M(\tau, \sigma) = x^M(\tau, \sigma + 2\pi)$, and two given initial conditions, i.e., the initial string location $x^M(0, \sigma) = \rho^M(\sigma)$ and the initial velocity of string points $\dot{x}^M(0, \sigma) = v^M(\sigma)$. Few results on global solutions of the Cauchy problem for nonlinear hyperbolic systems are known. Equations describing the strings dynamics pertain to such mathematical models in physics whose theoretical exploration is in the initial stage.

There are two main problems in the theory of numerical calculations. First, one must construct discrete approximations for equations and investigate the a priori characteristics of the quality of these approximations, which consists primarily in studying approximation inaccuracy, stability properties of approximations, and the related accuracy of the obtained difference scheme. Second, one must solve difference equations by direct or iteration methods chosen for reasons of economy of computational time for the calculation algorithm.

We now turn to constructing the difference scheme. For this, we introduce a rectangular lattice in the domain of the world-sheet variables τ and σ:

$$\tau_l = l\Delta\tau,\ l = 0,\dots,L,\ \sigma_m = m\Delta\sigma,\ m = 0,\dots,M, \tag{4}$$

where $\Delta\tau = \tau_{max}/L$, $\Delta\sigma = 2\pi/(M+1)$, and L and M are the numbers of sites for the respective variables τ and σ. In constructing the difference scheme, we use a method of difference approximation with which we can easily elaborate the scheme of the first- and second-order approximations on the rectangular lattice for equations with continuous and sufficiently smooth coefficients. We prefer implicit schemes because they converge better than explicit schemes. Then we take the template and compose a scheme with the following weights for space derivatives in different layers:

$$\hat{x} - 2x + \check{x} - \Lambda(\gamma\hat{x} + (1-2\gamma)x + \gamma\check{x}) + f = 0, \tag{5}$$

$$x_m = x^M(\tau_l, \sigma_m),\ \hat{x}_m = x^M(\tau_{l+1}, \sigma_m),$$

$$\check{x}_m = x^M(\tau_{l-1}, \sigma_m), \tag{6}$$

$$\Lambda x_m = h^2(x_{m+1} - 2x_m + x_{m-1}), \tag{7}$$

$$f = \frac{1}{4}(\Gamma^M_{PQ})_{l,m}[(x^P_{l+1,m} - x^P_{l-1,m})(x^Q_{l+1,m} - x^Q_{l-1,m}) -$$
$$-h^2(x^P_{l,m+1} - x^P_{l,m-1})(x^Q_{l,m+1} - x^Q_{l,m-1})], \tag{8}$$

where $h^2 = \frac{(\Delta\tau)^2}{(\Delta\sigma)^2}$. For all weights to be nonnegative, we must take $0 \leqslant \gamma \leqslant 1/2$. In addition to Eqs. (5)–(8) we also compose the difference equations for string constraints and initial conditions. Equation (5) is the implicit three-layer difference equation approximating a partial differential equation with an accuracy of $O((\Delta\tau)^2 + (\Delta\sigma)^2)$. We solve complete system of the equations using the iteration method.

We have tested full system against the well-known solutions for strings in the worm-hole background [12]. The test problems indicate that the proposed method is stable and the absolute error on the lattice $L \times M = 1000 \times 100$ does not exceed 10^{-3}.

For example, Fig. **??** shows consequent frames of string scattering on the three black holes. It is well seen that the string heavily deformed to form self-intersections and cusps due to tidal forces.

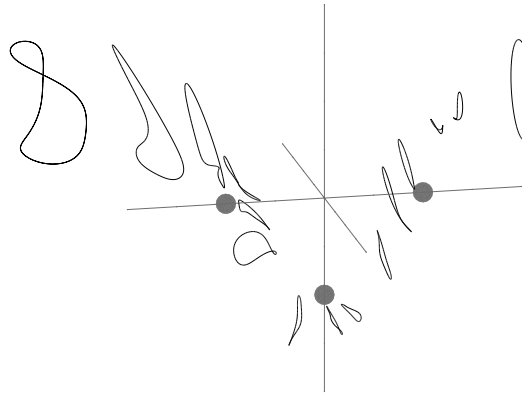

Fig. 1: Example of string scattering on three black holes. At initial moment the string is circular and moves from right to left

4. Conclusion

We have considered dynamics of cosmic strings in the next gravitational fields: stationary axially-symmetric cosmology model [13], Peres space-time, Schwarzschild and Majumdar-Papapetrou space-times etc., using finite-difference method. It is shown that motion of the strings is very complicated – the cosmic strings make complex oscillations and deformed to form loops and cusps. In particular, for Peres space-time, both in case of a radiation field, and in case of a strong gravitational wave, the cosmic string undergo scattering and capture or involve by the field. Animation of the string movement shows characteristic "tumbles" it together with expansion and compression of a string loop and its movement as whole.

For case of the stationary axially-symmetric cosmology model, analysis shows that the string performs complex oscillations and deformations in the process of movement. Moreover, depending on the initial data, cosmic string can be get involved in global Universe rotation into rotary motion about a rotation axis with a gradual winding on the axis. It is also possible, when the string is almost no feels global rotation and moves in an arbitrary manner, nevertheless performing oscillations and deformations to form a self-intersections and cusps.

For case of Majumdar-Papapetrou space-time the cosmic string undergo scattering and backscattering by the gravitational field of black holes. Also there is a strong deformation of the string due to tidal forces. As a result of deformation produced on the string cusps that after some time become loops.

Let's make some more last remarks. Of course, in the given work we have considered idealized situation of movement of a cosmic string as test body in the given curved space-time. We have neglected back reaction, possible radiation by a string of gravitational and electromagnetic waves, finiteness of cross-section of a string and other. However, even in such simplified model, the spent numerical modeling has revealed a rich spectrum of possible types of the string movement. It is characteristic for all nonlinear problems. Therefore for qualitative understanding of dynamics of a cosmic string the given approach is quite adequate and productive.

1. P.J.E. Peebles, *Principles of Physical Cosmology* (Princeton University Press, 1994).
2. A. Vilenkin and E.P.S. Shellard, *Cosmic Strings and Other Topological Defects* (Cambridge University Press, 1994).
3. H.J. de Vega, *Strings in Curved Space-Times*, (1993), arXiv:hep-th/9302052 [hep-th].
4. A.L. Larsen and N. Sanchez, *Strings and Multi-Strings in Black Hole and Cosmological Space-Times*, (1995), arXiv:hep-th/9504007 [hep-th].
5. M.R. Anderson, *The Mathematical Theory of Cosmic Strings* (Institute of Physics Publishing Bristol and Philadelphia, 2003).
6. A.V. Frolov and A.L. Larsen, *Chaotic Scattering and Capture of Strings by Black Hole*, (1999), arXiv:gr-qc/9908039v2 [gr-qc].
7. A.V. Zhovtan and S.N. Roshchupkin, Ukr. J. Phys. **50**, 639 (2005).
8. A.P. Lelyakov and S.N. Roshchupkin, Acta Phys. Polonica B **33**, 593 (2002).
9. A.A. Zheltukhin and S.N. Roshchupkin, Sov. J. Teor. Mat. Fiz. **111**, 402 (1997).
10. M. Snajdr, V. Frolov and J.P. de Villiers, *Scattering of a Long Cosmic String by a Rotating Black Hole*, (2002), arXiv: gr-qc/0208009v3 [gr-qc].
11. F. Dubath, M. Sakellariadou and C.M. Viallet, *Scattering of cosmic strings by black holes: loop formation*, (2006), arXiv: gr-qc/0609089v1 [gr-qc].
12. E.N. Zinchenko and S.N. Roshchupkin, Ukr. J. Phys. **47**, 113 (2002).
13. L.Ya. Arifov, E.N. Zinchenko, A.P. Lelyakov and S.N. Roshchupkin, Teor. Mat. Fiz. **141**, No. 2, 304 (2004).

PROSPECTS FOR THE ATLAS UPGRADE FOR THE HIGH LUMINOSITY LHC[1]

R. Brenner[2]
on behalf of the ATLAS collaboration

[2] *Uppsala University,*
Department of Physics and Astronomy, Sweden,
e-mail: richard.brenner@cern.ch

Abstract

The Large Hadron Collider (LHC) has by the discovery of the Higgs boson in 2012 successfully reached its first major research goal. In 2013 the CERN Council presented the updated strategy for particle physics where the LHC will continue to be the main infrastructure in Europe for the next decades. To maintain the physics potential of LHC the yearly integrated luminosity will need to be increased by a factor 10 compared to the original design value over the next decade. To achieve this the LHC machine will be upgraded in steps requiring two long shut-down periods. The ATLAS detector will need to correspondingly upgrade its detectors, trigger and data acquisition systems. The aim is to maintain a high data collection efficiency for Standard Model and Beyond Standard Model signals despite a much difficult environment caused by the increasing number of pileup events. Physics prospects for the ATLAS upgrade for the high luminosity LHC, as well as detector upgrades and their effects on the performance, are presented in the proceedings.

1. Introduction

The ATLAS Letter of Intent (LoI) [1] for a general-purpose pp experiment at the Large Hadron Collider(LHC) at CERN was submitted in 1992 followed by a Technical Design Report [2] in 1994.

[1] Received after the dead-line.

The detector was designed to identify as many signatures as possible using electron, photon, muon, jet, and missing transverse energy (energy not detected in the experiment) measurements, as well as b-jet tagging at $\sqrt{s} = 14$ TeV and a instantaneous design luminosity of 10^{34} cm^{-2}s^{-1}. The long life cycle of a modern particle physics experiment becomes rather obvious when counting 20 years from the LoI ATLAS to the discovery of the Higgs boson. Even if the project initially proposed still has many interesting years of data collection and analysis to come, the upgrade program has started in order for the new detector to be ready when the current detector has reached end of lifetime.

The most general motivation for upgrading an experiment with accuracy limited by statistics is to study the time required for the experiment to half the statistical error. In particle physics experiments this time increases in quadrature for a constant data rate hence the only way to significantly improve measurement precision over long time periods is to increase the data rate. For experiments at the LHC it means that the luminosity must increase for data to be produced and recorded with a higher rate. More data will also increase the sensitivity for rare physics processes that currently remain unaccessible.

2. LHC Upgrade Plan

In the first run period 2010–2012 the LHC provided pp-collisions at $\sqrt{s} = 7$–8 TeV and the ATLAS experiment collected around 25 fb^{-1} data. The highest luminosity and best beam quality was achieved with 50 ns bunch spacing. This is twice the design value. Despite running with half the number of bunches in the accelerator, a peak luminosity reaching 75% of the design value was obtained. The drawback for the ATLAS detector was that it had to cope with a more difficult background from in average 20.7 pile-up events per bunch crossing.

The LHC was shut down in February 2013 for the first long shutdown and it will resume collisions in 2015. The main shutdown activity is the consolidation of the high-current splices between the superconducting magnets which prevented the machine from running

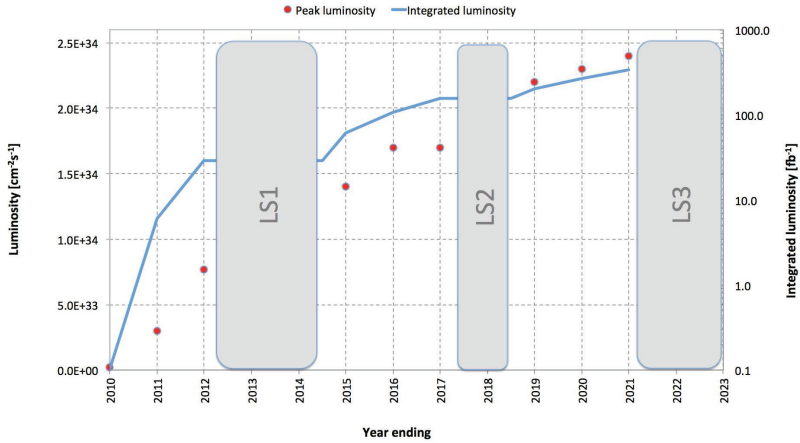

Fig. 1: The LHC upgrade plan. The peak luminosity is shown with red markers on the left axis. The integrated luminosity is shown with blue curve on the right axis [5]

at 14 TeV design energy. After the shutdown the LHC is expected to reach $\sqrt{s} = 13$–14 TeV with a peak luminosity of 1.7×10^{34} cm^{-2}s^{-1}. With higher energy and luminosity the bunch spacing has to be shortened to 25 ns for the pile-up condition to be tolerable to the experiments. Before the next long shutdown planned in 2018 the LHC is expected to deliver another 100 fb^{-1}. Improvements mainly in the injectors in the shutdown will further increase the peak luminosity to about 3 times the design value delivering 300 fb^{-1} to ATLAS in 3 years.

For the High Luminosity LHC (HL-LHC) major changes to the interaction region will be made which increases the yearly integrated luminosity to a peak luminosity limited to 5×10^{34} cm^{-2}s^{-1} not to exceed 200 pile-up events per bunch crossing. Luminosity levelling will be used to maintain this luminosity over a long time period [4]. The HL-LHC will be installed in a third long shut-down expected in 2021–2022. The goal is then to collect 3000 fb^{-1} data before the end of the HL-LHC project. Figure 1 presents the LHC upgrade schedule. A detailed description of the technical aspects of the LHC upgrade can be found in the report by the High Luminosity LHC project [3].

3. Physics Prospects of the ATLAS Detector

Many studies were done by the ATLAS collaboration to determine the detector requirements and to assess the physics potential of an upgraded ATLAS detector at HL-LHC. The studies were documented in a number of report submitted to the European strategy group for particle physics in 2012 [6]. It was assumed that the detector performance of the current detector will be maintained even at HL-LHC [7]. The detector and trigger will be designed to give offline trigger thresholds for single electrons of 25 GeV, photons and taus of 60 GeV and MET of 180 GeV. There is a strong connection between trigger thresholds and physics assumptions. Figure 2 shows the acceptance for three physics processes as a function of muon pt threshold. Higher threshold has a dramatic effect on acceptances.

Following the discovery of the Higgs boson the major goal for HL-LHC is to determine the nature of the new particle with the best possible precision. The study shows that the measurement precision of the Higgs boson can be improved by a factor 2-3 at HL-LHC [6]. Sensitivity to beyond Standard Model physics signatures scales rather well with centre-of-mass energy in the collisions but the dependence on luminosity is more complex. Studies of Super Symme-

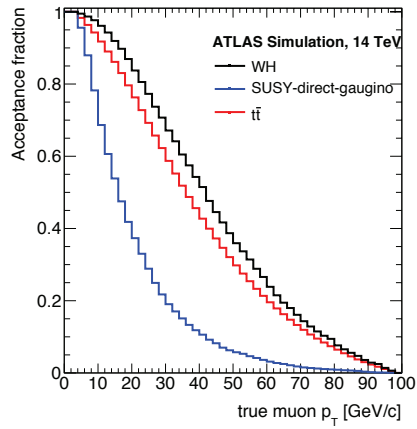

Fig. 2: Acceptance of muons from $t\bar{t}$, WH and SUSY processes as a function of true muon momentum

try show that the sensitivity to first and second generation squarks and gluinos improve by 400–500 GeV while the sensitivity to stops improve by 200 GeV [8]. The increase in sensitivity for studies of exotic signatures such as strongly- and weekly-produced $t\bar{t}$ resonances and narrow dilepton resonances is between 1.3 and 2.4 TeV [9].

4. ATLAS Upgrade Plan

The ATLAS detector need to be improved in many areas to take advantage from the higher luminosity [10], [11]. There are however constraints given by parts of the detector that cannot be replaced. The most important constraint comes from the Muon Drift Tubes (MDT) that are partially inaccessible hence cannot be replaced or upgraded.

The current tracking detector will reach end of its lifetime by the end of the decade. The leakage current and depletion voltage of the silicon detector layers are predicted with good accuracy by radiation damage models [12]. The depletion voltage for the innermost pixel and silicon strip layers have reached the limit of the High Voltage power supplies and cannot be run under full depletion. A second motivation for replacing the tracker is the intolerable occupancy in the Transition Radiation Tracker at high luminosity. The design and development of a new 200 m^2 Inner Tracker (ITK) entirely made of silicon sensors has already started to be ready for installation during the third long shutdown. By using new advanced materials, CO_2 cooling and by using a more efficient method for distributing power the radiation length of the new tracker will be twice longer than in the current tracker. This will reduce the particle conversions in the tracker for the benefit of the calorimeters and background.

A new trigger architecture will be introduced for HL-LHC. The new architecture has to be compatible with the operation of the MDT. Detailed investigations of the optimal parameters for the MDT at HL-LHC has been done. Based on that a new L0 trigger level was introduced. The L0 is very similar to the current L1 but running at 500 kHz acceptance rate compared to 75 kHz for the current L1. The L0 trigger will seed detector regions to be used in the L1 trigger decision. The new maximum L1 acceptance rate will be 200 kHz.

New for HL-LHC is the inclusion of the ITK in the L1 trigger. This is not possible in the current detector because of the short latency of the L1 trigger ($3\,\mu$s) and the long time required to read out the tracker. In the new trigger scheme the latency of the L1 trigger is extended to $20\,\mu$s. The data transfer from the ITK has been optimized by reading out only the part of the tracker required for the L1 trigger decision. This gives a data reduction of more than 90%.

Other major upgrade projects for improving the L1 trigger performance is the replacement of the front-end electronics in the calorimeters. The new electronics will be capable of transferring the all data off-detector at full event rate. This will allow the use of the full granularity in the L1 trigger. In addition to trigger tresholds based on energy sums more offline like feature like shape variables can be used in the L1 trigger. The calorimeter upgrade will already start during the second long shutdown. The L1 muon trigger will also be improved. A high granular muon detector detector, the New Small Wheel [13], will be installed in the end-cap between the current muon layers and the interaction point. This will reduce the high trigger rate that is mainly comming from fakes entering from the beam region. Two technologies, Micro Megas [14] and small Thin Gap Chambers [15], are developed to be used for the detector layer that will be installed in the second long shutdown.

5. Conclusions

The program for increasing the integrated luminosity in LHC by an order of magnitude has started. The background conditions for the ATLAS detector at HL-LHC will be challenging with up to 200 simultaneous pile-up events overlaying possible signals from interesting physics signatures. ATLAS will do many improvements to allow the detector to run at HL-LHC with trigger thresholds and sensitivity compatible with the current detector. The main upgrades are the replacement of the tracking detector and a new trigger scheme capable of higher trigger rate and with more advanced processing already at L1.

1. ATLAS Collaboration, ATLAS: letter of intent for a general-purpose pp experiment at the large hadron collider at CERN, CERN-LHCC-92-004; LHCC-I-2 (1992).
2. ATLAS Collaboration, ATLAS Technical Proposal for a General-Purpose pp Experiment at the Large Hadron Collider at CERN, CERN-LHCC-94-43; LHCC-P2 (1994).
3. High Luminosity LHC Project, `http://hilumilhc.web.cern.ch`
4. O.S. Brüning, HL-LHC Parameter Space and Scenarios, CERN-2012-006 and CERN-ATS-2012-069 (2012).
5. Review of LHC & Injector Upgrade Plans Workshop (RLIUP), `https://indico.cern.ch/conferenceDisplay.py?ovw=True&confId=260492`, (2013).
6. ATLAS Collaboration, Physics at a High-Luminosity LHC with ATLAS (Update), ATL-PHYS-PUB-2012-001; ATL-PHYS-PUB-2012-004 (2012).
7. ATLAS Collaboration, Performance assumptions for an upgraded ATLAS detector at a High-Luminosity LHC, ATLAS-PHYS-PUB-2013-004 (2013).
8. ATLAS Collaboration, Searches for Supersymmetry at the high luminosity LHC with the ATLAS Detector, ATL-PHYS-PUB-2013-002 (2013).
9. ATLAS Collaboration, Studies of Sensitivity to New Dilepton and Ditop Resonances with an Upgraded ATLAS Detector at a High-Luminosity LHC, ATL-PHYS-PUB-2013-003 (2013).
10. ATLAS Collaboration, ATLAS Phase-I Upgrade LoI, CERN-LHCC-2011-012; LHCC-I-020 (2011).
11. ATLAS Collaboration, ATLAS Phase-II Upgrade LoI, CERN-LHCC-2012-022; LHCC-I-023 (2012)
12. P.J. Dervan, T. Kondo, Performance and operation experience of the ATLAS Semiconductor Tracker, ATL-INDET-PROC-2013-009,(Submitted to PoS) (2013).
13. ATLAS Collaboration, New Small Wheel TDR, CERN-LHCC-2013-006; ATLAS-TDR-020 (2013).
14. Y. Giomataris *et al.*, *MICROMEGAS: A High granularity position sensitive gaseous detector for high particle flux environments*, Nucl. Instrum. Meth. A **37** (1996).
15. V. Smakhtin *et al.*, *Thin Gap Chamber upgrade for SLHC: Position resolution in a test beam*, Nucl. Instrum. Meth. A **598** (2009).

$t\bar{t}$ CHARGE ASYMMETRY AT HADRON COLLIDERS[1]

A. Chapelain

Irfu/SPP, CEA-Saclay, France
e-mail: antoine.chapelain@cea.fr

Abstract

We present the current status for the measurements of the $t\bar{t}$ charge asymmetry at the Tevatron and LHC colliders.

1. Introduction

At NLO, QCD predicts the top quark to be emitted preferentially in the direction of the incoming quark, while the top antiquark in the direction of the incoming antiquark. This charge asymmetry comes mainly from the interference between $q\bar{q} \rightarrow t\bar{t}$ tree diagram with the NLO box diagram, and from the interference of initial and final state radiations ($q\bar{q} \rightarrow t\bar{t}g$). Results from the CDF and D0 [3, 4] collaborations have driven a lot of attention because some of the measured asymmetries were significantly higher than the SM predictions. In this note we present the most recent results for the CDF, D0, ATLAS and CMS collaborations and compared them to the latest prediction based on the Standard Model [2].

2. Observables

The Tevatron and LHC colliders present different initial state particles at different energies. The Tevatron is a proton-antiproton collider at $\sqrt{s} = 1.96$ TeV and the LHC is a proton-proton collider at

[1]Received after the dead-line.

$\sqrt{s} = 7$ and 8 TeV. At the Tevatron $t\bar{t}$ pairs are mainly produced through quark-antiquark anihilation and there the laboratory frame is equivalent to the partonic rest frame. Thus at the Tevatron the charge asymmetry results into a forward-backward asymmetry (FB). At the LHC $t\bar{t}$ pairs are mainly produced through gluon-gluon fusion which does not contribute to the charge asymmetry. In the subdominant $q\bar{q} \to t\bar{t}$ process, the antiquark originates from the proton sea leading the $t\bar{t}$ system to be boosted in the direction of the top quark. Indeed the incoming quark carries on average a higher momentum than the incoming antiquark. In that case the charge asymmetry results into a forward-central asymmetry (FC).

We therefore define two different observables at the Tevatron and at the LHC to measure the $t\bar{t}$ charge asymmetry:

$$\text{Tevatron} \quad A_{FB}^{t\bar{t}} = \frac{N(\Delta y > 0) - N(\Delta y < 0)}{N(\Delta y > 0) + N(\Delta y < 0)}, \tag{1}$$

$$\text{where} \quad \Delta y = y_t - y_{\bar{t}},$$

$$\text{LHC} \quad A_C = \frac{N(\Delta|y| > 0) - N(\Delta|y| < 0)}{N(\Delta|y| > 0) + N(\Delta|y| < 0)}, \tag{2}$$

$$\text{where} \quad \Delta|y| = |y_t| - |y_{\bar{t}}|,$$

y_t and $y_{\bar{t}}$ are top quark and antiquark rapidity, respectively.

We also measure the $t\bar{t}$ charge asymmetry based on the leptons coming from the decay of the W boson coming from the top quark decay:

$$\text{Tevatron} \quad A^{\ell\ell} = \frac{N(\Delta\eta > 0) - N(\Delta\eta < 0)}{N(\Delta\eta > 0) + N(\Delta\eta < 0)}, \tag{3}$$

$$A_{\text{FB}}^{\ell} = \frac{N(q \times \eta > 0) - N(q \times \eta < 0)}{N(q \times \eta > 0) + N(q \times \eta < 0)}, \tag{4}$$

$$\text{where} \quad \Delta\eta = \eta_{\ell^+} - y_{\ell^-},$$

$$\text{LHC} \quad A_C^{\ell\ell} = \frac{N(\Delta|\eta| > 0) - N(\Delta|\eta| < 0)}{N(\Delta|\eta| > 0) + N(\Delta|\eta| < 0)}, \tag{5}$$

$$\text{where} \quad \Delta|\eta| = |\eta_{\ell^+}| - |\eta_{\ell^-}|,$$

η_{ℓ^+} and y_{ℓ^-} are positive and negative lepton pseudorapidity, respectively.

The interest of measuring such an asymmetry is that we do not need to reconstruct the $t\bar{t}$ kinematic and the lepton kinematic is well

measured. The leptonic asymmetry is also sensible to the top quark polarization if any.

3. Top Quark Signature and Reconstruction

The top quark decays almost 100% of the time into a W boson and in a b quark. We therefore classify the $t\bar{t}$ final state according to the W boson decay mode.

The ℓ+jets channel, where one W boson decays hadronically and the other leptonically, is characterized by one isolated lepton, at least four jets and missing energy due to the presence of a neutrino escaping the detector. This channel has a good production rate ($\sim 45\%$ of all $t\bar{t}$ events) and a reasonable amount of background. The main backgrounds in this channel are W+jets events estimated using simulation and data, and multijet production where one jet mimics a lepton. The later is estimated using data. The dilepton channel, where both W decay leptonically, is characterized by two oppositely charged leptons, at least two jets and missing energy due to the two neutrinos. This channel suffers from a smaller production rate ($\sim 5\%$) but has little background. The main backgrounds come from Drell-Yan process estimated using the simulation and W+jets and multijets background mimicking leptons estimated in data.

Beside the above requirement, the event selection, which aims at increasing the $t\bar{t}$ fraction in the analyzed sample, uses topological criteria as well as well as b-quark identification.

For the $t\bar{t}$-based asymmetry, the reconstruction of the $t\bar{t}$ kinematics is needed. This reconstruction is performed using kinematic fitters. In the reconstruction algorithm, the different lepton-jet permutations, the experimental resolutions, the b-quark identification are taken into account. The mass of the W boson and the top quark are fixed to their world average values within their widths. In the dilepton channel we additionally need to make some assumption about the neutrinos kinematic since their presence leaves the system unconstrained.

4. Measurement

After reconstruction the $t\bar{t}$ kinematic, we can measure the raw asymmetry, i.e. the asymmetry observed in the detector. To do so we

need to subtract the estimated background from data. At this level we cannot compare the measurements between experiments (CDF and D0 on the one hand and ATLAS and CMS on the other and) due to different detector effects and different acceptance cuts. The raw distribution need then to be unfolded to correct for these effects and get back to the production level asymmetry.

5. Results

Table 1 shows the inclusive production $t\bar{t}$-based and lepton-based asymmetries measured at the Tevatron compared to the predictions. We observe that there are differences up to about two standard deviations (SD) between measurement and predictions. Figure 1 shows the differential measurement of the $t\bar{t}$ asymmetry as a function of the invariant mass and the rapidity of the $t\bar{t}$ system performed by CDF [5]. We observe a significant difference between measurements and prediction up to about three SD. D0 does not observe such a difference.

Table 2 presents the inclusive production $t\bar{t}$-based and lepton-based asymmetries measured at the LHC compared to the predictions. The measurements are consistent with the predictions. ATLAS and CMS performed differential measurements of the $t\bar{t}$ asymmetry as a function the invariant mass, the transverse momentum and the rapidity of the $t\bar{t}$. We observe consistency between the measurements and the predictions also for for highly boosted $t\bar{t}$ system.

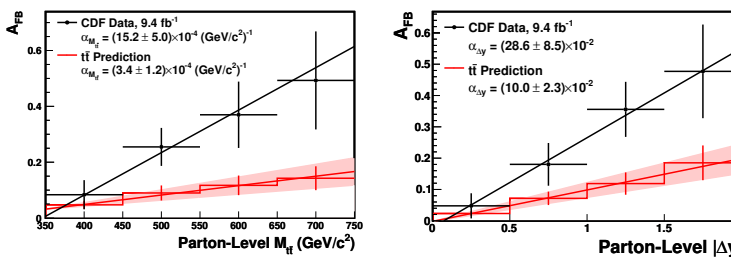

Fig. 1: $A_{\mathrm{FB}}^{t\bar{t}}$ as a function the invariant mass and rapidity of the $t\bar{t}$ system in CDF [5]

T a b l e 1: Inclusive production $t\bar{t}$-based and lepton-based asymmetry measured at the Tevatron. All values are given in %

	$A_{\mathrm{FB}}^{t\bar{t}}$			A_{FB}^{ℓ}			$A^{\ell\ell}$		
CDF ℓ+jets	16.4	$\pm$	4.5 [5]	9.4	$\pm$	$^{3.2}_{2.9}$ [6]		–	
CDF dilepton		–		7.2	$\pm$	6.0 [7]	7.6	$\pm$	8.1 [7]
D0 ℓ+jets	19.6	$\pm$	6.5 [4]	4.7	$\pm$	$^{2.6}_{2.7}$ [8]		–	
D0 dilepton		–		4.4	$\pm$	3.9 [9]	12.3	$\pm$	5.6 [9]
Prediction [2]	8.8	$\pm$	0.6	3.8	$\pm$	0.3	4.8	$\pm$	0.4

T a b l e 2: Inclusive production $t\bar{t}$-based and lepton-based asymmetry measured at the LHC. All values are given in %

	$A^{\ell\ell}$			$A_C^{\ell\ell}$		
ATLAS ℓ+jets	0.6	$\pm$	1.0 [10]		–	
ATLAS dilepton	5.7	$\pm$	2.8 [11]	2.3	$\pm$	1.4 [11]
CMS ℓ+jets	0.5	$\pm$	0.9 [12]		–	
CMS dilepton	5.0	$\pm$	$^{4.4}_{5.8}$ [13]	1.0	$\pm$	1.6 [13]
Prediction [2]	1.23	$\pm$	0.05	0.70	$\pm$	0.03

The final Tevatron measurements as well as the new LHC measurements performed at 8 TeV are expected to be published soon.

1. J. H. Kuhn, G. Rodrigo, Phys. Rev. Lett. **81** (1998) 49.
2. W. Bernreuther, Z.-G. Si, Phys. Rev. D **86**, 034026 (2012).
3. T. Aaltonen *et al.* (CDF Collaboration), Phys. Rev. D **83**, 112003 (2011).
4. V.M. Abazov *et al.* (D0 Collaboration), Phys. Rev. D **84**, 112005 (2011).
5. T. Aaltonen *et al.* (CDF Collaboration), Phys. Rev. D **87**, 092002 (2013).
6. T. Aaltonen *et al.* (CDF Collaboration), Phys. Rev. D **87**, 092002 (2013).
7. T. Aaltonen *et al.* (CDF Collaboration), CDF note 11035 (2013).
8. V.M. Abazov *et al.* (D0 Collaboration), D0 Note 6394-CONF (2013).
9. V.M. Abazov *et al.* (D0 Collaboration), arXiv:1308.6690 [hep-ex] (2013).
10. G. Aad *et al.* (ATLAS Collaboration), ATLAS-CONF-2013-078.
11. G. Aad *et al.* (ATLAS Collaboration), ATLAS-CONF-2012-057.
12. S. Chatrchyan *et al.* (CMS Collaboration), CMS PAS TOP-12-033.
13. S. Chatrchyan *et al.* (CMS Collaboration), CMS PAS TOP-12-010.

AUTHOR INDEX

New Trends in High-Energy Physics

Proceedings of the Conference
held in Alushta (Crimea) on September 23-29, 2013

Edited by
László Jenkovszky, Denis Savchenko and Georgiy Stelmakh